Atmos. Chem. Phys., 11, 6167–6183, 2011
www.atmos-chem-phys.net/11/6167/2011/
doi:10.5194/acp-11-6167-2011

Atmospheric Chemistry and Physics

A new method to detect long term trends of methane (CH_4) and nitrous oxide (N_2O) total columns measured within the NDACC ground-based high resolution solar FTIR network

J. Angelbratt[1], J. Mellqvist[1], T. Blumenstock[5], T. Borsdorff[4], S. Brohede[1], P. Duchatelet[2], F. Forster[4], F. Hase[5], E. Mahieu[2], D. Murtagh[1], A. K. Petersen[3,*], M. Schneider[5], R. Sussmann[4], and J. Urban[1]

[1]Chalmers University of Technology, Göteborg, Sweden
[2]Institute of Astrophysics and Geophysics, University of Liège, Liège, Belgium
[3]Institute of Environmental Physics, University of Bremen, Bremen, Germany
[4]Karlsruhe Institute of Technology (KIT), Institute for Meteorology and Climate Research (IMK-ASF), Garmisch-Partenkirchen, Germany
[5]Karlsruhe Institute of Technology (KIT), Institute for Meteorology and Climate Research (IMK-ASF), Karlsruhe, Germany
[*]present address: Max-Planck-Institute for Meteorology, Hamburg, Germany

Received: 21 December 2010 – Published in Atmos. Chem. Phys. Discuss.: 10 March 2011
Revised: 14 June 2011 – Accepted: 20 June 2011 – Published: 1 July 2011

Abstract. Total columns measured with the ground-based solar FTIR technique are highly variable in time due to atmospheric chemistry and dynamics in the atmosphere above the measurement station. In this paper, a multiple regression model with anomalies of air pressure, total columns of hydrogen fluoride (HF) and carbon monoxide (CO) and tropopause height are used to reduce the variability in the methane (CH_4) and nitrous oxide (N_2O) total columns to estimate reliable linear trends with as small uncertainties as possible. The method is developed at the Harestua station (60° N, 11° E, 600 m a.s.l.) and used on three other European FTIR stations, i.e. Jungfraujoch (47° N, 8° E, 3600 m a.s.l.), Zugspitze (47° N, 11° E, 3000 m a.s.l.), and Kiruna (68° N, 20° E, 400 m a.s.l.). Linear CH_4 trends between 0.13 ± 0.01-0.25 ± 0.02 % yr^{-1} were estimated for all stations in the 1996-2009 period. A piecewise model with three separate linear trends, connected at change points, was used to estimate the short term fluctuations in the CH_4 total columns. This model shows a growth in 1996–1999 followed by a period of steady state until 2007. From 2007 until 2009 the atmospheric CH_4 amount increases between 0.57 ± 0.22–1.15 ± 0.17 % yr^{-1}. Linear N_2O trends between 0.19 ± 0.01–0.40 ± 0.02 % yr^{-1} were estimated for all stations in the 1996-2007 period, here with the strongest trend at Harestua and Kiruna and the lowest at the Alp stations. From the N_2O total columns crude tropospheric and stratospheric partial columns were derived, indicating that the observed difference in the N_2O trends between the FTIR sites is of stratospheric origin. This agrees well with the N_2O measurements by the SMR instrument onboard the Odin satellite showing the highest trends at Harestua, 0.98 ± 0.28 % yr^{-1}, and considerably smaller trends at lower latitudes, 0.27 ± 0.25 % yr^{-1}. The multiple regression model was compared with two other trend methods, the ordinary linear regression and a Bootstrap algorithm. The multiple regression model estimated CH_4 and N_2O trends that differed up to 31 % compared to the other two methods and had uncertainties that were up to 300 % lower. Since the multiple regression method were carefully validated this stresses the importance to account for variability in the total columns when estimating trend from solar FTIR data.

Correspondence to: J. Mellqvist
(johan.mellqvist@chalmers.se)

1 Introduction

Methane (CH_4) and nitrous oxide (N_2O) are among the largest contributors to the greenhouse effect (IPCC, 2007).

The CH_4 concentration in the atmosphere is to a large extent determined by the removal caused by the hydroxyl radical (OH) in the troposphere and the strength of the surface emissions (Dlugokencky et al., 1994). The emission sources are due to microbial activity primarily under anaerobic conditions in wetlands, rice paddies and landfills. Other

important CH_4 emission sources are ruminants, natural gas leakage and fossil fuel and biomass burning. The amount of CH_4 in the atmosphere has increased during the later part of the twentieth century. Between 1978–1987 in situ measurements has shown that the growth rate was important, (i.e. $1.1\,\%\,yr^{-1}$), but during the late 1980 the growth rate was slowing down to $0.3–0.6\,\%\,yr^{-1}$ and even lower growth rates were reported during the 1990s (Simpson et al., 2006). In the early 2000s the CH_4 growth rate was nearly zero. During 2007 and 2008 however, CH_4 was on the rise again and global growth rates of $0.47 \pm 0.04\,\%\,yr^{-1}$ and $0.25 \pm 0.04\,\%\,yr^{-1}$ were reported each respective year (Dlugokencky et al., 2009).

In contrast to CH_4, the dominant N_2O source, both natural and anthropogenic, is microbial activity in soils. The source is strongly linked with the use of synthetic nitrogen fertilizers, which have increased during the later part of the twentieth century (Davidson, 2009). Other important N_2O sources include: biomass burning, sewers, livestock and emission from transport and industries. The main sink for N_2O is photodissociation in the stratosphere by ultraviolet light and reaction with excited oxygen atoms (Bates and Hays, 1967). Compared to the CH_4 trend, the N_2O accumulation in the atmosphere has been continuous. During the last three decades, the atmospheric N_2O burden has shown an almost (constant) linear increase with a reported annual change of $0.26\,\%\,yr^{-1}$ (IPCC, 2007).

This paper was carried out within the EU project HYMN (Hydrogen, Methane and Nitrous Oxide, http://www.knmi.nl/samenw/hymn/) and one of the goals was to improve and homogenize the CH_4 and N_2O retrievals from high-resolution solar FTIR (Fourier Transform Infra Red) measurements and to obtain, for both gases, total columns and vertical profiles as accurately as possible. Many of the participating ground-based FTIR stations have time series that cover 15 years of data or more and it is therefore possible and interesting to study long term trends. Trends from greenhouse gases from FTIR measurements have earlier also been performed within the EU project UFTIR (http://www.nilu.no/uftir/) (Vigouroux et al., 2008).

One advantage when using FTIR total columns for the estimation of long term trends is their insensitivity to local variations of the atmosphere. In addition, since the global circulation is zonal in the free troposphere and stratosphere, the air stays at approximately the same latitude and the measurement station will therefore represent the atmosphere at that latitude. Hence, only a few stations at different latitudes are needed to represent the whole atmosphere. One disadvantage with FTIR is the fact that the time series often are unevenly sampled since the solar absorption infrared measurements require clear sky conditions. Furthermore there are, for some stations, periods of missing data due to instrument failure and for the most northern stations because of the polar winter.

One of the common methods for estimating trends of atmospheric parameters is to use monthly average values (see for example Jones et al., 2009). The use of this method reduces the variability in the time series and removes the eventual periods of missing data. For an evenly sampled time series it is also possible to take the autocorrelation (also called serial correlation) into account (Tiao et al., 1990; Weatherhead et al., 1998). The FTIR data are autocorrelated on different timescales e.g., caused by meteorological patterns, seasonal cycles and other kinds of long-term variability. This correlation can best be described as a memory in the time series where a value at a certain time contains information of earlier values. Since our present FTIR time series include both unevenly sampling and in some instance significant gaps it is difficult to create representative monthly averages. It is for some stations even impossible without interpolation. We use instead a multiple regression model, including a linear trend, a seasonal component and anomalies from various atmospheric parameters to account for the time series variability and autocorrelation to estimate reliable trends. The method also gives a possibility to quantify the atmospheric parameters that affect the measured time series through their contributions to the fitted regression model.

2 FTIR measurements and data retrieval

In this paper we use total column time series of CH_4, N_2O, carbon monoxide (CO), hydrogen fluoride (HF) and ethane (C_2H_6) measured with FTIR spectrometers at four European stations, i.e. Jungfraujoch, Zugspitze, Harestua and Kiruna, within the NDACC network (Network for the Detection of Atmospheric Composition Change, http://www.ndsc.ncep.noaa.gov/). FTIR measurements have been performed since the mid 1990s, both in the Northern and Southern hemispheres. Information about the stations, instrumentations and retrievals are presented in Table 1. The CH_4 and N_2O trend analysis cover the 1996–2009 and 1996–2007 time periods, for respectively species.

All the FTIR spectrometers involved in this study operate in the mid infrared spectral region from $700\,cm^{-1}$ to $5000\,cm^{-1}$ (2 to 14 µm) and measure the molecular absorption of solar light in the atmosphere for a wide range of species. Derived atmospheric abundance is expressed in terms of total column, defined as the sum of molecules from the top of the atmosphere down to the measurement station, per unit area (often expressed as molecules per square centimetre). To be able to spectrally resolve the atmospheric absorption lines for a given species, high resolution spectrometers are needed. For the stations in this paper a typical spectral resolution of $0.0035–0.005\,cm^{-1}$ is used.

During the retrieval process a synthetic spectrum, based on a priori information of pressure, temperature, trace gas profiles and instrumental characteristics, is calculated, by utilizing a forward model, dividing the atmosphere into 41–66 layers and calculating the light propagation through these. The calculated spectrum is then fitted to the FTIR measurements

Table 1. FTIR stations included in the trend study.

	Jungfraujoch	Zugspitze	Harestua	Kiruna
Latitude (° N)	47	47	60	68
Longitude (° E)	8	11	11	20
Altitude (m a.s.l)	3600	3000	600	400
Instrument type	Bruker 120HR	Bruker 125HR[a]	Bruker 125M[b]	Bruker 125HR[c]
Retrieval code	SFIT2	SFIT2	SFIT2	PROFFIT
No. of measurement days, CH_4	1135	818	599	642
No. of measurement days, N_2O	1160	739	592	765

[a] before 2006 Zugspitze operated a Bruker 120HR, [b] before 2008 Harestua operated a Bruker 120M and [c] before 2007 Kiruna operated a Bruker 120HR.

by varying the mixing ratio profile of the target species together with interfering species such as H_2O and CO_2. In this manner vertical profile of the target species can be obtained. These are generally calculated into total columns using the available pressure and temperature information but for some species the data can also be divided into partial columns for instance dividing the total column into a tropospheric and stratospheric part. The height information available from the spectra is usually defined as the degrees of freedom (DOFs) which is obtained from averaging kernel calculations according the principles described by Rodgers (2000).

The retrievals in this paper are performed by the two algorithms SFIT2 (Rinsland et al., 1998) and PROFFIT (Hase et al., 2004). The two codes have been shown to be in excellent agreement with a deviation of only 1 % or less (Hase et al., 2004). To quantify the instrument performance regarding line broadening and phase shift gas-cell measurements are done regularly on all instruments. These measurements are evaluated with the LINEFIT program (Hase et al., 1999).

The CH_4 and N_2O retrievals are done with a common strategy developed within the EU project HYMN, where the micro-windows, spectroscopic line lists, retrieval parameters, sources of ancillary data like pressure-temperature profiles, and water vapour data for deriving dry air columns are identical for all involved stations and used to minimize the biases between the stations.

In an earlier FTIR trend study by Gardiner et al. (2008), the retrievals were carried out by the optimal estimation algorithm (Rodgers, 2000). In this retrieval algorithm a cost function is minimized which corresponds to a weighted combination of a multiple least square solution and the a priori information. In the case of CH_4 and N_2O severe oscillations in the profiles are obtained and therefore instead a retrieval algorithm based on Tikhonov regularization (Twomey, 1996) has been applied to minimize this problem. In the latter retrieval algorithm, a cost function is minimized which corresponds to a weighted combination of a multiple least square solution and a cost term that corresponds to the first derivative of the vertical profile. The latter term minimises oscillations of the retrieved profile versus height but reduces the profile information to 2–3 independent partial columns (DOFs). For more information regarding FTIR retrieval with Tikhonov see Sussmann and Borsdorf (2007) and Sussmann et al. (2005).

Table 2. Microwindows with interfering species used to retrieve the CH_4 and N_2O total columns.

Species	Microwindows (cm^{-1})	Interfering species
CH_4	2613.70–2615.40	HDO, CO_2
	2650.60–2651.30	HDO, CO_2
	2835.50–2835.80	
	2903.60–2904.03	NO_2
	2921.00–2921.60	H_2O, HDO, NO_2
N_2O	2481.28–2482.62	CO_2, CH_4
	2526.40–2528.20	CO_2, CH_4, HDO
	2537.84–2538.82	CH_4
	2540.00–2540.75	CH_4

In Table 2 information regarding the HYMN micro windows and interfering species are presented. For both CH_4 and N_2O Hitran 2004 linelist parameters are used.

The CO, C_2H_6 and HF total columns, used as atmospheric parameters in the multiple regression model, are retrieved with standard procedures that have earlier been developed within the NDACC community (Mellqvist et al., 2002) (De-Mazière et al., 2005). The retrieval procedure varies slightly from site to site but uses consistent micro window regions for CO (2057–2159 cm^{-1}), C_2H_6 (2976–2977 cm^{-1}) and HF (4038–4039 cm^{-1}).

3 The Odin satellite

The Sub-Millimeter Radiometer (SMR) onboard the Odin satellite, launched in Febuary 2001, observes thermal emission of a N_2O line at 502.3 GHz at the Earth limb. Measurements of the global N_2O field are obtained during about 15 (near polar, sun-synchronous) orbits per observation day

and were performed time-shared with other operation modes on every third day until April 2007 and on every second day since then, providing a quasi-continuous N_2O data set from 2001 to 2010. N_2O in the stratosphere is retrieved between roughly 12–14 km and 60 km with a vertical resolution of about 1.5 km and a single-scan precision of 10–15 % (below 30 km). For the here relevant level-2 data version 2.1 See e.g. Murtagh et al. (2002); Urban et al. (2005b,a); Urban (2006); and Strong et al. (2008) for a description of the Odin mission and information of the N_2O measurements, error analysis and validation studies.

4 Trend method

4.1 Linear regression

Regression analysis is a technique to study the connection between a dependent variable and one or several independent variables. In this paper we mean the dependency between the independent variable, time, and the dependent variable, the measured total column time series. The simplest way to detect a trend is by fitting a straight line with the least squares method to the data, the slope of the line then represents the trend. The estimated trend itself is of limited use without an estimate of its error which could be represented with a confidence interval. When calculating a trend and its confidence interval three assumptions are usually made: (1) the residuals (measured-model) are assumed to be free from autocorrelation, (2) the distribution of the residuals is assumed to be approximately normally distributed and (3) the residuals are assumed to have equal variance. Large deviations from these assumptions will result in errors in the estimated trends and its confidence intervals (Weatherhead et al., 1998; Tiao et al., 1990). Methods have been developed to account for autocorrelation when estimating trends but they all need data which have equidistant time steps between the measurements. However, due to local weather conditions and available sunlight hour's time series derived from FTIR observations are not sampled evenly and typically contain gaps. It is hence not possible to make representative weekly or monthly averages and thereby get time series with constant time spacing. To reduce the time series variability and estimate reliable trends a multiple regression model is used in this paper.

4.2 Atmospheric parameters

Several atmospheric parameters that are assumed to affect the measured total column of CH_4 and N_2O are discussed in this section. Data from the Harestua station have been used to test the effect of various atmospheric parameters on the measured total columns of CH_4 and N_2O. The parameters that have shown to have a significant effect on the measured total columns of CH_4 and N_2O at the Harestua station have then been applied to the FTIR data from the other participating stations.

Changes in the *air pressure* due to meteorological fluctuations will change the amount of molecules above the measurement station. A high pressure is expected to result in a high total column and vice versa. CH_4 and N_2O have their highest partial columns close to ground level, where they are intensively produced, and are therefore expected to be very sensitive to fluctuations in the air pressure. The *tropopause height* is expected to affect the stratospheric column of CH_4 and N_2O but also to stretch and compress the tropospheric column. A low tropopause height is thought to make the tropospheric contribution to the total column smaller and a high larger. The tropopause height data used here are from the ECMWF (European Centre for Medium Range Weather Forecasts, http://www.ecmwf.int/) model that defines the tropopause altitude as the lowest level where the lapse rate is $2\,^{\circ}\mathrm{C\,km^{-1}}$or less and no height within 2 km above this point exceeds this value. To account for the presence of the polar vortex a range of *PV (polar vorticity)* values, at different altitudes (10–25 km), is obtained from the ECMWF model. A high PV value is expected to correspond to the presence of vortex air above the measurements site and hence a low stratospheric column of CH_4 and N_2O.

The total column of the stratospheric species HF has been used in several other studies, among them Toon et al. (1997) and Mellqvist et al. (2002), as a proxy for stratospheric transport. This transport involves the downward motion of airmasses when the station is inside the polar vortex, the changes in tropopause height and the vertical and horizontal motion of air masses in the stratosphere. Hence, a large *total column of HF* is expected to result in a large stratospheric and a small tropospheric column of CH_4 and N_2O.

CH_4, N_2O, CO and C_2H_6 are all produced in fossil fuel and biomass burning. The *total columns of CO and* C_2H_6 are therefore used as a proxy for large scale biomass burning events as the ones present in Canada and Russia during the summers of 1998, 1999, 2002 and 2003 (Yurganov et al., 2004,2005). The *total columns of* C_2H_6 will in addition be used as a proxy for natural gas leakage. This has, as to our knowledge, not been tested on CH_4 and N_2O FTIR total columns before.

Other physical parameters that have been investigated are: the number of sunspots, the North Atlantic Oscillations (NAO) and the Quasi Biennial Oscillations (QBO).

4.3 Trend model

To estimate trends in the CH_4 and N_2O total column time series a multiple regression model is used. In the model we try to explain as much as possible of the structures in the measured total column of CH_4 and N_2O with atmospheric parameters, a background trend and a seasonal component. The background trend is represented by one or several continuous linear trends according to the piecewise regression concept described by Neter et al. (1990). The seasonal component consists of a sine function with a phase which has a period

of 12 months. The 12 month seasonal cycle is strongest at the high altitude stations due to the well mixed air i.e. the low influence of local sources. A more advanced representation of the seasonal cycle, a third order Fourier series, has also been tested in the model but did not improve the model compared to the basic one. To explain the time series variability, i.e. short term deviations from the background trend and seasonal fluctuations, anomalies derived from some of the atmospheric parameters described in Sect. 4.2 are used. These anomalies correspond to the detrended and deseasonalized time series of the atmospheric parameters.

To find the anomalies that affect the CH_4 and N_2O total columns all derived anomalies are inserted into the multiple regression model, presented in Eq. (1), and tested with the stepwise regression method. This means that the combination of anomalies that gives the best adjusted R^2 value and are statistically significant are used in the final trend model and all the others being excluded. We define statistically significant as a parameter for which the confidence interval excludes zero on a 2-σ level.

To estimate trends the anomalies found with the stepwise approach, the background trend and the seasonal component are inserted in the model in Eq. (1) and solved with the least squares method.

$$y = \beta_0 + \beta_1 \sin(2\pi t) + \beta_2 \cos(2\pi t) + \sum_{i=3}^{I} \beta_i a(t)_{i-2} + \beta_{I+1} t + \beta_{I+2}(t - \mathrm{cp1})A + \beta_{I+3}(t - \mathrm{cp2})B + \varepsilon$$

$$\text{where} \begin{cases} t > \mathrm{cp1}, \mathrm{A} = 1 \\ t \leq \mathrm{cp1}, \mathrm{A} = 0 \\ t > \mathrm{cp2}, \mathrm{B} = 1 \\ t \leq \mathrm{cp2}, \mathrm{B} = 0 \end{cases} \quad (1)$$

Where t is the time in fraction of years and cp1 and cp2 are change points when the trend is expected to change direction or magnitude. For CH_4, possible change points in 1999 and 2007 have been reported by Dlugokencky et al. (2003, 2009) who have made global in situ measurements. In a first trend estimation no change points will be used for CH_4 and N_2O while in a second estimation the change points of Dlugokencky et al. (2003, 2009) will be used for CH_4. When no change points are used only the first trend term in Eq. (1) will be present in the model. In Eq. (1) y is the dependent variable (CH_4 or N_2O) and β corresponds to the regression coefficients. The $a(t)_i$ terms represent the anomalies from the atmospheric parameters (i to I) and ε is the residual or unexplained part of the model. The term is assumed to be normal distributed with a constant variance around zero and free from auto correlation. In the regression model the anomalies, $a(t)_i$, t and y must all be of the same length. This means that for a certain day in the CH_4 or N_2O time series there must exist corresponding data for all of the calculated anomalies.

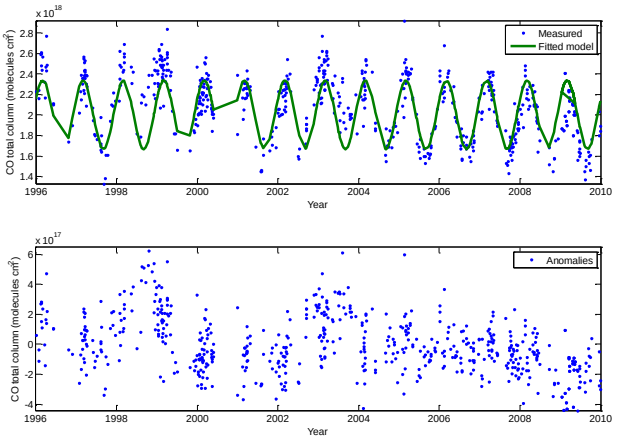

Fig. 1. Measured total column of CO at Harestua with fitted model (upper panel) and calculated anomalies (lower panel). To obtain the anomalies the fitted model is subtracted from the measured time series.

To estimate confidence intervals for the trends a method for hypothesis testing described by Montgomery et al. (2008) is used.

4.4 Deriving anomalies

To obtain anomalies from the atmospheric parameters presented in Sect. 4.2, a model consisting of a seasonal function and a polynomial with varying order is fitted to each of the atmospheric parameters, Eq. (2). The fitted model is then subtracted from the original atmospheric time series. To find the optimal polynomial fit for each atmospheric parameter the adjusted R^2 value is used (Montgomery et al., 2008). The value reflects the correlation between the model and the measurements and adjusts this correlation to the number of terms used in the regression model. If no adjustment is used the correlation always increase when increasing the number of terms in the regression model, this favours over fitting. An adjusted R^2 value close to one indicates a small residual and a good model fit while zero indicates the opposite.

$$y = \beta_0 + \beta_1 \sin(2\pi t) + \beta_2 \cos(2\pi t) + \beta_3 t + \beta_4 t^2 + \beta_5 t^3 \quad (2)$$

In Eq. (2) y is the dependent variable i.e. the atmospheric parameters (air pressure, tropopause height and so on) and β are the estimated regression coefficients. The optimal polynomial for each atmospheric process is found by step wise increasing the polynomial order, fit the models with the linear regression method and calculated the adjusted R^2 value. When the adjusted R^2 value no longer increases with more than 1 % the best fit is said to be found and the corresponding polynomial order is used to derive the anomaly. In Fig. 1 an example of the derived anomalies from the Harestua total column time series of CO is presented.

5 Results

5.1 Anomalies in the final regression model

The anomalies shown to affect the measured total columns of CH_4 are: the air pressure, the total column of CO and HF and the anomalies that affect the N_2O total columns are: the air pressure the total column of HF and the tropopause height. The air pressure, CO and tropopause height anomalies are derived using Eq. (2) along with a linear trend. For HF a second order polynomial is used in Eq. (2) for Harestua, Jungfraujoch and Zugspitze while a linear trend is used for the fit of the Kiruna dataset.

The stepwise regression model that was applied on the Harestua data showed a final model where C_2H_6 where included instead of CO, this due to a slightly higher adjusted R^2 value. At the time of performing the stepwise test not all stations were retrieving C_2H_6. Instead CO has to be used in the final model. Since C_2H_6 and CO shows a strong correlation this practical simplification was assumed to work properly. The linear correlations between all the tested anomalies are presented in Table 3. Except the CO-C_2H_6 correlation a slightly weaker correlation can be seen for the air pressure and the tropopause height. The other anomalies have much weaker or no linear correlations.

The final regression coefficients of the stepwise regression model for Harestua are presented in Table 4. In the table it can be seen that the air pressure and the total column of HF and CO is significant for both CH_4 and N_2O. PV375 is also significant for CH_4 and the tropopause height is significant for N_2O. Although their significance not all parameters are included in the final model due to the fact that the adjusted R^2 value not is improved.

The reduction of the variability in the CH_4 and N_2O time series due to the addition of anomalies are presented in Fig. 2a and b, respectively. The reduction is calculated by comparing the standard deviation of the residuals when only offset and linear trend/trends is fitted to the data with the standard deviations derived when each of the anomalies and the seasonal function is added to the trend model. The seasonal function accounts for a few to roughly 18 % of the variability of the two CH_4 cases. The value is slightly higher for N_2O which show up to 22 %. For both species the seasonal function has the greatest impact at Jungfraujoch and smallest at Harestua. In the two CH_4 cases the air pressure anomaly accounts for 30–40 % of the variability. The corresponding value for N_2O is roughly 30 %. The HF anomaly reduces the variability more for N_2O, ∼11–18 %, than for CH_4, ∼2–10 %. The anomalies from CO and tropopause height corresponds both to a variability reduction of a couple of percent each. There is still place for improvements in the trend model since 30–55 % of the variability is unexplained, depending on station and species. This has partly to do with the measurement noise from the instrument but most likely also with atmospheric processes not captured in this paper.

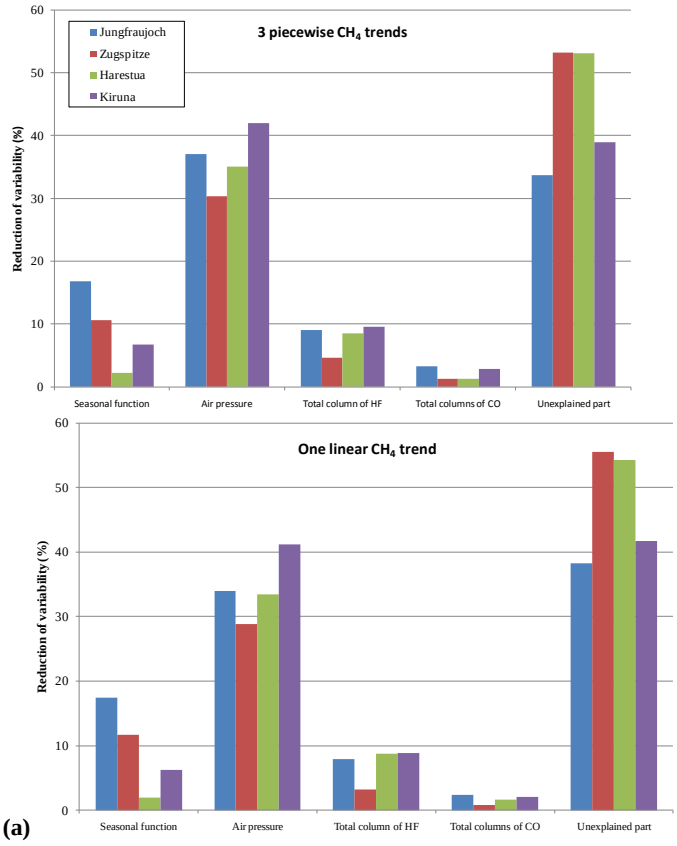

Fig. 2a. Reduction of the variability in the CH_4 time series from the anomalies and seasonal function in the regression model, presented as percent of total variability. The upper panel is when three piecewise trends are used and the lower is when a single linear trend is used.

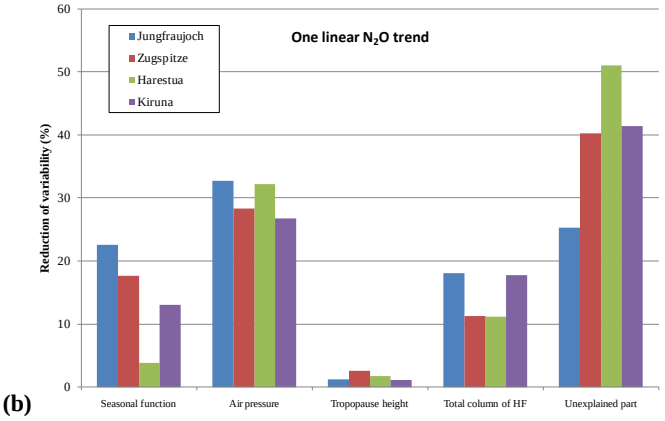

Fig. 2b. Reduction of the variability in the N_2O time series from the anomalies and seasonal function in the regression model, presented as percent of total variability.

It can be seen that the reduction of variability by each anomaly are fairly similar for all stations and species, this strengthen the choice of anomalies that are used in the trend

Table 3. Linear correlation calculated from the anomalies at the Harestua site. Correlations stronger or equal to 0.60 is marked in bold.

	CO	C_2H_6	HF	Trop. h.	Air pres.	PV475	PV400	PV350	Sunsp.	NAO	QBO
CO	1.00	**0.72**	0.16	0.22	0.29	0.19	−0.04	−0.01	0.00	0.05	0.01
C_2H_6	**0.72**	1.00	0.26	−0.11	0.00	0.24	−0.02	0.00	0.00	0.05	0.08
HF	0.16	0.26	1.00	−0.16	−0.21	0.51	−0.05	0.03	0.14	−0.07	−0.02
Trop. h.	0.22	−0.11	−0.16	1.00	**0.60**	0.13	0.02	−0.02	−0.08	0.03	−0.05
Air pres.	0.29	0.00	−0.21	**0.60**	1.00	0.03	−0.02	−0.04	−0.09	0.02	−0.07
PV475	0.19	0.24	0.51	0.13	0.03	1.00	0.04	0.02	−0.07	−0.08	−0.01
PV400	−0.04	−0.02	−0.05	0.02	−0.02	0.04	1.00	0.05	−0.04	0.00	0.05
PV350	−0.01	0.00	0.03	−0.02	−0.04	0.02	0.05	1.00	−0.05	−0.03	0.03
Sunsp.	0.00	0.00	0.14	−0.08	−0.09	−0.07	−0.04	−0.05	1.00	−0.09	0.04
NAO	0.05	0.05	−0.07	0.03	0.02	−0.08	0.00	−0.03	−0.09	1.00	0.01
QBO	0.01	0.08	−0.02	−0.05	−0.07	−0.01	0.05	0.03	0.04	0.01	1.00

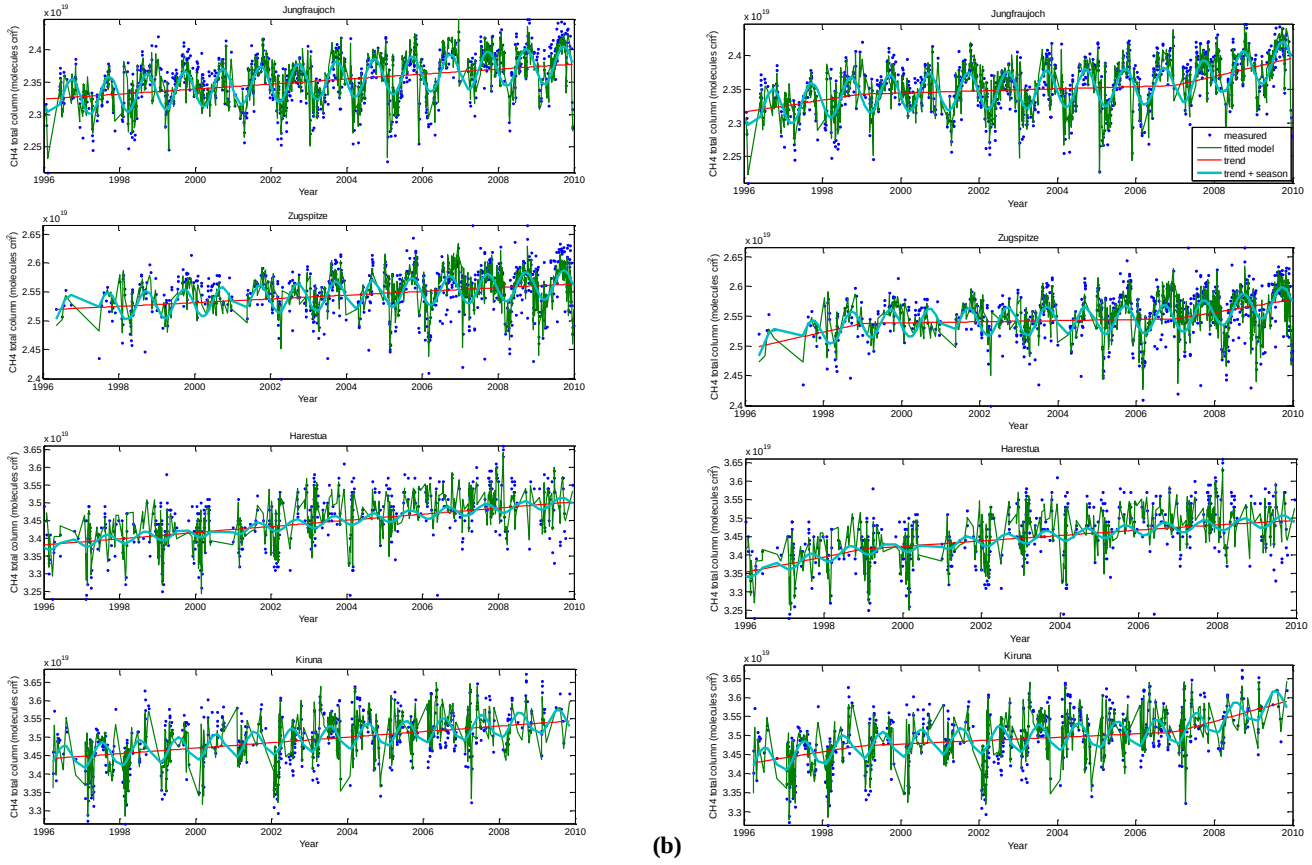

Fig. 3. CH_4 total column time series for all participating FTIR stations with fitted model, linear trend and seasonal cycle. The model is displayed in green and the measurements in blue, the seasonal cycle is displayed in thick cyan and the linear trend in red.

model. Although the small variability reduction by CO and tropopause height that is showed in this paper these anomalies can have larger effects on the estimated trends if the start and/or end period is chosen when there is strong forest fires or atmospheric dynamics.

5.2 CH_4 trends

The estimated linear trends from the multiple regression model are presented in Table 5 and the fitted models to the CH_4 time series are presented in Fig. 3a for the linear trend and Fig. 3b for the piecewise linear trends. For all

Table 4. Regression coefficients with associated 2-σ confidence intervals of the stepwise regression model used on the CH_4 and N_2O total columns of the Harestua data. Statistical significant anomalies are marked in bold.

Anomaly	CH_4	N_2O
CO	$\mathbf{9.8\times 10^{15}\pm 4.0\times 10^{15}}$	$\mathbf{1.9\times 10^{15}\pm 8.6\times 10^{14}}$
HF	$\mathbf{-1.4\times 10^{16}\pm 1.8\times 10^{15}}$	$\mathbf{-3.4\times 10^{15}\pm 4.0\times 10^{14}}$
Tropopause height	$2.1\times 10^{15}\pm 3.2\times 10^{15}$	$\mathbf{7.7\times 10^{14}\pm 7.0\times 10^{14}}$
Air pressure	$\mathbf{3.3\times 10^{17}\pm 2.8\times 10^{16}}$	$\mathbf{6.9\times 10^{16}\pm 6.0\times 10^{15}}$
PV475	$2.6\times 10^{14}\pm 1.4\times 10^{15}$	$-2.2\times 10^{13}\pm 2.9\times 10^{14}$
PV400	$5.7\times 10^{14}\pm 1.4\times 10^{15}$	$-3.4\times 10^{13}\pm 3.1\times 10^{14}$
PV350	$\mathbf{2.0\times 10^{15}\pm 1.4\times 10^{15}}$	$1.6\times 10^{14}\pm 3.5\times 10^{14}$
No. of sunspots	$-4.9\times 10^{14}\pm 4.9\times 10^{14}$	$9.4\times 10^{13}\pm 7.9\times 10^{13}$
NAO	$-3.6\times 10^{12}\pm 2.3\times 10^{13}$	$-1.7\times 10^{11}\pm 5.8\times 10^{11}$
QBO	$-2.2\times 10^{12}\pm 2.6\times 10^{13}$	$3.0\times 10^{11}\pm 2.0\times 10^{12}$

Table 5. Estimated linear trends from the multiple regression model. The trends are given as total column and as percent relative the average value of year 2000. The confidence limits for each trend are based on a 2-σ significance level.

	Time period		Jungfraujoch (47° N, 8° E)	Zugspitze (47° N, 11° E)	Harestua (60° N, 11° E)	Kiruna (68° N, 20° E)
CH_4	1996–2009	mol cm^{-2} 10^{16}	3.85 ± 0.13	3.24 ± 0.29	8.63 ± 0.52	7.5 ± 0.38
		% yr^{-1}	0.16 ± 0.01	0.13 ± 0.01	0.25 ± 0.02	0.21 ± 0.01
	1996–1999	mol cm^{-2} 10^{16}	9.00 ± 0.92	14.60 ± 0.95	20.80 ± 3.53	16.10 ± 2.65
		% yr^{-1}	0.38 ± 0.04	0.57 ± 0.04	0.61 ± 0.10	0.46 ± 0.08
	1999–2007	mol cm^{-2} 10^{16}	1.57 ± 1.97	0.95 ± 1.96	7.39 ± 7.54	4.45 ± 5.68
		% yr^{-1}	0.07 ± 0.08	0.04 ± 0.08	0.22 ± 0.22	0.13 ± 0.16
	2007–2009	mol cm^{-2} 10^{16}	21.10 ± 1.79	24.50 ± 1.34	19.70 ± 7.54	40.30 ± 5.92
		% yr^{-1}	0.90 ± 0.08	0.96 ± 0.05	0.57 ± 0.22	1.15 ± 0.17
N_2O	1996–2007	mol cm^{-2} 10^{15}	8.6 ± 0.26	8.5 ± 0.56	23.6 ± 1.25	17.2 ± 1.40
		% yr^{-1}	0.21 ± 0.01	0.19 ± 0.01	0.40 ± 0.02	0.29 ± 0.02

participating stations significant trends at the 2-σ level are found for the period of 1996–2009. The trends vary with latitude and weaker trends are observed at Jungfraujoch and Zugspitze (0.16 ± 0.01 % yr^{-1} and 0.13 ± 0.01 % yr^{-1}) and stronger trends at Harestua and Kiruna (0.25 ± 0.02 % yr^{-1} and 0.21 ± 0.01 % yr^{-1}). The trends at the Alpine stations are as expected in close agreement to each other due to their close geographical location. Earlier Gardiner et al. (2008) have estimated linear trends for FTIR data and these trends are close to the estimated ones in this paper, i.e. 0.40 ± 0.06 % yr^{-1} for Harestua and 0.17 ± 0.03 % yr^{-1} for Jungfraujoch. The data in the earlier paper corresponds to the years 1995–2004 and they were retrieved with standard optimal estimation as explained earlier and the trend were derived with the Bootstrap method, see discussion below.

Dlugokencky 2009 reports an increased CH_4 growth in 2007 and 2008 based on global averages from in situ flask samples. The same author has also reported a near zero trend between 1999 and 2007 and a positive trend before that. To investigate if these features also are present in the FTIR data we have applied piecewise regression (Neter et al., 1990) with three independent linear trends, choosing 1999 and 2007 as changing points in the trend model, Table 5. For all stations significant positive CH_4 growth rates are found for the 1996–1999 time period. The estimated values are between 0.38 % yr^{-1} and 0.61 % yr^{-1}. This could be compared with the globally averaged surface trend value of 0.45 % yr^{-1} based on the time period of 1984-1999 reported by Dlugokencky et al. (2003). For each station involved, no significant trends have been deduced for CH_4 for the 1999-2007 time period, this is in agreement with global surface CH_4 data for the time period of 2000–2006 (Dlugokencky et al., 2009). From 2007 to 2009 we found increased growth rates for all participating stations ranging

from 0.57–1.15 % yr^{-1}. The station with largest growth rate is Kiruna for which a positive value of 1.15 ± 0.17 % yr^{-1} is found. For comparison, Dlugokencky et al. (2009) report global averaged surface values of 0.47 ± 0.03 % yr^{-1} for 2007 and 0.25 ± 0.03 % yr^{-1} for 2008. The same authors also report a 0.78 ± 0.07 % yr^{-1} growth value for the polar northern latitudes in 2007 and 0.46 ± 0.09 % yr^{-1} for the low northern latitudes in 2008. The increased growth rates seen by Dlugokencky et al. (2009) for 2007 and 2008 is hence also observed at all FTIR stations.

5.3 N_2O trends

The fitted N_2O models are presented in Fig. 4 and the estimated trends are listed in Table 5. The N_2O trends vary from approximately 0.2 ± 0.01 % yr^{-1} at Jungfraujoch and Zugspitze to 0.29 ± 0.02 and 0.4 ± 0.02 % yr^{-1} at the two stations located further north. Earlier IPCC (2007) has reported a N_2O trend for the last decade of 0.26 % yr^{-1}. This trend is verified by in situ measurements by Haszpra et al. (2008) and total columns by Rinsland et al. (2009) who both report trends of 0.25 ± 0.003 % yr^{-1}. The estimated N_2O trends for Jungfraujoch and Zugspitze are a bit weaker than the earlier reported trends but in close agreement to each other. The trends for Kiruna and especially Harestua are stronger than the reported trends and are not in agreement with each other. This trend discrepancy is unexpected since N_2O is well mixed in the atmosphere due to its tropospheric lifetime of 114 years (Davidson, 2009). To exclude that instrumental errors are the cause for the deviating N_2O trends we have estimated total column trends also for CO_2 from Harestua and Kiruna. CO_2 was used because its atmospheric circulation time is similar to the lifetime N_2O and that both of the species are measured with the same type of detector (InSb detector). The CO_2 retrieval was conducted in the 2620-2630 cm^{-1} region with Hitran08 line parameters (R. Kohlhepp and F. Hase, private communication, 2010). The estimated CO_2 trends for the two stations showed to be very similar, 0.50 ± 0.06 % yr^{-1} for Harestua and 0.56 ± 0.04 % yr^{-1} for Kiruna on a 2-σ basis and this corresponds well to the in situ trend of roughly 0.51 % presented by IPCC (2007) (the trend is based on an increase of 19 ppm from 1995 to 2005). From this test it is concluded that the FTIR instruments at Harestua and Kiruna behaved well during the studied period.

To further investigate the trend discrepancy between the FTIR stations trends we derived tropospheric- and stratospheric partial columns from the FTIR data at each station. The partial columns was derived with a weight function described by Gardiner et al. (2008) which use the average tropopause height and its standard deviation, here taken from the ECMWF model. The trends in the partial columns were estimated with a function consisting of a linear trend and a seasonal cycle with a phase. All the estimated tropospheric trends were in the range of 0.19 ± 0.01 % yr^{-1} to 0.28 ± 0.03 % yr^{-1} while the stratospheric trends showed large inter station variability with strong positive trends at Harestua and Kiruna and weak positive trends at Jungfraujoch and Zugspitze, Table 6. Earlier, Gardiner et al. (2008) also showed this behaviour.

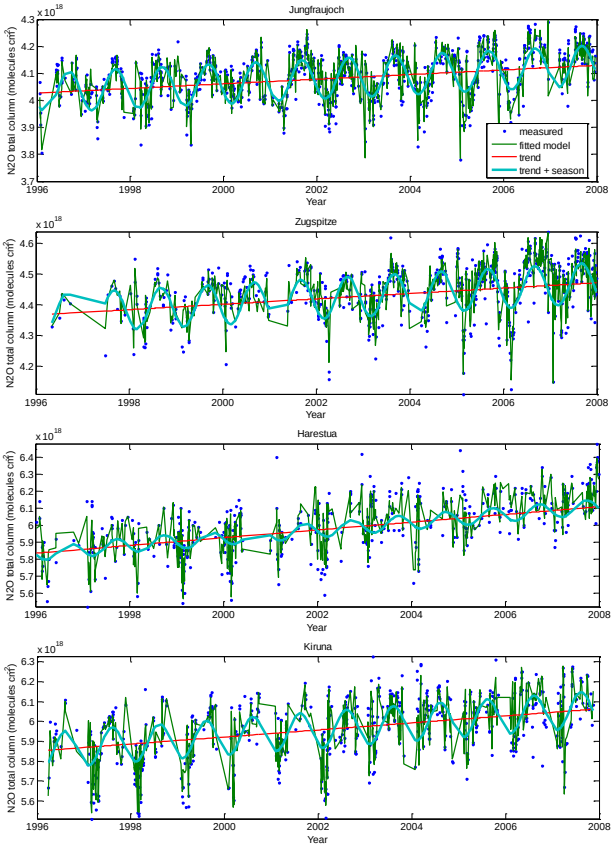

Fig. 4. As Fig. 3a but for N_2O total columns.

To verify the latitudinal differences in stratospheric N_2O trends detected by the solar FTIR measurements a comparison with N_2O limb measurements from the Odin satellite, see Sect. 3 was carried out. To get a rough estimation of the stratospheric N_2O columns at three locations (Jungfraujoch/Zugspitze, Harestua and Kiruna) SMR data were retrieved from altitudes covering 14–30 km within a radius of 500 km centred at each location. The satellite data quality in terms of measurement response and retrieval error were studied for all three locations and shown to be close to one and random scattered at approximately 10 % respectively. The stratospheric N_2O trends from the SMR instrument data were calculated with the same trend model as the tropospheric and stratospheric partial columns. The outcome of the trend study is presented in Table 6 and in Fig. 5. The rough FTIR-satellite comparison indicates that the stratospheric N_2O trends can vary with latitude. This has to the authors' knowledge not been reported before. The strongest positive trends for both FTIR and satellite data are estimated

Table 6. Stratospheric N_2O trends from SMR and FTIR data presented in % yr^{-1}. The trends are presented with associated 2-σ confidence intervals and use the 2005 average partial column as reference.

	Jungfraujoch	Zugspitze	Harestua	Kiruna
Odin/SMR (2001-2007)	0.27 ± 0.25		0.98 ± 0.28	0.60 ± 0.26
FTIR stratosphere (1996–2007)	0.15 ± 0.05	0.28 ± 0.07	1.13 ± 0.15	0.67 ± 0.12
FTIR troposphere (1996–2007)	0.27 ± 0.01	0.19 ± 0.01	0.28 ± 0.03	0.24 ± 0.03

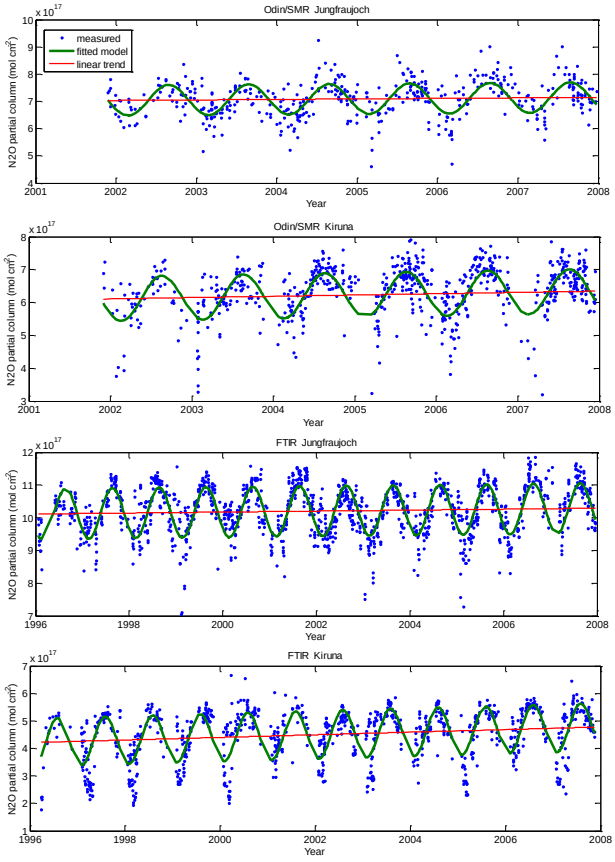

Fig. 5. Stratospheric partial columns of N_2O with fitted seasonal function and linear trend for Jungfraujoch and Kiruna from the SMR instrument onboard the Odin satellite and solar FTIR data.

at Harestua. A slightly weaker trend is seen in Kiruna and a much weaker trend is estimated in the Alp region. It hence seems that the difference in total column trends between the Alp region and Harestua and Kiruna is caused by the differences in the stratospheric column trends and it appears that the highest trend is found at the vortex edge, above Harestua as observed by FTIR and the SMR onboard Odin. We do not have an explanation for this behaviour but is likely related to the atmospheric circulation, since N_2O has a very long lifetime which would smooth out differences in sources and sinks.

5.4 Model stability

To obtain the confidence intervals, the residual from the model is assumed to be normally distributed with constant variance around a mean value of zero and to be free from autocorrelation. The residual distributions from the regression models for all FTIR stations are shown in the lower left panel in Fig. 6 (for CH_4) and in Fig. 7 (for N_2O), also presented is a normal distribution based on the standard deviation from each of the residuals. These distributions indicate that the assumption of normal distribution is justified. In the lower right panels in Figs. 6 and 7 the residuals are plotted as a function of the fitted model. To justify the constant variance assumption the residuals are expected to be randomly scattered around a constant level of zero. In our case we conclude that this assumption is justified for all the regression models. Also, to verify the assumption that no autocorrelation is present in the time series we look at the residual as a function of time, this can be seen in the upper panel in Figs. 6 and 7. Shapes such as cycles might indicate autocorrelation and may make the confidence intervals for the estimated trends larger. Based on the residual analysis we conclude that no strong autocorrelation is presented in any of the regression models.

When working with multiple regression models, one always needs to consider multicolinearity. Multicolinearity is when one or several of the independent variables in the regression model contain similar information, i.e. are linearly dependent. The presence of multicolinearity may result in physically unrealistic values or signs and large confidence intervals of the estimated regression coefficients. To investigate the presence of multicolinearity in the regression model the concept of the variance inflation factor, VIF factor, is used (Neter et al., 1990). A VIF factor of 1 indicates totally independent variables and a factor larger than 10 indicates serious multicolinearity in the model (Neter et al., 1990). In our case the calculated VIF factors are well below 10 for all FTIR stations and both of the species under investigation.

To verify that the 1 % criteria, earlier defined in Sect. 4.4, in the calculations of the anomalies is appropriate a sensitivity analysis is performed on all the regression models. In the analysis the estimated linear trend and the adjusted R^2 value is studied as the anomaly of one of the atmospheric parameters is changed, i.e. the order of the fitted polynomial to

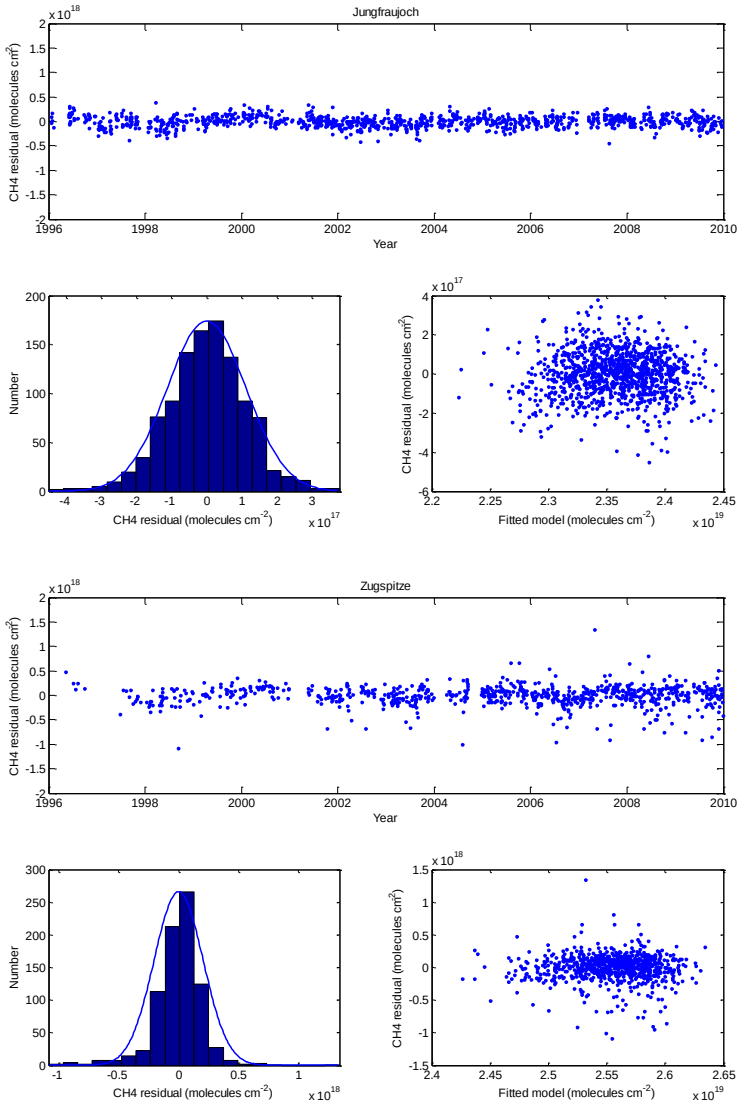

Fig. 6. CH_4 residuals and distributions of the Jungfraujoch and Zugspitze FTIR time series when a piecewise linear trend is used.

the parameter is changed. The change of the linear trend in the total columns of CH_4 and N_2O is largest when increasing from polynomial order zero to a first order and to a second order polynomial for the total column of HF (0, 1, 2) while for the other parameters the change is largest from zero to first (0,1). At higher order of polynomial only very small changes in the estimated trends are observed. It can also be seen that the adjusted R^2 value not increase for polynomials with higher order than two for HF and one for the other parameters. From the sensitivity analysis we conclude that the 1 % criterion is appropriate for deriving the anomalies.

5.5 Method comparison

The results of the multiple regression model has been compared to two other trend methods. The first method, referred to as the Bootstrap algorithm (Efron and Tibshirani, 1993; Gardiner et al., 2008), is based on the least squares fitting of a linear trend and a seasonal component to the data. From the residuals a large number of dataset is randomly sampled (Bootstrapped), these datasets represent the random effects in the data. Each of these dataset is then added to the original fitted function and a set of trends are estimated. The center point of the estimated trends represents the final trend estimation and the width is the confidence intervals. The bootstrap algorithm is a non parametric method since it does not rely on the normal distribution and equal variance assumption. The second tested trend method is a simple least squares fit of a straight line and a seasonal component including a phase, when using this method the normal distribution assumption is made. Linear trends were estimated by

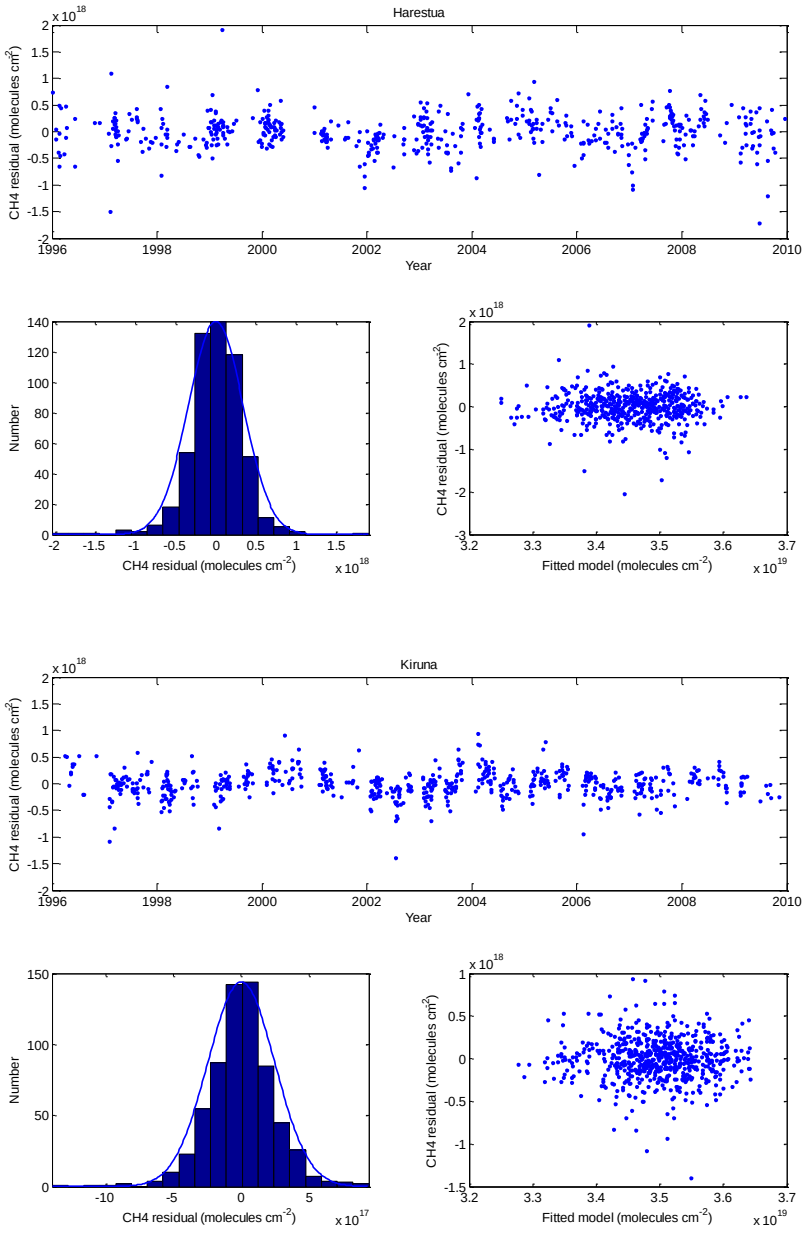

Fig. 6. Continued.

the multiple regression model, the Bootstrap algorithm and by the simple least squares fit of a straight line and a seasonal component, for the 1996–2009 and 1996–2007 period for CH_4 and N_2O total columns respectively. The outcome of the study is presented in Table 7 which shows the estimated trends with associated 95 % confidence limits. The three trend methods show all results that are in relatively close agreement to each other. In general, the multiple regression method has slightly smaller confidence intervals than the other two methods. The trends obtained from the Bootstrap algorithm and the model with a linear trend and seasonal function are very similar for all the participating FTIR stations and both the CH_4 and N_2O time series. The reason for this is that all the CH_4 and N_2O time series are close to normal distributed. In this case the Bootstrap resampling stage is not necessary and can in fact introduce errors in the trend estimate since it can create physically unrealistic time series, especially for the stations at northern latitudes. One example is the high CH_4 and N_2O values related to the presence of the polar vortex, typically during winter and early spring, which with the Bootstrap algorithm can be located to the summer or autumn season. When fitting a trend to these

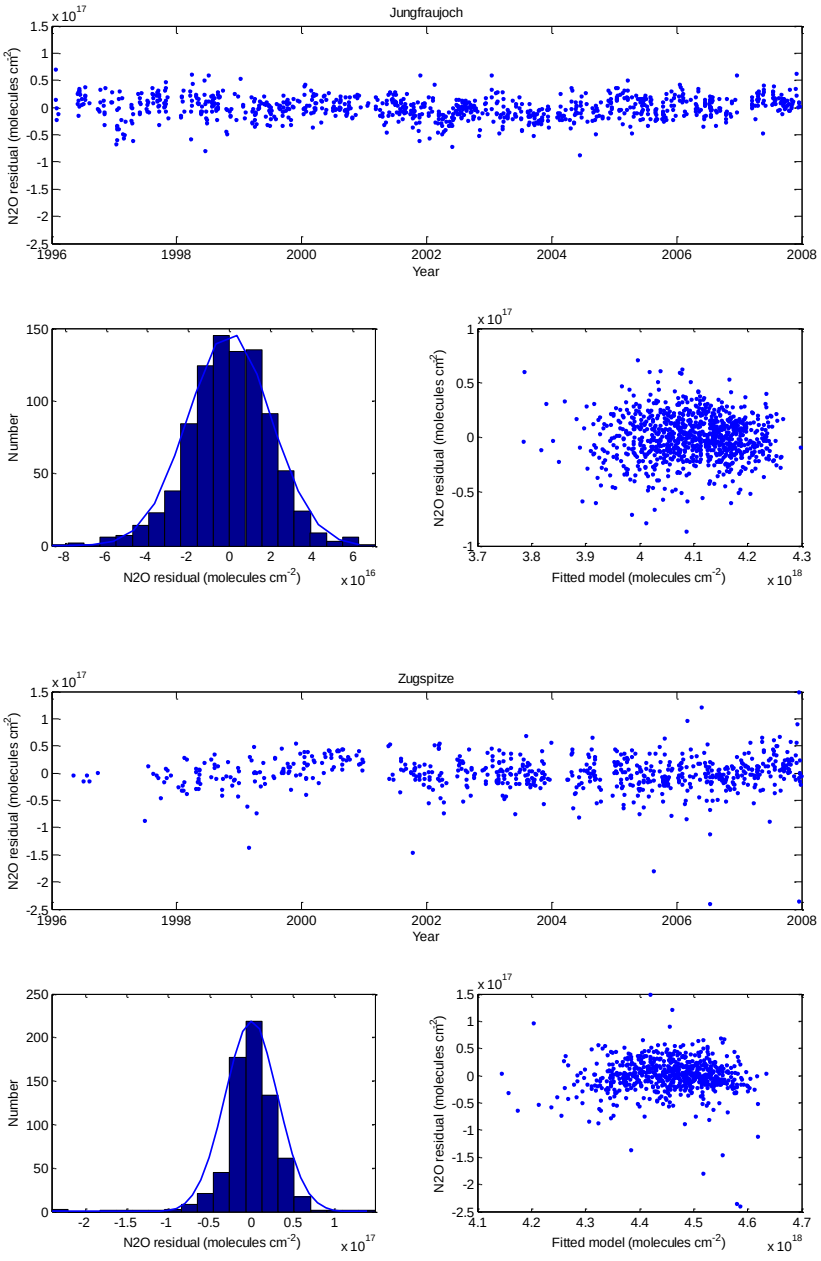

Fig. 7. N_2O residuals and distributions of the Jungfraujoch and Zugspitze FTIR time series.

time series the estimated trend values will have an impact on the final trend result and potentially make the confidence intervals wider.

The trends estimated from the multiple regression method differ in magnitude with up to 31 % and have an uncertainty that differs up to 300 % compared to the other two methods. This difference is most likely because the multiple regression model takes the atmospheric variability into account and hence reduces the unexplained part of the trend model. From the method comparison and model stability analysis we conclude that the multiple regression model gives the most reliable trends since it takes the atmospheric variability into account and fulfils the statistical assumptions presented in Sect. 5.4.

6 Discussion and conclusion

Long term CH_4 and N_2O trends from solar FTIR total columns have been estimated at four European stations. The estimated trends show latitudinal differences with stronger

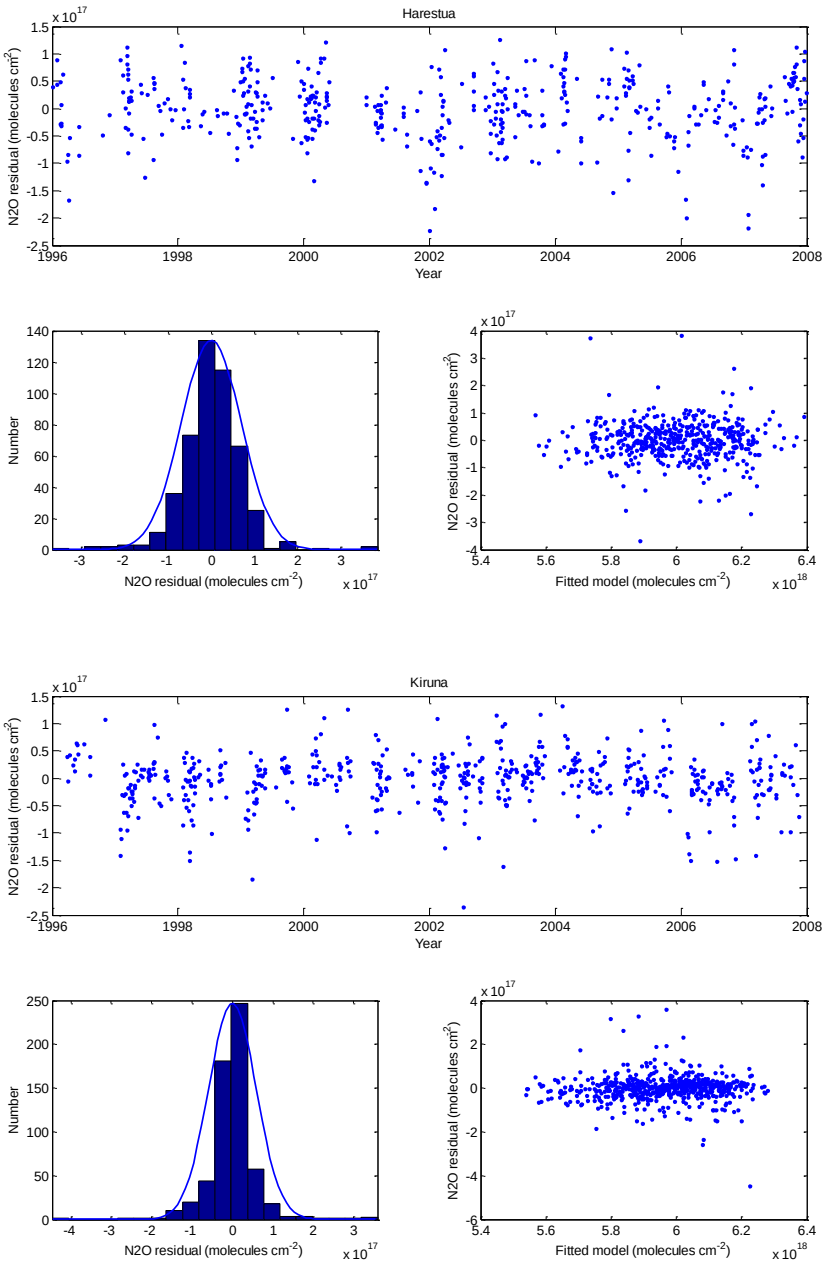

Fig. 7. Continued.

trends for both species at the northern sites and weaker trends at the Alpine stations.

When it comes to CH_4 this latitudinal difference is not surprising since the atmospheric concentration of the species are highly influenced by local sources. At high latitudes wetland contributes up to 25 % of the CH_4 total emissions and these wetlands have shown to be sensitive to climate change (Jackowicz-Korczynski et al., 2010). In addition Russian natural gas is produced at the same latitudes as Harestua and Kiruna. These might be two possible reasons for the stronger trends detected at the northern latitude sites (Harestua and Kiruna) compared to the two Alpine stations.

The latitudinal difference in the estimated N_2O trends is compared to CH_4 unexpected. Atmospheric N_2O has a lifetime that is more than 12 times longer than that of CH_4, 120 years instead of 9, and is thereby well mixed in the troposphere and relatively insensitive to local sources. In the Odin SMR comparison we conclude that the strong FTIR total column trends at Harestua and Kiruna most probably arise from very strong stratospheric trends at these sta-

Table 7. Estimated linear trends from the total columns of CH_4 and N_2O. The trends are presented in percent per year (% yr^{-1}) with the reference year given as the average value of year 2000. All trends are given with associated 95 σ confidence limits.

Trend model	Species	Jungfraujoch	Zugspitze	Harestua	Kiruna
Multiple regression model	CH_4	0.16 ± 0.01	0.13 ± 0.01	0.25 ± 0.02	0.21 ± 0.01
	N_2O	0.21 ± 0.01	0.19 ± 0.01	0.40 ± 0.02	0.29 ± 0.02
Bootstrap algorithm	CH_4	0.16 ± 0.02	0.09 ± 0.03	0.28 ± 0.04	0.26 ± 0.04
	N_2O	0.25 ± 0.03	0.22 ± 0.03	0.45 ± 0.06	0.33 ± 0.05
Linear trend with seasonal component	CH_4	0.16 ± 0.01	0.09 ± 0.02	0.28 ± 0.03	0.26 ± 0.02
	N_2O	0.25 ± 0.02	0.22 ± 0.02	0.46 ± 0.04	0.34 ± 0.03

tions. One possible explanation could be the strengthening of the Brewer Dobson circulation as described by Li et al. (2010). This circulation transports air masses from the tropical tropopause into the stratosphere and towards the poles. If the circulation gets stronger with time more N_2O is transported towards Harestua and Kiruna with a stratospheric trend as result. The stations located further south are less influenced by this transport and hence a weaker stratospheric trend is detected. Another possible reason to the trend differences could be a trend in the tropopause height due to climate change or other changes in the atmospheric dynamics. Linear trends were therefore estimated from the tropopause data, the earlier used ECMWF data, for the FTIR stations. All the estimated trends were close to zero and insignificant. From this we conclude that a change in the tropopause altitude is most likely not responsible for the stratospheric N_2O trends. We conclude that more studies are needed regarding the latitudinal difference in stratospheric N_2O.

Acknowledgements. This paper is funded by the EU project HYMN. The author would like to thank Anders Strandberg and Glenn Persson for Harestua FTIR measurement and Marston Johnston for ECMWF data. P. Duchatelet and E. Mahieu have further been supported by the Belgian Federal Science Policy Office (BELSPO, Brussels). The International Foundation High Altitude Research Stations Jungfraujoch and Gornergrat (HFSJG, Bern) is also acknowledged. T. Blumenstock, F. Hase and M. Schneider would like to thank the Institute of Space Physics (IRF) Kiruna and in particular Uwe Raffalski (IRF) for supporting the measurements at Kiruna. Odin is a Swedish-led satellite project funded jointly by the Swedish National Space Board (SNSB), the Canadian Space Agency (CSA), the Centre National d'Etudes Spatiales (CNES) in France and the National Technology Agency of Finland (Tekes). The Odin mission is since 2007 supported through the 3rd party mission programme of the European Space Agency (ESA).

Edited by: C. Gerbig

References

Bates, D. R. and Hays, P. B.: Atmospheric Nitrous Oxide, Planet. Space Sci., 15, 189–197, 1967.

Davidson, E. A.: The contribution of manure and fertilizer nitrogen to atmospheric nitrous oxide since 1860, Nat. Geosci., 2, 659–662, doi:10.1038/Ngeo608, 2009.

DeMazière, M., Vigouroux, C., Gardiner, T., Coleman, M., Woods, P., Ellingsen, K., Gauss, M., Isaksen, I., Blumenstock, T., Hase, F., Kramer, I., Camy-peyret, C., Chelin, P., Mahieu, E., Demoulin, P., Duchatelet, P., Mellqvist, J., Strandberg, A., Velazco, V., Notholt, J., Sussmann, R., Stremme, W., and Rockmann, A.: The exploitation of ground-based Fourier transform infrared observations for the evaluation of tropospheric trends of greenhouse gases over Europe, Environm. Sci., 2, 283–293, 2005.

Dlugokencky, E. J., Steele, L. P., Lang, P. M., and Masarie, K. A.: The Growth-Rate and Distribution of Atmospheric Methane, J. Geophys. Res.-Atmos., 99, 17021–17043, 1994.

Dlugokencky, E. J., Houweling, S., Bruhwiler, L., Masarie, K. A., Lang, P. M., Miller, J. B., and Tans, P. P.: Atmospheric methane levels off: Temporary pause or a new steady-state?, Geophys. Res. Lett., 30, 1992, doi:10.1029/2003gl018126, 2003.

Dlugokencky, E. J., Bruhwiler, L., White, J. W. C., Emmons, L. K., Novelli, P. C., Montzka, S. A., Masarie, K. A., Lang, P. M., Crotwell, A. M., Miller, J. B., and Gatti, L. V.: Observational constraints on recent increases in the atmospheric CH_4 burden, Geophys. Res. Lett., 36, L18803, doi:10.1029/2009gl039780, 2009.

Efron, B. and Tibshirani, R.: An introduction to the bootstrap, Monographs on statistics and applied probability, 57, Chapman & Hall, New York, USA, xvi, 436 pp., 1993.

Gardiner, T., Forbes, A., de Mazière, M., Vigouroux, C., Mahieu, E., Demoulin, P., Velazco, V., Notholt, J., Blumenstock, T., Hase, F., Kramer, I., Sussmann, R., Stremme, W., Mellqvist, J., Strandberg, A., Ellingsen, K., and Gauss, M.: Trend analysis of greenhouse gases over Europe measured by a network of ground-based remote FTIR instruments, Atmos. Chem. Phys., 8, 6719–6727, doi:10.5194/acp-8-6719-2008, 2008.

Hase, F., Blumenstock, T., and Paton-Walsh, C.: Analysis of the instrumental line shape of high-resolution Fourier transform IR spectrometers with gas cell measurements and new retrieval software, Appl. Optics, 38, 3417–3422, 1999.

Hase, F., Hannigan, J. W., Coffey, M. T., Goldman, A., Hopfner,

M., Jones, N. B., Rinsland, C. P., and Wood, S. W.: Intercomparison of retrieval codes used for the analysis of high-resolution, ground-based FTIR measurements, J. Quant. Spectrosc. Ra., 87, 25–52, doi:10.1016/j.jqsrt.2003.12.008, 2004.

Haszpra, L., Barcza, Z., Hidy, D., Szilagyi, I., Dlugokencky, E., and Tans, R.: Trends and temporal variations of major greenhouse gases at a rural site in Central Europe, Atmos. Environ., 42, 8707–8716, doi:10.1016/j.atmosenv.2008.09.012, 2008.

IPCC: Contribution of Working Group I to the Fourth Assessment Report of the Intergovernmental Panel on Climate Change, 2007, Cambridge University Press, Cambridge, United Kingdom and New York, NY, USA, 2007.

Jackowicz-Korczynski, M., Christensen, T. R., Backstrand, K., Crill, P., Friborg, T., Mastepanov, M., and Strom, L.: Annual cycle of methane emission from a subarctic peatland, J. Geophys. Res.-Biogeo., 115, G02009, doi:10.1029/2008jg000913, 2010.

Jones, A., Urban, J., Murtagh, D. P., Eriksson, P., Brohede, S., Haley, C., Degenstein, D., Bourassa, A., von Savigny, C., Sonkaew, T., Rozanov, A., Bovensmann, H., and Burrows, J.: Evolution of stratospheric ozone and water vapour time series studied with satellite measurements, Atmos. Chem. Phys., 9, 6055–6075, doi:10.5194/acp-9-6055-2009, 2009.

Li, F., Newman, P. A., and Stolarski, R. S.: Relationships between the Brewer-Dobson circulation and the southern annular mode during austral summer in coupled chemistry-climate model simulations, J. Geophys. Res.-Atmos., 115, D15106, doi:10.1029/2009jd012876, 2010.

Mellqvist, J., Galle, B., Blumenstock, T., Hase, F., Yashcov, D., Notholt, J., Sen, B., Blavier, J.-F., Toon, G. C., and Chipperfield, M. P.: Ground-Based FTIR observations of chlorine activation and ozone depletion inside the Arctic vortex during the winter of 1999/2000, J. Geophys. Res., 107, 8263, doi:10.1029/2001JD001080, 2002.

Montgomery, D. C., Jennings, C. L., and Kulahci, M.: Introduction to time series analysis and forecasting, in: Wiley series in probability and statistics, edited by: Hoboken, N. J., Wiley-Interscience, xi, 445 pp., 2008.

Murtagh, D., Frisk, U., Merino, F., Ridal, M., Jonsson, A., Stegman, J., Witt, G., Eriksson, P., Jimenez, C., Megie, G., de la Noe, J., Ricaud, P., Baron, P., Pardo, J. R., Hauchcorne, A., Llewellyn, E. J., Degenstein, D. A., Gattinger, R. L., Lloyd, N. D., Evans, W. F. J., McDade, I. C., Haley, C. S., Sioris, C., von Savigny, C., Solheim, B. H., McConnell, J. C., Strong, K., Richardson, E. H., Leppelmeier, G. W., Kyrola, E., Auvinen, H., and Oikarinen, L.: An overview of the Odin atmospheric mission, Can. J. Phys., 80, 309–319, doi:10.1139/P01-157, 2002.

Neter, J., Wasserman, W., and Kutner, M. H.: Applied linear statistical models : regression, analysis of variance, and experimental designs, 3rd edn., Irwin, Homewood, IL, xvi, 1181 pp., 1990.

Rinsland, C. P., Jones, N. B., Connor, B. J., Logan, J. A., Pougatchev, N. S., Goldman, A., Murcray, F. J., Stephen, T. M., Pine, A. S., Zander, R., Mahieu, E., and Demoulin, P.: Northern and southern hemisphere ground-based infrared spectroscopic measurements of tropospheric carbon monoxide and ethane, J. Geophys. Res.-Atmos., 103, 28197–28217, 1998.

Rinsland, C. P., Chiou, L., Boone, C., Bernath, P., Mahieu, E., and Zander, R.: Trend of lower stratospheric methane (CH4) from atmospheric chemistry experiment (ACE) and atmospheric trace molecule spectroscopy (ATMOS) measurements, J. Quant. Spectrosc. Ra., 110, 1066–1071, doi:10.1016/j.jqsrt.2009.03.024, 2009.

Rodgers, C. D.: Inverse Methods for Atmospheric Sounding, Series on Atmospheric, Oceanic and Planetary Physics, 2, 55–63, 2000.

Simpson, I. J., Rowland, F. S., Meinardi, S., and Blake, D. R.: Influence of biomass burning during recent fluctuations in the slow growth of global tropospheric methane, Geophys. Res. Lett., 33, L22808, doi:10.1029/2006gl027330, 2006.

Strong, K., Wolff, M. A., Kerzenmacher, T. E., Walker, K. A., Bernath, P. F., Blumenstock, T., Boone, C., Catoire, V., Coffey, M., De Mazire, M., Demoulin, P., Duchatelet, P., Dupuy, E., Hannigan, J., Hpfner, M., Glatthor, N., Griffith, D. W. T., Jin, J. J., Jones, N., Jucks, K., Kuellmann, H., Kuttippurath, J., Lambert, A., Mahieu, E., McConnell, J. C., Mellqvist, J., Mikuteit, S., Murtagh, D. P., Notholt, J., Piccolo, C., Raspollini, P., Ridolfi, M., Robert, C., Schneider, M., Schrems, O., Semeniuk, K., Senten, C., Stiller, G. P., Strandberg, A., Taylor, J., Tétard, C., Toohey, M., Urban, J., Warneke, T., and Wood, S.: Validation of ACE-FTS N_2O measurements, Atmos. Chem. Phys., 8, 4759–4786, doi:10.5194/acp-8-4759-2008, 2008.

Sussmann, R. and Borsdorff, T.: Technical Note: Interference errors in infrared remote sounding of the atmosphere, Atmos. Chem. Phys., 7, 3537–3557, doi:10.5194/acp-7-3537-2007, 2007.

Sussmann, R., Stremme, W., Buchwitz, M., and de Beek, R.: Validation of ENVISAT/SCIAMACHY columnar methane by solar FTIR spectrometry at the Ground-Truthing Station Zugspitze, Atmos. Chem. Phys., 5, 2419–2429, doi:10.5194/acp-5-2419-2005, 2005.

Tiao, G. C., Reinsel, G. C., Xu, D. M., Pedrick, J. H., Zhu, X. D., Miller, A. J., Deluisi, J. J., Mateer, C. L., and Wuebbles, D. J.: Effects of Autocorrelation and Temporal Sampling Schemes on Estimates of Trend and Spatial Correlation, J. Geophys. Res.-Atmos., 95, 20507–20517, 1990.

Toon, G. C., Blavier, J.-F., Sen, B., Salawitch, R. J., G. B. Osterman, Notholt, J., Rex, M., McElroy, C. T., and Russell, J. M.: Ground-based observations of Arctic O3 loss during spring and summer 1997, J. Geophys. Res., 104, 497–510, 1997.

Twomey, S.: Introduction to the mathematics of inversion in remote sensing and indirect measurements, Dover Publications, Mineola, N.Y., x, 237 pp., 1996.

Urban, J., Lautie, N., Le Flochmoen, E., Jimenez, C., Eriksson, P., de La Noe, J., Dupuy, E., Ekstrom, M., El Amraoui, L., Frisk, U., Murtagh, D., Olberg, M., and Ricaud, P.: Odin/SMR limb observations of stratospheric trace gases: Level 2 processing of ClO, N_2O, HNO_3, and O-3, J. Geophys. Res.-Atmos., 110, D14307, doi:10.1029/2004jd005741, 2005a.

Urban, J., Lautie, N., Le Flochmoen, E., Jimenez, C., Eriksson, P., de La Noe, J., Dupuy, E., El Amraoui, L., Frisk, U., Jegou, F., Murtagh, D., Olberg, M., Ricaud, P., Camy-Peyret, C., Dufour, G., Payan, S., Huret, N., Pirre, M., Robinson, A. D., Harris, N. R. P., Bremer, H., Kleinbohl, A., Kullmann, K., Kunzi, K., Kuttippurath, J., Ejiri, M. K., Nakajima, H., Sasano, Y., Sugita, W., Yokota, T., Piccolo, C., Raspollini, P., and Ridolfi, M.: Odin/SMR limb observations of stratospheric trace gases: Validation of N_2O, J. Geophys. Res.-Atmos., 110, D09301, doi:10.1029/2004jd005394, 2005b.

Urban, J., Murtagh, D., Lautié, N., Barret, B., Dupuy, E., de La Noë, J., Eriksson, P., Frisk, U., Jones, A., Le Flochmoën, E., Olberg, M., Piccolo, C., Ricaud, P., and Rösevall, J.: Odin/SMR Limb

Observations of Trace Gases in the Polar Lower Stratosphere during 2004–2005, Proc. ESA First Atmospheric Science Conference, edited by: Lacoste, H., ESA-SP-628, ISBN-92-9092-939-1, 2006.

Weatherhead, E. C., Reinsel, G. C., Tiao, G. C., Meng, X. L., Choi, D. S., Cheang, W. K., Keller, T., DeLuisi, J., Wuebbles, D. J., Kerr, J. B., Miller, A. J., Oltmans, S. J., and Frederick, J. E.: Factors affecting the detection of trends: Statistical considerations and applications to environmental data, J. Geophys. Res.-Atmos., 103, 17149–17161, 1998.

Vigouroux, C., De Mazière, M., Demoulin, P., Servais, C., Hase, F., Blumenstock, T., Kramer, I., Schneider, M., Mellqvist, J., Strandberg, A., Velazco, V., Notholt, J., Sussmann, R., Stremme, W., Rockmann, A., Gardiner, T., Coleman, M., and Woods, P.: Evaluation of tropospheric and stratospheric ozone trends over Western Europe from ground-based FTIR network observations, Atmos. Chem. Phys., 8, 6865–6886, doi:10.5194/acp-8-6865-2008, 2008.

Yurganov, L. N., Blumenstock, T., Grechko, E. I., Hase, F., Hyer, E. J., Kasischke, E. S., Koike, M., Kondo, Y., Kramer, I., Leung, F. Y., Mahieu, E., Mellqvist, J., Notholt, J., Novelli, P. C., Rinsland, C. P., Scheel, H. E., Schulz, A., Strandberg, A., Sussmann, R., Tanimoto, H., Velazco, V., Zander, R., and Zhao, Y.: A quantitative assessment of the 1998 carbon monoxide emission anomaly in the Northern Hemisphere based on total column and surface concentration measurements, J. Geophys. Res.-Atmos., 109, D15305, doi:10.1029/2004jd004559, 2004.

Yurganov, L. N., Duchatelet, P., Dzhola, A. V., Edwards, D. P., Hase, F., Kramer, I., Mahieu, E., Mellqvist, J., Notholt, J., Novelli, P. C., Rockmann, A., Scheel, H. E., Schneider, M., Schulz, A., Strandberg, A., Sussmann, R., Tanimoto, H., Velazco, V., Drummond, J. R., and Gille, J. C.: Increased Northern Hemispheric carbon monoxide burden in the troposphere in 2002 and 2003 detected from the ground and from space, Atmos. Chem. Phys., 5, 563–573, doi:10.5194/acp-5-563-2005, 2005.

Atmos. Meas. Tech., 7, 3861–3872, 2014
www.atmos-meas-tech.net/7/3861/2014/
doi:10.5194/amt-7-3861-2014

Atmospheric Measurement Techniques
Open Access

Long-term evolution and seasonal modulation of methanol above Jungfraujoch (46.5° N, 8.0° E): optimisation of the retrieval strategy, comparison with model simulations and independent observations

W. Bader[1], T. Stavrakou[2], J.-F. Muller[2], S. Reimann[3], C. D. Boone[4], J. J. Harrison[5], O. Flock[1], B. Bovy[1], B. Franco[1], B. Lejeune[1], C. Servais[1], and E. Mahieu[1]

[1]Institute of Astrophysics and Geophysics of the University of Liège, Liège, Belgium
[2]Belgian Institute for Space Aeronomy, Avenue Circulaire 3, 1180, Brussels, Belgium
[3]Laboratory for Air Pollution and Environmental Technology, Swiss Federal Laboratories for Materials Testing and Research (Empa), Dübendorf, Switzerland
[4]Department of Chemistry, University of Waterloo, Ontario, Canada
[5]Department of Chemistry, University of York, York, UK

Correspondence to: W. Bader (w.bader@ulg.ac.be)

Received: 11 April 2014 – Published in Atmos. Meas. Tech. Discuss.: 8 May 2014
Revised: 2 October 2014 – Accepted: 16 October 2014 – Published: 21 November 2014

Abstract. Methanol (CH_3OH) is the second most abundant organic compound in the Earth's atmosphere after methane. In this study, we present the first long-term time series of methanol total, lower tropospheric and upper tropospheric–lower stratospheric partial columns derived from the analysis of high resolution Fourier transform infrared solar spectra recorded at the Jungfraujoch station (46.5° N, 3580 m a.s.l.). The retrieval of methanol is very challenging due to strong absorptions of ozone in the region of the selected υ_8 band of CH_3OH. Two wide spectral intervals have been defined and adjusted in order to maximise the information content. Methanol does not exhibit a significant trend over the 1995–2012 time period, but a strong seasonal modulation characterised by maximum values and variability in June–July, minimum columns in winter and a peak-to-peak amplitude of 130 %. Analysis and comparisons with in situ measurements carried out at the Jungfraujoch and ACE-FTS (Atmospheric Chemistry Experiment-Fourier transform spectrometer) occultations have been performed. The total and lower tropospheric columns are also compared with IMAGESv2 model simulations. There is no systematic bias between the observations and IMAGESv2 but the model underestimates the peak-to-peak amplitude of the seasonal modulations.

1 Introduction

Methanol (CH_3OH) is the second most abundant organic molecule in the atmosphere after methane, with concentrations between 1 (Singh et al., 2001) and 20 ppbv (Heikes et al., 2002), despite a lifetime that has been estimated to lie between 4.7 days (Millet et al., 2008) and 12 days (Atkinson et al., 2006). Plant growth is the largest source of methanol with a 65–80 % contribution to its emissions (Galbally and Kirstine, 2002; Jacob et al., 2005). The atmospheric production of CH_3OH through peroxy radical reactions represents up to 15–23 % of its sources (Madronich and Calvert, 1990; Tyndall et al., 2001). Other sources of methanol are plant matter decaying (Warneke et al., 1999), biomass burning (Dufour et al., 2006; Paton-Walsh et al., 2008), fossil fuel combustion, vehicular emissions, solvents and industrial activities.

Methanol influences the oxidising capacity of the atmosphere through reaction with the hydroxyl radical (Jiménez et al., 2003), its main sink, leading to the formation of water vapour and either CH_3O or CH_2OH radicals, which both react with O_2 to give HO_2 and formaldehyde (H_2CO) (Millet et al., 2006). The photo-oxidation of formaldehyde, a key intermediate in the oxidation of numerous volatile organic compounds, leads to the formation of HO_2 radicals and carbon monoxide (CO). As a consequence, CH_3OH is considered as

a source of CO with a yield close to 1 (Duncan et al., 2007). The main sources and sink of methanol are characterised by significant seasonal modulations. This results in a strong signal for CH_3OH, with maximum and minimum abundances observed in the Northern Hemisphere at the beginning of July and in December, respectively (Rinsland et al., 2009; Stavrakou et al., 2011; Wells et al., 2012; Cady-Pereira et al., 2012), reflecting the seasonality of biogenic sources.

In the past decade, ground-based (Schade and Goldstein, 2001, 2006; Karl et al., 2003; Carpenter et al., 2004), ship (Warneke et al., 2004) and aircraft (Singh et al., 2006; Fehsenfeld et al., 2006) in situ measurements combined with space-based measurements, including the Infrared Atmospheric Sounding Interferometer (IASI) onboard the MetOp-A satellite (Razavi et al., 2011), the TES (Tropospheric Emission Spectrometer) nadir-viewing Fourier transform spectrometer (FTS), on board the Aura satellite (Beer et al., 2008), and the solar occultations recorded by the Atmospheric Chemistry Experiment-FTS (ACE-FTS, Bernath et al., 2005; Dufour et al., 2006, 2007) have supplied numerous observations of CH_3OH, which have provided valuable insights on the distribution and budget of methanol at the global scale. In addition, previous studies have reported the measurement of methanol from ground-based infrared solar absorption observations performed at Kitt Peak (31.9° N, 111.6° W, 2090 m a.s.l.; Rinsland et al., 2009) and at Saint-Denis (Reunion Island, 21° S, 55° E, 50 m a.s.l.; Stavrakou et al., 2011; Vigouroux et al., 2012). However, there still remain large uncertainties in our knowledge of the methanol global sources and sinks, as indicated by the large discrepancies existing between different measurement-based estimates of the total sources (Galbally and Kirstine, 2002; Tie et al., 2003; von Kuhlmann et al., 2003a, b; Jacob et al., 2005; Millet et al., 2008; Stavrakou et al., 2011).

In this paper, we report the first long-term methanol time series (17 years) derived from ground-based high-resolution infrared spectra recorded with a Fourier transform infrared (FTIR) spectrometer operated under clear sky conditions at the high-altitude International Scientific Station of the Jungfraujoch (ISSJ, Swiss Alps, 46.5° N, 8.0° E, 3580 m a.s.l.; Zander et al., 2008) providing a valuable tool for model and satellite validation. Most of the available spectra have been recorded within the framework of the Network for Detection of Atmospheric Composition Change monitoring activities (NDACC; see http://www.ndacc.org) complementing the NDACC measurements at northern mid-latitudes. A detailed analysis was conducted to optimise the retrieval strategy of atmospheric methanol in order to minimise the fitting residuals while maximising the information content. A thorough discussion of the retrieval strategy, data characterisation (information content and error budget), long-term trend and seasonal cycle of total and partial columns of methanol above Jungfraujoch is presented here. This paper is organised as follows. A detailed description of the optimised retrieval strategy is given in Sect. 2. The characterisation of our data by their eigenvectors and error budget is discussed in Sect. 3. Finally, in Sect. 4, we present and discuss the results, focusing on the intra-annual and intra-day variability of methanol at ISSJ along with comparisons with in situ measurements, satellite occultations and model calculations.

2 Retrieval strategy

Regular FTIR observations have been carried out at the ISSJ with a homemade spectrometer since 1984, complemented in the early 1990s and then definitely replaced by a commercial Bruker IFS120HR instrument (Zander et al., 2008). This spectrometer is equipped with HgCdTe and InSb cooled detectors, allowing us to cover the 650 to 4500 cm^{-1} region of the electromagnetic spectrum. Since 1991, the FTIR instruments are affiliated with the NDACC network.

The Bruker observational database consists of more than 6500 spectra recorded between 1995 and 2012 with an optical filter covering the 700 to 1400 cm^{-1} domain encompassing the fundamental C-O stretching mode υ_8 of methanol at 1033 cm^{-1}. Spectral resolution, defined as the reciprocal of twice the maximum optical path difference, alternates between 0.004 and 0.006 cm^{-1}. Signal-to-noise (S / N) ratios vary between 250 and 1800 (average spectra resulting from several successive individual Bruker scans, when solar zenith angles vary slowly). The optimisation of the retrieval strategy was based on a subset of 314 spectra covering the year 2010.

The CH_3OH column retrievals and profile inversions have been performed using the SFIT-2 v3.91 fitting algorithm. This retrieval code has been specifically developed to derive mixing ratio profiles of atmospheric species from ground-based FTIR spectra (Rinsland et al., 1998). It is based on the semi-empirical implementation of the Optimal Estimation Method (OEM) developed by Rodgers (1990). Vertical profiles are derived from simultaneous fits to one or more spectral intervals in at least one solar spectrum with a multi-layer, line-by-line calculation that assumes a Voigt line shape (Drayson, 1976). The model atmosphere adopted above the Jungfraujoch altitude consists of a 39 layers scheme with progressively increasing thicknesses, from 3.58 km to reach the 100 km top altitude. The pressure-temperature profiles are provided by the National Center for Environmental Prediction (NCEP, Washington DC, USA, http://www.ncep.noaa.gov/) while the solar line compilation supplied by F. Hase (KIT) (Hase et al., 2006) has been assumed for the solar absorptions. Line parameters used in the spectral fitting process were taken from the HITRAN 2008 spectroscopic compilation (Rothman et al., 2009). Methanol lines were added to the HITRAN compilation for the first time in 2004 (Rothman et al., 2005). The parameters for the 10 µm region are described in the paper by Xu et al. (2004) and were derived from measurements with two high-spectral resolution FTS instruments.

Two spectral windows both encompassing the υ_8 C–O stretch absorption band of methanol have been defined. Synthetic spectra (6.1 mK or 0.0061 cm^{-1}, zenith angle of 80°) have been computed for the first and second order absorbers in both selected windows and are illustrated in Fig. 1. The first interval ranges from 992 to 1008.3 cm^{-1} and is based on windows used in previous investigations. A 992–998.7 cm^{-1} window was employed for the retrieval of CH_3OH from Kitt Peak FTS spectra (Rinsland et al., 2009) and a 984.9–998.7 cm^{-1} window was used for the initial retrievals of methanol from ACE-FTS occultation observations (Dufour et al., 2007). The latest ACE-FTS CH_3OH retrievals (version 3.5) use an extended window from 984.9 to 1005.1 cm^{-1}. Measuring in the limb, ACE-FTS measurements start to saturate for wavenumbers above 1005.1 cm^{-1} for occultations with higher than average O_3 levels. As ground-based observations do not have this problem, we included supplemental methanol features up to the 1008.3 cm^{-1} limit. The second interval, ranging from 1029 to 1037 cm^{-1} is used by Vigouroux et al. (2012).

Absorption by the main ozone isotopologue (^{16}O-^{16}O-^{16}O or O_3) captures nearly 93 and 98 % of the IR radiation in the "1008" and "1037" windows respectively and is close to saturation in the latter one. Methanol features are much weaker, with mean absorption of 1.7 and 1.8 % in the "1008" and "1037" windows respectively. Additional absorptions are associated with O_3 isotopologues, such as O_3(668) or (^{16}O-^{16}O-^{18}O), O_3(686) or (^{16}O-^{18}O-^{16}O), O_3(676) or (^{16}O-^{17}O-^{16}O) and O_3(667) or (^{16}O-^{16}O-^{17}O) as well as carbon dioxide (CO_2) and water vapour (H_2O). Since the CH_3OH absorption lines are quite weak, only spectra with solar zenith angles greater than 65° and up to 80° have been analysed. During the retrievals, both windows were for the first time fitted simultaneously.

The a priori mixing ratio profile for the CH_3OH target is a zonal mean (for the 41–51° N latitude band) of 903 occultations recorded by the ACE-FTS instrument (version 3.5) between 27 March 2004 and 3 August 2012, extending from 5.5 to 30 km tangent altitudes. The profile was extrapolated to 1 ppbv to the surface (Singh et al., 2001; Heikes et al., 2002), and to 0.05 ppbv (Singh et al., 2006; Dufour et al., 2007) for upper layers. The covariance matrix is specified for each layer as a percentage of the a priori profile and an ad hoc correlation length, which is interpreted as a correlation between layers decaying along a Gaussian. For methanol, we adopted a 50 % km^{-1} diagonal covariance and a Gaussian half width of 4 km for extra diagonal elements. A priori profiles for all interfering molecules are based on the WACCM (version 5, the Whole Atmosphere Community Climate Model, e.g. Chang et al., 2008) model climatology for the 1980–2020 period and the ISSJ station. The vertical profiles of CH_3OH, O_3 and O_3(668) are fitted during the iterative process while the a priori distributions of O_3(686), O_3(676), O_3(667), H_2O and CO_2 are scaled. Since the fitting quality is significantly different in both windows, two different values

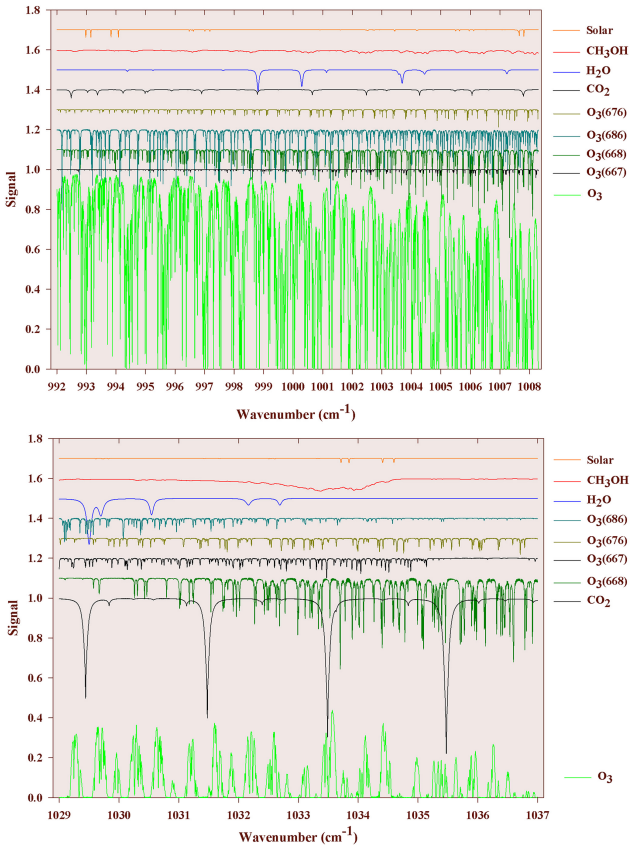

Figure 1. Simulation for Jungfraujoch, 80° zenith angle, 6.1 mK. For both windows, we display the synthetic spectra for individual contributors (see colour codes). HITRAN 2008 and averaged mixing ratio profiles based on the WACCM model climatology have been used for the simulations, except for CH_3OH for which our a priori was used (see text). For clarity, the contributions of each species have been vertically shifted.

for the signal-to-noise ratio for inversion have been selected, i.e. 180 and 40 for the "1008" and "1037" domains, respectively.

When fitted independently, we observe a compact correlation between the corresponding CH_3OH total columns retrieved from both windows with a small bias of 15 ± 13 % (2σ). When comparing ozone total columns respectively retrieved from the strategy described in this work and from the retrieval strategy applied within the NDACC network (window limits: 1000–1005 cm^{-1}, Vigouroux et al., 2008), no significant bias emerges from the comparison between the two ozone total column sets, with a mean relative difference of -0.8 ± 2.4 % (2σ), demonstrating a proper fit of the main interference involved in our methanol retrieval strategy. Additional functions are also included in the fitting process to account for deviations from a perfectly aligned FTS. As an effective apodization function, we assumed a polynomial function of order 2 (Barret et al., 2002). The effective apodization parameter (EAP) gives the value of the effective

apodization function at the maximum optical path difference and is synonymous of a well-aligned instrument when it is close to 1.0. The inversion of the EAP has been included in our retrieval as well as in the NDACC's retrieval strategy of ozone. The EAP derived from both strategies proved to be consistent, with a mean relative difference of $0.7 \pm 2.6\,\%$ (2σ). Those three latter points give confidence in the combination of the two selected windows and in our optimised retrieval strategy.

3 Data characterisation and error budget

Information content has been carefully evaluated and typical results are displayed on Fig. 2. The information content is significantly improved, with a typical degree of freedom for signal (DOFS) of 1.82, in comparison with DOFS of about 1 in previous studies (e.g. Rinsland et al., 2009; Vigouroux, et al., 2012). In Fig. 2, the first eigenvector and eigenvalue (see left panel, in orange) show that the corresponding information is mainly coming from the retrieval (99 %). The increase of information content allows us to retrieve a tropospheric column (Tropo, from 3.58 to 10.72 km) with only 1 % of a priori dependence as well as two partial columns with less than 30 % of a priori dependence (second eigenvector), i.e. a low-tropospheric (LT, from 3.58 to 7.18 km) and an upper troposphere–lower stratosphere (UTLS, from 7.18 to 14.84 km).

The error budget is calculated following the formalism of Rodgers (2000), and can be divided into three different error sources: the smoothing error expressing the uncertainty due to finite vertical resolution of the remote sounding system, the forward model parameters error, and the measurement noise error. The right panel of Fig. 2 gives the corresponding error budget, with identification of the main error components, together with the assumed variability. Error contributions for total and all three partial columns are reported in Table 1.

Through a perturbation method, we also accounted for other error sources: systematic errors, such as the spectroscopic line parameters and the misalignment of the instrument, while uncertainty on the temperature and on the solar tracking is considered to be source of random error. Table 1 provides an error budget resulting from major instrumental and analytical uncertainties. For the spectroscopic line parameters, we included in our error budget the uncertainty on line intensities provided by the HITRAN database. As methanol line intensities matter, a rough idea of the accuracy of the intensities can be obtained from Table 8 of the Xu et al. (2004) study, as it reports an RMS deviation of 7 %. It should be noted that the uncertainty on ozone and its isotopologues lines, according to HITRAN-08 parameters, amounts to between 5 and 10 % (Rothman et al., 2009). However, an extremely high accuracy of ozone spectroscopic parameters is required in order to retrieve methanol columns properly.

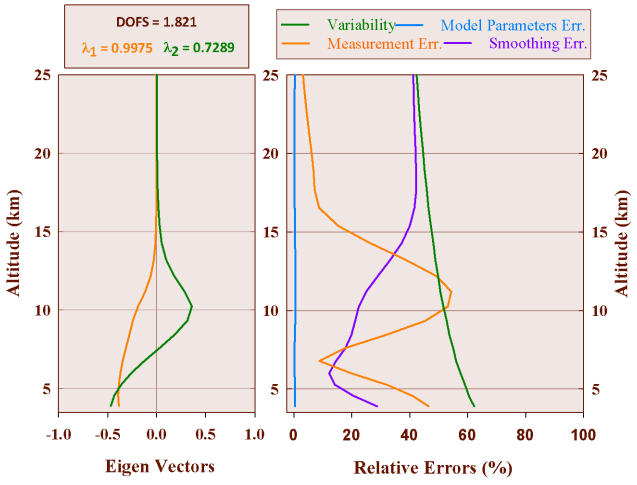

Figure 2. Typical results for information content and error budget. Left frame: first eigenvectors and corresponding eigenvalues. Right frame: error budget, with identification of the main error components, together with the assumed variability (see colour codes and Table 1 for additional information).

We noted that the SFIT-2 algorithm fails to perform a satisfying retrieval when using spectroscopic parameters with ozone lines intensity incremented by 10 %, suggesting that the error on the concerned lines intensity is more likely to be closer to 5 (or even lower) than to 10 %. Therefore, we accounted for an error on ozone and its isotopologues line intensities of 5 % in our error budget.

We accounted for an error of 10 % on the instrument alignment at the maximum path difference. By comparing the two official NDACC algorithms, Hase et al. (2004) and Duchatelet et al. (2010) have established that the forward model may induce a maximum error of 1 % on the retrieved columns for a suite of FTIR target gases. The uncertainty on the pressure–temperature profiles is provided by NCEP with an error of 1.5 K from the ground to an altitude of about 20 km. Concerning the upper levels, the uncertainty increases with altitude, from 2 K around 25 km until 9 K at the top. The uncertainty on the solar zenith angle (SZA) is estimated at 0.2°.

We also provide in Table 1 the mean relative standard deviation for each daily mean for days with three or more measurements. It is found to be of the same order of magnitude as the random error. The dominant contribution to the systematic error is the error on methanol spectroscopic lines, while the measurement noise error is the main component of random error. Both systematic and random errors are given in Table 1, with 7 % and around 5 % respectively on the total columns.

Table 1. Error budget for total and all three partial columns. TC: total column, Tropo: tropospheric column, LT: lower tropospheric layer, UTLS: upper troposphere/lower stratosphere.

Error sources	Max. error (%)				
	TC	Tropo	LT	UTLS	
Variability	46	50	57	48	
	Systematic errors (%)				Comments
	TC	Tropo	LT	UTLS	
Line intensity of CH_3OH	7.02	7.11	6.39	9.22	Xu et al. (2004)
Line intensity of interfering gases	1.00	1.73	3.96	0.91	Rothman et al. (2009) and ± 5 % for all O_3 isotopologues lines
ILS	0.41	0.33	1.19	2.39	± 10 % misalignment
Forward model	1	< 1	< 1	< 1	Retrieval algorithm-related
Total	7.17	7.39	7.68	9.62	
	Random errors (%)				
	TC	Tropo	LT	UTLS	
P-T profiles	1.2	2.3	11.3	8.6	From NCEP
SZA	0.2	0.4	3.1	1.4	0.2°
Smoothing	0.4	4.4	16.1	15.2	Barret et al. (2002)
Measurement noise	5.2	19.4	35.9	37.5	
Model parameters	0.7	0.6	0.5	1.2	
Total	5.37	20.04	40.18	41.43	
Relative standard deviation	6.60	8.34	22.59	21.11	

4 Results and comparisons

Since the improvement in information content allows us to compute partial columns with only a 30 % a priori dependence and as the random error on the tropospheric column is about four times the error on total columns (see Table 1), we focus our trend analysis on total, LT and UTLS columns. Therefore, an analysis of the seasonal variation of methanol in the lower troposphere and the UTLS has been performed, including comparisons with in situ measurements (Legreid et al., 2008) and to ACE-FTS occultation observations, respectively. Comparisons with simulations obtained from the IMAGESv2 global chemistry-transport model (Stavrakou et al., 2011) have also been conducted.

4.1 Data description

In situ measurements have been performed at the ISSJ station from air samples collected on a two-stage adsorbent system connected to a gas chromatograph–mass spectrometer (GC-MS; Legreid et al., 2008). The system was in operation during four measurement campaigns in 2005, which were performed from 8 February until 8 March 2005 for the winter measurements, spring measurements followed from 22 April until 30 May, in summertime measurements start from 5 August until 19 September and autumn measurements from 14 October until 1 November, with a frequency of about one sample every 50 min. A total of 1848 measurements of methanol on 122 days have been compared with our lower-tropospheric column time series for the year 2005.

Monthly mean UTLS columns have been derived from measurements taken by the ACE-FTS instrument and compared to our UTLS product. We selected and converted into partial columns the mixing ratios measured by ACE-FTS during ~ 140 occultations performed in the altitude range of 7.5–14.5 km (version 3.5; Boone et al., 2013) in the 41.5 to 51.5 northern latitude zone between 30 March 2004 and 20 February 2013.

Two model simulations of daily methanol mixing ratios in the 2004–2012 time period obtained from the IMAGESv2 global chemistry-transport model (fully described in Stavrakou et al., 2011) are presented here. The IMAGESv2 model was run at a resolution of 2 in latitude and 2.5 in longitude and with a time step of 6 h. It has 40 vertical (hybrid sigma-pressure) levels between the Earth's surface and the lower stratosphere 25 (44 hPa). Daily averaged mixing ratios calculated by the model at the model pixel comprising the ISSJ station were used to calculate the partial and total columns above the station. The first simulation "MEGAN", is performed using MEGANv2.1 bottom-up emissions, which are calculated using an emission model fitted to net ecosystem flux measurements. The second one, "IASI", uses emissions constrained by IASI vertical column data in an inverse modelling framework based on the adjoint of IMAGESv2.

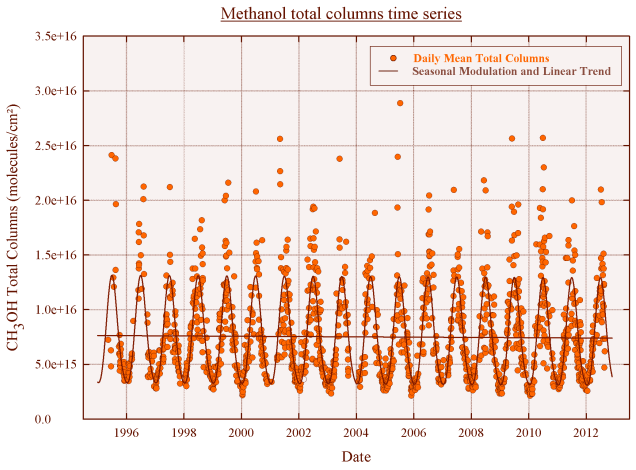

Figure 3. Daily mean total (orange circles) column time series of CH_3OH above Jungfraujoch. Brown curves show the linear and seasonal trend components computed with the bootstrap resampling method (Gardiner et al., 2008).

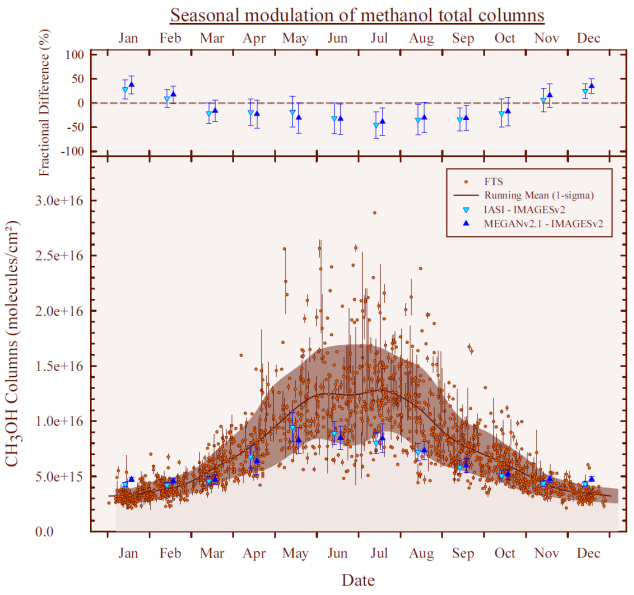

Figure 4. Seasonal modulation of methanol total columns. Dots with vertical lines represent the daily mean total columns over a 1-year time base and their associated standard deviation. The brown curve corresponds to a running mean fit to all data points, with a 15-day step and a 2-month wide integration time. The area corresponds to the 1σ standard deviation associated to the running mean curve. Up and down blue triangles are the monthly means of the model IMAGESv2 simulations for MEGAN and IASI respectively. Upper frame shows monthly fractional difference between FTIR results and IMAGESv2 simulations.

4.2 Time series and long-term trend

In order to produce the first long-term time series of atmospheric methanol above Jungfraujoch, three criteria were used to reject noisy measurements or weak absorption: (i) when negative methanol mixing ratios are retrieved; (ii) when RMS (root mean square, difference between calculated and observed absorption) was out of the interval defined by the 95 % level of confidence (2σ); (iii) when the number of iterations reached the fixed maximum. After implementation of these criteria, the total number of valid measurements is 4271 obtained on 1476 days of measurements between 1995 and 2012. For the trend calculations, we used the statistical tool developed by Gardiner et al. (2008) that employs a bootstrap resampling method. The function fitted to the time series is a combination of a linear component and a 3rd order Fourier series, i.e.:

$$\begin{aligned} F(t,b) = {} & c_0 + c(t-t_0) + b1\cos 2\pi(t-t_0) \\ & + b2\sin 2\pi(t-t_0) + b3\cos 4\pi(t-t_0) \\ & + b4\sin 4\pi(t-t_0) + b5\cos 6\pi(t-t_0) \\ & + b6\sin 6\pi(t-t_0), \end{aligned} \quad (1)$$

where c_0 is the abundance at the reference time t_0 for the linear component (seasonalised data), and c is the annual trend. Figure 3 shows the whole times series of daily mean methanol total columns above Jungfraujoch. We evaluated the trend of methanol total columns over the 1995–2012 time period and found a yearly negative trend of $(-1.34 \pm 2.71) \times 10^{13}$ molecules cm^{-2} or -0.18 ± 0.36 % (2σ), i.e. a non-significant trend at this level of confidence, which is consistent with the trend computed by Rinsland et al. (2009). A non-significant trend has been computed also for both partial column subsets. Hence the results indicate a long-term trend which is not statistically significant and a strong seasonal variation.

4.3 Methanol seasonal modulation

As the results for the full time series do not indicate a statistically significant trend, we illustrate in Fig. 4 the daily mean total columns over a 1-year time base. The strong seasonal modulation of methanol is characterised by minimum values and variability in December to February and maximum columns in June–July. The methanol maximum in summer indicated by our results is consistent with the maximum observed for free tropospheric methanol above Kitt Peak (Rinsland et al., 2009) and the analysis of IASI tropospheric measurements over Europe (Razavi et al., 2011). The mean peak-to-peak amplitude of a seasonal cycle computed by Gardiner's tool and expressed as a percentage of the corresponding CH_3OH yearly mean column amounts to 130.1 ± 1.6 % (1σ), while the seasonal modulation above Kitt Peak amounts to 64.6 ± 0.1 % showing a similar amplitude with the IASI measurements (Razavi et al., 2011) for subtropical regions.

The IMAGESv2 model estimates a seasonal modulation of methanol in phase with the one we measured, but underestimates the peak-to-peak amplitude with 88.6 ± 1.3 % and

70.4 ± 1.2 % for "IASI" and "MEGAN" respectively. The MEGAN emission fluxes are dependent on temperature, visible ration fluxes, leaf area index and leaf age, and they show a pronounced seasonal variation at mid-latitudes, with peak values in early summer. The IASI-derived emissions peak somewhat earlier than in the MEGAN inventory, a result consistent with modelling studies using TES methanol data (Wells et al., 2012; Cady-Pereira et al., 2012) as well as with other studies based on in situ concentration measurements (Jacob et al., 2005) or on flux measurements (Laffineur et al., 2012), which showed substantially higher methanol emission rates by young leaves compared to mature or senescent leaves.

No systematic bias is observed on the whole time series, but a seasonal bias is characterised (see Fig. 4): the maximum fractional difference [(IMAGES-FTIR) / ((IMAGES + FTIR) / 2)] between monthly mean results from FTIR measurements and both "IASI" and "MEGAN" simulations is found to occur in July, with −45 ± 27 % and −39 ± 28 %, respectively. The minimum fractional difference amounts to 28 ± 20 % and 38 ± 19 % respectively in January and shows an overestimation of methanol during wintertime by the IMAGESv2 model. The underestimation of methanol by the "IASI" simulation during summertime is unexpected, since this simulation reproduced very well the methanol total columns measured by IASI over Western Europe (Fig. 5 in Stavrakou et al., 2011). Noting that ISSJ does not sample the lower troposphere below 3.58 km altitude, this discrepancy might reflect an overestimation of the simulated vertical gradient of methanol mixing ratios at continental mid-latitudes, which is suggested by comparisons with aircraft campaigns in spring and summer over the United States (Stavrakou et al., 2011). It is not clear, however, why this issue does not also lead to a similar model underestimation of the methanol column above ISSJ in spring. The overestimated gradient in IMAGES may be due to a well-known problem in chemical transport models, i.e. the overestimation of the hydroxyl radical concentration in the Northern Hemisphere (Krol and Lelieveld, 2003). It could also be related to the large uncertainties in the ocean/atmosphere flux of methanol, given that even the sign of this flux is not well constrained (Millet et al., 2008), and since IASI data were not considered sufficiently reliable over the ocean in the optimisation of emissions using IMAGES by Stavrakou et al. (2011).

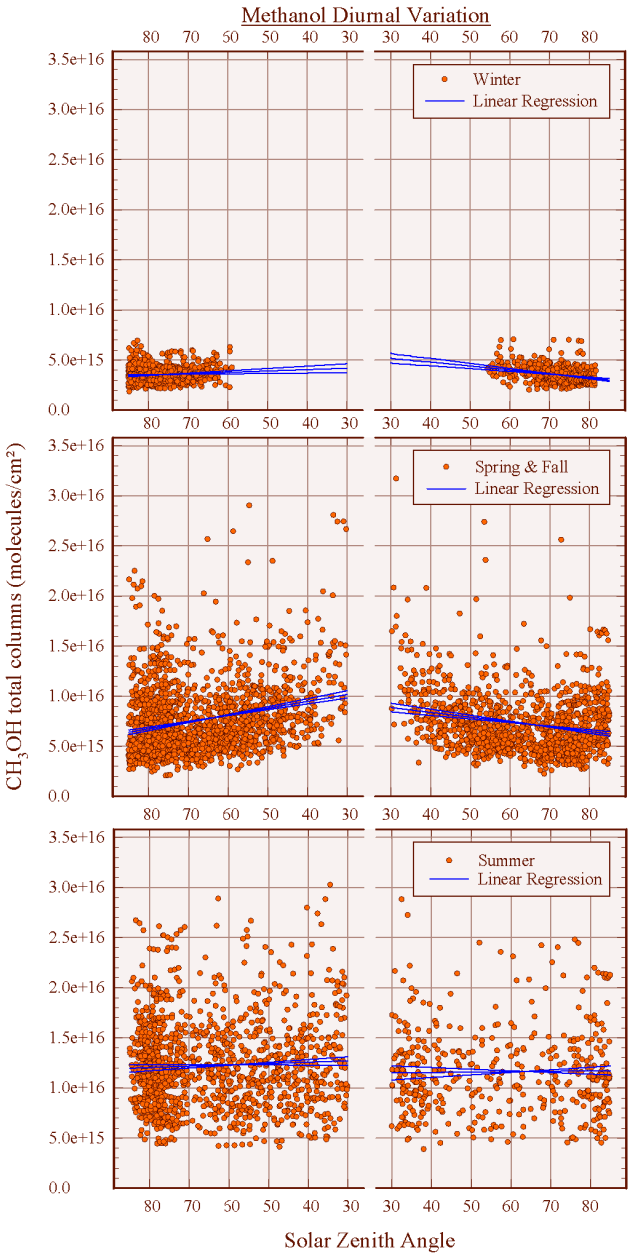

Figure 5. Methanol diurnal variation. Total columns versus the solar zenith angle for winter, summer and the rest of the year. Blue lines represent linear regressions and their corresponding standard deviation (1σ).

4.4 Methanol diurnal variation

The variation of the methanol abundance throughout the day has also been characterised on Fig. 5. To this end, we extended the targeted range of solar zenith angle (SZA) going from 30 to 85° and selected only those whose retrieval provided a DOFS of at least 1. Due to the large seasonal variation, we divided our measurements into three subsets corresponding to summer (June, July, August), winter (December, January, February) and the rest of the year. Even though we found no significant trend of methanol through the day in summer, a significant increase during winter and the rest of the year has been evaluated at 0.4 ± 0.3 and 1.1 ± 0.2 % degree^{-1} in the morning. For the afternoon, the corresponding rates amount to −0.9 ± 0.2 and −0.5 ± 0.1 % degree^{-1}, showing significant decreases. A rough approximation of those trends gives an increase of approximately 5.5×10^{13} and 2.7×10^{14} molecules cm^{-2} h^{-1}

in the morning and to a decrease of -1.6×10^{14} and -1.9×10^{14} molecules cm^{-2} h^{-1} in the afternoon for winter and the rest of the year, respectively.

The causes for the observed diurnal variation are not clear. Major methanol sources such as biogenic production by living plants and photochemical production are stronger during daytime, due to the key role played by solar radiation in photosynthesis and other biotic processes, as well as in the generation of OH radicals through photolytic processes (Logan et al., 1981). However, these sources are expected to peak during the summer, when the diurnal variation of the column is found to be negligible. Since the photochemical sink of methanol (i.e. reaction with OH) is strongest during the day, the observed diurnal variation (and absence thereof during summer) could result from the variable balance between sources and sinks. However, OH fields, produced by the GEOS-CHEM model (Bey et al., 2001) have been examined and no direct correlation with our methanol total columns has been found. Moreover, since the IMAGES model includes those processes but still fails to reproduce the observed diurnal variation, it appears likely that other factors play a significant role, e.g. orography-induced wind patterns bringing boundary layer air to the free troposphere above the station's altitude. Besides model simulations, in situ measurements have also been explored. However, the existing data sets being "campaign-type", the statistics are too weak to draw clear conclusions on this subject. More efforts should be put in further research on processes governing the methanol diurnal variation.

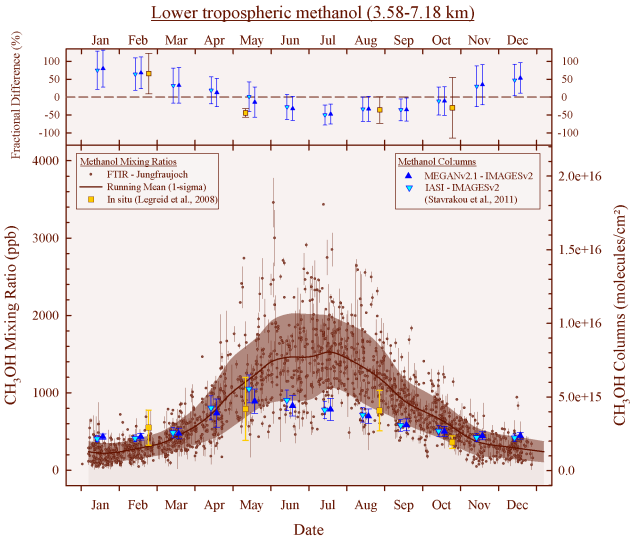

Figure 6. Lower-tropospheric methanol (3.58–7.18 km). Dots with vertical lines represent the daily mean lower-tropospheric columns over a 1-year time base and their associated standard deviation. The brown curve corresponds to a running mean fit to all data points, with a 15-day step and a 2-month wide integration time. The area corresponds to the 1σ standard deviation associated to the running mean curve. Up and down blue triangles are monthly means of the model IMAGESv2 simulations for MEGAN and IASI respectively (Stavrakou et al., 2011). Yellow squares are seasonal means of methanol in situ measurements (Legreid et al., 2008). The upper panel shows monthly fractional difference between the FTIR results and IMAGESv2 simulations and seasonal fraction difference with in situ measurements.

4.5 Methanol in the lower troposphere

In Fig. 6, our lower tropospheric columns show a seasonal modulation with characteristics close to the seasonal variation of total columns with similar occurrence of maximum and minimum but a wider peak-to-peak amplitude of 168 ± 3 %. The upper panel of Fig. 6 also shows monthly fractional differences between the FTIR results and both simulations from the IMAGESv2 model (Stavrakou et al., 2011) as well as seasonal differences with in situ measurements performed at the Jungfraujoch (Legreid et al., 2008).

Neither of the IMAGESv2 series stands out, since they both underestimate the peak-to-peak amplitude with 78 ± 2 % and 101 ± 2 % for MEGAN and IASI, respectively. For both series, methanol is overestimated in winter (DJF) and shows a good agreement in spring (MAM) as well as in October and November. During summertime, results during July are significantly underestimated but the difference for the remaining 3 months (June, August and September) is close to non-significant.

The seasonal amplitude shows a good agreement on the data dispersion (see error bars) except for the autumn season with more compact values. The high standard deviation in summer appears to be due to only a few days with high methanol mixing ratios. These days are characterised by trajectories originating from the south, where biogenic sources are more active. Indeed, it has been established by Legreid et al. (2008), that there is a considerable contribution of methanol from the south since methanol is emitted in large amounts from biogenic sources (Fall, 2003; Jacob, 2002; Jacob et al., 2005; Singh et al., 1994) more active in the south of the Alps than in the north. Furthermore, air masses from the south are transported over Northern Italy, which is a highly industrialised area with considerable anthropogenic emissions.

4.6 Methanol in the upper troposphere–lower stratosphere (UTLS)

The comparison between the UTLS FTIR columns, both IMAGES data sets and monthly mean results from ACE-FTS occultations illustrated in Fig. 7 shows an overall agreement within the estimated uncertainties. As for total and lower-tropospheric columns, methanol variability is underestimated by the IMAGESv2 model. On the other hand, the seasonal cycle of methanol UTLS columns is satisfactorily characterised by FTIR results and the IMAGES simulations in terms of absolute value with a non-significant mean fractional difference with FTIR of -6 ± 49 % and 1 ± 48 %,

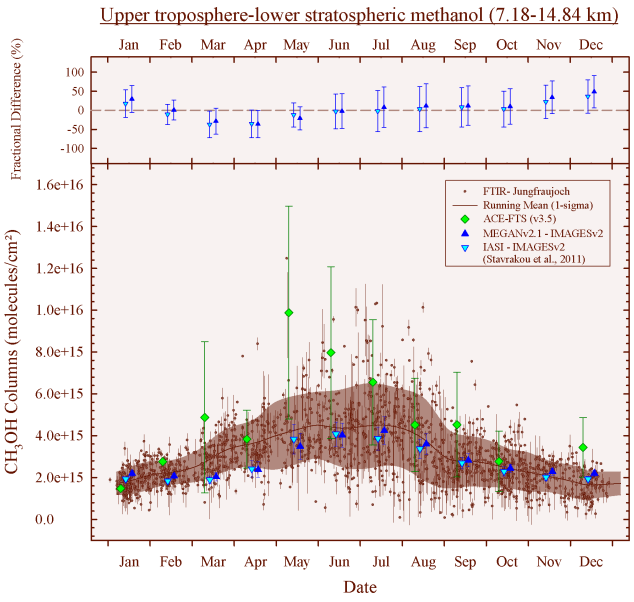

Figure 7. Upper troposphere–lower stratospheric methanol (7.18–14.84 km). Dots with vertical lines representing daily mean lower-tropospheric columns over a 1-year time base and their associated standard deviation. The brown curve corresponds to a running mean fit to all data points, with a 15-day step and a 2-month wide integration time. The area corresponds to the 1σ standard deviation associated to the running mean curve. Up and down blue triangles are the monthly means of the model IMAGESv2 simulations for MEGAN and IASI respectively (Stavrakou et al., 2011). Green diamonds are the monthly means of methanol retrieved from ACE-FTS occultations with the error bars representing the standard deviation (2σ). Upper frame show monthly fractional difference between FTIR results and IMAGESv2 simulations and ACE-FTS results.

respectively for MEGAN and IASI. The peak-to-peak amplitudes of the three series, i.e. 93 ± 2 % for FTIR, 82 ± 2 for MEGAN and 92 ± 2 % for IASI are in very good agreement as well as the timing of the maximum (June–July).

A close to statistical agreement is observed between Jungfraujoch results and the UTLS columns derived from ACE-FTS data with a mean fractional difference of 33 ± 30 % despite substantially higher ACE methanol columns in March and May. The differences for these 2 months may be attributed to the fact that the monthly mean results from ACE-FTS encompass a 10° latitudinal band and therefore occultations may be capturing local events such as plumes from biomass burning out of range for the Jungfraujoch station.

Biases in the ACE methanol retrievals have recently been addressed by Harrison et al. (2012). Adoption of a new set of infrared absorption cross sections for methanol led to the determination of ACE UTLS columns higher by up to 25 % (calculations based two occultations; see Fig. 6 of Harrison et al., 2012), depending on the temperature of the measurement. Therefore, by applying those new cross sections to our Jungfraujoch retrievals, we would likely identify a bias in the same range, depending on the season and thus the vertical temperature distribution. The effect on total (and partial) columns will have to be evaluated on the basis of larger statistics for each season and using the new cross sections of Harrison et al. (2012).

5 Conclusions

A long-term time series of methanol has been determined from the analysis of a 17-year time series of infrared solar absorption spectra recorded with a commercial Fourier transform spectrometer Bruker IFS120HR, operated at the high-altitude International Scientific Station of the Jungfraujoch (ISSJ, Swiss Alps, 45° N, 8.0° E, 3580 m a.s.l.; Zander et al., 2008) providing a valuable tool for model and satellite validation and complementing the NDACC measurements at northern mid-latitudes.

The results were analysed using the SFIT-2 v3.91 fitting algorithm and thanks to the combination of spectral windows used in previous studies for the retrieval of methanol from FTS spectra (Dufour et al., 2007; Rinsland et al., 2009; Vigouroux, et al., 2012), we have significantly improved the information content. With a typical DOFS of 1.82, a total column and two partial columns time series are available, i.e. a lower-tropospheric (LT, 3.58–7.18 km) and an upper tropospheric–lower stratospheric one (UTLS, 7.18–14.84 km). Both random and systematic error sources have been identified and characterised using the spectra recorded in the year 2010, and are found to be respectively 5 and 7 % for the total column.

The analysis of the time series does not reveal a significant long-term trend but shows a high peak-to-peak amplitude of the seasonal cycle of 129.4 ± 5.5 % (1σ) for total columns. Methanol total and partial columns are characterised by a strong seasonal modulation with minimum values and variability in December to February and maximum columns in June–July. First analysis of methanol diurnal variation shows an increase of methanol in the morning and a decrease during the afternoon for all seasons but summer.

Comparisons with methanol measurements obtained with other techniques (in situ and satellite) give satisfactory results. The FTIR lower tropospheric data compared to in situ measurements generally shows a good agreement regarding the data dispersion. Concerning the UTLS partial columns, there is a close to statistical agreement with ACE-FTS occultations despite higher ACE columns of methanol in March and May.

The IMAGESv2 simulations underestimate the peak-to-peak amplitude for total and lower-tropospheric columns. Despite the absence of a systematic bias between our results and the IMAGESv2 simulations, comparisons show seasonal differences with an overestimation of winter methanol

and an underestimation during summertime, which might be explained by an overestimation of the vertical gradient of methanol mixing ratios by the model. Regarding UTLS columns, the peak-to-peak amplitude and timing of the maximum (June–July) in both IMAGESv2 simulations are in very good agreement with the FTIR results.

Even though the role of plant growth in methanol budget is confirmed by its seasonality, large uncertainties remain in the methanol budget. Thanks to the improvement of the information content of our retrieval and therefore our vertical resolution, our partial column time series should contribute to better constraints for model simulations and therefore may lead to a better understanding of methanol budget.

Acknowledgements. The University of Liège's involvement has primarily been supported by the PRODEX and SSD programs funded by the Belgian Federal Science Policy Office (Belspo), Brussels. The Swiss GAW-CH program is further acknowledged. E. Mahieu is Research Associate with the F.R.S. – FNRS. The FRS-FNRS and the Fédération Wallonie Bruxelles contributed to observational activities support. We thank the International Foundation High Altitude Research Stations Jungfraujoch and Gornergrat (HFSJG, Bern) for supporting the facilities needed to perform the observations. The contribution of BIRA-IASB was supported by the PRODEX projects A3C (2011–2013) and ACROSAT (2014–2015) funded by Belspo. The ACE mission is supported primarily by the Canadian Space Agency. We further acknowledge the vital contribution from all our Belgian colleagues in performing the Jungfraujoch observations used here.

Edited by: F. Boersma

References

Atkinson, R., Baulch, D. L., Cox, R. A., Crowley, J. N., Hampson, R. F., Hynes, R. G., Jenkin, M. E., Rossi, M. J., Troe, J., and IUPAC Subcommittee: Evaluated kinetic and photochemical data for atmospheric chemistry: Volume II – gas phase reactions of organic species, Atmos. Chem. Phys., 6, 3625–4055, doi:10.5194/acp-6-3625-2006, 2006.

Barret, B., De Mazière, M., and Demoulin, P.: Retrieval and characterization of ozone profiles from solar infrared spectra at the Jungfraujoch, J. Geophys. Res., 107, 4788, doi:10.1029/2001JD001298, 2002.

Beer, R., Shephard, M. W., Kulawik, S. S., Clough, S. A., Eldering, A., Bowman, K. W., Sander, S. P., Fisher, B. M., Payne, V. H., Luo, M., Osterman, G. B., and Worden, J. R.: First satellite observations of lower tropospheric ammonia and methanol, Geophys. Res. Lett., 35, L09801, doi:10.1029/2008GL033642, 2008.

Bernath, P. F., McElroy, C. T., Abrams, M. C., Boone, C. D., Butler, M., Camy-Peyret, C., Carleer, M., Clerbaux, C., Coheur, P.-F., Colin, R., DeCola, P., DeMazière, M., Drummond, J. R., Dufour, D., Evans, W. F. J., Fast, H., Fussen, D., Gilbert, K., Jennings, D. E., Llewellyn, E. J., Lowe, R. P., Mahieu, E., McConnell, J. C., McHugh, M., McLeod, S. D., Michaud, R., Midwinter, C., Nassar, R., Nichitiu, F., Nowlan, C., Rinsland, C. P., Rochon, Y. J., Rowlands, N., Semeniuk, K., Simon, P., Skelton, R., Sloan, J. J., Soucy, M.-A., Strong, K., Tremblay, P., Turnbull, D., Walker, K. A., Walkty, I., Wardle, D. A., Wehrle, V., Zander, R., and Zou, J.: Atmospheric Chemistry Experiment (ACE): Mission overview, Geophys. Res. Lett., 32, L15S01, doi:10.1029/2005GL022386, 2005.

Bey, I., Jacob, D. J., Yantosca, R. M., Logan, J. A., Field, B. D., Fiore, A. M., Li, Q., Liu, H. Y., Mickley, L. J., and Schultz, M. G.: Global modeling of tropospheric chemistry with assimilated meteorology?: Model description and evaluation, J. Geophys. Res., 106, 23073–23095, 2001.

Boone, C. D., Walker, K. A., and Bernath, P. F.: Version 3 retrievals for the atmospheric chemistry experiment Fourier transform spectrometer (ACE-FTS), in The Atmospheric Chemistry Experiment ACE at 10: A solar occultation anthology, 103–127, edited by: Bernath, P. F., Hampton, Virignia, USA, 2013.

Cady-Pereira, K. E., Shephard, M. W., Millet, D. B., Luo, M., Wells, K. C., Xiao, Y., Payne, V. H., and Worden, J.: Methanol from TES global observations: retrieval algorithm and seasonal and spatial variability, Atmos. Chem. Phys., 12, 8189–8203, doi:10.5194/acp-12-8189-2012, 2012.

Carpenter, L. J., Lewis, A. C., Hopkins, J. R., Read, K. A., Longley, I. D., and Gallagher, M. W.: Uptake of methanol to the North Atlantic Ocean surface, Global Biogeochem. Cy., 18, GB4027, doi:10.1029/2004GB002294, 2004.

Chang, L., Palo, S., Hagan, M., Richter, J., Garcia, R., Riggin, D., and Fritts, D.: Structure of the migrating diurnal tide in the Whole Atmosphere Community Climate Model (WACCM), Adv. Space Res., 41, 1398–1407, doi:10.1016/j.asr.2007.03.035, 2008.

Drayson, S. R.: Rapid computation of the Voigt profile, J. Quant. Spectrosc. Ra., 16, 611–614, doi:10.1016/0022-4073(76)90029-7, 1976.

Duchatelet, P., Demoulin, P., Hase, F., Ruhnke, R., Feng, W., Chipperfield, M. P., Bernath, P. F., Boone, C. D., Walker, K. A., and Mahieu, E.: Hydrogen fluoride total and partial column time series above the Jungfraujoch from long-term FTIR measurements: Impact of the line-shape model, characterization of the error budget and seasonal cycle, and comparison with satellite and model data, J. Geophys. Res., 115, D22306, doi:10.1029/2010JD014677, 2010.

Dufour, G., Boone, C. D., Rinsland, C. P., and Bernath, P. F.: First space-borne measurements of methanol inside aged southern tropical to mid-latitude biomass burning plumes using the ACE-FTS instrument, Atmos. Chem. Phys., 6, 3463–3470, doi:10.5194/acp-6-3463-2006, 2006.

Dufour, G., Szopa, S., Hauglustaine, D. A., Boone, C. D., Rinsland, C. P., and Bernath, P. F.: The influence of biogenic emissions on upper-tropospheric methanol as revealed from space, Atmos. Chem. Phys., 7, 6119–6129, doi:10.5194/acp-7-6119-2007, 2007.

Duncan, B. N., Logan, J. A., Bey, I., Megretskaia, I. A., Yantosca, R. M., Novelli, P. C., Jones, N. B., and Rinsland, C. P.: Global budget of CO, 1988–1997: Source estimates and validation with a global model, J. Geophys. Res.-Atmos., 112, D22301, doi:10.1029/2007JD008459, 2007.

Fall, R.: Abundant Oxygenates in the Atmosphere: A Biochemical Perspective, Chem. Rev., 103, 4941–4952, doi:10.1021/cr0206521, 2003.

Fehsenfeld, F. C., Ancellet, G., Bates, T. S., Goldstein, A. H., Hardesty, R. M., Honrath, R., Law, K. S., Lewis, A. C., Leaitch, R.,

McKeen, S., Meagher, J., Parrish, D. D., Pszenny, A. A. P., Russell, P. B., Schlager, H., Seinfeld, J., Talbot, R., and Zbinden, R.: International Consortium for Atmospheric Research on Transport and Transformation (ICARTT): North America to Europe – Overview of the 2004 summer field study, J. Geophys. Res., 111, D23S01, doi:10.1029/2006JD007829, 2006.

Galbally, I. E. and Kirstine, W.: The Production of Methanol by Flowering Plants and the Global Cycle of Methanol, J. Atmos. Chem., 43, 195–229, doi:10.1023/A:1020684815474, 2002.

Gardiner, T., Forbes, A., de Mazière, M., Vigouroux, C., Mahieu, E., Demoulin, P., Velazco, V., Notholt, J., Blumenstock, T., Hase, F., Kramer, I., Sussmann, R., Stremme, W., Mellqvist, J., Strandberg, A., Ellingsen, K., and Gauss, M.: Trend analysis of greenhouse gases over Europe measured by a network of ground-based remote FTIR instruments, Atmos. Chem. Phys., 8, 6719–6727, doi:10.5194/acp-8-6719-2008, 2008.

Harrison, J. J., Allen, N. D. C., and Bernath, P. F.: Infrared absorption cross sections for methanol, J. Quant. Spectrosc. Ra., 113, 2189–2196, doi:10.1016/j.jqsrt.2012.07.021, 2012.

Hase, F., Hannigan, J. W., Coffey, M. T., Goldman, A., Höpfner, M., Jones, N. B., Rinsland, C. P., and Wood, S. W.: Intercomparison of retrieval codes used for the analysis of high-resolution, ground-based FTIR measurements, J. Quant. Spectrosc. Ra., 87, 25–52, doi:10.1016/j.jqsrt.2003.12.008, 2004.

Hase, F., Demoulin, P., Sauval, A. J., Toon, G. C., Bernath, P. F., Goldman, A., Hannigan, J. W., Rinsland, C. P., Hase, F., Demoulin, P., Sauval, A. J., Toon, G. C., Bernath, P. F., Goldman, A., Hannigan, J. W., and Rinsland, C. P.: An empirical line-by-line model for the infrared solar transmittance spectrum from 700 to 5000 cm(-1), J. Quant. Spectrosc. Ra., 102, 450–463, doi:10.1016/j.jqsrt.2006.02.026, 2006.

Heikes, B. G., Chang, W., Pilson, M. E. Q., Swift, E., Singh, H. B., Guenther, A., Jacob, D. J., Field, B. D., Fall, R., Riemer, D., and Brand, L.: Atmospheric methanol budget and ocean implication, Global Biogeochem. Cy., 16, 1133, doi:10.1029/2002GB001895, 2002.

Jacob, D. J.: Atmospheric budget of acetone, J. Geophys. Res., 107, ACH5.1–ACH5.17, doi:10.1029/2001JD000694, 2002.

Jacob, D. J., Field, B. D., Li, Q., Blake, D. R., de Gouw, J., Warneke, C., Hansel, A., Wisthaler, A., Singh, H. B., and Guenther, A.: Global budget of methanol: Constraints from atmospheric observations, J. Geophys. Res., 110, D08303, doi:10.1029/2004JD005172, 2005.

Jiménez, E., Gilles, M., and Ravishankara, A.: Kinetics of the reactions of the hydroxyl radical with CH_3OH and C_2H_5OH between 235 and 360 K, J. Photochem. Photobio. A, 157, 237–245, doi:10.1016/S1010-6030(03)00073-X, 2003.

Karl, T., Guenther, A., Spirig, C., Hansel, A., and Fall, R.: Seasonal variation of biogenic VOC emissions above a mixed hardwood forest in northern Michigan, Geophys. Res. Lett., 30, 2186, doi:10.1029/2003GL018432, 2003.

Krol, M. and Lelieveld, J.: Can the variability in tropospheric OH be deduced from measurements of 1,1,1-trichloroethane (methyl chloroform)?, J. Geophys. Res., 108, 4125, doi:10.1029/2002JD002423, 2003.

Laffineur, Q., Aubinet, M., Schoon, N., Amelynck, C., Müller, J.-F., Dewulf, J., Van Langenhove, H., Steppe, K., and Heinesch, B.: Abiotic and biotic control of methanol exchanges in a temperate mixed forest, Atmos. Chem. Phys., 12, 577–590, doi:10.5194/acp-12-577-2012, 2012.

Legreid, G., Folini, D., Staehelin, J., Balzani Lööv, J., Steinbacher, M., and Reimann, S.: Measurements of organic trace gases including oxygenated volatile organic compounds at the high alpine site Jungfraujoch (Switzerland): Seasonal variation and source allocations, J. Geophys. Res., 113, D05307, doi:10.1029/2007JD008653, 2008.

Logan, J. A., Prather, M. J., Wofsy, S. C., and McElroy, M. B.: Tropospheric chemistry: A global perspective, J. Geophys. Res., 86, 7210, doi:10.1029/JC086iC08p07210, 1981.

Madronich, S. and Calvert, J. G.: Permutation reactions of organic peroxy radicals in the troposphere, J. Geophys. Res., 95, 5697–5715, doi:10.1029/JD095iD05p05697, 1990.

Millet, D. B., Jacob, D. J., Turquety, S., Hudman, R. C., Wu, S., Fried, A., Walega, J., Heikes, B. G., Blake, D. R., Singh, H. B., Anderson, B. E., and Clarke, A. D.: Formaldehyde distribution over North America: Implications for satellite retrievals of formaldehyde columns and isoprene emission, J. Geophys. Res., 111, D24S02, doi:10.1029/2005JD006853, 2006.

Millet, D. B., Jacob, D. J., Custer, T. G., de Gouw, J. A., Goldstein, A. H., Karl, T., Singh, H. B., Sive, B. C., Talbot, R. W., Warneke, C., and Williams, J.: New constraints on terrestrial and oceanic sources of atmospheric methanol, Atmos. Chem. Phys., 8, 6887–6905, doi:10.5194/acp-8-6887-2008, 2008.

Paton-Walsh, C., Wilson, S. R., Jones, N. B., and Griffith, D. W. T.: Measurement of methanol emissions from Australian wildfires by ground-based solar Fourier transform spectroscopy, Geophys. Res. Lett., 35, L08810, doi:10.1029/2007GL032951, 2008.

Razavi, A., Karagulian, F., Clarisse, L., Hurtmans, D., Coheur, P. F., Clerbaux, C., Müller, J. F., and Stavrakou, T.: Global distributions of methanol and formic acid retrieved for the first time from the IASI/MetOp thermal infrared sounder, Atmos. Chem. Phys., 11, 857–872, doi:10.5194/acp-11-857-2011, 2011.

Rinsland, C. P., Jones, N. B., Connor, B. J., Logan, J. A., Pougatchev, N. S., Goldman, A., Murcray, F. J., Stephen, T. M., Pine, A. S., Zander, R., Mahieu, E. and Demoulin, P.: Northern and southern hemisphere ground-based infrared spectroscopic measurements of tropospheric carbon monoxide and ethane, J. Geophys. Res., 103, 28197–28217, doi:10.1029/98JD02515, 1998.

Rinsland, C. P., Mahieu, E., Chiou, L. and Herbin, H.: First ground-based infrared solar absorption measurements of free tropospheric methanol (CH_3OH): Multidecade infrared time series from Kitt Peak (31.9° N 111.6° W): Trend, seasonal cycle, and comparison with previous measurements, J. Geophys. Res., 114, D04309, doi:10.1029/2008JD011003, 2009.

Rodgers, C.: Inverse methods for atmospheric sounding, Vol. 2 of Series on Atmospheric, Oceanic and Planetary Physics, 2000.

Rodgers, C. D.: Characterization and error analysis of profiles retrieved from remote sounding measurements, J. Geophys. Res., 95, 5587–5595, doi:10.1029/JD095iD05p05587, 1990.

Rothman, L. S., Jacquemart, D., Barbe, A., Chris Benner, D., Birk, M., Brown, L. R., Carleer, M. R., Chackerian, C., Chance, K., Coudert, L. H., Dana, V., Devi, V. M., Flaud, J.-M., Gamache, R. R., Goldman, A., Hartmann, J.-M., Jucks, K. W., Maki, A. G., Mandin, J.-Y., Massie, S. T., Orphal, J., Perrin, A., Rinsland, C. P., Smith, M. A. H., Tennyson, J., Tolchenov, R. N., Toth, R. A., Vander Auwera, J., Varanasi, P. and Wagner, G.: The HITRAN

2004 molecular spectroscopic database, J. Quant. Spectrosc. Ra., 96, 139–204, doi:10.1016/j.jqsrt.2004.10.008, 2005.

Rothman, L. S., Gordon, I. E., Barbe, A., Benner, D. C., Bernath, P. F., Birk, M., Boudon, V., Brown, L. R., Campargue, A., Champion, J.-P., Chance, K., Coudert, L. H., Dana, V., Devi, V. M., Fally, S., Flaud, J.-M., Gamache, R. R., Goldman, A., Jacquemart, D., Kleiner, I., Lacome, N., Lafferty, W. J., Mandin, J.-Y., Massie, S. T., Mikhailenko, S. N., Miller, C. E., Moazzen-Ahmadi, N., Naumenko, O. V., Nikitin, A. V., Orphal, J., Perevalov, V. I., Perrin, A., Predoi-Cross, A., Rinsland, C. P., Rotger, M., Šimečková, M., Smith, M. A. H., Sung, K., Tashkun, S. A., Tennyson, J., Toth, R. A., Vandaele, A. C. and Vander Auwera, J.: The HITRAN 2008 molecular spectroscopic database, J. Quant. Spectrosc. Ra., 110, 533–572, doi:10.1016/j.jqsrt.2009.02.013, 2009.

Schade, G. W. and Goldstein, A. H.: Fluxes of oxygenated volatile organic compounds from a ponderosa pine plantation, J. Geophys. Res., 106, 3111–3123, doi:10.1029/2000JD900592, 2001.

Schade, G. W. and Goldstein, A. H.: Seasonal measurements of acetone and methanol: Abundances and implications for atmospheric budgets, Global Biogeochem. Cy., 20, GB1011, doi:10.1029/2005GB002566, 2006.

Singh, H. B., O'Hara, D., Herlth, D., Sachse, W., Blake, D. R., Bradshaw, J. D., Kanakidou, M., and Crutzen, P. J.: Acetone in the atmosphere: Distribution, sources, and sinks, J. Geophys. Res., 99, 1805–1819, doi:10.1029/93JD00764, 1994.

Singh, H., Chen, Y., Staudt, A., Jacob, D., Blake, D., Heikes, B., and Snow, J.: Evidence from the Pacific troposphere for large global sources of oxygenated organic compounds, Nature, 410, 1078–1081, doi:10.1038/35074067, 2001.

Singh, H. B., Brune, W. H., Crawford, J. H., Jacob, D. J., and Russell, P. B.: Overview of the summer 2004 Intercontinental Chemical Transport Experiment–North America (INTEX-A), J. Geophys. Res.-Atmos., 111, D24S01, doi:10.1029/2006JD007905, 2006.

Stavrakou, T., Guenther, A., Razavi, A., Clarisse, L., Clerbaux, C., Coheur, P.-F., Hurtmans, D., Karagulian, F., De Mazière, M., Vigouroux, C., Amelynck, C., Schoon, N., Laffineur, Q., Heinesch, B., Aubinet, M., Rinsland, C., and Müller, J.-F.: First space-based derivation of the global atmospheric methanol emission fluxes, Atmos. Chem. Phys., 11, 4873–4898, doi:10.5194/acp-11-4873-2011, 2011.

Tie, X., Guenther, A., and Holland, E.: Biogenic methanol and its impacts on tropospheric oxidants, Geophys. Res. Lett., 30, 1881, doi:10.1029/2003GL017167, 2003.

Tyndall, G. S., Cox, R. A., Granier, C., Lesclaux, R., Moortgat, G. K., Pilling, M. J., Ravishankara, A. R., and Wallington, T. J.: Atmospheric chemistry of small organic peroxy radicals, J. Geophys. Res., 106, 12157–12182, doi:10.1029/2000JD900746, 2001.

Vigouroux, C., De Mazière, M., Demoulin, P., Servais, C., Hase, F., Blumenstock, T., Kramer, I., Schneider, M., Mellqvist, J., Strandberg, A., Velazco, V., Notholt, J., Sussmann, R., Stremme, W., Rockmann, A., Gardiner, T., Coleman, M., and Woods, P.: Evaluation of tropospheric and stratospheric ozone trends over Western Europe from ground-based FTIR network observations, Atmos. Chem. Phys., 8, 6865–6886, doi:10.5194/acp-8-6865-2008, 2008.

Vigouroux, C., Stavrakou, T., Whaley, C., Dils, B., Duflot, V., Hermans, C., Kumps, N., Metzger, J.-M., Scolas, F., Vanhaelewyn, G., Müller, J.-F., Jones, D. B. A., Li, Q., and De Mazière, M.: FTIR time-series of biomass burning products (HCN, C_2H_6, C_2H_2, CH_3OH, and HCOOH) at Reunion Island (21° S, 55° E) and comparisons with model data, Atmos. Chem. Phys., 12, 10367–10385, doi:10.5194/acp-12-10367-2012, 2012.

von Kuhlmann, R., Lawrence, M. G., Crutzen, P. J., and Rasch, P. J.: A model for studies of tropospheric ozone and nonmethane hydrocarbons: Model description and ozone results, J. Geophys. Res., 108, 4294, doi:10.1029/2002JD002893, 2003a.

von Kuhlmann, R., Lawrence, M. G., Crutzen, P. J., and Rasch, P. J.: A model for studies of tropospheric ozone and nonmethane hydrocarbons: Model evaluation of ozone-related species, J. Geophys. Res., 108, 4729, doi:10.1029/2002JD003348, 2003b.

Warneke, C., Karl, T., Judmaier, H., Hansel, A., Jordan, A., Lindinger, W., and Crutzen, P. J.: Acetone, methanol, and other partially oxidized volatile organic emissions from dead plant matter by abiological processes: Significance for atmospheric HO_x chemistry, Global Biogeochem. Cy., 13, 9–17, doi:10.1029/98GB02428, 1999.

Warneke, C., de Gouw, J. A., Goldan, P. D., Kuster, W. C., Williams, E. J., Lerner, B. M., Jakoubek, R., Brown, S. S., Stark, H., Aldener, M., Ravishankara, A. R., Roberts, J. M., Marchewka, M., Bertman, S., Sueper, D. T., McKeen, S. A., Meagher, J. F., and Fehsenfeld, F. C.: Comparison of daytime and nighttime oxidation of biogenic and anthropogenic VOCs along the New England coast in summer during New England Air Quality Study 2002, J. Geophys. Res., 109, D10309, doi:10.1029/2003JD004424, 2004.

Wells, K. C., Millet, D. B., Hu, L., Cady-Pereira, K. E., Xiao, Y., Shephard, M. W., Clerbaux, C. L., Clarisse, L., Coheur, P.-F., Apel, E. C., de Gouw, J., Warneke, C., Singh, H. B., Goldstein, A. H., and Sive, B. C.: Tropospheric methanol observations from space: retrieval evaluation and constraints on the seasonality of biogenic emissions, Atmos. Chem. Phys., 12, 5897–5912, doi:10.5194/acp-12-5897-2012, 2012.

Xu, L.-H., Lees, R. M., Wang, P., Brown, L. R., Kleiner, I., and Johns, J. W. C.: New assignments, line intensities, and HITRAN database for CH_3OH at 10 µm, J. Mol. Spectrosc., 228, 453–470, doi:10.1016/j.jms.2004.05.017, 2004.

Zander, R., Mahieu, E., Demoulin, P., Duchatelet, P., Roland, G., Servais, C., Mazière, M. D., Reimann, S., and Rinsland, C. P.: Our changing atmosphere: Evidence based on long-term infrared solar observations at the Jungfraujoch since 1950, Sci. Total Environ., 391, 184–195, doi:10.1016/j.scitotenv.2007.10.018, 2008.

Faculty of Sciences

Institute of Astrophysics and Geophysics

Long-term study of methane and two of its derivatives from solar observations recorded at the Jungfraujoch station

A dissertation presented by Whitney Bader in fulfillment of the thesis requirement for the degree of Doctor of Philosophy in Sciences

2015

It's been a long day
without you my friend
and I'll tell you all about it
when I see you again.

À François.

Abstract

A long-term study of methane and two of its derivatives, i.e. ethane and methanol from ground-based FTIR solar observations recorded at the high alpine International Scientific Station of the Jungfraujoch (3580 m a.s.l.) is reported. Those three gases act as tropospheric ozone precursors through their removal pathway and therefore have an impact on air quality. In the stratosphere, methane influences the content of ozone and in the production of water vapor. Moreover, both methane and ethane impact the greenhouse radiative forcing. While the latter is an indirect greenhouse gas because of its sinks, the former is the second most important anthropogenic greenhouse gas after CO_2.

The primary challenge of this work is the development and optimization of retrieval strategies for the three studied gases from FTIR spectra recorded at the Jungfraujoch station, in the framework of the Network for Detection of Atmospheric Composition Change (NDACC), in order to assess their concentrations in the atmosphere and to study their long-term trend and recent changes as well as their seasonal variations. The development and optimization of a retrieval strategy, based on the selection of the best combination of parameters, aims to limit interferences, minimize residuals, and maximize information content. To this end, the best retrieval strategy has been selected from a great number of available combinations thanks to a method for error analysis developed through this work.

A 17-year time series of methanol is presented thanks to the combination of spectral windows for the first time for ground-based observations resulting in the improvement of the information content. We therefore present the first long-term time series of methanol total, lower tropospheric and upper tropospheric–lower stratospheric partial columns. We found no significant long-term trend of methanol but its seasonal cycle shows a high peak-to-peak amplitude of ~103 % for total columns characterized by minimum values in winter and maximum values during summertime. The presented time series provides a valuable tool for model and satellite validation and complement the few NDACC measurements at northern mid-latitudes.

Regarding ethane, we have for the first time included a combination of improved spectroscopic parameters as well as an improved a priori state that substantially reduce fitting residuals and enhance information content. Analysis of the long-term trend of ethane covering 20 years of observations revealed a strong positive trend of ethane from 2009 onwards of ~5 %/year. We hypothesize that this recent ethane upturn may be the result of a large increase in fugitive emissions from the massive exploitation of shale gas and tight oil reservoirs on the North American continent.

Finally, we quantified the changes of methane since 2005 from 10 ground-based NDACC sites, with a mean global increase of 0.30 %/year. Investigations into the source(s) responsible for this re-increase are performed with a GEOS-Chem tagged simulation that provides the contribution of each emission source and one sink to the total methane simulated. From the analysis of the GEOS-Chem tracers on both the local and global scales, we determined that the increasing anthropogenic emissions such as coal mining, gas and oil transport and exploitation, have played a major role in the increase of atmospheric methane observed since 2005 while they are secondary contributors to the total methane budget.

Résumé

Une étude à long terme du méthane et de deux de ses dérivés, à savoir l'éthane et le méthanol utilisant des observations solaires enregistrées à la station scientifique internationale du Jungfraujoch (3580 m d'altitude) est présentée. Ces trois gaz, précurseurs d'ozone troposphérique, ont un impact sur la qualité de l'air. Dans la stratosphère, le méthane influence le contenu en ozone et est source de vapeur d'eau. En outre, le méthane et l'éthane ont un impact sur le forçage radiatif global. En effet, alors que ce dernier est un gaz à effet de serre indirect en raison de ses puits, le méthane est le deuxième gaz à effet de serre anthropique le plus abondant après le CO_2.

Le principal objectif de ce travail est le développement et l'optimisation de la stratégie d'inversion des trois gaz étudiés à partir de spectres FTIR enregistrés au Jungfraujoch, dans le cadre du réseau NDACC (*Network for Detection of Atmospheric Composition Change*); et ce, afin d'évaluer leurs concentrations atmosphériques et d'étudier leurs tendances à long et court terme ainsi que leur variation saisonnière. Il s'agit de limiter les interférences, minimiser les résidus, et maximiser le contenu en information sur base de la meilleure combinaison de paramètres disponibles. La sélection de la meilleure stratégie d'inversion s'effectue notamment grâce à la méthode d'analyse d'erreur développée ici.

Une stratégie d'inversion du méthanol offrant une nette amélioration du contenu en information est obtenue grâce à la combinaison de deux fenêtres spectrales. Nous déduisons des séries temporelles longues de 17 ans de colonnes totales et partielles, pour la basse troposphère et haute troposphère-basse stratosphère. Alors que l'analyse des séries temporelles ne montre aucune tendance significative à long-terme, le cycle saisonnier des colonnes totales de méthanol caractérisé par des valeurs minimales en hiver et maximales en été, montre une forte amplitude de ~103%. Les séries temporelles produites fournissent un outil précieux pour la validation de modèles et satellites et complètent les mesures NDACC aux latitudes moyennes de l'hémisphère nord.

En ce qui concerne l'éthane, nous avons pour la première fois combiné de meilleurs paramètres spectroscopiques et amélioré l'état a priori, réduisant sensiblement les résidus et améliorant le contenu en information. L'analyse de tendances pour la période 1994-2014 a révélé une forte augmentation de l'éthane à partir de 2009 qui équivaut à ~5 %/an. Nous émettons l'hypothèse que cette récente reprise de l'éthane peut être le résultat d'une forte augmentation des émissions liées à l'exploitation massive de gaz de schiste et des réservoirs de pétrole sur le continent nord-américain.

Enfin, nous avons quantifié l'augmentation moyenne globale du méthane depuis 2005 à 0.30 %/an à partir d'observations au sol de 10 stations NDACC. Une simulation taguée du modèle GEOS-Chem qui fournit la contribution de chaque source d'émission (et un puit) au méthane total simulé nous permet d'investiguer la(les) source(s) responsable(s) de cette ré-augmentation. A partir d'une analyse locale et globale des traceurs GEOS-Chem, nous avons déterminé que l'augmentation des émissions anthropiques telles que l'exploitation des mines de charbon, du gaz naturel et du pétrole ainsi que leur transport, ont joué un rôle déterminant dans l'augmentation du méthane atmosphérique après 2005 alors qu'ils ne sont que des contributeurs secondaires au budget total du méthane.

Acknowledgments

First of all, I would like to thank my supervisor Dr. Emmanuel Mahieu for his boundless support. His crucial guidance through those four years helped set my research career on the right track. I am grateful for his time spent on continuous training, constructive discussions, and proofreading. He provided me the best working conditions and helped me find my way.

I am also very thankful to Dr. Agnès Perrin (Laboratoire Interuniversitaire des Systèmes Atmosphériques, Paris, France), Dr. Jean-François Müller (Belgian Institute for Space Aeronomy), Prof. Louis François and Prof. Michel Erpicum (University of Liège) who have agreed to join my thesis committee. Prof. Pierre Magain (University of Liège) is further acknowledged for accepting to be the chairman of my jury.

Many thanks further go to my colleagues of the GIRPAS team, contributors to collecting FTIR data at Jungfraujoch over the years, for their constant support during this research: Benoit Bovy, Bernard Lejeune, Bruno Franco, Olivier Flock, Diane Zander, Christian Servais, and Ginette Roland. I also would like to thank Rodolphe Zander who started it all. He will be deeply missed.

This work has been supported by the AGACC-II project of the Science for Sustainable Development (SSD) program and ACCC project of the PRODEX program. Both SSD and PRODEX programs are funded by the Belgian Science Policy Office (BELSPO, Brussels). Support is also brought by the NORS project from the European Community's Seventh Framework Programme. We thank the International Foundation High Altitude Research Stations Jungfraujoch and Gornergrat (HFSJG, Bern) for supporting the facilities needed to perform the observations. The Swiss GAW-CH program is further acknowledged.

I personally would like to thank my parents who always taught me to be the best version of myself. I would like to tell my mother that love is what makes us grow together against all odds, no matter the differences that set us apart more often than we may have wished. To my father, I know that you are a proud father and that you are there when needed. I would like to dedicate this work to my wonderful little sister and three little brothers who let me enjoy the amazing opportunity of being their big sister. Now it is your turn to find what makes you feel alive and to give everything in your power to make it real no matter what it may be. I would like to thank my dearest friend Pauline who always found the bright side of every situation even when I thought there was none. I also would like to thank my friends and my #friends who showed so #muchlove and endured every good and bad day I had for four years now. You guys are all amazing!

Finally, I would like to thank my dearest, loveliest and charming Juan who showed support even when I did not expect him to (and those days were rare…), who showed confidence when I had none left and who showed patience when I was in over my head. I couldn't have dreamed of a better partner for this adventure that is a doctorate and for the greatest adventure of all that is life.

Table of contents

Introduction

Doing research in geophysics, more specifically in atmospheric chemistry and composition, is the obvious choice when having a bachelor's degree in chemistry and a master's degree in climatology. While the background in chemistry I acquired provides a knowledge on the composition, structure and properties of matter, two years studying climatology taught me the phenomena of climatic conditions. This multidisciplinary formation enables me to study topics applied to environmental and societal questions.

Since the composition of the Earth's atmosphere continuously evolves, notably due to the accumulation of an increasing number of gaseous constituents – very often chemically and radiatively active – emitted from the surface by human activities, the state of the Earth's atmosphere has been in the midst of preoccupations since the 1980s. More specifically, in 1985, with the discovery of the ozone hole [*Farman et al.*, 1985], and during the Vienna Convention for the Protection of the Ozone Layer where the United Nations raised awareness on the impact of anthropogenic activities on the atmospheric composition change and its consequences. The Vienna Convention outlined the responsibilities of the signatory states for protecting human health and environment against the effects of ozone depletion. In 1987, on the basis of the Vienna Convention, the Montreal protocol on substances that deplete the ozone layer was negotiated and signed. After two substantial amendments in 1990 and 1992, the Montreal Protocol was ratified by 197 states who were legally bound to phase out the production and consumption of compounds that deplete ozone in the stratosphere such as chlorofluorocarbons, halons, carbon tetrachloride, and methyl chloroform. Nowadays, the Montreal Protocol proved to be the "the single most successful international agreement to date" [K. *Annan*, Former Secretary General of the United Nations, 2003].

In 1992, consequently to the development of concerns about climate change, an international environmental treaty was negotiated and adopted at the Earth Summit, in Rio de Janeiro, the United Nations Framework Convention on Climate Change (UNFCCC). The governing body of the international convention is called a conference of the parties (COP) and takes place every year since 1995. In 1997, based on the principle that some anthropogenic emitted atmospheric gases, called greenhouse gases, interact with incoming and outgoing radiation and thus play a role in controlling the temperature of the Earth, the Kyoto Protocol was adopted outlining the reduction of their emissions to limit their concentrations in the atmosphere to "a level that would prevent dangerous anthropogenic interference with the climate system" [*Article 2 of the United Nations Framework Convention on Climate Change*, 1997]. The Kyoto Protocol is based on the principle that developed countries are historically responsible for the current levels of greenhouse gases in the atmosphere differentiating the common responsibilities of the 191 ratifying countries. In 2010, at the COP 16, parties to the UNFCCC agreed on the need to take urgent action to reduce global greenhouse gas emissions to limit future global warming and therefore limit the global average temperature below 2°C relative to the pre-industrial temperature level [*Report of the Conference of the Parties on its sixteenth session, United Nations*, 2011].

In order to help governments and policymakers develop informed decisions about ozone depletion and climate change, the Chemical Science Division (CSD) of the National Oceanic and Atmospheric Administration (NOAA, www.noaa.org), ensured to provide clear scientific information for decisions. Since its inception in 1987, the Scientific Assessment of Ozone Depletion sponsored by the World Meteorological Organization (WMO) and the United Nations Environment Programme (UNEP) contributed and still contributes to our understanding of the processes controlling the ozone distribution and changes in the framework of the Montreal Protocol [Latest Ozone Assessment Report; *World Meteorological Organization*, 2014a]. Regarding climate change, the leading body for its assessment is the Intergovernmental Panel on Climate Change (IPCC, www.ipcc.ch). Established in 1988 by the UNEP and the WMO, it provides a clear scientific view on the current state of knowledge in climate change and its potential environmental and socio-economic impacts. The role of the IPCC is to review and assess the most recent scientific information produced worldwide [Latest assessment report; *Intergovernmental Panel on Climate Change (IPCC)*, 2014].

As atmospheric components interacting with incoming and outgoing radiation affect the Earth's energy budget thanks to their physical properties (described in Chapter 1), it is possible to determine their concentrations in the atmosphere from infrared solar observations through a process called inversion. In such context, the "Groupe InfraRouge de Physique Atmosphérique et Solaire" (GIRPAS, Institute of Astrophysics and Geophysics, University of Liège) observes solar radiation in the infrared since the mid-fifties at the International Scientific Station of the Jungfraujoch (ISSJ, Swiss Alps, 46.5°N, 8.0°E, 3580 m a.s.l.), in the framework of the Network for Detection of Atmospheric Change (NDACC, www.ndacc.org). Systematic monitoring of the chemical composition of the Earth's atmosphere started in 1984 by using two state-of-the-art Fourier Transform InfraRed (FTIR) instruments, while grating spectrometers were used previously in the early 1950s, and from the mid-1970s onwards.

Through this work, we focused our interest into three atmospheric compounds, i.e. methane, ethane and methanol (see Chapter 2). The three of them have an impact on air quality since their removal pathway affects the production of ozone in the atmosphere whereas methane and ethane act as direct and indirect greenhouse gases, respectively.

The primary challenge of this work is to develop and optimize strategies for inversion of methane, ethane and methanol concentrations from FTIR spectra recorded at the Jungfraujoch station. The development of those strategies, described in Chapter 3, consists in: systematic search for and evaluation of absorption lines of the target species and determination of the best combination of spectral windows, spectroscopic linelist (for the target and interfering species), a priori vertical distribution profile, among others in order to limit uncertainties and maximize the altitude sensitivity range. The choice of the best retrieval strategy is further determined by analysis of uncertainties associated to the inversion by a method developed in the framework of this thesis.

In the second part of this work, dedicated to the results obtained, we address the long-term time series of methanol above Jungfraujoch (see Chapter 4) whose inversion is very challenging due to high ozone interferences. In addition to long-term trend, analysis of the seasonal cycle of methanol in the atmosphere above Jungfraujoch is presented along with analysis of the diurnal variation. Those analysis are supported and compared with in situ surface measurements, satellite observations and Chemical Transport Model simulations.

Regarding ethane, improved spectroscopic parameters are combined to optimize the retrieval strategy of ethane from ground-based FTIR solar observations recorded at the Jungfraujoch station. A time series of ethane above Jungfraujoch going from 1994 onwards along with analysis of long-term trend are presented in Chapter 5 in addition to comparisons between ethane seasonal cycle as observed at Jungfraujoch and as simulated by the Chemical Transport Model GEOS-Chem.

As of methane, the source(s) responsible for its recent global increase since the mid-2000s remain unidentified [*Kirschke et al.*, 2013]. Therefore, we investigate on its concentration changes since 2005 using FTIR solar observations performed at 10 ground-based sites, all members of the NDACC. As support, we used the GEOS-Chem model tagged simulation that allows us to quantify the contribution of each emission source (or one sink) to the global methane change based on emissions inventories and transport. Analysis of methane changes since 2005 as simulated by GEOS-Chem is given along with analysis of the contribution of each tracer to this recently observed increase.

The long-term study of methanol is subject to an article published in Atmospheric Measurement and Techniques [*Bader et al.*, 2014] while the recent ethane upturn has been reported in the Journal of Quantitative Spectroscopy and Radiative Transfer [*Franco et al.*, 2015]. As of our research on methane changes since 2005, a manuscript is in preparation for submission in Atmospheric Chemistry and Physics in the framework of the special issue "*Twenty-five years of operations of the Network for the Detection of Atmospheric Composition Change (NDACC) (AMT/ACP/ESSD Inter-Journal SI)*". The complete investigations and results mentioned above are presented in the following chapters.

Chapter 1 – The greenhouse gases in the Earth's atmosphere

In this chapter, the physical properties that characterize the incoming and outgoing radiation are presented. The interactions between atmospheric constituents and the latter are explained as well as the impact they have on the Earth's energy budget. We further describe those atmospheric constituents in terms of concentration, concentration change since pre-industrial times and radiative impact on the Earth's energy budget.

1.1. Radiation

1.1.1. Electromagnetic spectrum

Electromagnetic radiation may be viewed as an ensemble of waves propagating at the speed of light ($c = 2.998 \times 10^8$ m.s^{-1} through vacuum). As for any wave with a known speed of propagation, frequency, wavelength, and wavenumber are interdependent. Wavenumber is the reciprocal of wavelength λ:

$$\tilde{\nu} = 1/\lambda \qquad (1.1)$$

and the frequency, ν, can be expressed as:

$$\nu = c \times \tilde{\nu} = c/\lambda \qquad (1.2)$$

Radiative transfer in planetary atmospheres involves an ensemble of waves with a continuum of wavelengths and frequencies, called the electromagnetic spectrum. It is partitioned into two categories named shortwave (λ < 4 μm) and longwave (λ > 4 μm) referring to the wavelength band encompassing most of the radiation respectively coming from the sun and emitted from the Earth (see next section). The spectrum is typically subdivided into regions as illustrated in Figure 1.1. The high frequency x-ray region, which extends from wavelengths of 10^{-5} μm to 0.01 μm, is an ionizing radiation used in many applications including medical imaging and crystallography. The ultraviolet region extending from 0.01 μm to 0.04 μm will play a role in the production of ozone (see section 1.4.3). The visible region, ranging between 0.39 and 0.76 μm, is defined by the range of wavelength that the human eye is sensitive to. The near infrared region which extends from the boundary of the visible up to ~4 μm, is dominated by solar radiation and thus included in the shortwave radiation while the remainder of the infrared region is dominated by terrestrial radiation. Finally, while microwave radiation, with wavelengths ranging from 1 mm to 1m, does not contribute to the Earth's energy balance, it is widely used in remote sensing due to its ability to penetrate through clouds [*Wallace and Hobbs*, 2006].

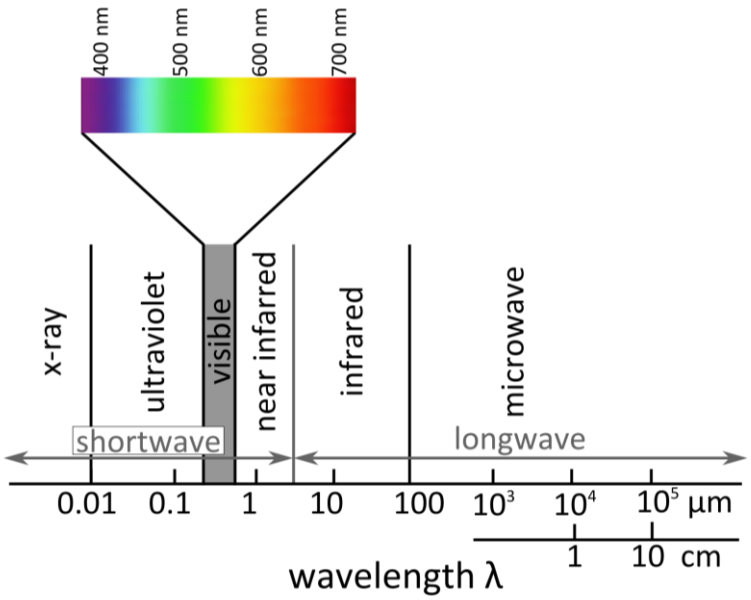

Figure 1.1. The Electromagnetic spectrum [*Wallace and Hobbs*, 2006].

1.1.2. Solar and terrestrial emission spectra

A blackbody is defined as a surface that completely absorbs all incident radiation. The intensity of radiation emitted by a blackbody, i.e. its emission spectrum is given by the Planck's function:

$$I(\lambda, T) = \frac{2hc^2}{\lambda^5} \frac{1}{e^{\frac{hc}{\lambda k_B T}} - 1} \quad (W.sr^{-1}.m^{-3}) \qquad (1.3)$$

where h is the Planck's constant (6.626 x 10^{-34} J.s), c is the speed of light in vacuum, k_B is the Boltzmann constant, λ is the wavelength of the electromagnetic radiation, and T is the absolute temperature of the blackbody. The Boltzmann constant equals 1.381 x 10^{-23} $J.K^{-1}$ and is defined as the ratio between the gas constant (R = 8.314 J.K-1.mol-1) and the number of Avogadro (N_A = 6.022 x 10^{23} mol^{-1}). The plot of the emission spectra of black bodies as a function of wavelength in Figure 1.2 exhibits a sharp wavelength cut-off, a steep rise to a maximum at wavelength λ_m, and a slow drop off toward longer wavelengths.

From this, the Wien's displacement law can be translated by the fact that there is a shift of the wavelength at which the blackbody emission spectrum is maximum, i.e. λ_m, in function of the temperature:

$$\lambda_m(\mu m) = \frac{2.898 \times 10^2 (\mu m.K)}{T\ (K)} \qquad (1.4)$$

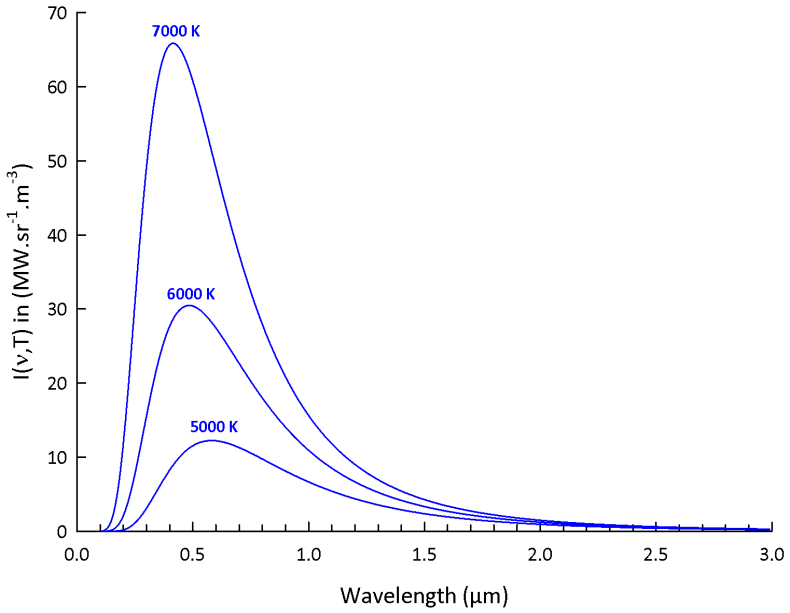

Figure 1.2. Emission spectra of blackbodies with absolute temperature as indicated. Based on [*Wallace and Hobbs*, 2006].

The equation (1.4) is obtained by differentiating I(λ,T) with respect to λ and setting the derivative to zero. In fact, the respective emission spectra of the sun with an absolute temperature of 5780 K and of the Earth whose absolute temperature amounts at 255 K implies that solar radiation is concentrated in the visible region and near infrared (shortwave, λ < 4 μm) while radiation emitted from the Earth is confined to the infrared (longwave, λ > 4 μm), as shown in Figure 1.3.

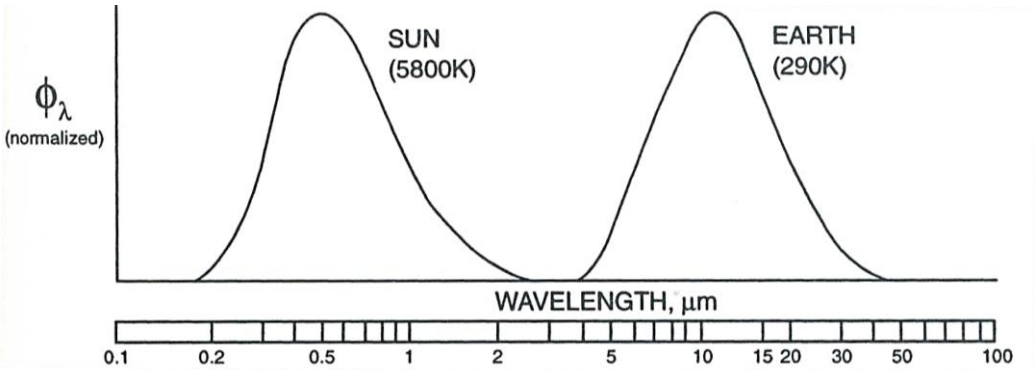

Figure 1.3. Solar and terrestrial emission spectra. [*Jacob*, 1999].

Since solar and terrestrial radiation occupy different ranges of the electromagnetic spectrum, the Earth's atmosphere is relatively transparent to incoming solar radiation and opaque to outgoing infrared radiation emitted by the Earth's surface.

1.2. Interaction mater radiation

1.2.1. Absorption lines

The internal energy (E) of a molecule can be divided into kinetic (E_k) due to thermal agitation, electronic (E_e), rotational (E_r) and vibrational (E_v) energies:

$$E = E_k + E_e + E_r + E_v \tag{1.5}$$

The last three kind of energy are quantized, meaning that the energy stored by the molecule can only correspond to specific levels that depend on the molecule characteristics (energy levels illustrated in Figure 1.4). A molecule may undergo a transition of its internal energy level to a higher level by absorbing electromagnetic radiation or to a lower level by emitting radiation with discrete changes in energy level ΔE. In theory, an absorption corresponding to the transition from a lower level of energy E'' to a higher level E', as a result of incident radiation, equals:

$$\Delta E = E'' - E' = h\nu_0 \tag{1.6}$$

where ν_0 is the frequency of the absorption line center and h is the Planck's constant. As illustrated in Figure 1.4, electronic transitions, i.e. transitions to a higher electronic state, generally require UV radiation while rotational transitions require far-infrared or microwave radiation (> 20 μm). Finally, vibrational transitions require infrared radiation (0.7-20 μm), corresponding to the wavelength range of peak terrestrial radiation (see Figure 1.3).

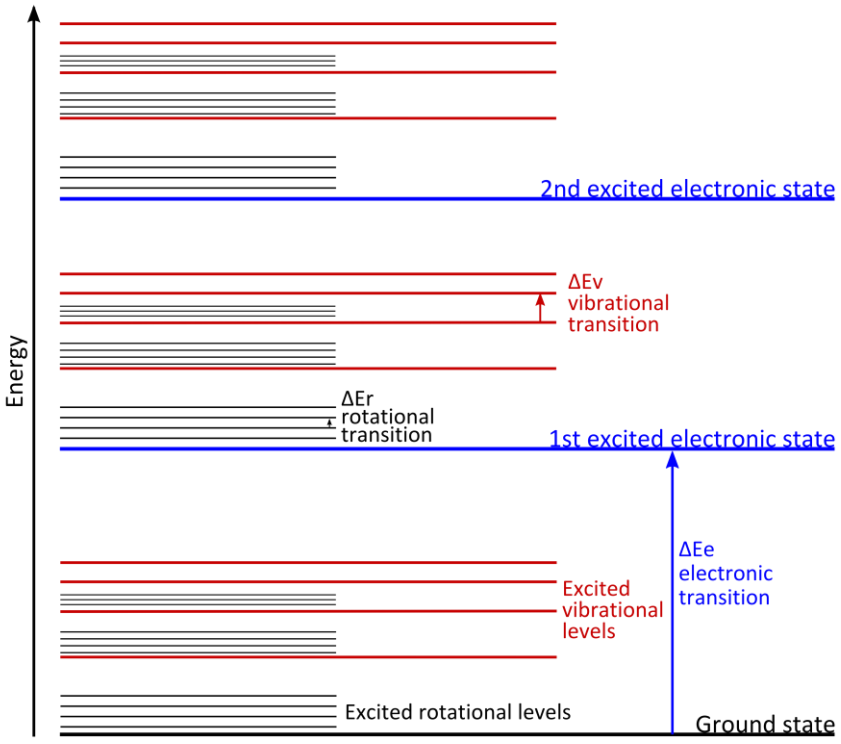

Figure 1.4. Molecule energy levels.

The probability for a particular spectroscopic transition to take place is expressed through quantum selection rules that are used to determine whether a transition is allowed or not. For vibrational transitions, the selection rule for a transition between two vibrational levels v is:

$$\Delta v = \pm 1, \pm 2, \pm 3, \ldots \quad (1.7)$$

The transition from v = 0 to v = 1 is called the fundamental vibration, while transitions with larger Δv are called overtones. Moreover, while |Δv| > 1 are allowed, the intensity of the peaks become weaker as |Δv| increases.

Regarding the rotational selection rule, it requires that transitions between rotational levels, associated to the quantum number J, with:

$$\Delta J = \pm 1 \quad (1.8)$$

are allowed. Transitions with ΔJ = 1 are defined as R branch transitions, while those with ΔJ = -1 are defined as P branch transitions. Transitions corresponding to ΔJ = 0, defined as Q branch transitions are allowed only when there is an additional electronic or vibrational transition involved. A transition of energy levels combining both a rotational and vibrational transition are called ro-vibrational transition. The ro-vibrational transitions allowed and associated with the fundamental vibration are illustrated in Figure 1.5.

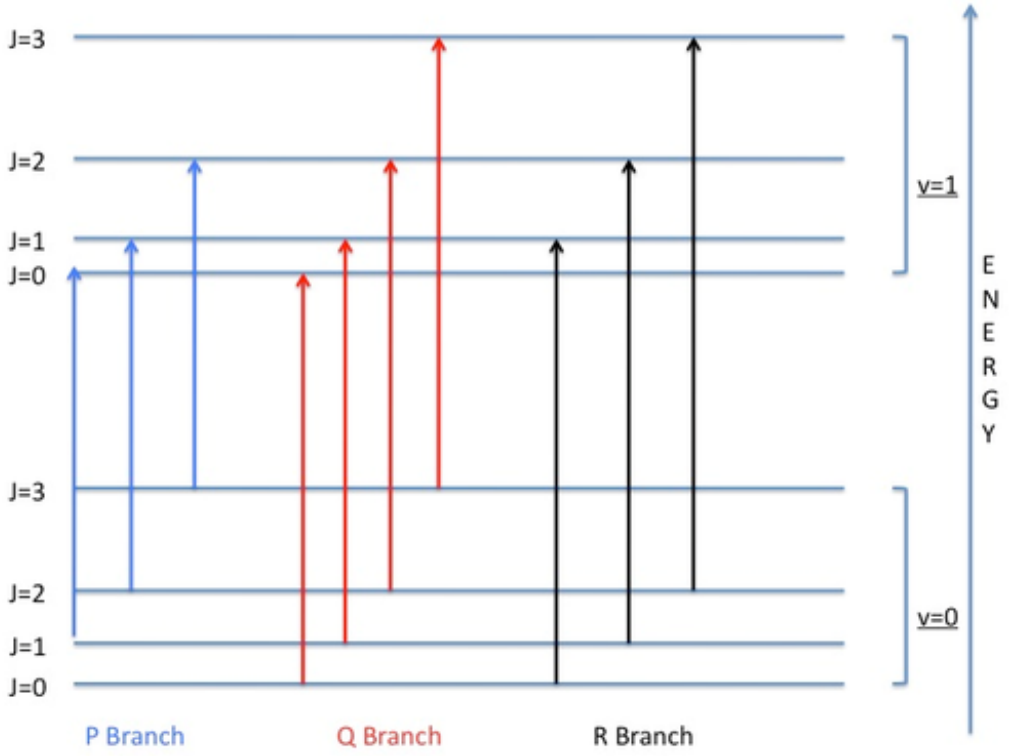

Figure 1.5. Schematic diagram of P, Q, and R branch transitions. [*UC Davis ChemWiki*, 2015]

1.2.2. Vibrational modes

In infrared spectroscopy, an additional selection rule from quantum mechanics is that vibrational transitions are allowed only if there is a change in the dipole moment. A molecule presents a dipole moment when it holds a non-uniform distribution of positive and negative charges on the various atoms it is made of. The combinations of the atomic displacements that give the simplest description of molecular vibrations are called the normal modes of vibration (NMV). The NMVs depend on the symmetry of the molecule and on the number of atoms it bears. To each NMV is associated a frequency of vibration. The vibrational state of a molecule with N atoms is defined by a combination of (3N-6) normal modes of vibrations (except for linear molecules that have 3N-5 NMVs). From this, the frequency of overtones is a linear combination of the frequencies associated with the NMVs.

For example, a molecule of carbon dioxide (CO_2) has four normal modes of vibration as illustrated in Figure 1.6 and bears an increment of positive charge on the atom of carbon and an increment of negative charge on each oxygen atom. CO_2 is not infrared active when it stretches symmetrically (v_1 mode), since it has no dipole moment in this mode due to a perfectly symmetric distribution of charges. Oppositely, the bending (v_2) or the asymmetric stretching (v_3) of CO_2 changes the dipole moment of the molecule. Therefore, the v_2 and v_3 modes are infrared active. In addition, CO_2 has another bending mode in a different plane that has the same energy. Two NMVs with the same frequency, i.e. energy, are called degenerated levels.

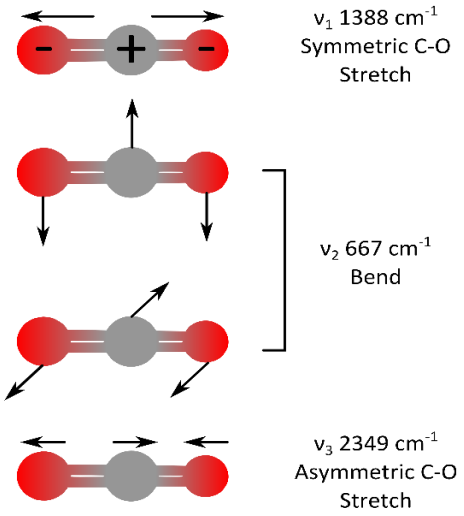

Figure 1.6. Normal modes of vibration of CO_2. Wavenumber values associated to each NMV is given on the right hand side [*NASA Astrobiology Institute's Virtual Planetary Laboratory*, 2015].

In brief, thanks to the molecules physical properties, we may identify key signatures of atmospheric components. Indeed, from a spectrum of transmitted light, spectroscopists may distinguish frequencies for which there is absorption of infrared radiation, assign them to a molecule and determine the corresponding quantum numbers of the transition.

1.2.3. Broadening of absorption lines

In practice, the absorption of radiation is not purely monochromatic. Indeed, the absorption lines of molecules are widened due to the uncertainty on the frequency of the absorption. This natural broadening allows for an interval (ν_0-$\Delta\nu$, ν_0+$\Delta\nu$) within which the absorption is significant. However, this broadening is considered to be negligible compared to the broadening due to the motions and collisions of the gas molecules. The integrated intensity of the line, S(T) is written:

$$S(T) = \int_{\nu_0-\Delta\nu}^{\nu_0+\Delta\nu} \varepsilon \, d\nu \qquad (1.9)$$

where ε is the absorption coefficient defined as

$$\varepsilon = S(T).f(\nu - \nu_0, T, p) \qquad (1.10)$$

The function f is the line profile; it reflects the distribution of the absorption around the frequency ν_0. It depends on the temperature and the pressure and is normalized:

$$\int_{\nu_0-\Delta\nu}^{\nu_0+\Delta\nu} f \, d\nu = 1 \qquad (1.11)$$

The relative motion of the absorbing molecule with respect to the absorbed photon results in what is called the Doppler effect, causing the broadening of the absorption line. The Doppler line shape is a Gaussian distribution expressed by the following equation:

$$f_D(\nu - \nu_0) = \frac{1}{\alpha_D\sqrt{\pi}} \, exp\left[-\left(\frac{\nu-\nu_0}{\alpha_D}\right)^2\right] \qquad (1.12)$$

where ν_0 is the position of the center of the line. The half-width, i.e. the distance between the center of the line and the points at which the amplitude is equal to half the peak amplitude equals:

$$\alpha_D\sqrt{ln\,2} \qquad (1.13)$$

where

$$\alpha_D = \frac{\nu_0}{c}\left(\frac{2kT}{m}\right)^{1/2} \qquad (1.14)$$

and where m is the mass of the molecule, c the speed of light, k is the Boltzmann constant, and T is the temperature.

Inelastic collisions between two molecules also contributes to the broadening of the line shape. It is called the pressure broadening. Its corresponding line shape is a Lorentzian profile characterized by the following function:

$$f_L(\nu - \nu_0) = \frac{\alpha_L}{\pi[(\nu-\nu_0)^2 + \alpha_L^2]} \qquad (1.15)$$

In this expression, the half-width is proportional to the frequency of molecular collisions. Thus, it varies depending on the pressure and the temperature:

$$\alpha_L \propto \frac{p}{T^N} \qquad (1.16)$$

where T and p are the temperature and pressure of the environment surrounding the molecule, N is a coefficient reflecting the temperature dependence of α_L and ranges between 0.3 and 1 depending on the molecule.

If physical conditions are such that both the Doppler effect and the pressure broadening contribute simultaneously and independently to the broadening of the spectral lines, their theoretical profiles are then the result of the convolution of the Lorentz profile and the Doppler one which is called the Voigt line shape:

$$f_V = f_L * f_D \qquad (1.17)$$

Those three profiles are illustrated in the Figure 1.7.

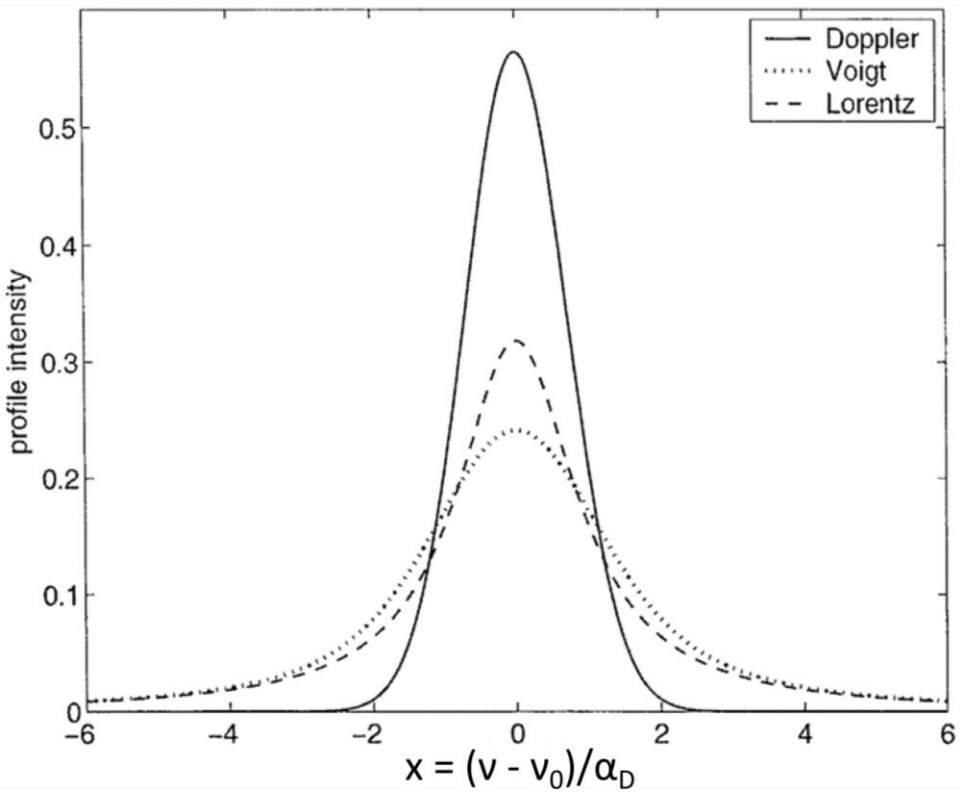

Figure 1.7. Lorentz (solid line), Doppler (dashed line) and Voigt profiles (dotted line) with $\alpha_D = \alpha_L = 1\ cm^{-1}$. [*Huang and Yung*, 2004]

1.2.3. Infrared spectroscopy

In the case of pure absorption spectra, the Beer-Lambert law may be applied. It expresses that for each frequency, the attenuation of the luminance, i.e. the absorbance, is proportional to this luminance and to the number of molecules, located on the path of the light:

$$dL(\nu) = -\varepsilon(\nu, p, T).L(\nu).C.dl \qquad (1.18)$$

where C is the number of molecules absorbing the radiation per volume unit, dl is the length of the path of the radiation and ε is the absorption coefficient which depends on the frequency ν, the temperature T and the pressure p. Considering an initial radiation, L_0, the transmittance will be defined as:

$$T = \frac{L}{L_0} \qquad (1.19)$$

Therefore, knowing L_0, from the measurement of the transmittance, we can quantify the amount of molecules responsible for the absorbance.

Hence, we can determine the atmospheric composition and quantify it with infrared spectroscopy thanks to physical properties such as:

- vibrational transitions of a molecule emitting infrared radiation;
- vibrational transitions of a molecule occurring at a specific energy, frequency and wavenumber;
- the amount of energy absorbed being directly proportional to the number of molecules absorbing.

1.3. The greenhouse effect

As detailed in *Stocker et al.* [2013], solar radiation powers the climate system. Indeed, the main source of heat is solar energy. While some solar radiation is reflected by the Earth and the atmosphere, about half the solar radiation is absorbed by the Earth's surface and warms it. On the other side, some of the infrared radiation emitted from the Earth's surface and that passes through the atmosphere is trapped by clouds and some atmospheric components called greenhouse gases. Indeed, the efficiency of absorption of radiation by the atmosphere is illustrated in Figure 1.8 in parallel with the solar and terrestrial emission spectra of Figure 1.3. On Figure 1.8, major absorbers are illustrated and they will be described in the next section. The region where the absorption is minimum is called the atmospheric window and it covers the 8-14 µm wavelength range.

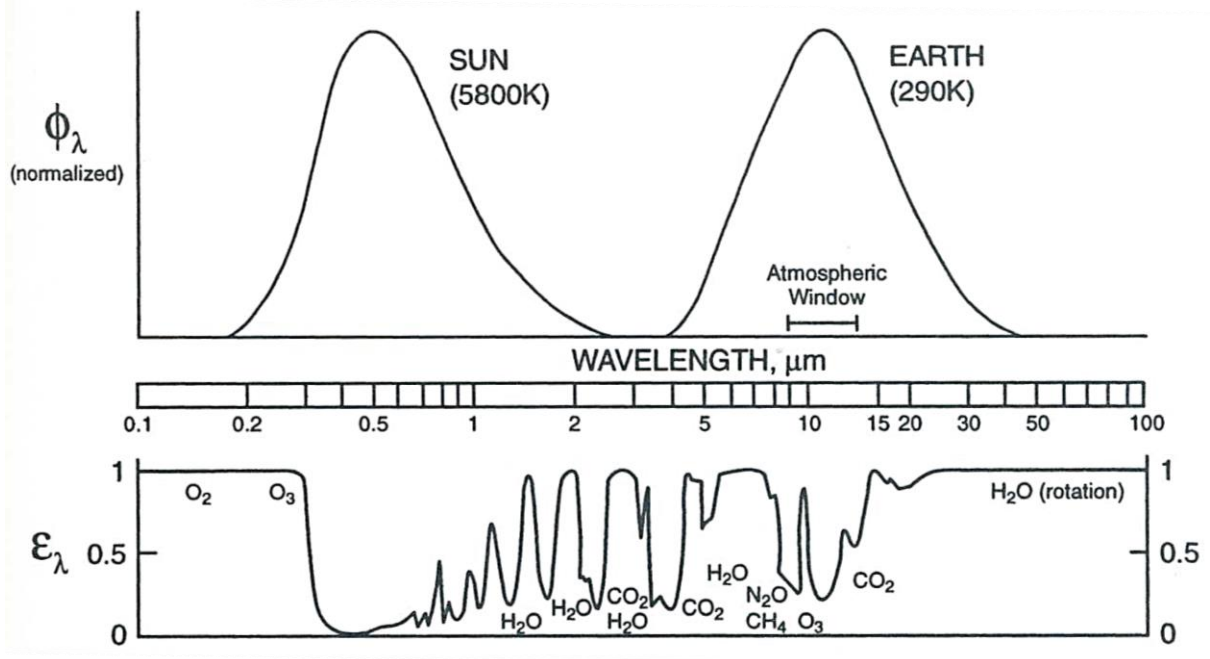

Figure 1.8. Efficiency of absorption of radiation by the atmosphere as a function of wavelength. Major absorbers are identified. [Jacob, 1999]

The greenhouse effect (Figure 1.9) is therefore the re-emission of infrared radiation in all directions by the atmosphere leading to the warming of the surface. It has been established by *Stocker et al.* [2013] that without the natural greenhouse effect, the average temperature at Earth's surface would be around -18 °C. However, human activities have greatly intensified this natural greenhouse effect [*Stocker et al.*, 2013].

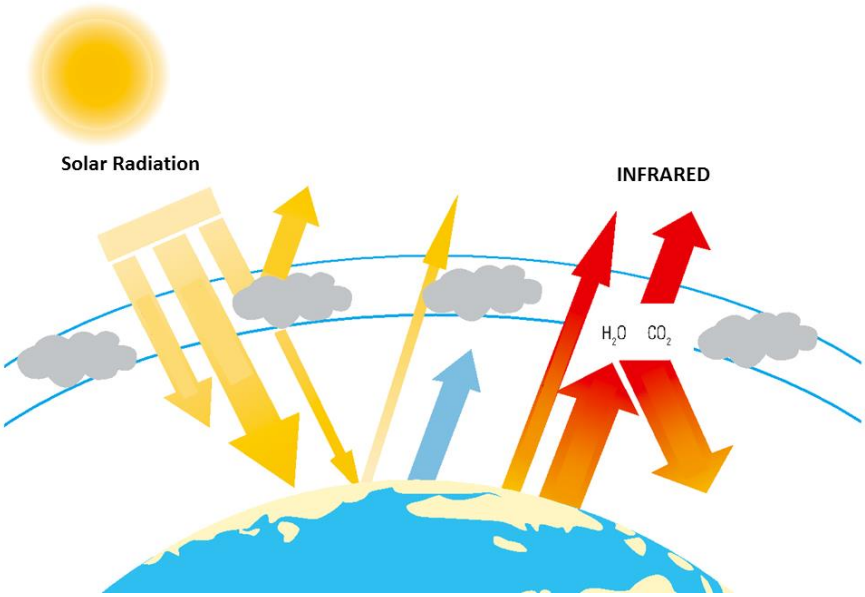

Figure 1.9. The greenhouse effect. [http://etat.environnement.wallonie.be/]

To measure the influence of atmospheric components on the balance of incoming and outgoing energy in the Earth-atmosphere system, the radiative forcing (RF) is defined and expressed in watts per square meter ($W.m^{-2}$). It is an index of the importance of the considered atmospheric component to the climate change mechanism since a positive RF leads to surface warming, negative RF leads to surface cooling. In the latest report of the International Panel for Climate Change [IPCC, *Stocker et al.*, 2013], the radiative forcing is calculated at the tropopause or at the top of the atmosphere.

In order to compare the relative impact of the greenhouse gases on the climate change, the IPCC defines a Global Warming Potential index (GWP) which is based on the time-integrated global mean radiative forcing of a 1 kg pulse emission of an atmospheric gas relative to the emission of the same amount of the reference gas: CO_2 [*Shine et al.*, 1990]. The time period on which the global mean radiative forcing is integrated is commonly fixed at a hundred years ("100-year horizon"). This notion is therefore not absolute. In brief, the GWP expresses the amount of heat "trapped" over a hundred years by a certain mass of the considered gas in comparison to a similar mass of carbon dioxide.

1.4. The Earth's atmosphere

1.4.1. The atmosphere's temperature profile

The atmosphere is defined by layers delimited by a reversal of the temperature gradient (i.e. the variation of temperature with altitude). The layers are named, from space to the surface: the exosphere, the thermosphere, the mesosphere, the stratosphere and the troposphere (see Figure 1.10). The exosphere, starting around 500 km, is the layer where collisions are sparse enough for particles to follow quasi-ballistic trajectories so that lighter ones such as atomic and molecular Hydrogen or Helium atoms can escape the gravity field (if their speed is higher than the escape velocity, 11km/s) during the long intervals between molecular collisions.

Starting at around 140 km, the thermosphere, with a positive temperature gradient due to absorption of highly energetic solar radiation, is where the heat is propagated by conduction. Below the altitude of around 100 km, at the turbopause, the turbulent mixing dominates. This region is known as the homosphere and extends down to the surface. The homosphere is the region of the atmosphere where the chemical composition is uniform for inert chemical species. For example, the ratio O_2:N_2 remains constant at 21:78 whereas highly reactive chemicals tend to exhibit great concentration variability throughout the homosphere. By opposition, the region above the turbopause is the heterosphere, where molecular diffusion dominates and the chemical composition of the atmosphere varies according to chemical species.

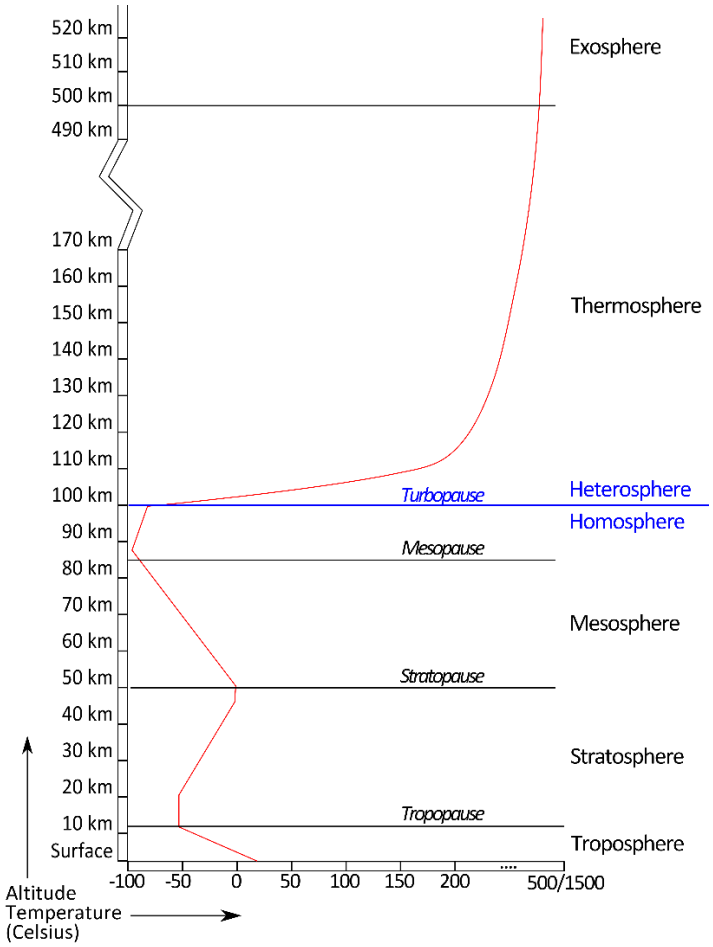

Figure 1.10. Atmospheric temperature profile regions.

Below the thermosphere lies the mesosphere where vertical heat exchanges take place between a minimum of temperature of -73 °C at the mesopause (85 km) where infrared radiation is emitted through space by components such as carbon dioxide (CO_2) or nitrogen monoxide (NO) and a maximum of 0 °C at the stratopause (50 km) where ozone (O_3) absorbs solar radiation with a wavelength of less than 300 nm. This results in a negative temperature gradient.

The stratosphere, a stratified and vertically stable domain due to a positive temperature gradient extends below the stratopause. This stratification inhibits vertical movement and therefore favors rapid horizontal movements. Within the layer, heat is mostly propagated by radiation. The stratosphere is extremely dry and contains around 90 % of the atmospheric ozone which constitutes the ozone layer. The stratosphere has the potential to significantly affect the conditions at the surface. In fact, since the ozone layer absorbs around 98 % of the ultraviolet radiation, changes in stratospheric ozone imply changes in surface ultraviolet irradiance and therefore changes in the supply of tropospheric ozone (see section 1.4.3).

The stratosphere ends at the tropopause, a transition zone, defined by the modification of temperature gradient causing it to be stable. The tropopause acts as dynamic barrier thus limiting the income of constituents from the troposphere to the stratosphere. The altitude of the tropopause varies with season and latitude (See Figure 1.11) and ranges between ~8 km at the Poles and ~18 km at the Equator.

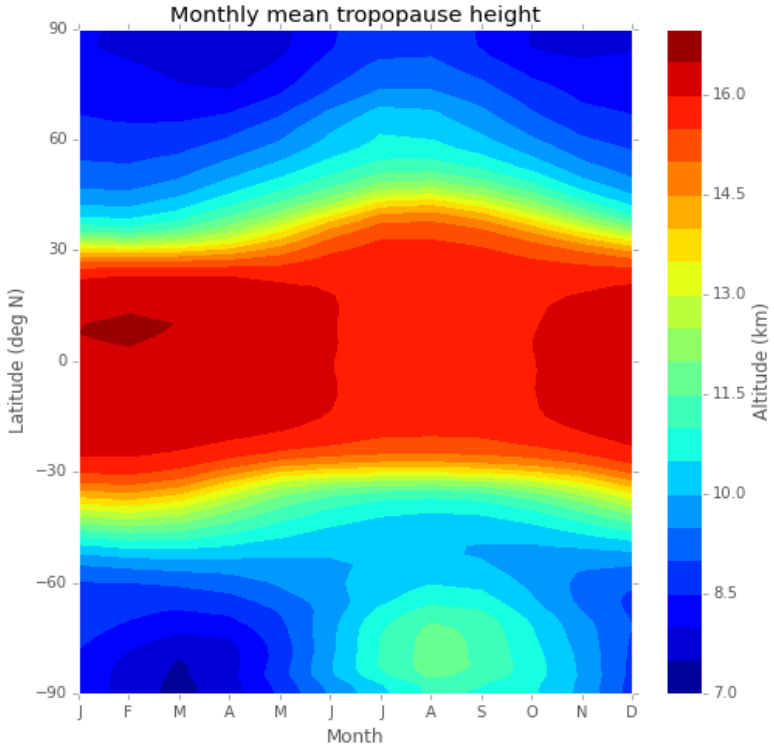

Figure 1.11. Monthly mean tropopause height from NCEP reanalysis [*NOAA/ESRL*, 2015].

Finally, the lowest layer of the atmosphere is named troposphere and contains more than 80 % of the atmospheric mass. The troposphere is the layer where occur the most significant weather events as well as horizontal and vertical atmospheric motions. The temperature decreases with increasing altitude at a rate typically between 5 °C (saturated adiabatic lapse rate) and 10 °C (dry adiabatic lapse rate) per kilometer to reach around -55 °C at the tropopause. Since convection ensures vertical energy and matter exchanges at time scales of a few weeks, the troposphere is dynamically unstable. It is divided into two layers: the atmospheric boundary layer with an average thickness of 1 km that is directly influenced by the surface (i.e. changes in temperature and humidity) and the free troposphere that lies above the latter.

1.4.2. Global atmospheric circulation

Global circulation in the atmosphere plays a major role in the vertical and latitudinal distribution of trace gases. Indeed, the distribution of atmospheric components with relatively long atmospheric lifetime is not only governed by chemical processes but also by transport through the atmosphere. In the global circulation, we distinguish the zonal circulation (along a latitude circle) and the meridional circulation (along a meridian).

The zonal circulation is illustrated in Figure 1.12 and can be divided into five zones. The direction of zonal winds is governed by the Coriolis effect. Indeed, due to the Earth's rotation, the Coriolis forces induce the deviation of a horizontally moving object on Earth. Therefore, the Coriolis forces deviate air masses of the Northern Hemisphere towards the East, while air masses of the Southern Hemisphere are deviated towards the West. The first zone is the intertropical zone (between the latitudes 30°N and 30°S) that is dominated by North-East trade winds in the Northern hemisphere and by South-Eastern trade winds in the Southern Hemisphere. Trade winds converge on the InterTropical Convergence Zone (ITCZ). The ITCZ is a highly convective band of about hundreds kilometers characterized by heavy rainfalls. The temperate zones characterized by western winds called westerlies extend from 30° to 60° of latitude in both hemispheres. Finally, the polar zones beyond 60° of latitude, are characterized by easterlies, i.e. eastern winds.

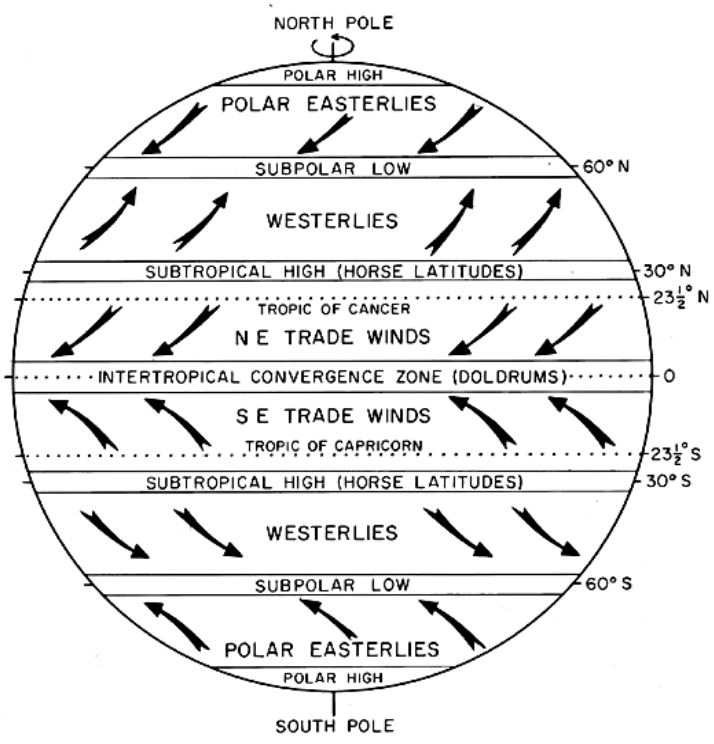

Figure 1.12. Atmospheric zonal transport [Baker et al., 1986].

The meridional circulation is illustrated in Figure 1.13. In the troposphere, the meridional circulation is associated with convection and can be resumed into three types of convective cells. The Hadley cells are

characterized by convection at the ITCZ and extend to around 30° at subtropical latitudes with subsidence of airmasses. The polar cells starting from 60° where warm and moist air masses rise due to convection and move through the pole. When the airmasses reach the polar area, it has cooled considerably and descends to a cold, dry high-pressure area, the polar high. At the polar highs, cold low-pressure areas strengthened in the winter spanning less than 1 000 kilometers in diameter are formed. Polar stratospheric clouds that support heterogeneous chemical reactions may form inside polar vortices at very low temperatures [- 78 °C; *World Meteorological Organization*, 2014b]. Within each polar vortex, due to the Coriolis effect, the air circulates respectively in the counter-clockwise and clockwise direction in the Northern and Southern Hemisphere. Finally, due to the subsidence at the subtropical high associated with the Hadley cell and the convection at the subpolar low associated with the polar cell, a circulation cell between 30° and 60° of latitude is formed, the Ferrel cell.

In the stratosphere, the meridional circulation is governed by the Brewer-Dobson circulation. This basic physical model had been proposed by Dobson and Brewer to explain observations of high concentration of ozone in the Arctic in spring and low concentrations in the Tropics [*Dobson et al.*, 1929; *Dobson*, 1956] and the stratospheric distribution of water vapor [H_2O; *Brewer*, 1949]. While numerous models described the Brewer-Dobson circulation, it can be resumed into two circulation cells. First, the single-cell time-averaged model referred as the Brewer-Dobson circulation in *Butchart* [2014] describes how air circulates by a slow mean motion into the stratosphere at the equator, moves poleward in the stratosphere and sinks into the troposphere in temperate and polar regions [*Brewer*, 1949]. In addition, *Plumb* [2002] described how air circulates at higher altitude in the stratosphere from the tropics to the winter hemisphere.

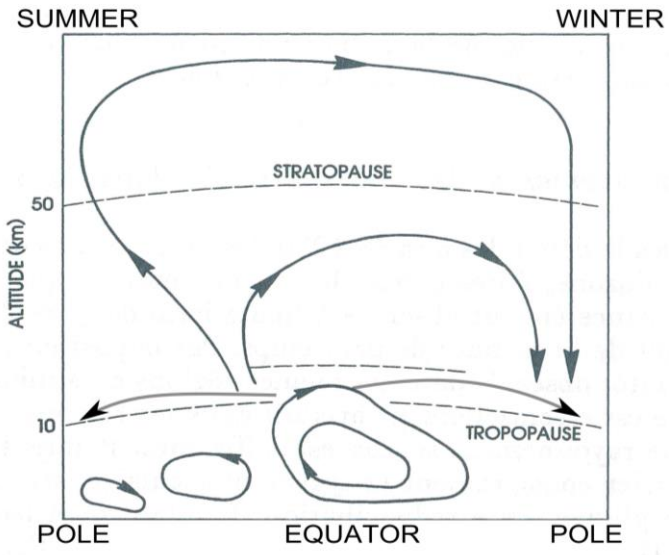

Figure 1.13. Atmospheric meridional transport. Figure from [*Mégie*, 1989] *edited on the basis of* [*Plumb*, 2002].

In contrast to the stratospheric Brewer-Dobson circulation, the mesospheric mass transport is only from the summer to winter pole. At higher levels there is ascent over the summer pole and descent over the winter pole with a well-defined flow towards the winter pole above 50 km [*Murgatroyd and Singleton*,

1961; *Dunkerton*, 1978]. This mechanism is strong enough to pump significant descent of mesospheric air deep into the stratosphere, as shown in Figure 1.13.

Finally, stratospheric-tropospheric exchange (STE) will have an important role on the vertical distribution of some atmospheric components. The upward exchange happen slower due to the stratification of the stratosphere. Indeed, it takes 5 to 10 years for exchanges from the troposphere to the stratosphere while components are removed from the stratosphere to reach the troposphere after only 1 to 2 years. The STE will impact the stratospheric ozone depletion (by upward and downward transport through the tropopause of species involved in the removal mechanism of ozone) as well as the radiative forcing (by downward transport from the stratosphere of greenhouse gases such as ozone) [*Holton et al.*, 1995].

1.4.3. Atmospheric composition

The Earth's atmosphere, among other planets of the solar system, has a specific composition which can be depicted in terms of major, minor and trace constituents (Table 1.1). The Earth's atmosphere is composed mainly of nitrogen (N_2), oxygen (O_2), and argon (Ar). These gases do not interact with the infrared radiation emitted by the Earth and have limited interaction with incoming solar radiation. Regarding minor constituents such as carbon dioxide (CO_2), methane (CH_4), nitrous oxide (N_2O) and ozone (O_3), while they contribute to less than 0.1 % of the total atmospheric content, they play a crucial role in the Earth's energy budget as greenhouse gases since they absorb and emit infrared radiation. Moreover, the atmosphere contains water vapor, which is a natural greenhouse gas. Its mixing ratio is highly variable, but is typically in the order of 1%.

Gas Name	***Chemical Formula***	***Percent Volume***
Major Constituents		
Nitrogen	N_2	78.08 %
Oxygen	O_2	20.95 %
Argon	Ar	0.93 %
Minor Constituents		
Carbon Dioxide	CO_2	0.039 %
Stratospheric Ozone	O_3	0.0005 %
Methane	CH_4	0.00018 %
Nitrous Oxide	N_2O	0.0000326 %
Water vapor	H_2O	variable
Trace gases		
CFC-12	CCl_2F_2	$5.28\ 10^{-8}$ %
CFC-11	CCl_3F	$2.37\ 10^{-8}$ %
HCFC-22	$CHClF_2$	$2.13\ 10^{-8}$ %
HFC-23	CHF_3	$2.4\ 10^{-9}$ %
Sulphur hexafluoride	SF_6	$7.3\ 10^{-10}$ %

Table 1.1. Dry atmosphere average composition from [*World Meteorological Organization*, 2014b] *and* [*Stocker et al.*, 2013].

More than 40 greenhouse gases have been reported by the IPCC including hydrocarbons and halocarbons [*Forster et al.*, 2007]. The main contributors to the increase in radiative forcing since pre-industrial times are detailed in the following paragraph (except for CH_4 that will be further described in chapter 2 and 6) and in Table 1.2 along with their respective concentrations [*World Meteorological Organization*, 2014b], GWP, radiative forcing and lifetime [*Stocker et al.*, 2013]. Their concentrations are expressed in mixing ratio unit. The mixing ratio or mole fraction is the ratio of the number of moles of a constituent in a given volume to the total number of moles of all constituents in that volume. It is usually reported for dry air. Units frequently used are part per million (ppm, 10^{-6}), part per billion (ppb, 10^{-9}) and part per trillion (ppt, 10^{-12}).

Greenhouse Gas	Formula	Concentration	GWP	Radiative Forcing (W m^{-2})	Atmospheric lifetime (years)
Carbon dioxide	CO_2	396 ppm[(a)]	1	1.68 ± 0.35	
Methane	CH_4	1824 ppm[(a)]	28	0.97 ± 0.23	8-10
Nitrous oxide	N_2O	325.9 ppb[(a)]	265	0.17 ± 0.04	131
CFC-12	CCl_2F_2	528.5 ppt[(b)]	10 200		100
CFC-11	CCl_3F	237.7 ppt[(b)]	4 660	halocarbons	45
HCFC-22	$CHClF_2$	213.3 ppt[(b)]	1760	0.18 ± 0.17	11.9
HFC-23	CHF_3	24 ppt[(b)]	12 400		222
Sulfur hexafluoride	SF_6	7.29 ppt[(b)]	23 500		3200

Table 1.2. Global surface concentrations (a) in 2013 from World Meteorological Organization, [2014b] *or (b) in 2011 from Stocker et al.*, [2013]*, Global Warming Potential, Radiative Forcing relative to 1750 (in W.m^{-2}) and atmospheric lifetime (in years) for the main greenhouse gases. [Stocker et al., 2013].*

Carbon dioxide, the main anthropogenic greenhouse gas, contributed to 65 % of the anthropogenic radiative forcing since 1750 (RF of 1.68 ± 0.35 W.m^{-2}). Atmospheric CO_2 never ceases to increase. In fact, it reached 142% of the pre-industrial level in 2013, which is mainly due to emissions from combustion of fossil fuels and cement production. Over the last 10 years its concentration has increased by 20.7 ppm to reach a global concentration of 396.0±0.1 ppm [*World Meteorological Organization*, 2014b]. The main natural sources of CO_2 are the animal and plant respiration and exchanges between the ocean and the atmosphere. Emissions of CO_2 in the atmosphere from human activities in the atmosphere accounts for emissions through fossil fuel burning (transport, heating, air conditioning, cement production, electricity production,…) and land use change. CO_2 main sinks are oceans uptakes (leading to ocean acidification through dissolution), soil uptakes, peatlands, forests and vegetation. In addition, the permanent increase of CO_2 enhances the ocean-atmosphere exchanges by 10 % thus increasing both the source and sink it represents for atmospheric CO_2 [*World Meteorological Organization*, 2014b].

Water vapor concentrations exhibit a very large variability in the troposphere both with space and time depending on meteorological conditions. Human activities have a weak direct impact on water vapor abundance in the atmosphere as they are connected only through climate feedbacks. Therefore, water vapor is not among the Kyoto Protocol target species [*Stocker et al.*, 2013]. In the stratosphere, the water

vapor content is controlled by transport through the tropopause region and subsequent oxidation of methane, its stratospheric source. In fact, increases in stratospheric water vapor act to cool the stratosphere but to warm the troposphere and conversely. Since 2000, stratospheric water vapor contents decreased by about 10 % which acted to slow the rate of increase in global surface temperature over 2000–2009 by about 25% compared to what would have occurred due only to carbon dioxide and other greenhouse gases [*Solomon et al.*, 2010].

Nitrous oxide is the fourth most important contributor to the anthropogenic radiative forcing and acts as an emission source of ozone-depleting substance in the stratosphere [*World Meteorological Organization*, 1985; *Prather and Hsu*, 2010] as the source of stratospheric nitrogen oxides [NO_x; *Crutzen*, 1970b]. With a radiative forcing of 0.17 ± 0.04 $W.m^{-2}$, it contributed to ~6% of the radiative forcing since 1750 [*World Meteorological Organization*, 2014b]. The pre-industrial atmospheric N_2O burden reflected a balance between emissions from soils and the ocean, and chemical losses in the stratosphere. Nowadays, additional anthropogenic emissions are mainly from synthetic nitrogen fertilizers (direct emissions from agricultural fields and indirect emissions from waterways affected by agricultural runoff), fossil fuel combustion, and biomass burning and accounts for 40 % of total N_2O emissions [*World Meteorological Organization*, 2014b]. N_2O increased by 21 % since pre-industrial level (270 ppb in 1750) to reach a mean global concentration of 325.9 ± 0.1 ppb in 2013 mainly due to synthetic nitrogen fertilizers. Between 2012 and 2013, the globally averaged N_2O concentration increased by 0.8 ppb which is comparable to the mean growth rate over the past 10 years (0.82 ppb yr^{-1}).

Halocarbons are molecules in which one or more carbon atoms are linked by covalent bonds with one or more halogen atoms (i.e. fluorine, chlorine, bromine or iodine atoms). Halocarbons are mainly known for their destructive effect on stratospheric ozone towards the release of free atoms of chlorine or bromine first described by [*Molina and Rowland*, 1974]. In addition, halocarbons are generally very strong greenhouse gases. Due to their interesting chemical and physical properties (highly stable, inert, non-flammable), halocarbons like chlorofluorocarbons (CFC) have been widely produced and used by industrial and domestic applications resulting in a rapid accumulation in the atmosphere thanks to their long lifetime (Table 1.2), in addition to natural species such as methyl bromide and methyl chloride. Since their transport and photodissociation in the stratosphere lead to the release of chlorine atoms responsible for the ozone depletion, the production of CFCs has been tightly controlled, then banned, since the Montreal Protocol in 1987. As a decisive result, concentrations of many ozone depleting and halogenated GHGs are now declining. Due to the somewhat contrasted lifetimes of halocarbons in our atmosphere, the impact of the Montreal Protocol has been more rapid for some gases than others. As the Montreal Protocol imposed a phase out of the CFCs, they have been gradually replaced by other types of halocarbons: hydrochlorofluorocarbons (HCFCs) and hydrofluorocarbons (HFCs). These two later categories of halocarbons are strong greenhouse gases by contributing to 12% of the anthropogenic radiative forcing since 1750. The anthropogenic emissions of HCFCs and HFCs are respectively regulated by the Montreal Protocol of 1987 and by the Kyoto Protocol of 1997. While CFCs and most halocarbons are decreasing, HCFCs and HFCs, are increasing at rapid rates, although they are still low in abundance [see Figure 1.14; *Stocker et al.*, 2013; *World Meteorological Organization*, 2014b]. Overall, the chlorine loadings are decreasing in both the troposphere and the stratosphere [*Carpenter et al.*, 2014].

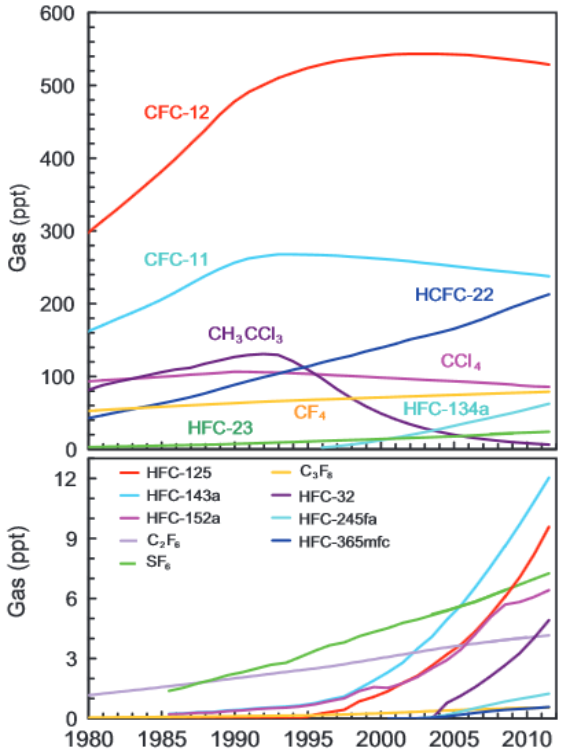

Figure 1.14. Globally averaged dry-air mixing ratios at the Earth's surface of the major halogen-containing greenhouse gases [*Stocker et al.*, 2013].

Finally, sulphur hexafluoride emissions are almost entirely anthropogenic. It is nonflammable, nontoxic, noncorrosive, relatively inert and inexpensive. It is therefore used in many technical applications, such as electrical equipment, double glazing or in shoes soles. Its current concentration is about twice the level observed in the mid-1990s. SF_6 accumulates in the atmosphere due to its very long atmospheric lifetime of 3 200 years [*Stocker et al.*, 2013].

Many pollutants, such as carbon monoxide (CO), nitrogen oxides or volatile organic compounds (VOCs), although not referred to as greenhouse gases, have small direct or indirect effects on radiative forcing. Moreover, O_3, acts as a tropospheric greenhouse gas and as a stratospheric filter for UV radiation while the hydroxyl radical (OH) is the detergent of the atmosphere by being the main sink of most tropospheric gases. Therefore, volatile organic compounds such as ethane (C_2H_6) or methanol (CH_3OH) through reaction with hydroxyl radical have an impact on radiative forcing since they limit the availability of OH to deplete most greenhouse gases. In fact, *Collins et al.* [2002] even estimated a GWP for ethane of 5.1. We therefore need to better understand the mechanisms of formation and destruction of O_3 and OH in order to apprehend the atmospheric chemistry of tropospheric components such as the gases studied through this work, i.e. methane, ethane or methanol.

1.4.4. Ozone

In the atmosphere, ozone plays crucial but different roles in the troposphere and in the stratosphere. In the stratosphere, ozone acts as a filter for ultraviolet radiation since it absorbs around 98 % of the ultraviolet radiation in the 240-300 nm range [*Delmas et al.*, 2005]. With a maximum abundance of ozone at around 25 km, ozone heats the stratosphere from inside up until 50 km which explains that the lower stratosphere is quasi isothermal until an altitude of 30 km. On the other hand, tropospheric ozone is the third most important greenhouse gas [*World Meteorological Organization*, 2014b].

a- Stratospheric ozone

In 1930, S. Chapman [1930] proposed the first theory for ozone formation in the stratosphere as part of the Chapman cycle that describes the equilibrium between the production and depletion of ozone. Stratospheric ozone is formed by photodissociation of molecular oxygen, as follows:

$$O_2 + h\nu \rightarrow O + O \qquad \lambda < 242\ nm \qquad (1.20)$$

$$O_2 + O + M \rightarrow O_3 + M + heat \qquad (1.21)$$

where M can either be O_2 or N_2. The formation of O_3 from O_2 requires the formation of a O-O bond which is an exothermic process (1.21). The energy related to this reaction is released in the stratosphere and induces its warming impacting the stratospheric temperature profile (Figure 1.9). In addition, atomic oxygen can also recombine as follows:

$$O + O + M \rightarrow O_2 + M \qquad (1.22)$$

Regarding the depletion of ozone, *Chapman* [1930] showed:

$$O_3 + O \rightarrow 2\ O_2 \qquad (1.23)$$

$$O_3 + h\nu \rightarrow O_2 + O \qquad (1.24)$$

Chapman's cycle is active only during the day where photodissociation reactions (1.20 and 1.24) are active. During the night only the 1.19, 1.20 and 1.21 reactions are active depleting all atomic oxygen.

Stratospheric ozone can also be depleted through further photodissociation reactions (1.25 and 1.26) and through catalytic cycles. The photodissociation of ozone consists of two pathways depending on the wavelength:

$$O_3 + h\nu \rightarrow O_2 + O(^1D) \qquad \lambda < 310\ nm \qquad (1.25)$$

$$O_3 + h\nu \rightarrow O_2 + O(^3P) \qquad \lambda > 310\ nm \qquad (1.26)$$

The formation of active oxygen, O^1D, returns to its fundamental state, $O(^3P)$ by collision with main components of the atmosphere, N_2 and O_2. However, in the meantime, O^1D acts as an oxidant in the stratosphere for species such as CH_4 or N_2O.

The catalytic cycle responsible for the depletion of ozone can be synthesized by:

$$X + O_3 \rightarrow XO + O_2 \quad (1.27)$$

$$\underline{XO + O \rightarrow X + O_2} \quad (1.28)$$

$$\textit{Balance :} \quad O_3 + O \rightarrow 2\,O_2 \quad (1.29)$$

where X can either be an atom of hydrogen, an hydroxyl radical [*Bates and Nicolet*, 1950], nitric oxide [*Crutzen*, 1970; *Johnston*, 1971], an atom of chlorine [*Stolarski and Cicerone*, 1974], or an atom of bromine [*Wofsy et al.*, 1975].

At a global scale, ozone concentrations reach a maximum at high latitudes and a minimum in the tropics mainly due to meridional transport. The polar vortex associated with high meridional temperature gradient in the winter hemisphere are therefore characterized by a maximum of subsidence at their edge. Therefore, high concentrations of ozone are located at the edges of the polar vortex whereas O_3 is missing from inside the vortex creating what is called the ozone hole. Inside the ozone hole occurs heterogeneous chemistry favored by polar stratospheric clouds leading to the strong depletion of ozone. The polar vortices are not symmetrical and while the southern polar vortex is very cold and very stable, the northern vortex is less stable and cold due to the more complex distribution of continents at mid- and high-northern latitudes.

b- Tropospheric ozone

Tropospheric ozone is the third most important contributor to greenhouse radiative forcing with a radiative forcing of 0.40 ± 0.20 $W.m^{-2}$ [*Stocker et al.*, 2013]. In addition, it acts as a surface air pollutant and as a precursor of the hydroxyl radical, the detergent of the atmosphere (see next section). Ozone is produced in the troposphere by photochemical oxidation of CO, CH_4 and non-methane VOCs (NMVOCs) in the presence of NO_x [*Chameides and Walker*, 1973; *Crutzen*, 1973]. In fact, the oxidation of those compounds will lead to the formation of reactive radicals that will convert NO to nitrogen dioxide or NO_2. The NO_2 formed will in turn produce ozone through the following reactions:

$$NO_2 + h\nu \rightarrow NO + O \quad (1.30)$$

$$O + O_2 \rightarrow O_3 \quad (1.31)$$

Another source of tropospheric ozone is the stratosphere-troposphere exchange (STE). Although STE is only a minor term in the global ozone budget, it carries ozone to the upper troposphere where it impacts the most the radiative forcing [*Forster et al.*, 2007]. Sinks of tropospheric ozone include photochemical and chemical reactions and dry deposition.

1.4.5. The hydroxyl radical

Because of its high reactivity with both inorganic and organic compounds, OH acts as the main detergent of the atmosphere. Indeed, oxidation by OH is the major sink for most atmospheric trace gases. Since it rapidly reacts with CO and hydrocarbons, the tropospheric lifetime of OH is very short, of about a few seconds [*Lelieveld*, 2002].

The formation of OH is governed by ozone. A small fraction of stratospheric O_3 is transported to the troposphere, which constitutes a baseline OH source. Additionally and most importantly, OH is formed from O_3 that is depleted according to (1.25) leading to the formation of $O(^1D)$:

$$O(^1D) + M \rightarrow O(^3P) + M \qquad (97\ \%) \qquad (1.32)$$

$$O(^3P) + O_2 + M \rightarrow O_3 + M \qquad (1.33)$$

$$O(^1D) + H_2O \rightarrow 2\ OH \qquad (3\ \%) \qquad (1.34)$$

Primary OH formation is thus controlled by ozone (1.25), UV radiation and water vapor (1.34). Therefore OH levels are highest in the tropics where the stratospheric ozone layer is thinnest and the absolute humidity is highest [*Lelieveld*, 2002].

Although oxidation of CH_4 and CO constitutes an efficient sink of OH, these reactions do not necessarily deplete OH due to its recycling by two pathways depending on the presence of NO_x. In the presence of NO_x, recycling of OH will lead to ozone production.

$$CO + OH \rightarrow CO_2 + H \qquad (1.35)$$

$$H + O_2 + M \rightarrow HO_2 + M \qquad (1.36)$$

$$NO + HO_2 \rightarrow NO_2 + OH \qquad (1.37)$$

$$NO_2 + h\nu \rightarrow NO + O(^3P) \qquad \lambda < 420\ nm \qquad (1.38)$$

$$\underline{O(^3P) + O_2 + M \rightarrow O_3 + M} \qquad (1.39)$$

$$\text{Balance:} \quad CO + 2\ O_2 \rightarrow CO_2 + O_3 \qquad (1.40)$$

In the absence of sufficient NO_x for example far from pollution sources (1.37) is insignificant and the alternative cycle prevails:

$$CO + OH \rightarrow CO_2 + H \qquad (1.41)$$

$$H + O_2 + M \rightarrow HO_2 + M \qquad (1.42)$$

$$\underline{O_3 + HO_2 \rightarrow 2\ O_2 + OH} \qquad (1.43)$$

$$\text{Balance} \quad CO + O_3 \rightarrow CO_2 + O_2 \qquad (1.44)$$

In the latter case O_3 is destroyed and the hydrogen oxide radicals (HO_x) can recombine into hydrogen peroxide (H_2O_2). This can terminate the radical reaction chain because a large part of the H_2O_2 is removed by dry and wet deposition. While some of the HO_x can be regained from H_2O_2 through photolysis, deposition is a definitive sink for about half the HO_x radicals that form H_2O_2 [*Lelieveld*, 2002]. In those two mechanisms, while CO is the main driver, it can be replaced by any VOC that will in turn lead to the formation of CO when oxidized.

Chapter 2 – Methane and two of its derivatives

In this work, we study methane and two of its derivatives, i.e. namely ethane and methanol. Methane, with the chemical formula CH_4, is a tetrahedral molecule made of one atom of carbon and four atoms of hydrogens, and is the simplest alkane. Ethane is a hydrocarbon with the chemical formula C_2H_6 while methanol, with the chemical formula CH_3OH, is the simplest alcohol.

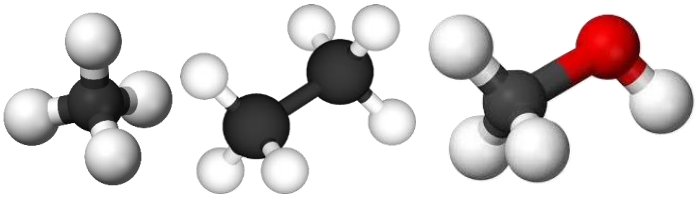

Figure 2.1. Methane, ethane and methanol.

In the atmosphere, methane is the second most abundant anthropogenic greenhouse gas with an abundance of 1824 pbb in 2013 [*World Meteorological Organization*, 2014b], ethane shows an hemispheric averaged abundance of 1 049 ppt in the Northern Hemisphere over the 1984−2010 time period [*Simpson et al.*, 2012] and methanol's abundance ranges between 1 [*Singh et al.*, 2001] and 20 ppbv [*Heikes et al.*, 2002]. Their lifetime have been estimated at around 8−10 years for methane [*Kirschke et al.*, 2013], approximately 2 months for ethane [*Rudolph*, 1995] and between 4.7 days [*Millet et al.*, 2008] and 12 days [*Atkinson et al.*, 2006] for methanol.

In the troposphere, those three gases have an impact on air quality through their removal pathway. In fact, their oxidation impacts the atmospheric content of carbon monoxide, an ozone precursor [CO; *Aikin et al.*, 1982; *Rinsland*, 2002; *Jiménez et al.*, 2003; *Duncan et al.*, 2007] and of nitrogen oxide radicals (NOx), a driver of the production and loss of tropospheric ozone. Through their tropospheric chemistry, they therefore act as ozone precursors [*Rudolph*, 1995; *Rinsland*, 2002; *Montzka et al.*, 2011; *Fischer et al.*, 2014].

In the stratosphere, while ethane and methanol's abundances remain low or even negligible, stratospheric methane influences the content of ozone and the production of water vapour an important driver of decadal global surface climate change [*Solomon et al.*, 2010].

Moreover, both methane and ethane impact the greenhouse radiative forcing. Indeed, with a radiative forcing (RF) of 0.97 ± 0.23 $W.m^{-2}$, methane is the second anthropogenic greenhouse gas after CO_2 [RF of CO_2 in 2011: 1.68 ± 0.35 $W.m^{-2}$; *Stocker et al.*, 2013]. Moreover, although CH_4 is 200 times less abundant than CO_2 [abundance of CO_2 at 396.0±0.1 ppm, *Bates et al.*, 2014], it has a global warming potential of 28 [on a 100-year time horizon, *Stocker et al.*, 2013]. As of ethane, because of its sinks, it is an indirect greenhouse gas with a global warming potential of 5.5 [on a 100-year time horizon, *Collins et al.*, 2002].

The following sections will detail how these three atmospheric compounds share common sources and sinks and how their chemistry is closely connected. In addition, vertical distribution as well as trends and seasonal cycles are described.

2.1. Budget: sources and sinks

The methane budget [*Kirschke et al.*, 2013] includes anthropogenic contributions such as domestic ruminant animals (17 %), oil and gas exploitation (12 %), waste management (11 %), coal mining (7 %), rice cultivation (7 %), biomass burning (4 %), and natural contributions such as wetlands (34 %), termites (4 %), methane hydrates and ocean (3 %). While there still remain uncertainties on its budget, above-mentioned estimated contributions to the atmospheric content of methane are based on *Fung et al.* [1991], *Chen and Prinn* [2006], *Kirschke et al.* [2013] and on emission inventories used for the GEOS-Chem v9-02 CH_4 simulation, *Turner et al.* [2015].

Processes leading to the emission of methane in the atmosphere can alternatively be regrouped into three other categories, i.e. biogenic, thermogenic and pyrogenic emissions [*Kirschke et al.*, 2013]. The biogenic sources involve microbes generating methane. They comprise anaerobic environments such as natural wetlands and rice paddies, oxygen-poor freshwater reservoirs (such as dams), digestive systems of ruminants and termites, and organic waste deposits (such as manure, sewage and landfills). The formation of CH_4 over millions of years through geological processes pertains to thermogenic source. It is vented from the ground into the atmosphere through natural features (such as terrestrial seeps, marine seeps and mud volcanoes), or through the exploitation of coal, oil and natural gas. Indeed, coal mine venting, associated gas from oil wells, and leaks from natural gas wells, storage, pipelines and end use lead to emissions of methane in the atmosphere. Finally, pyrogenic CH_4 is produced by the incomplete combustion of biomass and soil carbon during wildfires, and of biofuels and fossil fuels. Anthropogenic emission sources such as the exploitation of coal, gas and oil are mainly located in the Northern Hemisphere [*Chen and Prinn*, 2006]. On the other hand, natural sources such as biomass burning [*Hao and Ward*, 1993; *Duncan*, 2003], forested and non-forested swamps [*Fung et al.*, 1991] as well as termites, lakes and other fresh waters [*Sanderson*, 1996] show maximum values in the tropics and especially in Africa and tropical South America for the latter.

In the same way than methane, ethane is emitted from leakage from the production, transport of natural gas loss (62%) from biofuel consumption (20%) and from biomass burning (18%), mainly in the Northern Hemisphere [*Logan et al.*, 1981; *Rudolph*, 1995; *Xiao et al.*, 2008]. In contrast, biogenic and oceanic sources show really small contributions to the ethane budget [*Rudolph*, 1995].

For methanol, large uncertainties remain on its atmospheric budget and many studies are dedicated to the quantification of each emission contribution [*Galbally and Kirstine*, 2002; *Tie et al.*, 2003; *von Kuhlmann*, 2003; *Jacob*, 2005; *Millet et al.*, 2008]. Overall, plant growth is the largest source of methanol with a contribution to its emissions from 60 to 85 % [*Galbally and Kirstine*, 2002; *Jacob*, 2005]. Methanol atmospheric production represents up to 15–23% of its sources [*Madronich and Calvert*, 1990; *Tyndall et*

al., 2001]. Indeed, CH_3OH is formed from methylperoxy radicals (CH_3O_2) in the atmosphere according to the following equations:

$$CH_3O_2 + CH_3O_2 \rightarrow CH_3OH + CH_2O + O_2 \quad (2.1)$$

$$CH_3O_2 + RO_2 \rightarrow CH_3OH + R'CHO + O_2 \quad (2.2)$$

The latter reactions occur at a rate of 85/15 % respectively for (2.1)/(2.2). RO_2 is produced from biogenic isoprene (C_5H_8) confined to the continental boundary layer while in the remote atmosphere CH_3O_2 is coming from the oxidation of methane and to a lesser extent of ethane [*Jacob*, 2005]. Other sources of methanol are plant matter decaying [9 %; *Warneke et al.*, 1999; *Millet et al.*, 2008], biomass burning and biofuels combustion [6 %; *Jacob*, 2005; *Dufour et al.*, 2006; *Paton-Walsh et al.*, 2008], fossil fuel combustion, vehicular emissions, solvents and industrial activities [3 %; *Galbally and Kirstine*, 2002].

In the troposphere, where they are the most abundant, the main sink of those three gases is the oxidation by hydroxyl radicals [see next section for chemistry; *Aikin et al.*, 1982; *Jiménez et al.*, 2003; *Chen*, 2005]. In addition, in the stratosphere, reaction with chlorine atoms dominates for both methane and ethane [*Aikin et al.*, 1982; *Chen*, 2005]. For methane, other sinks include consumption by soil bacteria at the surface, by reaction with chlorine atoms in the marine boundary layer, and by reaction with $O(^1D)$, OH, and by photodissociation in the stratosphere [*Chen*, 2005]. Finally, other sinks for methanol are deposition to land through uptake microbial and foliar by vegetation [26 %, *Jacob*, 2005], wet deposition through scavenging of water-soluble methanol by convective updrafts, convective anvils or large scale precipitation [6 %, *Liu et al.*, 2001], uptake within the ocean mixed layer [5 %, from 0 to 50 m, *Millet et al.*, 2008], and heterogeneous oxidation by OH in aerosols and clouds [1 %, *Jacob*, 2005].

2.2. Chemistry

In the troposphere, methane, ethane and methanol's respective chemistry are closely connected and play an important role in the overall tropospheric chemistry since the three of them influence the oxidizing capacity of the atmosphere through reaction with the hydroxyl radical. Figure 2.2 illustrates the main reactional pathway of the oxidation of those three compounds in the troposphere by OH.

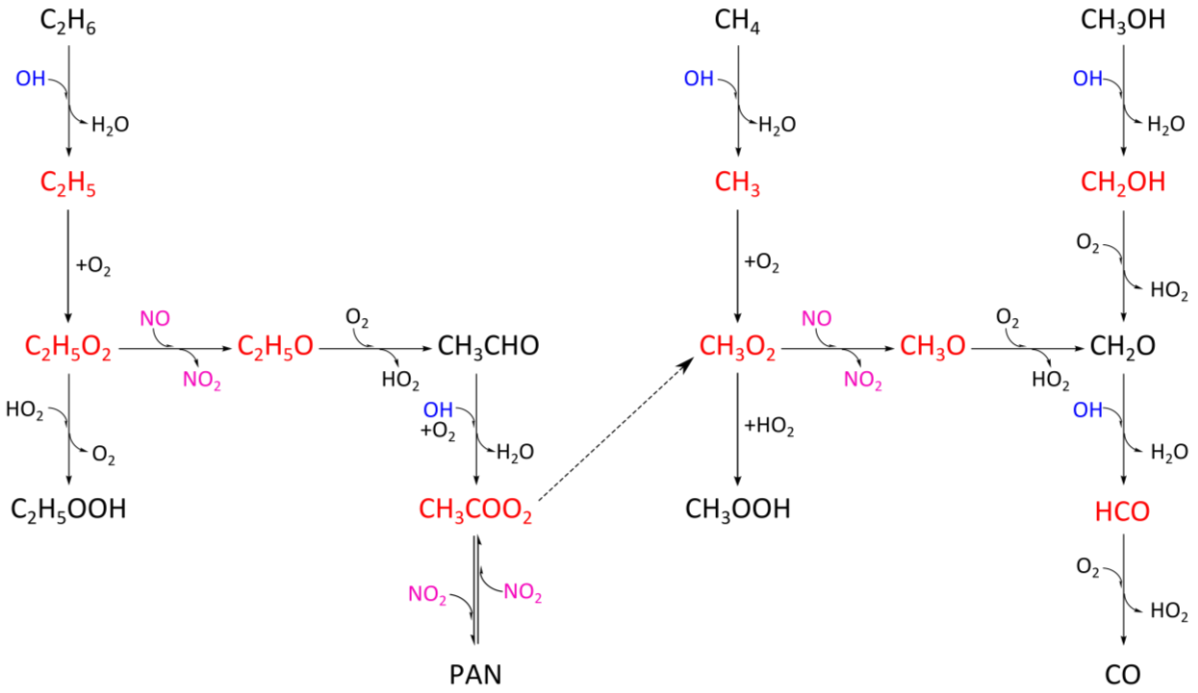

Figure 2.2: Tropospheric chemistry of methane, ethane and methanol. Radicals are shown in red while stable molecules are in black.

While methane, ethane and methanol are chemically quite inert in the atmosphere, they do react with atomic species and molecular radicals which in the troposphere consists mainly of OH. Oxidation of ethane by OH leads to the formation of unstable ethyl radical (C_2H_5) that in turn will react with dioxygen to form ethylperoxy radicals ($C_2H_5O_2$). The reaction between ethyl radicals and dioxygen may also lead to the formation of ethylene (C_2H_4). However, it has been measured that for atmospheric conditions, the interaction of C_2H_5 with O_2 to form $C_2H_5O_2$ radicals is by far the dominant pathway [99 %, *Kaiser et al.*, 1990; *Miller et al.*, 2000; Equation II.A4.88 in *Atkinson et al.*, 2006].

The fate of $C_2H_5O_2$ radicals depends on the local availability of nitrogen monoxide (NO) as illustrated in Figure 2.2. If insufficient NO is available then $C_2H_5O_2$ will react with hydroperoxyl radicals (HO_2) to form the relatively unreactive ethyl hydroperoxide (C_2H_5OOH). On the contrary, if sufficient NO is available (displayed in pink in Figure 2.2), then a rapid reaction sequence follows leading to the recycling of the OH radicals and contributing to the formation of tropospheric ozone by recycling the NO to NO_2 (see Chapter 1, section 1.4.3):

$$C_2H_5O_2 + NO \rightarrow NO_2 + C_2H_5O \qquad (2.3)$$

$$C_2H_5O + O_2 \rightarrow HO_2 + CH_3CHO \qquad (2.4)$$

$$HO_2 + NO \rightarrow NO_2 + OH \qquad (2.5)$$

During this recycling of OH, acetaldehyde (CH_3CHO) is formed. Acetaldehyde can either be photodissociated (see Figure 2.3) to form methane or methyl radicals (CH_3) depending on the wavelength of the photodissociation or be oxidized by hydroxyl radicals to form peroxyacetyl radicals (CH_3COO_2).

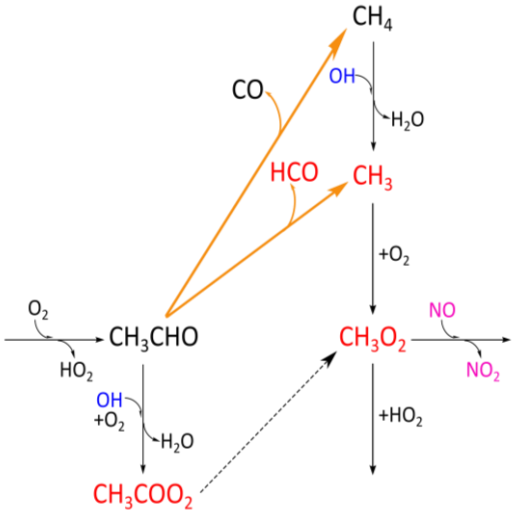

Figure 2.3: Photodissociation of acetaldehyde.

Peroxyacetyl radicals have many pathways of depletion. Its first pathway leads to the formation of peroxyacetic nitric anhydride ($CHCOO_2NO_2$), also called, peroxyacetyl nitrate (PAN, see Figure 2.4) which is produced reversibly by reaction of CH_3COO_2 with NO_2:

$$CH_3COO_2 + NO_2 + M \rightarrow PAN + M \qquad (2.6)$$

where M is a third body (typically N_2 or O_2). It is worth mentioning that PAN's dominant role in the atmosphere is that it acts as an organic reservoir for NO_x [*Roberts et al.*, 1995; *Bertram et al.*, 2013] and thus impacts the production of tropospheric ozone and the hydroxyl radical [*Singh and Hanst*, 1981].

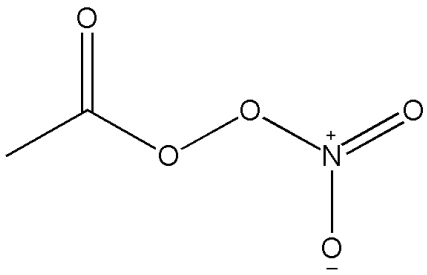

Figure 2.4. PAN or peroxyacetyl nitrate or peroxyacetic nitric anhydride.

As detailed in *Tyndall et al.* [2001], CH_3COO_2 can also form the methylperoxy radical (CH_3O_2) involving a complex series of reactions via many pathways and through the $CH_3C(O)O$ intermediate. The main pathways for the formation of this intermediate are:

$$CH_3COO_2 + NO \rightarrow CH_3C(O)O + NO_2 \quad (2.7)$$

$$CH_3COO_2 + CH_3COO_2 \rightarrow 2\ CH_3C(O)O + O_2 \quad (2.8)$$

This intermediate will then decompose into CH_3 and CO_2 according to the following equation:

$$CH_3C(O)O + M \rightarrow CH_3 + CO_2 + M \quad (2.9)$$

The methyl radical, CH_3, either formed in the atmosphere by OH oxidation of methane (see Figure 2.2), by the photodissociation of acetaldehyde (see Figure 2.3) or by decomposition of peroxyacetyl radicals through a complex series of reactions (2.7, 2.8 and 2.9), will react with O_2 to form methylperoxy radicals, CH_3O_2. The decomposition of CH_3O_2 will lead to the formation of methyl hydroperoxyde (CH_3OOH) if no sufficient NO is available while under "high NO" conditions, it will lead to the formation of the radical CH_3O and contribute to the recycling of NO_2 and thus to the formation of tropospheric ozone. It should also be mentioned that the recycling of methanol through atmospheric production (see 2.1 and 2.2) consumes less than 10 % of the CH_3O_2 atmospheric reservoir sink [*Jacob*, 2005].

The oxidation of methanol by OH leads to the formation of either CH_3O or hydroxymethyl radicals (CH_2OH) in addition to water vapour (see Figure 2.5). However, it has been reported by *Atkinson et al.* [2006] based on the thermochemistry, that the formation of the latter is prevailing in the atmosphere.

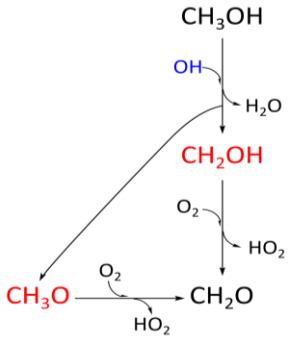

Figure 2.5: Oxidation of methanol by OH.

The CH_3O either formed by oxidation of methanol or from methylperoxy radicals, will react with dioxygen to form formaldehyde (CH_2O). Formaldehyde is the most abundant organic carbonyl compound in the remote troposphere and is directly emitted in a small fraction from biogenic (e.g., vegetation), pyrogenic (mainly biomass burning) and anthropogenic (e.g., industrial emissions) sources [*Franco et al.*, 2015 and references therein]. However, background levels of formaldehyde are built up by oxidation of long-lived VOCs such as methane according to the pathways described in this section.

Finally, formaldehyde is also oxidized by OH to form formyl radicals that will in turn react with dioxygen to form carbon monoxide (CO). Carbon monoxide, with a moderately long tropospheric lifetime of 52 days [*Hough*, 1991], is an important indicator of tropospheric pollution and transport since it is emitted primarily by anthropogenic sources [*Logan et al.*, 1981; *Rudolph*, 1995]. It has been reported by *Duncan et al.* [2007] that as a consequence, CH_3OH is considered as a source of CO with a yield close to 1.

In the same way methane, ethane and methanol are oxidized by OH in the troposphere, they react with chlorine atoms in the stratosphere and then proceed through the same reaction pathway [*Atkinson et al.*, 2006]. In addition, methane reacts with chlorine atoms in the marine boundary layer, and by reaction with $O(^1D)$, OH, and by photodissociation in the stratosphere [*Chen*, 2005]. The oxidation of methane by OH leads to the formation of water vapour, making it a great contributor to the stratospheric water vapour budget, an important driver of decadal global surface climate change [*Solomon et al.*, 2010].

In brief, methane, ethane and methanol share a common tropospheric sink: the oxidation by the radical OH. The chemical pathways described in Figure 2.1 illustrates how their oxidation leads to the formation of PAN, a thermally unstable reservoir for nitrogen oxide radicals, to the recycling of NO_2 thus contributing to the ozone production and by the formation of carbon monoxide through formaldehyde, impacting the air quality of the atmosphere.

2.3. Methane and two of its derivative in the atmosphere

2.3.1. Vertical distribution

All three compounds vertical distribution for the Northern mid-latitudes are illustrated in Figure 2.6. Since methane, ethane and methanol main sources are located at the surface, we find quite good mixing in the first layers of their respective profiles especially for methanol and methane. The longer their atmospheric lifetime, the higher they move to upper levels such as the upper-troposphere lower-stratosphere (UTLS) to reach the stratosphere. Indeed, methanol, with a lifetime of 4.7 to 12 days, is well-mixed until around 10 km of altitude and then rapidly drops to a tenth of its mixing ratio value. On the other side, the vertical distribution of ethane with a lifetime of around 2 months, shows a slower drop of its mixing ratio to reach a negligible value close to zero up until 20 km. Finally, methane, with a lifetime of around 8-10 years, shows a mixing ratio profile that remains constant below the tropopause. Indeed, due to its relatively long atmospheric lifetime in addition to its main sources located at the surface, it is well-mixed in the troposphere before reaching the stratosphere where it will react with $O(^1D)$ or OH or be photodissociated (see previous section).

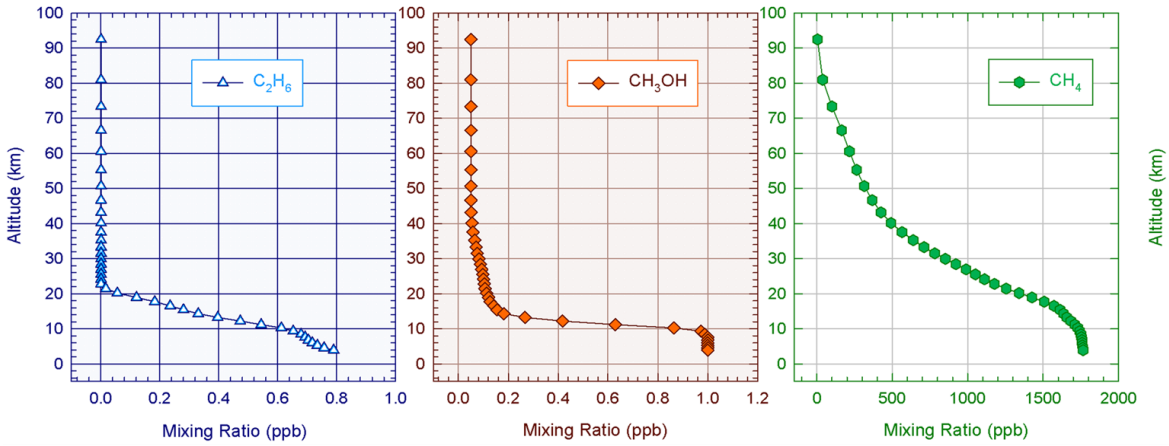

Figure 2.6. Vertical distribution of ethane, methanol and methane expressed in mixing ratio for the Northern mid-latitude.

2.3.2. Seasonal cycles

Methane, ethane and methanol show specific seasonal variations. In the Northern hemisphere, minimum concentrations of methane occur during summer (June-August), rapidly rising to maximum values during fall [September-November, *Khalil and Rasmussen*, 1983] while in the Southern hemisphere, the contrary is observed with minimum concentrations in fall. The methane seasonal cycle is in agreement with the seasonal cycle of atmospheric OH concentrations which is enhanced during summer [*Khalil and Rasmussen*, 1983].

Regarding ethane, its ethane seasonal cycle is characterized by a maximum in March–April and a minimum in August–September. Since fossil fuel production is the main source of C_2H_6 emissions [*Xiao et al.*, 2008] and does not present a particular seasonal cycle during the year [*Pozzer et al.*, 2010], the strong seasonal cycle of C_2H_6 burden is primarily driven by the photo chemical oxidation rate by OH radicals [*Schmidt et al.*, 1991; *Simpson et al.*, 2012].

Finally, in the Northern Hemisphere the strong seasonal modulation of methanol is characterised by minimum values and variability in December to February and maximum columns in June–July [*Bader et al.*, 2014] which can be explained by the primordial role that plant growth plays in the methanol budget. Indeed, plant growth and the production of methanol associated to it is more active during summer than during winter [*Galbally and Kirstine*, 2002; *Jacob*, 2005].

2.3.3. Trends

Figure 2.7 shows the times series of daily mean methanol total columns above Jungfraujoch. We evaluated the trend of methanol total columns over the 1995–2012 time period and found a yearly negative trend of (-1.34 ± 2.71) x 10^{13} molecules.cm^{-2}.year^{-1} or -0.18 ± 0.36 %.year^{-1} (2-σ), i.e. a non-significant trend at this level of confidence, which is consistent with the trend computed by [*Rinsland et al.*, 2009]. Since no significant trend of methanol total columns over the 1995–2012 time period has been identified, the chapter 4 of this work will be dedicated to the analysis of the strong seasonal modulation of methanol and

to its diurnal variation, involving comparisons with other measurements. The optimized retrieval strategy described by *Bader et al.* [2014] in chapter 4 allows us to derive two partial columns, i.e. a lower-tropospheric (LT, 3.58–7.18 km) and an upper tropospheric–lower stratospheric one (UTLS, 7.18−14.84 km). Since these partial column time series do not show any significant trend either, the Chapter 4 is also focused on the seasonal cycle analysis of both partial columns.

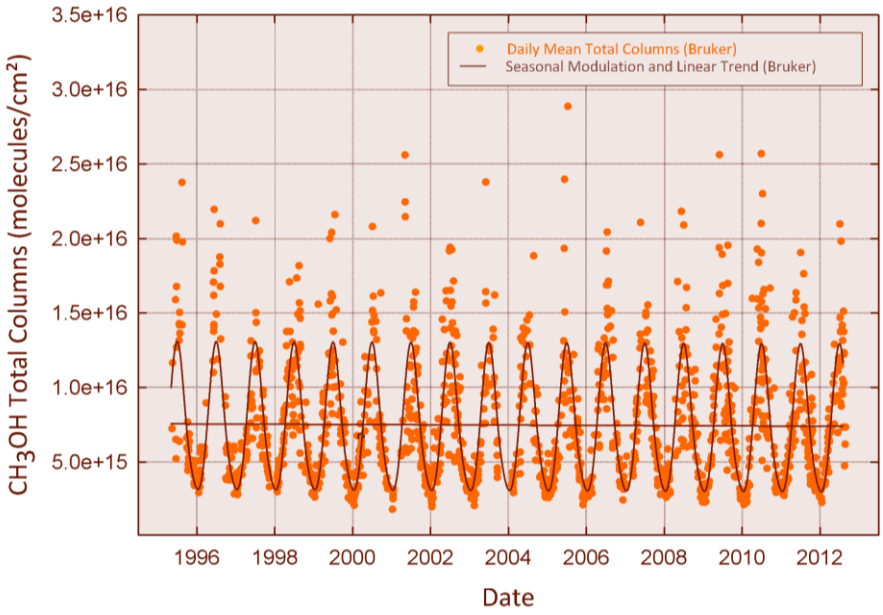

Figure 2.7. Methanol total column above Jungfraujoch time series. Orange circles are daily mean total columns and brown lines show the seasonal modulation and linear trend associated to it.

As to ethane, analysis of the 1994–2008 timespan reveals a regular decrease of the C_2H_6 amounts above the Jungfraujoch station by - 0.92 ± 0.18 %.year^{-1} relative to 1995.0 [*Franco et al.*, 2015a]. This negative trend is consistent with measurements and corresponding trends of atmospheric C_2H_6 burden presented in [*Aydin et al.*, 2011; *Simpson et al.*, 2012], both studies attributed the decline of global C_2H_6 emissions from the mid-1980s to reduced fugitive emissions from fossil fuel sources in Northern Hemisphere rather than a decrease in biomass burning and biofuel use (the other major sources of C_2H_6). However, our study reported in chapter 5 reports recent and unexpected ethane increase since 2009 above the Swiss Alps.

Finally, methane concentrations have increased by 260% since the beginning of the industrialization to reach 1824 pbb in 2013 [*World Meteorological Organization*, 2014]. From the 1980s until the beginning of the 1990s, atmospheric methane was significantly on the rise by about 13 parts ppb per year [*Nisbet et al.*, 2014], then stabilized during 1999-2006 [*Dlugokencky*, 2003] to rise again afterwards [*Nisbet et al.*, 2014]. The source (or sink) attribution of this latter increase is still questioned [*Rigby et al.*, 2008; *Dlugokencky et al.*, 2009; *Bousquet et al.*, 2011; *Sussmann et al.*, 2012]. In the last chapter of this work, we provide analysis of the GEOS-Chem Chemical Transport Model tagged simulation that accounts for the contribution of each emission source and one sink in the total CH_4 simulated based on emissions inventories and transport in parallel with methane changes analysis since 2005 from FTIR observations recorded at ten NDACC stations in order to address what source(s) or sink is responsible for this renewed increase.

Chapter 3 – Atmospheric composition monitoring

Now that the first chapter has established the physical principles allowing us to identify and quantify infrared active atmospheric constituents from infrared solar observations, a description of the instrumentation employed for the recording of observations as presented in the second part of this work is given. This chapter is therefore dedicated to the description of how from FTIR solar observations we retrieve amounts of atmospheric constituents and how those concentrations are characterized.

First, the operating principle of a ground-based Fourier Transform InfraRed spectrometer is illustrated in Figure 3.1. Once the radiation has passed through the atmosphere, it is collected by a coelostat and is sent to a Michelson Interferometer via a series of mirrors. This interferometer consists essentially of a mobile and a fixed mirror, as well as of a beamsplitter. The two beams recombine after their respective path and the signal is recorded at the detector in several discrete positions of the continuously moving mirror to form an interferogram. The spectrum is then built from the interferogram with a Fourier Transform and expresses an intensity of transmitted light, i.e. a transmittance, depending on the wavelength in wavenumber unit, cm^{-1}. Therefore with this technique, we do not measure directly the abundance of atmospheric constituents. In order to retrieve the number of molecules which have absorbed infrared radiation along the path of the light i.e. a total column, we therefore have to perform what is called an "inversion".

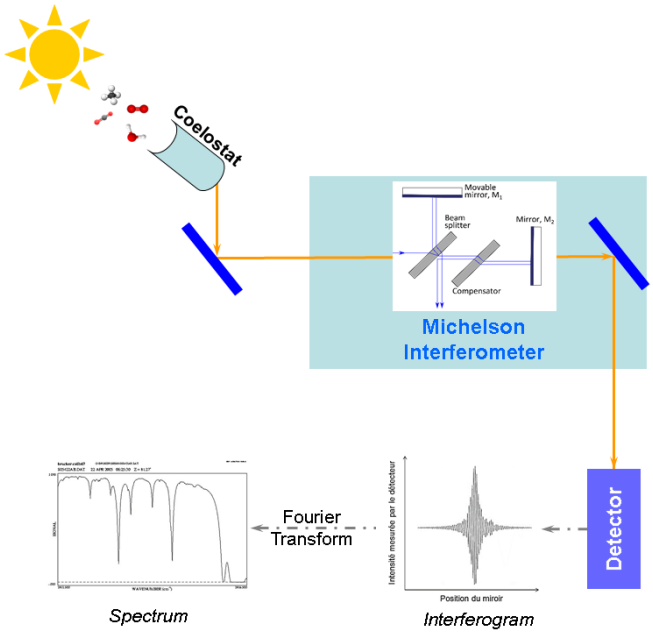

Figure 3.1. Operating principle of a Fourier Transform Spectrometer

The first section of this chapter will depict a typical Michelson interferometer along with the description of the filters and detectors routinely used. The second section will describe how an inversion is performed thanks to the SFIT-2 algorithm, what the necessary input parameters are and how the inversion can be constrained. The third section will describe the method employed for the characterization of the results retrieved from the observations in terms of uncertainties. The fourth section is dedicated to the

description of the Jungfraujoch station, affiliated to the Network for Detection of Atmospheric Composition Change (NDACC, www.ndacc.org, see section 3.5.1), its history, what kind of information this exceptional site provides us on the atmosphere state and its objectives for the atmospheric composition monitoring. Finally, the fifth section provides a description of other datasets dedicated to the atmospheric composition monitoring and exploited in the second part of this work such as satellite observations, in situ measurements and model simulation.

3.1. Fourier Transform Spectrometer

A Fourier Transform spectrometer (FTS) is based on a Michelson type interferometer, illustrated in Figure 3.2. It essentially consists of two mirrors, a movable one (M_1) and a fixed one (M_2), and a beam-splitter. The incoming light hits the beam-splitter where it is divided into two beams of equal intensities by partial reflection and transmission. The compensator ensures both beams pass through the same thickness of material. At the Jungfraujoch, the correction is realized thanks to a low resolution measurement around the zero path difference in order to evaluate the shift induced by the thickness of the beam-splitter. Both beams recombine after having covered their respective path to form an interferogram. The recorded signal is therefore measured at many discrete positions of the moving mirror. This recorded signal is maximum for the zero optical path difference (ZPD) leading to a maximum constructive interference, i.e. when the position of the moving mirror corresponds to equal optical path lengths for both the transmitted and reflected beams. The spectrum is reconstructed using a Fourier transform of the interferogram.

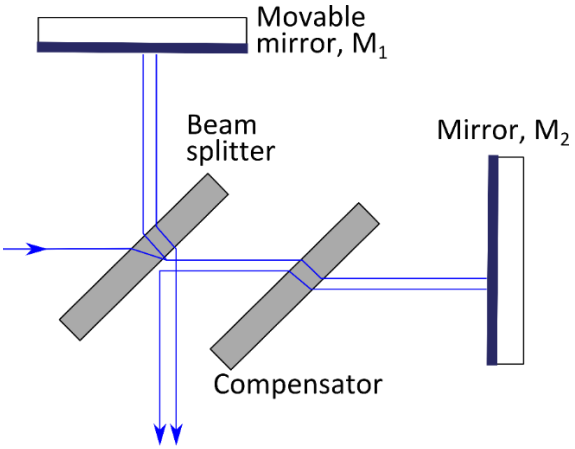

Figure 3.2. Michelson Interferometer.

The FTS installed at the Jungfraujoch station (see section 3.4) is equipped with a potassium bromide (KBr) beam-splitter and two cooled detectors, i.e. a Mercury-Cadmium-Tellurium (HgCdTe or MCT) and an Indium-Antimonide (InSb) covering the 650 to 4500 cm^{-1} region of the electromagnetic spectrum. They achieve resolution, defined as the reciprocal of twice the maximum Optical Path Difference (OPD), which ranges between 0.00285 and 0.006cm^{-1} respectively corresponding to an OPD of 175.6 and 82 cm. Five optical filters are routinely and consecutively used in order to maximize the signal-to-noise ratio (see color codes in Figure 3.3).

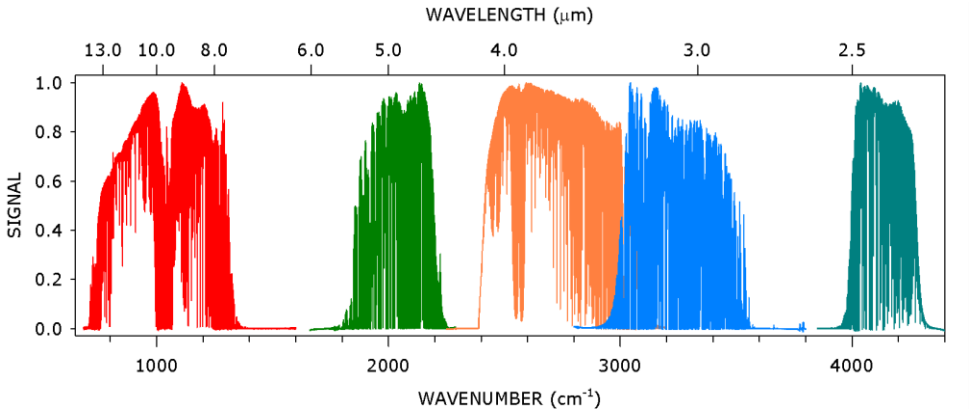

Figure 3.3. Optical filters. The regions covered by the filters are respectively covering the 350-1600 cm^{-1} (in red), 1660-2250 cm^{-1} (in green), 2200-3300 cm^{-1} (in orange), 2800-3800 cm^{-1} (in blue), 3850-4400 cm^{-1} (in cyan) ranges. Mahieu et al., 2015.

3.2. Inversion

3.2.1 The SFIT algorithm

The algorithm has been specifically developed by C. P. Rinsland (National Aeronautics and Space Administration, NASA, Langley Research Center, Hampton, Virginia, USA), with support from B. J. Connor (National Institute of Water and Atmospheric Research, NIWA, Lauder, New Zealand), for the inversion of the vertical mixing ratio profiles of atmospheric gases from high resolution ground-based infrared solar absorption spectra recorded with FTIR instruments. The forward model in SFIT-2 has been previously described by *Pougatchev et al.*, 1995 and *Rinsland et al.*, 1998.

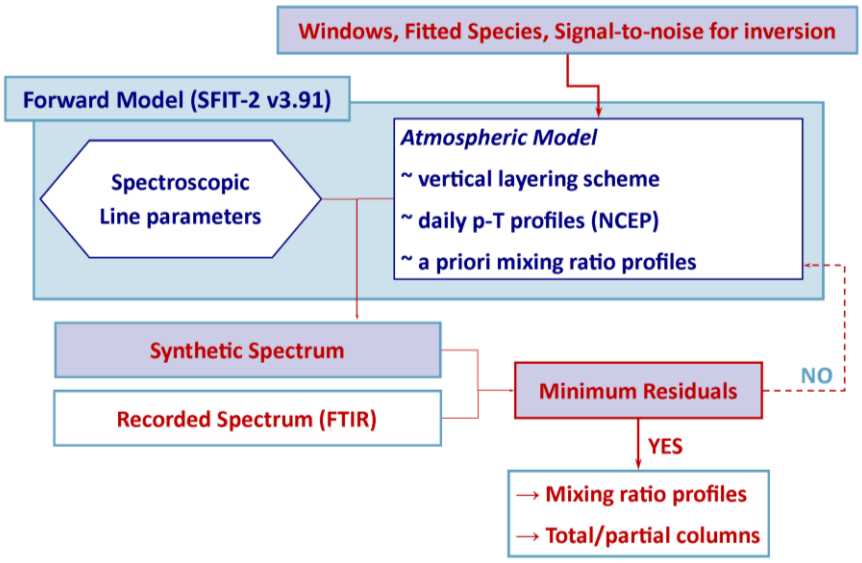

Figure 3.4. Operating principle of the SFIT-2 algorithm.

In this work, SFIT-2 v3.91 is used to retrieve total vertical columns of methane, its operating principle is described in Figure 3.4. SFIT consists in a forward model that comprises (i) a spectroscopic database characterizing the position and intensity of the targeted lines and (ii) an atmospheric model associated with a vertical layering scheme accounting for the daily pressure-temperature profiles and with a priori mixing ratio profiles to be adjusted. This model will compute a synthetic spectrum on a domain of wavelength of up to several tenth of wavenumber that contains specific absorption lines of the target gas. This domain is named a window. Through an iterative process the mixing ratio profiles will be adjusted (as well as adjustment of other parameters associated with the forward model) until the convergence to a minimum of the residuals, i.e. the difference between the synthetic and the recorded spectra.

3.2.1.1. Input parameters

All input parameters necessary for the retrieval of total columns from FTIR solar observations are described in the following paragraphs.

a- Spectroscopic line parameters

In order for SFIT-2 to compute the transmittance associated to a specific spectral line in the atmosphere, the algorithm needs information on the absorption coefficient as a function of wavenumber for each line. The four essential parameters for each line, are the frequency on which the absorption is centered, the intensity per absorbing molecule, the line width parameter and the lower energy state [*McClatchey et al.*, 1973]. Those line-by-line spectroscopic data are read from a compilation of spectrometric parameters, such as HITRAN (HIgh-resolution TRANsmission molecular absorption database, https://www.cfa.harvard.edu/hitran/). The HITRAN compilation includes the official HITRAN line parameters [*Rothman et al.*, 2013 and references therein], infrared cross-sections, UV line-by-line parameters and cross-sections, aerosol refractive indices, and documentation. The spectroscopic parameters available in the HITRAN linelist are essentially coming from laboratory works. New versions of HITRAN are published every four years while updates or corrections are made available for specific gases on a more frequent basis. Currently, the latest version, HITRAN-2012 [*Rothman et al.*, 2013], contains 7,400,447 spectral lines for 47 different molecules, incorporating 120 isotopologues.

Nevertheless, as outlined in *Rothman et al.* [1987], no line parameters are available for several atmospheric molecules with significant infrared features. This category includes more complicated molecules, for which line-by-line parameters are available only in specific spectral region. In this case, the HITRAN database provides a separate file of high resolution cross-sections. Until further information becomes available, the cross sections can either be incorporated directly into a line-by-line calculation as additive spectral values or be built from a simulation of the spectra by generating artificial line parameters. It has been emphasized by *Rothman et al.* [1987] that, while the accuracy of the cross-sectional method is limited (especially for strong absorptions), omitting them in spectral regions where no line parameters are available leads to much larger errors in the interpretation of line-by-line simulations of atmospheric spectra.

Since SFIT-2 does not allow direct use of cross-section parameters, they need to be converted into pseudolines. To this end, laboratory cross-section spectra are interpolated (or extrapolated) in temperature and pressure [*Toon et al.*, 2015] by performing spectral fits to laboratory transmittance spectra. The lab transmittance spectra are re-created using the temperature- and pressure-dependent cross-sections available. Its objective is not to supplant proper quantum-mechanically-based linelists but to provide spectroscopic information on spectral bands that still remain unresolved or unidentified, to this day.

In addition, as mentioned in *Hase et al.* [2006], since the solar spectrum in the mid-infrared spectral region is far from a smooth blackbody spectrum we need to include a model of the solar absorption features in SFIT-2. To this end, the solar line compilation provided by F. Hase [Karlsruhe Institute of Technology, Institute of Meteorology and Climate Research, Karlsruhe, Germany; *Hase et al.*, 2006] has been assumed for the solar absorptions.

b- Pressure-Temperature profiles

For our retrievals, we have adopted pressure (p) and temperature (T) profiles as provided by the National Centers for Environmental Prediction (NCEP; Washington, D.C.; http://www.ncep.noaa.gov) from the National Oceanic and Atmospheric Administration (NOAA) and made available to the NDACC principal investigators. The p-T profiles are specifically computed for each NDACC station on a daily basis noon time. NCEP meteorological data analyses are based upon a rawinsonde onboard the NOAA polar orbiting operational satellites that collect atmospheric parameters and measures wind speed and direction to transmit them by radio to a ground receiver. Each satellite contains three multichannel instruments, namely the High-resolution Infrared Sounder (HIRS), the Microwave Sounding Unit (MSU) and the Stratospheric Sounding Unit (SSU), which altogether form the Television infrared observation satellite (TIROS) Operational Vertical Sounder (TOVS).

In practice, pressure and temperature profiles provided by NCEP are interpolated on the altitude levels defined in the vertical layering scheme adopted in our retrievals. The vertical layering consists in layers of increasing depths with increasing altitude and adapted to the altitude of each station up to ~100 km. In the retrieval process, each layer is considered homogenous in terms of atmospheric pressure, temperature and volume mixing ratio of the target and interfering gases. For the Jungfraujoch station, we use a 39-levels altitude grid. Since the NCEP datasets also include the uncertainties on the temperature profiles, the impact of temperature profile uncertainties on our retrieved total columns has been included in our error budget (see section 3.3).

c- A priori profiles, covariance matrix and inter-layer correlation

In order to produce a synthetic spectrum, we need to define an a priori state that will account for the vertical distribution of the target and interfering gases considered for the retrieval and that will be adjusted by SFIT-2 to minimize residuals. To this end, we select profiles that represent at best the mean atmospheric situations prevailing above the considered station. Ideally, these vertical profiles represent a climatology of the considered gas which is built from actual observations such as satellite observations

and are expressed in mixing ratio units (as defined in Chapter 1) in function of the altitude, the vertical reference in SFIT-2. However, while satellite observations may provide better vertical resolution on the vertical distribution depending on their respective line of sight (e.g. ACE-FTS' limb viewing provides better vertical resolution than FTIR and the nadir-viewing Infrared Atmospheric Sounding Interferometer, IASI), they have their limitations in the altitude range they are covering. In addition, their temporal coverage might not provide enough information in order for us to build a representative climatology.

In order to compensate the lack of vertical and/or temporal information provided by satellite measurements, simulations from Chemical Transport Model (CTM) are used. In addition to a better vertical resolution, they present better availability of data since they only depend on best estimates of the vertical distribution of the studied gas from best emission inventories.

In practice, we adopt a priori profiles generated within the NDACC from simulation of the Whole Atmosphere Community Climate Model, [WACCM, *Chang et al.*, 2008]. However, when developing an optimized retrieval strategy for a specific species and/or station, in order to avoid that SFIT-2 produces oscillating profiles responsible for ungeophysical negative mixing ratio profiles, it may be required to combine information from satellite observations as well as from CTM simulation depending on the case studied. This way, we optimize the representativeness of the selected a priori vertical distribution. For example, as illustrated in Figure 3.5, in order to build a priori vertical distribution of ethane (C_2H_6), we first combined and tested a number of datasets available including satellite observations from the Atmospheric Chemistry Experiment-Fourier Transform Spectrometer (ACE-FTS), CTMs simulations and in situ measurements, for the purpose of the optimization of a retrieval strategy for C_2H_6 for the Jungfraujoch station (see Chapter 5).

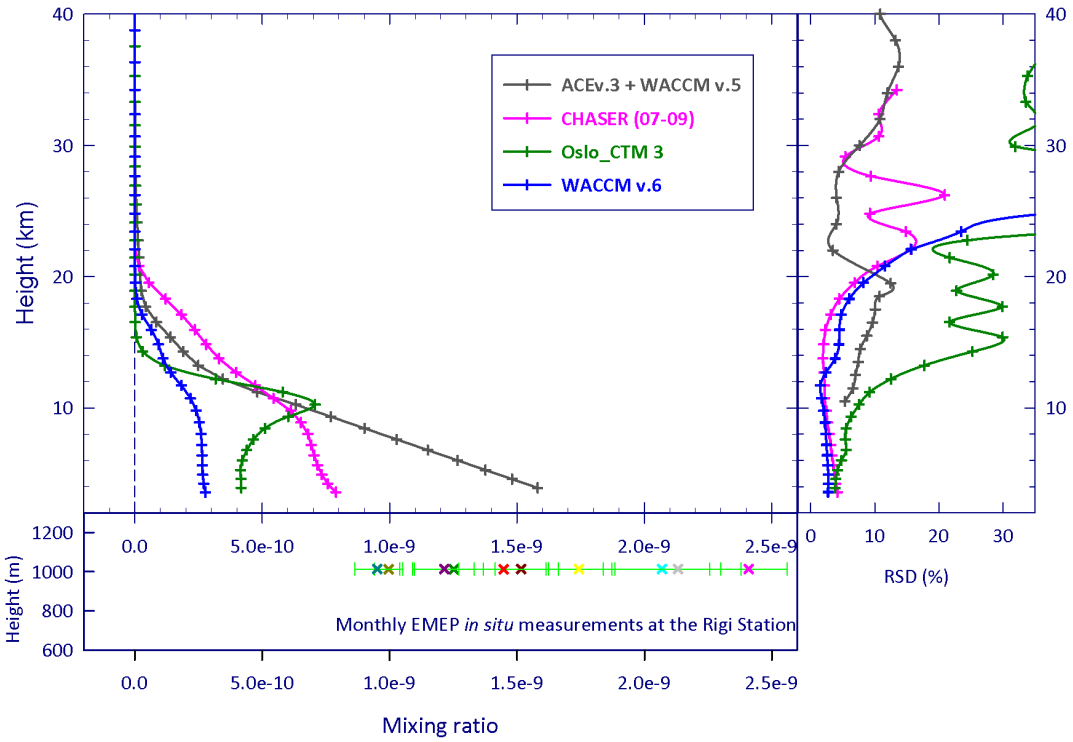

Figure 3.5. Vertical distribution of ethane above the Jungfraujoch station (left panel) and their associated relative standard deviation (right panel). The bottom panel shows EMEP [European Monitoring and Evaluation Programme, http://www.emep.int/] in situ gas chromatography surface measurements at the Rigi station (47.07 °N, 8.45 °E, 1031 m a.s.l., at a distance of 68 km from the Jungfraujoch station). Pink crosses is the a priori profile issued from the CHASER 3D Chemical Transport Model [Sudo, 2002] developed at the Center for Climate System Research, University of Tokyo/National Institute for Environmental Studies (NIES). Chemical Transport Model v.2 and v.3 from the Center for International Climate and Environmental Research Oslo (CICERO, Oslo, Norway) and the university of Oslo [Berntsen and Isaksen, 1997] are plotted in dark and light green crosses, respectively. The grey crosses are a zonal mean (for the 41-51°N latitude band) of 771 occultations recorded by the ACE-FTS instrument between the 2nd of November in 2004 and the 8th of February in 2011 extending from 8.5 to 20 km. The profile extension down to the Jungfraujoch altitude, 3.58 km, is based on EMEP in situ measurements while the upper extension to 100 km is based on the WACCM model climatology.

From Figure 3.5, we see that all dataset available provide a wide range of mixing ratio vertical distribution for ethane. Indeed, the version 6 of the WACCM model provides the lowest mixing ratio with 277 ppt while with 1590 ppt the version 5 of the same model is the highest mixing ratio value for ethane at the altitude of Jungfraujoch. Moreover, the variability of ethane associated to all model-based vertical profiles show a wide range of values more specifically around the tropopause altitude. The challenge is therefore to choose the vertical a priori distribution that will prevent SFIT to produce oscillating retrieved profiles while maximizing the vertical sensitivity and information content.

In addition to the a priori vertical distribution of the interfering gases considered in the retrieval, a covariance matrix, accounting for the relative standard deviation associated to the a priori profile needs to be specified. This covariance matrix will then establish a statistical value range within which the SFTI-2 algorithm is allowed to adjust the vertical distribution of the target gases. Ideally, the a priori full

covariance matrix, $\boldsymbol{S}_a$, should express the natural variability of the target gas. However, because of a lack of data, a full matrix is often not available and simplest matrices, such as pure diagonal or ad hoc matrices, are used. Extra-diagonal elements of the $\boldsymbol{S}_a$ matrix expresses the fact that an inter-layer correlation (ILC) exists between the concentrations of the target gas at different altitudes. For example, the SFIT-2 algorithm allows us to introduce such extra-diagonal elements by defining a Gaussian or an exponential inter-correlation with selected length. The first case is the most commonly used. However, while a covariance matrix built from climatological data is more realistic, we may need to palliate a lack of data to construct a reasonable a priori through a retrieval constraint.

d- Forward model parameters

It may be required for an optimized retrieval to adjust additional parameters that are not necessarily perfectly known by the user. For example, parameters such as the wavenumber shift or background curve parameters (e.g. slope and curvature) are comprised in the forward model parameters. In addition, SFIT-2 allows for the use of an effective apodisation function that expresses the stability of the mirror while it moves assessing for the good alignment of the instrument through a recording. The effective apodisation function can either be defined as a polynomial function of degree N, as a Fourier series of order N or as any other tabulated function. The effective apodisation parameter (EAP) gives the value of the effective apodisation function at the maximum OPD. Consequently, an EAP value close to 1.0 indicates a well-aligned instrument. Therefore, the retrieval of the EAP, as allowed by SFIT-2, ads to the list of adjusted model parameters. As an example, for the retrieval of methanol in chapter 4, the EAP has been adjusted.

3.2.1.2. Retrieval and constraints

As described in *Rodgers*, 2000 and summarized in *Sussmann et al.*, 2007, the inverse problem consists in finding the best estimator of the true target profile, through the forward model F that maps from the true state into the measurement and knowing the a priori information and the measurement vector $\boldsymbol{y}$. The forward model is defined as:

$$F(\boldsymbol{x}, \boldsymbol{b}) = \boldsymbol{y} + \boldsymbol{\varepsilon} - \Delta \boldsymbol{f} \qquad (3.1)$$

where $\boldsymbol{b}$ is the forward model parameters, $\boldsymbol{\varepsilon}$ is the measurement noise and $\Delta\boldsymbol{f}$ the error in the forward model relative to physics. On the other hand, the true physical relation between the measurement vector $\boldsymbol{y}$ and the true target profile, $\boldsymbol{x}$ is described by the forward function f:

$$\boldsymbol{y} = f(\boldsymbol{x}, \boldsymbol{b}, \boldsymbol{b}') + \boldsymbol{\varepsilon} \qquad (3.2)$$

where $\boldsymbol{b}'$represents all forward function parameters which are ignored in the construction of F. For FTIR measurements, the measurement vector $\boldsymbol{y}$ corresponds to an intensity measured in function of the wavelength within the window(s) limits. In addition, the forward model parameters are not always perfectly known by the user, like spectroscopic parameters or parameters related to the instrument.

Since the forward model $\boldsymbol{F}$ is nonlinear, the optimal solution is iteratively reached by use of the Gauss-Newton method starting from the a priori state and until the difference between the measurement and

the calculated state, i.e. the residuals, is minimized. The contribution of the a priori state is then balanced by a regularization term. This regularization term, $\boldsymbol{R} \in \Re^{n \times n}$, a square matrix of dimension n (being the number of layers of the atmospheric model, see 3.2.1.1.) allows us to add information about the shape of the retrieved profile. In the following, we present 3 types of $\boldsymbol{R}$, the simple scaling operation, the optimal estimation [*Rodgers*, 1976] and the Tikhonov regularization [*Tikhonov*, 1963].

a- Simple scaling

When the regularization term is the identity matrix $\boldsymbol{I}$, the retrieved profile is obtained by applying a simple scaling operation to the a priori profile $\boldsymbol{x_a}$. This scaling operation is often applied for lower-resolution spectra or for minor interfering retrieved species.

b- Optimal Estimation Method (OEM)

The OEM is a climatological constraint where $\boldsymbol{R}$ is setup using the relation:

$$\boldsymbol{R} = \boldsymbol{S}_a^{-1} \tag{3.3}$$

where $\boldsymbol{S}_a \in \Re^{n \times n}$ is the a priori covariance matrix. In the ideal case, $\boldsymbol{S}_a$ is a climatological covariance constructed from an ensemble of true profiles covering the full range of possible atmospheric states (see previous section). The optimal estimation method has been used in this work for the retrieval of both methanol and ethane (see the second part of this work).

c- Tikhonov regularization

In the case of the Tikhonov regularization, a smoothing constraint, $\boldsymbol{R}$ is setup using the relation:

$$\boldsymbol{R} = \alpha\, \boldsymbol{L}^T\, \boldsymbol{L} \tag{3.4}$$

where α is the strength of the constraint and $\boldsymbol{L}$ is the constraint operator. For example, the first-order operator $\boldsymbol{L}_1$

$$\boldsymbol{L}_1 = \begin{pmatrix} -1 & 1 & 0 & \cdots & 0 \\ 0 & -1 & 1 & \ddots & \vdots \\ \vdots & \ddots & \ddots & \ddots & 0 \\ 0 & \cdots & 0 & -1 & 1 \end{pmatrix} \in \Re^{n \times (n-1)} \tag{3.5}$$

constrains the shape of the retrieved profile but not its absolute values which are determined by the measurement. The following discussion is restricted to two limiting cases of α values:

- $\alpha \to \infty$ represents an infinitely strong constraint to the profile shape and a zero constraint to the absolute value of the profile scaling factor which is equivalent to a simple profile scaling,

- $\alpha \to 0$ describes a retrieval without any regularization. The retrieval will then provide a perfect fit without any residuals but will show strong ungeophysical profile oscillations.

In between, when using the Tikhonov regularization, the α values can be tuned to target a given Degree of Freedom for Signal (DOFS). For example, it has been established within the NDACC network that the regularization strength of the methane retrieval strategy would be optimized so that the DOFS reaches a mean value of approximately 2 [Sussmann et al., 2011].

The difference between the climatological OEM constraint and the smoothing Tikhonov regularization is that the determination of the absolute values is done through the information that is, for the latter, located in the measurement and not in the constraint. While the climatological constraint is more realistic, since it is based on actual measurements, the smoothing regularization can palliate a lack of data to construct reasonable a priori and help us avoid the appearance of non-geophysical oscillations in the retrieved profiles.

3.2.2. Information content

An effective way to express the ability of the observations to constrain the true values to be retrieved is with the averaging kernel matrix $\boldsymbol{A} = \partial\hat{\boldsymbol{x}}/\partial\boldsymbol{x}$, representing the sensitivity of the retrieved profile $\hat{x}$ to the true profile x. $\boldsymbol{A}$ is the product of the gain matrix $\boldsymbol{G_y} = \partial\hat{\boldsymbol{x}}/\partial\boldsymbol{y}$ and the Jacobian matrix $\boldsymbol{K_x} = \nabla_x F = \partial\boldsymbol{y}/\partial\boldsymbol{x}$ which respectively expresses the sensitivity of the retrieved profile to the measurement and the sensitivity of the observation variables $\boldsymbol{y}$ to the true state $\boldsymbol{x}$:

$$\boldsymbol{A} = \boldsymbol{G_y}\,\boldsymbol{K_x} \qquad (3.6)$$

A simplified way to define the retrieved profile would then, according to [*Jacob*, 2007], be:

$$\hat{\boldsymbol{x}} = \boldsymbol{A}\,\boldsymbol{x} + (\boldsymbol{I_n} - \boldsymbol{A})\boldsymbol{x_a} \qquad (3.7)$$

where I_n is the identity matrix of dimension n. A is a weighting factor for the relative contributions to the retrieval from the true profile versus the a priori profile. The first term of (3.7) represents the contribution of the true state to the solution while the second term illustrates the contribution from the a priori. A perfect observational system would have $\boldsymbol{A} = \boldsymbol{I_n}$ while where $\boldsymbol{A} = 0$, the retrieved profile merges with the a priori profile. Since our observational system is not ideal, the rows and columns of the averaging kernel matrix will represent peaked functions (see Figure 3.6), with the width of the peak being a qualitative measure of the vertical resolution of the observing system [*Rodgers*, 1990]. In the process of optimizing the retrieval strategy, a careful and systematic inspection of the averaging kernels is performed to assess the quality of the retrieval and determine the best strategy.

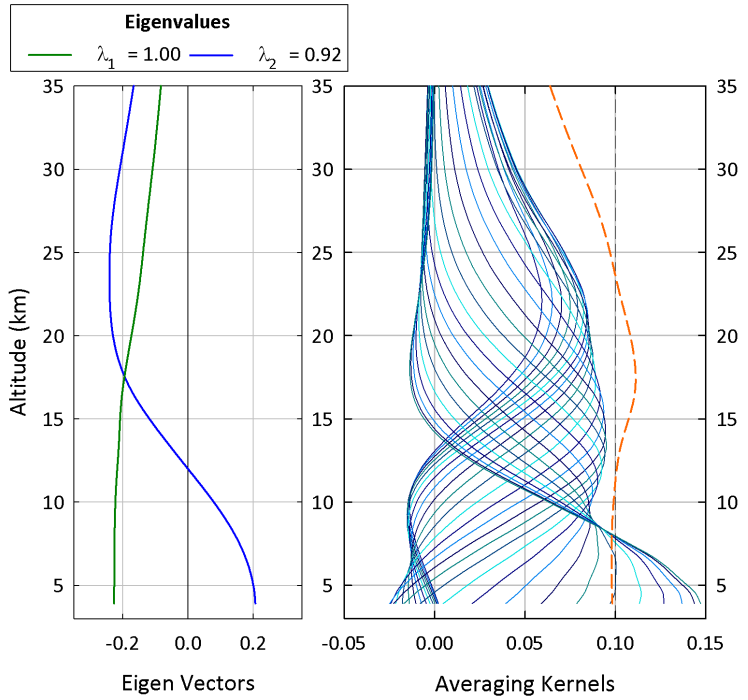

Figure 3.6. Right panel shows first eigenvectors and associated eigenvalues while individual averaging kernels for each layer between the 3.58 and 35.3 km altitude range and total column averaging kernel (orange dashed line; divided by 10 for visibility purpose) characterizing the FTIR retrievals of CH_4 at the Jungfraujoch station. The information content has been established on the basis of all the individual retrieved profiles from fall measurements throughout the 2000–2013 time span.

The trace of the $\boldsymbol{A}$ matrix provides the Degree Of Freedom for Signal (DOFS), i.e. the number of independent pieces of information that can be retrieved from the retrieval also called the information content of a retrieval. On the other side, eigenvectors of $\boldsymbol{A}$ and their associated eigenvalues (see Figure 3.6) allow us to quantify the contribution of the a priori to these independent pieces of information. It implies that eigenvalues equal or close to 1 characterizes a piece of information completely coming from the measurement and thus independent of the a priori. Oppositely, eigenvalues close to zero mainly reproduce the a priori state.

Since it gives information about the observational system, the averaging kernel matrix is also essential to compare two different datasets collected by different observation system used to determine $\boldsymbol{x}$. The difference in sensitivity between two observational systems has to be accounted for before performing any comparison. According to [*Connor et al.*, 1994], one way to proceed is to "degrade" the resolution of the vertical profile $\boldsymbol{x_h}$ characterized by the higher resolution for it to match the lower-resolution vertical profile's resolution in order to obtain a smoothed version $\boldsymbol{x_s}$ of it:

$$\boldsymbol{x_s} = \boldsymbol{x_a} + \boldsymbol{A}\,(\boldsymbol{x_h} - \boldsymbol{x_a}) \qquad (3.8)$$

in which the $\boldsymbol{A}$ matrix is the averaging kernels of the lower resolution observational system. This smoothing allows us to represent the retrieved vertical profile that would be observed by the observational system with the higher resolution if this instrument was set in the same observational

conditions as the lower observational system. This smoothing is mandatory for comparisons between observations and model data since models usually provide results with a greater vertical resolution than a ground-based instrument[1].

3.3. Error budget

In the framework of this work, a method for error analysis [*Bader et al.*, 2014; *Franco et al.*, 2015a, 2015b] has been established for the *Groupe Infrarouge de l'Atmosphère Physique et Solaire* (GIRPAS, Institute of Astrophysics and Geophysics, University of Liège, Belgium, http://girpas.astro.ulg.ac.be,) that combines the classical formulation of error analysis of remote sounding by *Rodgers* [1990] and a perturbation method.

3.3.1. Rodgers formalism

According to *Rodgers* [1990, 2000], the retrieved target profile $\hat{x}$ is related to the true target profile x via the relation:

$$\begin{aligned} \hat{\boldsymbol{x}} - \boldsymbol{x} = (\boldsymbol{A} - \boldsymbol{I})(\boldsymbol{x} - \boldsymbol{x_a}) &\quad \text{smoothing error} \\ + \boldsymbol{G_y K_b}\left(\boldsymbol{b} - \hat{\boldsymbol{b}}\right) &\quad \text{model parameter error} \\ + \boldsymbol{G_y} \Delta f(\boldsymbol{x}, \boldsymbol{b}, \boldsymbol{b'}) &\quad \text{forward model error} \\ + \boldsymbol{G_y}\, \boldsymbol{\varepsilon} &\quad \text{retrieval noise} \end{aligned} \qquad (3.9)$$

where $\boldsymbol{A} = \partial\hat{\boldsymbol{x}}/\partial\boldsymbol{x}$ is the averaging kernel, $\boldsymbol{K_b} = \partial F/\partial\boldsymbol{b}$ expresses the sensitivity of the measurement to the forward model parameters, $\boldsymbol{G_y} = \partial\hat{\boldsymbol{x}}/\partial\boldsymbol{y}$ is the gain matrix representing the sensitivity of the retrieved profile to the measurement, and x_a represents the a priori profile.

First, the smoothing error expresses the uncertainty related to finite vertical resolution of the remote sounding system. Regarding the model parameter error, it accounts for the difference between the true value of the forward model parameters, represented by $\boldsymbol{b}$, and $\hat{\boldsymbol{b}}$, our best estimate of the latter. On the other hand, the forward model error is based on the relation between the forward model F and the forward function f:

$$\Delta f(\boldsymbol{x}, \boldsymbol{b}, \boldsymbol{b'}) = f(\boldsymbol{x}, \boldsymbol{b}, \boldsymbol{b'}) - F(\boldsymbol{x}, \boldsymbol{b}) \qquad (3.10)$$

and expresses the error in the forward model relative to real physics. Finally, measurement noise is described by the error term ε and represents the contribution from the random observational error.

[1] Indeed, this method has been applied in Chapter 6 for the comparison of methane results from FTIR ground-based observations and from the GEOS-Chem Chemical Transport Model.

3.3.2. Perturbation method

The perturbation method developed considers the worst identified case scenario and thus gives a maximum error on the retrieved columns [*Bader et al.*, 2014; *Franco et al.*, 2015a, 2015b]. A non-exhaustive list of the most common parameters considered includes systematic errors, such as the spectroscopic line parameters or the misalignment of the instrument, while uncertainty on the temperature and on the solar pointing is considered to be source of random error. If relevant, other parameters may be included within the error budget. As an example, one can quantify the impact of the choice of the target species a priori profile on the retrieved columns with a perturbation method by fitting a subset of representative spectra with other reliable a priori [*Franco et al.*, 2015a, 2015b].

Errors on the retrieved columns to line intensity uncertainties have been addressed with the *Error_spec* code. *Error_spec* has been specifically developed in the framework of this thesis to produce linelist files with incremented and decremented line intensities (or air-broadening width). To this end, *Error_spec* reads the uncertainty indices corresponding to the lines of the target species as detailed in [Table 5 of *Rothman et al.*, 2005] to assume the maximum errors associated to it. This way, replacing the spectroscopic linelists by the incremented linelists enables us to quantify the impact of the line intensity −or air-broadening width– on the retrieved columns.

In addition, we accounted for an error of 10% on the instrument alignment at the maximum path difference and for a 0.2° error in the solar pointing. The uncertainty on the pressure−temperature profiles is provided by NCEP, i.e. 1.5 °C up to 20 km, 2 °C up to 30 km, 5 °C near 35 km and then progressively increasing up to 9 °C at 50 km. By comparing the two official NDACC algorithms, *Hase et al.* [2004] and *Duchatelet et al.* [2010] have established that the forward model may induce a maximum error of 1% on the retrieved columns for a suite of tropospheric and stratospheric FTIR target gases with either broad or narrow absorption lines.

When water vapor is a strong absorber in the retrieved spectral window(s) and since it shows a great intra-annual variability, the impact of the choice of the a priori state of the water vapor profile may contribute to the random component of the error budget. Indeed, it is of great importance on the error budget as the interfering species (H_2O in this case) need to not be correlated to the target gas. For the Jungfraujoch station, the perturbation corresponds to the variation of the slope of the tropospheric H_2O and HDO a priori mixing ratio profiles simulated by WACCM by a factor 2 [*Duchatelet*, 2011; *Franco et al.*, 2015a, 2015b]. This latter corresponds approximately to the change of slope when taking the 2-σ standard deviation limits around the annually-averaged H_2O mixing ratio profile retrieved above the ISSJ according to [*Sussmann et al.*, 2009].

Through this work, the primary objective was to develop and optimize retrieval strategies for methane, ethane and methanol from solar observations recorded at the Jungfraujoch station. The development and optimization of a retrieval strategy includes: systematic search for and evaluation of absorption lines of the target species and determination of the best combination of spectral windows, spectroscopic linelist (for the target and interfering species), a priori mixing ratio profile, retrieval constraint, among others in

order to limit the interferences, minimize the residuals and maximize the information content and thus maximize the altitude sensitivity range. In addition, the method for error analysis is performed on each available combination of parameters and serves as an indicator for the selection of the best retrieval strategy to be employed.

3.4. The Jungfraujoch station

Results presented in the second part of this work include or are based on ground-based FTIR observations performed at the International Scientific Station of the Jungfraujoch (ISSJ). The ISSJ (Figure 3.7, Swiss Alps, 46.55° N, 7.98° E, 3580 m a.s.l.) is located on the saddle between the Jungfrau (4158m a.s.l.) and the Mönch (4107m a.s.l.) summits. This research station offers unique conditions for infrared solar observations because of weak local pollution (no major industries within 20 km) and very high dryness due to the high-altitude (in dry conditions around two-thirds of water vapor lies below the altitude of 3.6 km) and the presence of the Aletsch Glacier in its immediate vicinity. Indeed, the amount of water vapor (H_2O), a strong absorber in the infrared that often interferes with absorption features of other telluric gases, can be as low as twenty times less than at sea level. The ISSJ allows us to investigate the atmospheric background conditions over central Europe and the mixing of air masses between the planetary boundary layer and the free troposphere [*Reimann*, 2004].

Figure 3.7. The Jungfraujoch station. [*Grindelwald Tourismus*, 2015]

In 1950, M. Migeotte (ULg) started pioneering infrared solar observations at the Jungfraujoch, with a 1 m focal length grating spectrometer reaching resolutions going from 0.12 to 0.40 cm^{-1}. At this stage, resolutions were high enough to record strong features characteristic of minor constituents of the Earth's atmosphere, like methane, CH_4 [*Nielsen and Migeotte*, 1952] or carbon monoxide, CO [*Migeotte and Neven*, 1950]. Eight years later, L. Delbouille and G. Roland installed a more efficient 7.3 m focal length grating spectrometer. This instrument, receiving solar light from a coelostat installed outside on the observatory terrace, was mainly used to systematically record observations for the production of two solar spectrum atlases in the infrared, visible and near-UV [*Delbouille and Roland*, 1963; *Delbouille et al.*, 1973].

Forty years ago, R. Zander (ULg) detected the presence of hydrogen fluoride in the atmosphere from infrared solar spectra recorded by the Liège group with a double-pass 2.5-meter focal length grating instrument during a stratospheric balloon flight over Texas (USA) in 1974 [*Zander*, 1975], demonstrating that the products issued from the photodissociation of CFCs reach the stratosphere. Detection of HF in the atmosphere in addition to the identification of the catalytic cycles involved in stratospheric ozone depletion [*Crutzen*, 1970; *Johnston*, 1971; *Molina and Rowland*, 1974; *Stolarski and Cicerone*, 1974] prompted the ULg scientists to resume their atmospheric-oriented observations at the Jungfraujoch station, to monitor the abundance of gases such as HCl, HF and CH_4.

To this end, in 1976, the Jungfraujoch 7.3 m focal length double-pass spectrometer was equipped with a special grating and a liquid nitrogen-cooled InSb detector for solar observations to be extended in the infrared, out to about 5.4 µm. It achieved spectral resolution of nearly 0.02 cm^{-1} and signal-to-noise ratio of up to 250. Narrow infrared spectral windows encompassing isolated lines of HF, HCl, N_2O, CH_4 and NO_2 have been regularly recorded with this instrument until 1989.

The need for larger signal-to-noise ratios allowing to detect and quantify an increasing number of chemically important trace gases present at very low concentrations required the design, development and adoption of a Fourier Transform Spectrometer [*Roland*, 1965; *Malbrouck*, 1977]. In particular, a Connes-type [*Connes*, 1971] stepping-mode FTIR spectrometer of 1 m optical path difference (ultimate spectral resolution of 0.005 cm^{-1}) equipped with a lead-sulphide detector (PbS) was developed at ULg and installed at the coudé focus of the Jungfraujoch telescope in 1974. It was successfully operated for recording infrared solar spectra from about 1 to 3 µm [*Malbrouck*, 1977]. However, the stepping mode allows for slow scanning speed and was not adequate for fast observations needed in atmospheric composition studies at low solar height observations. Indeed, in order to observe weakly absorbing trace gases, long atmospheric slant paths are more convenient.

In 1978, improvements of that instrument such as an extension of the spectral infrared coverage out to 14 µm, a doubling of the optical path difference, to reach a spectral resolution of 0.0025 cm^{-1} (see Figure 3.8), and a scanning speed increase by a factor 100 obtained by adopting a continuous scanning mode instead of the stepping one were designed [*Delbouille and Roland*, 1995]. This upgraded home-made FTIR instrument was tested then put into regular operation in 1984. The double-pass grating spectrometer was retired in 1989, allowing for regular comparisons between results obtained with the homemade and the double-pass grating spectrometers over up to 5 years [*Zander et al.*, 2008].

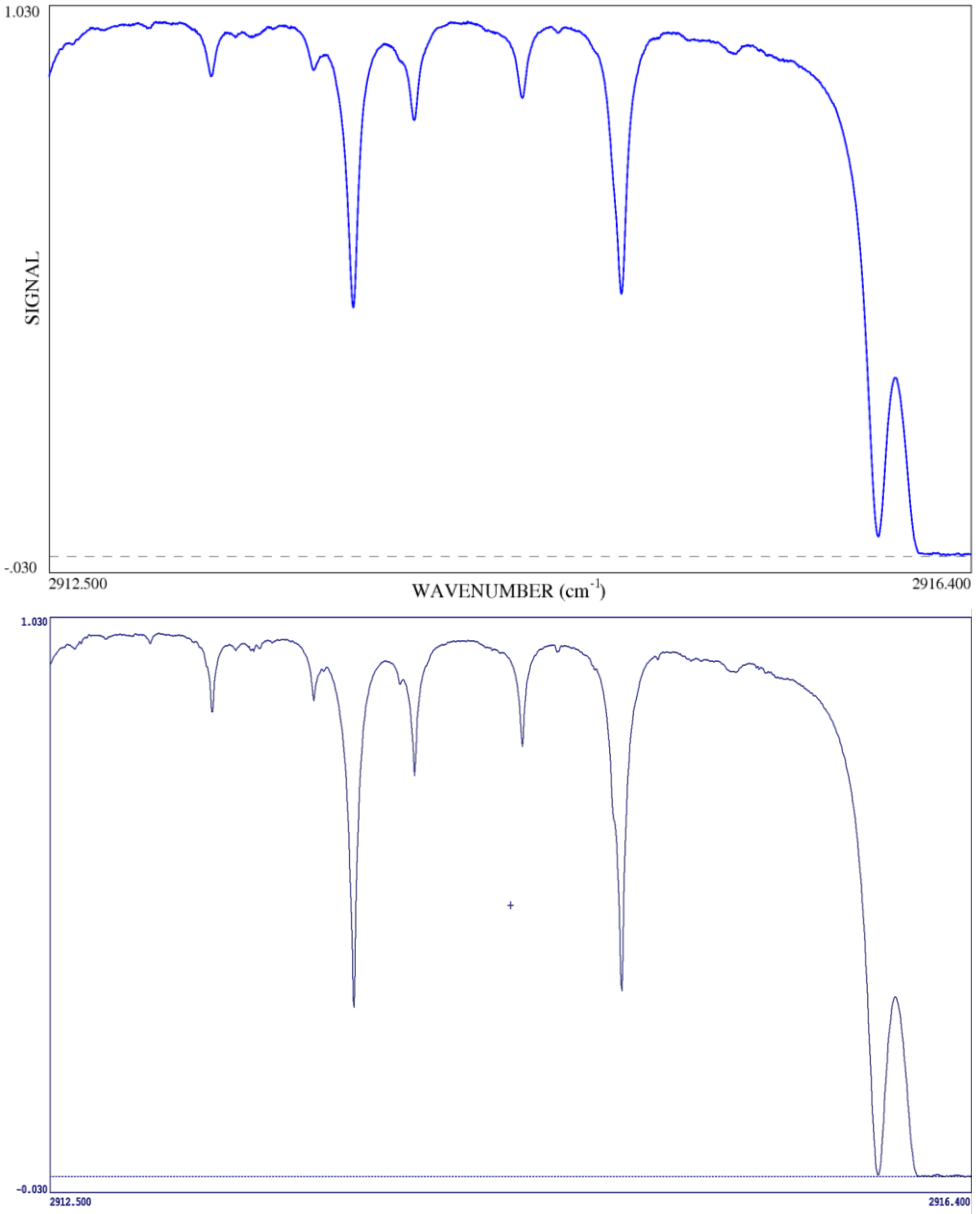

Figure 3.8. Spectrum from the DPGS (upper frame) and FTIR (lower frame) spectrometers on the 2912.5–2916.4 cm^{-1} domain recorded respectively on the 24th of April 1987 and on the 18th of April 2003, with solar zenith angle of 76.12 ° and 76.16 °, respectively.

In 1990, as a result of the creation of the Network for the Detection of Stratospheric Change (NDSC, currently known as the Network for Detection for Atmospheric Change Composition or NDACC since 2005, the slow scanning speed and low throughput Double-Pass Grating Spectrometer (DPGS) was replaced by an FTIR instrument, namely a commercial Bruker IFS-120 HR, achieving an ultimate spectral resolution of 0.001 cm^{-1} and a signal-to-noise ratio exceeding several thousands. Intercomparison tests between the homemade and the Bruker FTIR systems were useful in assessing any level of biasing between retrieved column abundances from simultaneous observations. Currently, infrared spectral domains covered by the Bruker FTIR spectrometer allows for short-, middle- and long-term study, of the evolution of more than

25 atmospheric species such as detailed in Table 3.1. Regular observations with both the homemade and the Bruker spectrometer in addition to the double-pass grating spectrometer gather a unique worldwide collection of solar observations of more than 45 000 spectra that covers more than 39 years of uninterrupted IR monitoring. Figure 3.9 illustrates harmonized total column time series of methane above Jungfraujoch from *Bader* [2011] as retrieved from observations recorded with different instruments such as the double-pass grating spectrometer and both FTIR instruments in addition to historic CH_4 observations from [*Zander et al.*, 1989].

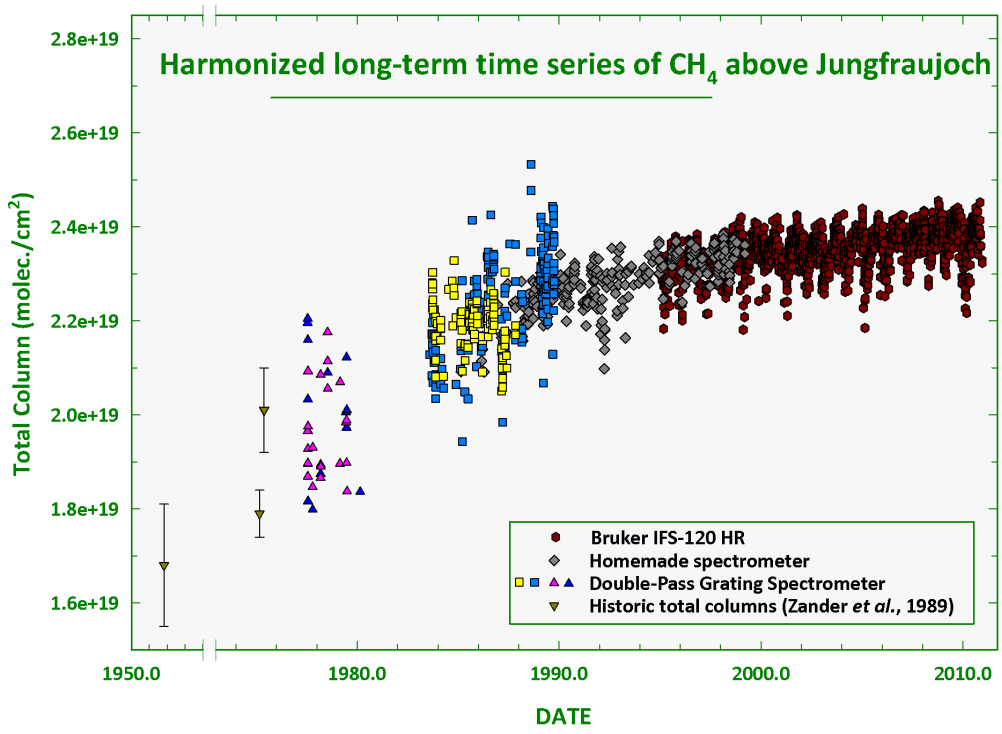

Figure 3.9. Harmonized long-term time series of methane above Jungfraujoch from [*Bader*, 2011]. *Methane total column retrieved from (i) the Bruker IFS-120 HR spectrometer (dark red circles), (ii) the homemade spectrometer (grey diamonds), (iii) the Double-Pass Grating Spectrometer (yellow and blue squares, and blue and pink triangles), and (iv) historic observations (dark yellow down triangles) with their associated uncertainties (black bars) from* [*Zander et al.*, 1989].

Climate-relevant, i.e. greenhouse gases as support to the Kyoto protocol	H_2O, CO_2, [(a)]CH_4, N_2O, CF_4, SF_6
Ozone-relevant as support to the Montreal protocol	O_3, NO, NO_2, HNO_3, $ClONO_2$, HCl, HF, COF_2, CFC-11, CFC-12, HCFC-22, HCFC-142b, CCl_4
Air quality, biomass burning,…	CO, [(b)]CH_3OH, [(c)]C_2H_6, C_2H_2, C_2H_4, HCN, HCHO, HCOOH, NH_3
Others	OCS, N_2, many isotopic forms (HDO, CH_3D, $^{13}CH_4$, ^{13}CO,…)

Table 3.1. Atmospheric species currently targeted at the ISSJ. [*Mahieu et al.*, 2015]. *(a) See chapter 6. (b) See chapter 4. (c) See chapter 5.*

3.5. Atmospheric monitoring: other datasets involved

This section provides a brief description of the several datasets used through the second part of this work for comparisons with our FTIR results. They comprise both observations and model simulations.

3.5.1. Observations

2.5.1.1. The NDACC network

The international Network for the Detection of Atmospheric Composition Change (http://www.ndacc.org/) is composed of more than 70 high-quality, remote-sensing research stations worldwide for observing and understanding the physical and chemical state of the atmosphere, for gauging the atmospheric composition changes and for assessing its impact on global climate or air quality. The NDACC network is divided into 9 working groups, each one associated to one type of instrument that were selected on the basis of their remote-sensing capabilities and their demonstrated stability for long-term operation (for details of site locations and operating equipment, see http://www.ndacc.org).

In 1986, the decision was made to set up a Network for the Detection of Stratospheric Change (NDSC) in support of the 1985 Vienna Convention for the Protection of the Ozone Layer. This ground-based long-term measuring network was designed to provide the earliest possible detection of changes in the composition and structure of the stratosphere and to understand the causes of those changes. After five years of planning, instrument design and implementation, the NDSC began network operations in January 1991. As *Kurylo* [1991] mentioned, the network's short-term goals are: to study the temporal and spatial variability of atmospheric composition and structure, to provide the basis for ground truth and complementary measurements for satellite systems, and to critically test multidimensional stratospheric models and provide the broad data base required for improved model development.

While the NDSC remained committed to monitoring changes in the stratosphere with an emphasis on the long-term evolution of the ozone layer, as a result of its increasing capabilities of monitoring tropospheric source gases, its priorities have broadened considerably to encompass issues such as the detection of trends in overall atmospheric composition and understanding their impacts on the stratosphere and troposphere, and establishing links between climate change and atmospheric composition [*Zander et al.*, 2008]. In 2005, the NDSC formally supported the Kyoto Protocol by extending the range of target species to atmospheric components targeted by the Kyoto Protocol. Consequently, in 2005, the NDSC has been renamed Network for the Detection of Atmospheric Composition Change (NDACC).

Among the 9 working groups, the Infrared Working Group (IRWG, https://www2.acom.ucar.edu/irwg) represents a worldwide network of infrared Fourier-transform spectrometers. It is a multi-national collection of over twenty high resolution spectrometers that regularly perform ground-based solar observations in order to record the atmospheric absorption spectrum from sites distributed from pole to pole. The Figure 3.10 displays the measurements stations which are affiliated to the NDACC as part of the infrared working group.

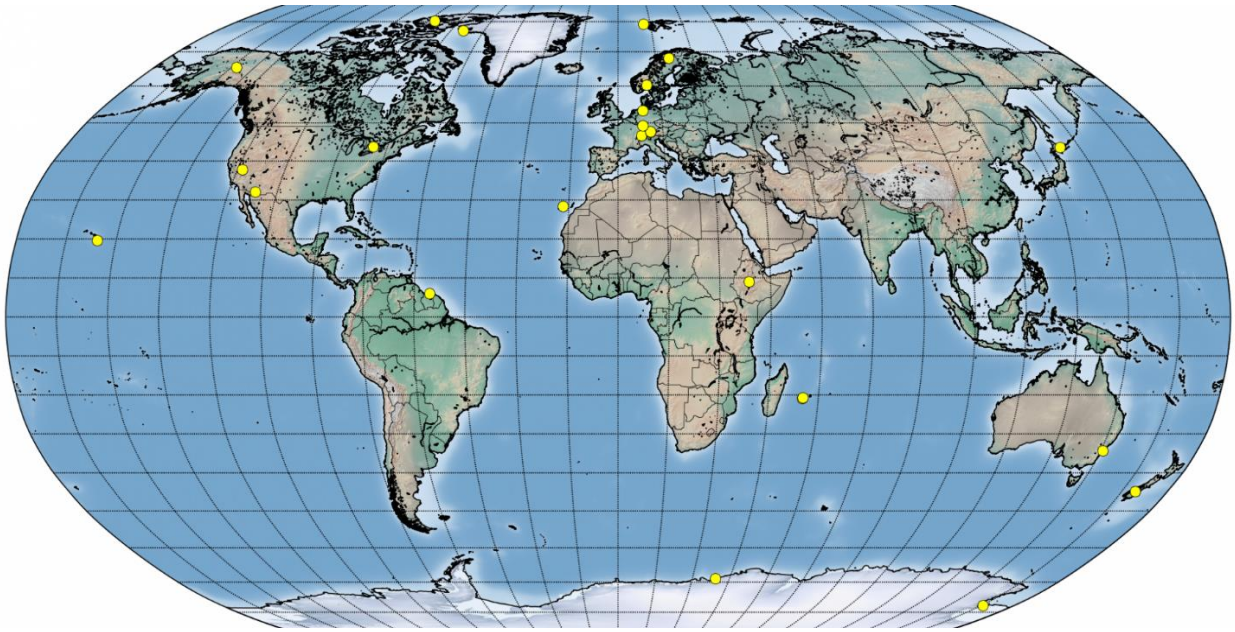

Figure 3.10. Map of measurement stations as part of the NDACC Infrared working group. From Dr. D. Feist, Max Planck Institute for Biogeochemistry, Jena, Germany.

3.5.1.2. ACE-FTS

The SCISAT-1, also known as the Atmospheric Chemistry Experiment [ACE, *Bernath et al.*, 2005], is a Canadian satellite mission whose concept is based on the successful ATMOS (Atmospheric Trace Molecule Spectroscopy) instrument that first flew as part of the Spacelab 3 (SL-3) Space Shuttle in 1985 and three times on the ATLAS (Atmospheric Laboratory for Applications and Science) space shuttle missions [*Gunson et al.*, 1996] for remote sensing of the Earth's atmosphere. The ACE was launched into low Earth circular orbit (650 km) and at a high inclination (74°) in August 2003, benefiting of a coverage of tropical, mid-latitude, and polar regions. ACE aims to understand the chemical and dynamical processes that control the distribution of ozone in the stratosphere and upper troposphere, particularly in the Arctic, to explore the relationship between atmospheric chemistry and climate change, to study the effects of biomass burning on the free troposphere and to measure aerosols and clouds to reduce the uncertainties in their effects on the global energy balance.

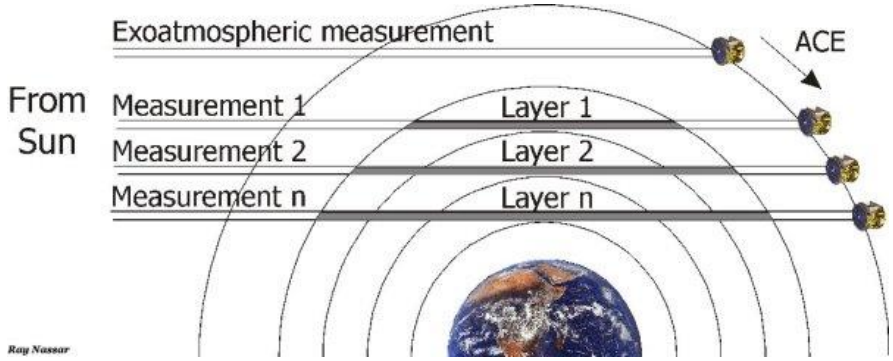

Figure 3.11. Solar occultations as performed by ACE-FTS. http://www.ace.uwaterloo.ca/solar_occultation.html.

The main instrument onboard ACE is a Fourier Transform Spectrometer (FTS) built by ABB-Bomem and equipped with two detectors (InSb and HgCdTe) that covers from 750 to 4400 cm^{-1} with a high resolution of 0.02 cm^{-1} to measure vertical distribution of trace gases and temperature. As illustrated in Figure 3.11, during sunrise and sunset, the FTS measures sequences of atmospheric absorption spectra in the limb viewing geometry with different slant paths and tangent heights. As described in *Bernath et al.*, [2005], the ACE-FTS measurement sequence during a sunset occultation starts with the suntracker pointing to deep space to record a set of instrument self-emission spectra. The deep space spectra are followed by a set of high sun reference spectra obtained by pointing to the center of the sun, and then a sequence of occultation spectra starting at 150 km tangent altitude are obtained at a rate of one scan every 2 s as the sun sets. These spectra are then inverted into vertical profiles of atmospheric constituents, with a vertical resolution of about 4 km from the cloud tops up to about 150 km.

3.5.1.3. in situ GC-MS surface measurements

The Jungfraujoch station also welcomes continuous gas chromatography-mass spectrometry (GC-MS) measurements of gases performed by the Laboratory for Air Pollution and Environmental Technology, Swiss Federal Laboratories for Materials Testing and Research (EMPA) in the framework of the Global Atmosphere Watch (GAW) program of the World Meteorological Organization (WMO, www.wmo.int).

The gas-chromatography coupled with mass spectrometry is a technique that allows for a qualitative and quantitative analysis of several components found within the initial sample. Gas chromatography is an analytical separation technique used to analyze volatile substances in the gas phase such as air samples. Through this separation technique, the components of a sample are separated by dragging of a mobile phase through a stationary phase. The separation will then occur either by the successive adsorption and desorption on the stationary phase or by a difference of solubility into each phase. Regarding mass spectrometry, this analytical chemistry technique allows the quantification of a sample's composition by measuring the mass-to-charge ratio. Indeed, in a typical mass spectrometry procedure, the sample is ionized and the formed ions are separated according to their mass-to-charge ratio.

Networks involved in monitoring the atmosphere composition with either continuous or flask gas chromatography MS measurements at the surface, include the Earth System Research Laboratory from the National Oceanic and Atmospheric Administration (NOAA/ESRL, Boulder, CO, USA, http://www.esrl.noaa.gov/gmd/), the Advanced Global Atmospheric Gases Experiment (AGAGE; Massachusetts Institute of Technology, Cambridge, MA; https://agage.mit.edu/) and the GAW programme. The NOAA/ESRL formerly known as the Climate Monitoring and Diagnostics Laboratory (CMDL) began measurements of climatically important gases on an expanded scale in the mid-1970s. The measurement program includes around the clock measurements at 4 baseline observatories and 8 tall towers, air samples collected at more than 50 sites, and air samples collected regularly from small aircraft mostly in North America. Its mission involves answering key scientific questions in climate forcing, ozone depletion, and air quality. AGAGE has been measuring the composition of the global atmosphere continuously since 1978 from its 14 coastal or mountain stations around the world. The GAW programme (http://www.wmo.int/pages/prog/arep/gaw/gaw_home_en.html) is a partnership involving 30 global and

more than 400 regional atmospheric research stations in 80 countries created in 1989 by the consolidation of two observing networks established during the in 1950s. The three of them share the same objective to provide reliable and accurate measurements of trace gases and information on the chemical composition of the atmosphere, its natural and anthropogenic change. The data collected therefore help to improve the understanding of interactions between the atmosphere, the oceans and the biosphere.

3.5.2. Models

In the second part of this work, model simulations are used as support to interpret our observations and results interpretation. This section provides a quick overview of the models involved in the studies presented in the second part while a more complete description of the simulations employed will be given when mentioned.

3.5.2.1. WACCM

The Whole Atmosphere Community Climate Model [WACCM; *Chang et al.*, 2008; https://www2.cesm.ucar.edu/working-groups/wawg] is a circulation model developed at the National Center for Atmospheric Research (NCAR, Boulder, CO). Chemistry and tracers are calculated using the Model for Ozone and Related Tracers (MOZART), while mesospheric and thermospheric physics are implemented from the Thermosphere Ionosphere Mesosphere Electrodynamics General Circulation Model (TIME-GCM). The model spans the range of altitude from the surface to 140 km.

Within the IRWG, in the use of WACCM outputs for a priori vertical distribution of atmospheric constituents to retrieve is recommended with the aim of using an harmonized and consistent set as a priori profiles for all sites. The vertical distributions are built from monthly WACCMv6 averaged over the 1980-2020 time period and then interpolated to each site from the model output. It includes more than 90 species including major greenhouse gases and air pollutants. Currently, the latest version of WACCM, i.e. version 6, should replace all previous version. However, we will show in chapter 5 that in order to develop a retrieval strategy optimized for a specific station (the Jungfraujoch station in our case) WACCM may not provide the best results in terms of residuals, information content and retrieved vertical profiles. Therefore, it may be required to use additional datasets such as other models and/or observations

3.5.2.2. IMAGES

The Intermediate Model of the Annual and Global Evolution of Species [IMAGES; *Müller and Brasseur*, 1995, 1999] is a global three-dimensional chemical transport model which extends from the surface to the lower stratosphere on 25 vertical levels (up to the pressure of 50 hPa or approximately 22.5 km). IMAGES is run at a resolution of 5° in latitude and longitude with a time step equal to 6 hours. The model simulates the concentration of 59 long- and short-lived atmospheric constituents through a chemical mechanism including 133 gas-phase reactions, 29 photodissociations, and 3 heterogeneous reactions on the surface of sulfate aerosols. Large-scale transport parameters are driven by averaged climatological fields from the European Centre for Medium-Range Weather Forecasts (ECMWF, http://www.ecmwf.int/).

3.5.2.3. CHASER

The CHemical AGCM for Study of atmospheric Environment and Radiative forcing model [CHASER; *Sudo*, 2002; *Sudo and Akimoto*, 2007], has been developed mainly in the Nagoya University and the Japan Agency for Marine-Earth Science and Technology (JAMSTEC) in the framework of the Model for Interdisciplinary Research on Climate-Earth System Model, MIROC-ESM-CHEM [*Watanabe et al.*, 2011]. CHASER is a chemistry coupled climate model used in cooperation with the aerosol component model SPRINTARS [Spectral Radiation-Transport Model for Aerosol Species; *Takemura*, 2005]. It studies tropospheric ozone and related chemistry and their impact on climate by simulating detailed chemistry in the troposphere and stratosphere with an on-line aerosol simulation including production of particulate nitrate and secondary organic aerosols.

3.5.2.4. GEOS-Chem

GEOS-Chem [*Bey et al.*, 2001a; www.geos-chem.org] is a global 3-D CTM for atmospheric composition driven by meteorological input from the Goddard Earth Observing System (GEOS) of the NASA Global Modeling and Assimilation Office and managed by the GEOS-Chem Support Team, based at Harvard University and Dalhousie University with support from the US NASA Earth Science Division and the Canadian National and Engineering Research Council. The model supports input data from GEOS-4 (1° x 1.25° horizontal resolution, 55 vertical levels), GEOS-5 (0.5° x 0.666°, 72 levels), MERRA (0.5° x 0.666°, 72 levels), and GEOS-FP (0.25° x 0.3125°, 72 levels, starting in April 2012). The GEOS meteorological data archive has a temporal resolution of 3 hours (MERRA, GEOS-FP) or 6 hours (GEOS-4, GEOS-5).

GEOS-Chem simulations can be conducted at the native resolution of the GEOS fields or at coarser resolution (2° x 2.5° or 4° x 5°). Standard GEOS-5 and GEOS-FP nested windows for aerosol-oxidant simulations are available for East Asia [*Chen et al.*, 2009], North America [*van Donkelaar et al.*, 2012; *Zhang et al.*, 2012], and Europe [*van Donkelaar et al.*, 2013].

GEOS-Chem includes detailed HO_x-NO_x-VOC-ozone-BrO_x tropospheric chemistry as originally described by [*Bey et al.*, 2001a] and with addition of BrO_x chemistry by *Parrella et al.*, [2012]. GEOS-Chem simulation modes consists of a full chemistry, tagged CO [*Bey et al.*, 2001b], tagged Ox, tagged CH_4 [*Wang*, 2004; *Wecht et al.*, 2014], offline aerosols and CO_2 [*Suntharalingam*, 2004].

Chapter 4 – Methanol

Chapter 4 − Methanol

4.1. Introduction

The primary challenge on the methanol study was to develop a retrieval strategy optimized for observations recorded at the Jungfraujoch station. The development of a methanol retrieval strategy included testing of numerous inversion strategies (see Table 4.0) for evaluation of methanol absorption lines as used in previous studies [*Dufour et al.*, 2007; *Rinsland et al.*, 2009; *Vigouroux et al.*, 2012] and determination of the best combination of spectral windows, the solar zenith angle range, the methanol a priori mixing ratio profile [*Chang et al.*, 2008], and the signal-to-noise ratio for inversion, among others. The successive tests for an optimized retrieval strategy were based on a subset of 314 spectra covering the year 2010, representative of each season and of the range of solar zenith angle. We selected the best strategy on the basis of minimum interferences, minimum residuals and maximum information content. In addition, a systematic and careful error budget has been determined further guiding the choice of the best retrieval strategy for methanol above Jungfraujoch. The evaluations were performed according to the method developed through this work and described in section 2.3. This retrieval strategy is the object of a paper published in the Atmospheric Measurement and Techniques journal [see next section; *Bader et al.*, 2014].

Parameter	Number of tests
Solar zenith angle range	4
Windows, interfering species to retrieve	14
Signal-to-noise ratio for inversion	26
CH_3OH a priori profile	8
Effective apodisation parameter	4
Other	6
Total	**62**

Table 4.0. Overview of tests performed for the optimization of the methanol retrieval strategy for Jungfraujoch.

The evaluation of the combination of spectral windows is based on previous work from the retrieval of CH_3OH from FTIR observations performed at Kitt Peak [*Rinsland et al.*, 2009], from ACE-FTS occultation observations [*Dufour et al.*, 2007] and from FTIR observations at Reunion Island [*Vigouroux et al.*, 2012]. We have for the first time –for ground-based FTIR observations– combined several spectral windows, as illustrated in Figure 4.0.1. The identification of best window limits and of the interfering species to be accounted for has been performed through 14 inversions. Moreover, since the fitting quality is significantly different in both windows, values for the signal-to-noise ratio for inversion (SNR) have been selected for each window individually. The different SNR for both window has been taken into account in the error budget.

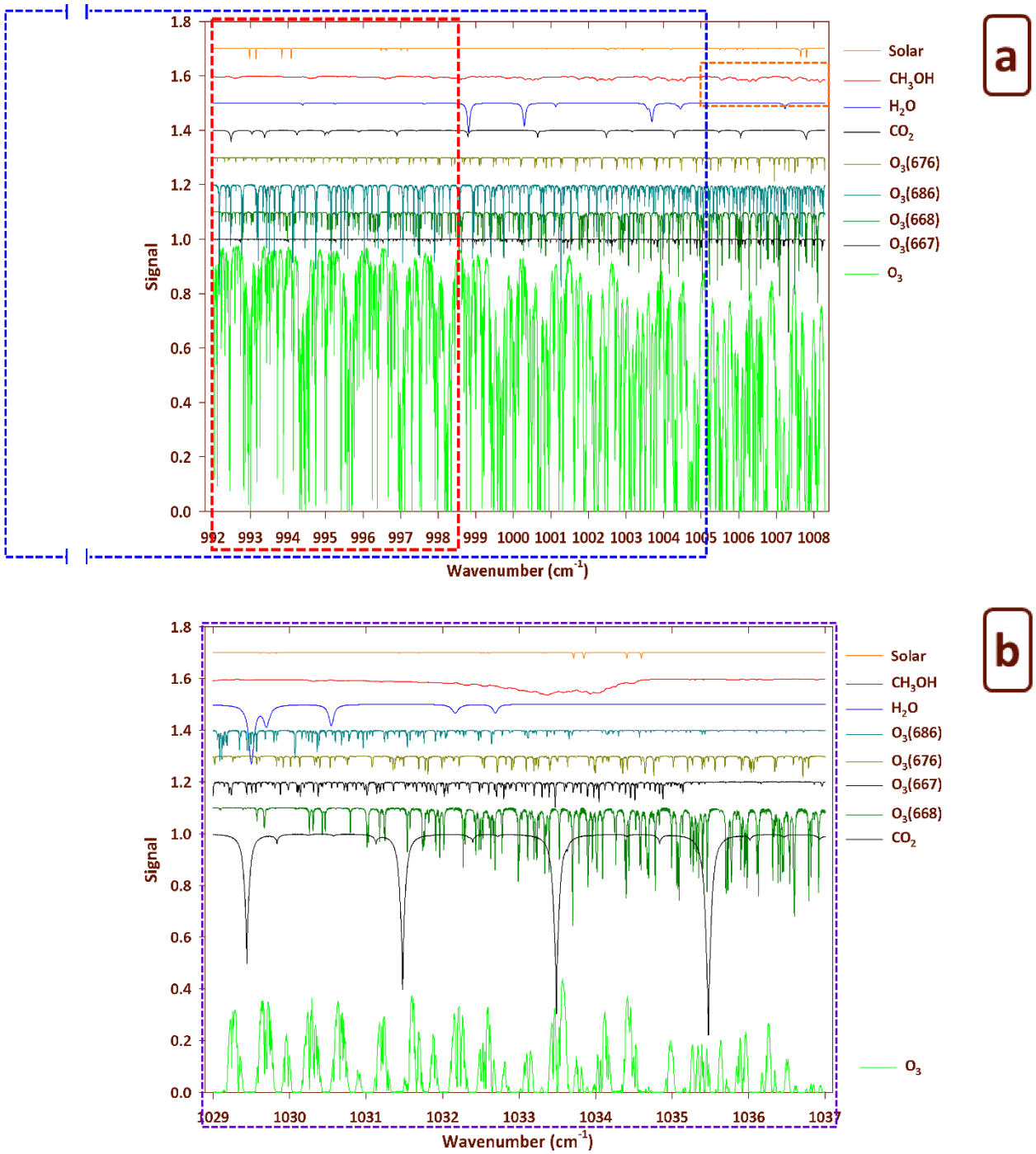

Figure 4.0.1. Simulation for Jungfraujoch, 80° zenith angle, resolution of 6.1 mK or 0.0061 cm^{-1}. For both windows, we display the synthetic spectra for individual contributors (see color codes). HITRAN 2008 and averaged mixing ratio profiles based on the WACCM model climatology have been used for the simulations, except for CH3OH for which our a priori was used (see 4.2.2.). For clarity, the contributions of each species have been vertically shifted. (a) First spectral window used for the retrievals ranging from 992 to 1008.3 cm^{-1}, the red frame shows the 992–998.7 cm^{-1} window from Rinsland et al., [2009]*, the blue frame shows the 984.9–1005.1 cm^{-1} window from ACE-FTS CH3OH retrievals (version 3.5) in addition to supplemental methanol features up to the 1008.3 cm^{-1} limit in the orange frame. (b) The second spectral window defined ranges from 1029 to 1037 cm^{-1} and is from Vigouroux et al., [2012] illustrated by the purple frame.*

Since the CH_3OH absorption lines are quite weak, we needed to restrain the spectra selection from the 498 observations available for the year 2010 to a specific range of solar zenith angle (SZA). To this end, we performed the inversion for the whole SZA range available (Figure 4.0.2) and determined that a minimum SZA of 60° is required to reach a DOFS of approximately 1.

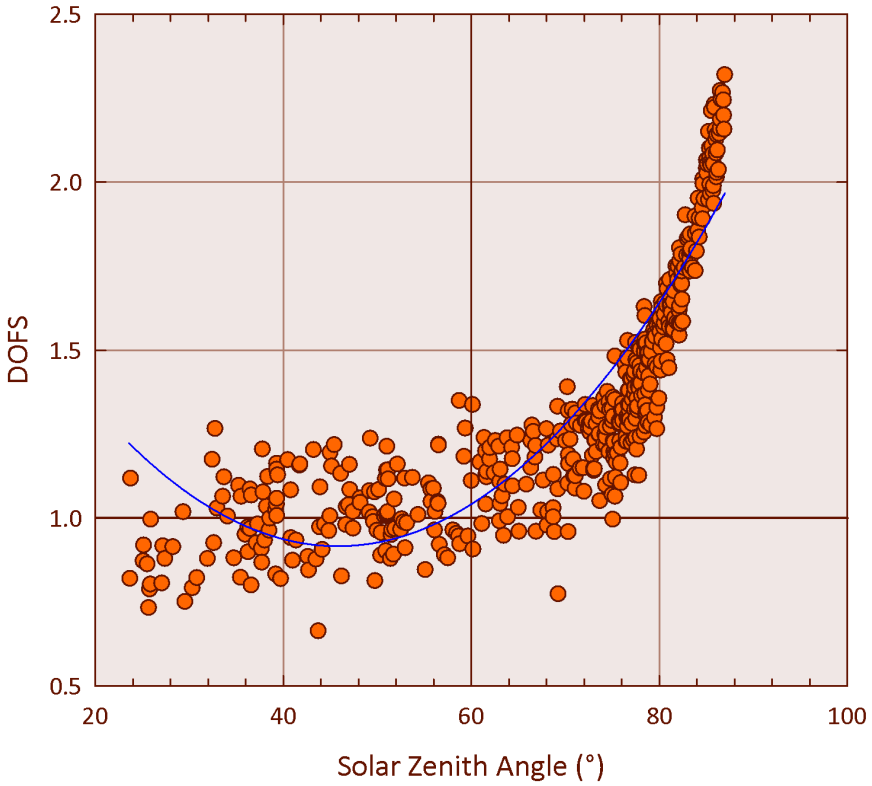

Figure 4.0.2. DOFS as a function of the solar zenith angle. Blue curve is a second order polynomial fit of data.

Even if *Rinsland et al.* [2009] showed evidence of a methanol contribution to the spectra from Kitt Peak FTIR observations (2090 m a.s.l.), we needed to ascertain that retrieved methanol columns were independent of retrieved ozone columns since the Jungfraujoch observations have likely less absorption by CH_3OH due to the high altitude of the station (3580 m a.s.l.). In fact, as illustrated in Figure 4.0.3, retrieved methanol columns are neither correlated with retrieved total columns of O_3 nor $O_3(686)$ with coefficient of determination respectively of 0.0084 and 0.0006. Other parameters have been examined and included in the retrieval strategy such as adjustment of the slope and curvature of the spectrum, the effective apodisation parameter accounting for the good alignment of the instrument.

Harmonization efforts to include homemade FTIR measurements in order to extend the time series of methanol back to 1987 were not conclusive. Indeed, because of their lower signal-to-noise ratio [*Mahieu et al.*, 2014], too many CH_3OH vertical profiles we retrieved showed strong oscillations associated to ungeophysical negative mixing ratio values in the lower-troposphere. Therefore, in [*Bader et al.*, 2014] we only presented results retrieved from the Bruker spectrometer.

Once the retrieval strategy is optimized and the product characterized in terms of information content and uncertainty, we were able to move on with trend and seasonal cycle analysis along with diurnal variations with support –and comparison with– from GC-MS in situ surface measurements [*Legreid et al.*, 2008], ACE-FTS occultations observations [*Dufour et al.*, 2007] and simulations from the model IMAGESv2 [*Stavrakou et al.*, 2011]. This study contributes to filling the gap in FTIR methanol studies. As there still remain large uncertainties in the methanol budget, long-term time series of methanol observations should provide better constraints for model and satellite validation.

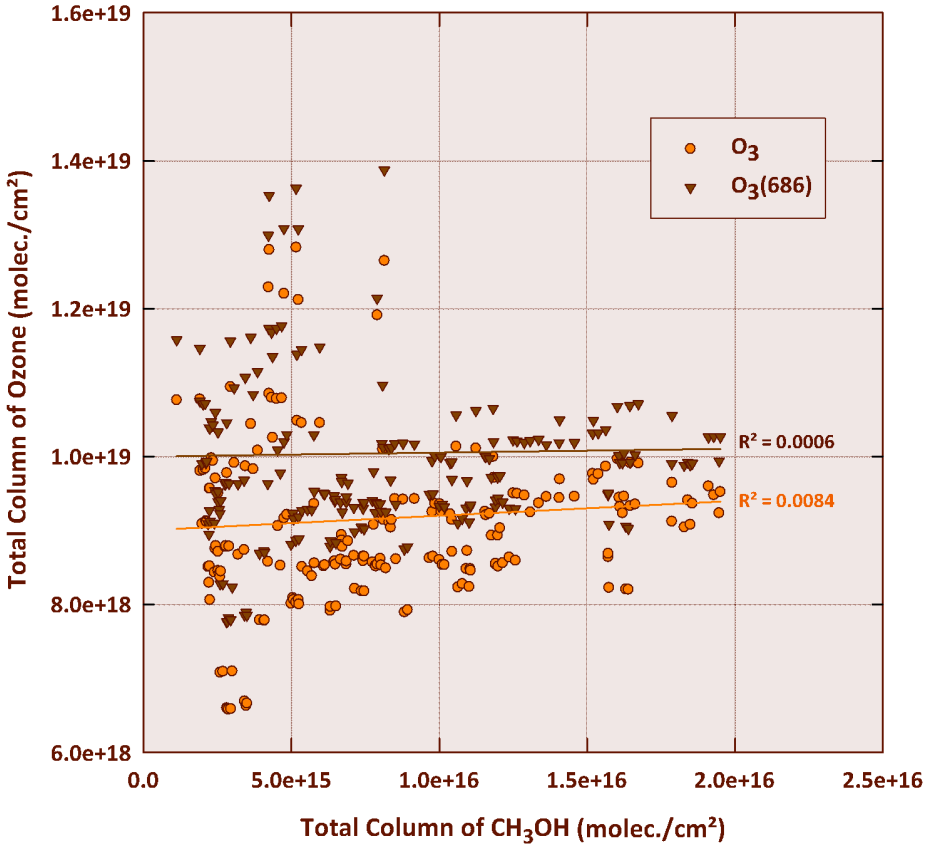

Figure 4.0.3. Total column of ozone (O_3 in orange and O_3(686) in brown) as a function of retrieved total column of methanol. Straight lines show respective linear fit with their associated coefficient of determination.

4.2. Long-term evolution and seasonal modulation of methanol above Jungfraujoch (46.5°N, 8.0°E): optimization of the retrieval strategy, comparison with model simulations and independent observations

Reference: Bader, W., Stavrakou, T., Muller, J.-F., Reimann, S., Boone, C. D., Harrison, J. J., Flock, O., Bovy, B., Franco, B., Lejeune, B., Servais, C., and Mahieu, E.: Long-term evolution and seasonal modulation of methanol above Jungfraujoch (46.5°N, 8.0°E): optimization of the retrieval strategy, comparison with model simulations and independent observations, Atmos. Meas. Tech., 7, 3861-3872, doi: 10.5194/amt-7-3861-2014, 2014.

W. Bader[1], T. Stavrakou[2], J.-F. Muller[2], S. Reimann[3], C. D. Boone[4], J. J. Harrison[5], O. Flock[1], B. Bovy[1], B. Franco[1], B. Lejeune[1], C. Servais[1], and E. Mahieu[1]

[1] Institute of Astrophysics and Geophysics of the University of Liège, Liège, Belgium
[2] Belgian Institute for Space Aeronomy, Avenue Circulaire 3, 1180, Brussels, Belgium
[3] Laboratory for Air Pollution and Environmental Technology, Swiss Federal Laboratories for Materials Testing and Research (EMPA), Dübendorf, Switzerland
[4] Department of Chemistry, University of Waterloo, Ontario, Canada 5Department of Chemistry, University of York, York, UK

Received: 11 April 2014 – Published in Atmos. Meas. Tech. Discuss.: 8 May 2014
Revised: 2 October 2014 – Accepted: 16 October 2014 – Published: 21 November 2014
Edited by: F. Boersma

Abstract

Methanol (CH_3OH) is the second most abundant organic compound in the Earth's atmosphere after methane. In this study, we present the first long-term time series of methanol total, lower tropospheric and upper tropospheric– lower stratospheric partial columns derived from the analysis of high resolution Fourier transform infrared solar spectra recorded at the Jungfraujoch station (46.5°N, 3580 m a.s.l.). The retrieval of methanol is very challenging due to strong absorptions of ozone in the region of the selected v8 band of CH_3OH. Two wide spectral intervals have been defined and adjusted in order to maximize the information content. Methanol does not exhibit a significant trend over the 1995–2012 time period, but a strong seasonal modulation characterized by maximum values and variability in June–July, minimum columns in winter and a peak-to-peak amplitude of 130 %. Analysis and comparisons with in situ measurements carried out at the Jungfraujoch and ACE-FTS (Atmospheric Chemistry Experiment-Fourier Transform Spectrometer) occultations have been performed. The total and lower tropospheric columns are also compared with IMAGESv2 model simulations. There is no systematic bias between the observations and IMAGESv2 but the model underestimates the peak-to-peak amplitude of the seasonal modulations.

4.2.1. Introduction

Methanol (CH_3OH) is the second most abundant organic molecule in the atmosphere after methane, with concentrations between 1 [*Singh et al.*, 2001] and 20 ppbv [*Heikes et al.*, 2002], despite a lifetime that has been estimated to lie between 4.7 days [*Millet et al.*, 2008] and 12 days [*Atkinson et al.*, 2006]. Plant growth is the largest source of methanol with a 65–80 % contribution to its emissions [*Galbally and Kirstine*, 2002; *Jacob*, 2005]. The atmospheric production of CH_3OH through peroxy radical reactions represents up to 15–23 % of its sources [*Madronich and Calvert*, 1990; *Tyndall et al.*, 2001]. Other sources of methanol are plant matter decaying [*Warneke et al.*, 1999], biomass burning [*Dufour et al.*, 2006; *Paton-Walsh et al.*, 2008], fossil fuel combustion, vehicular emissions, solvents and industrial activities.

Methanol influences the oxidizing capacity of the atmosphere through reaction with the hydroxyl radical [*Jiménez et al.*, 2003], its main sink, leading to the formation of water vapor and either CH_3O or CH_2OH radicals, which both react with O_2 to give HO_2 and formaldehyde (H_2CO) [*Millet et al.*, 2006]. The photo-oxidation of formaldehyde, a key intermediate in the oxidation of numerous volatile organic compounds, leads to the formation of HO_2 radicals and carbon monoxide (CO). As a consequence, CH_3OH is considered as a source of CO with a yield close to 1 [*Duncan et al.*, 2007]. The main sources and sink of methanol are characterized by significant seasonal modulations. This results in a strong signal for CH_3OH, with maximum and minimum abundances observed in the Northern Hemisphere at the beginning of July and in December, respectively [*Rinsland et al.*, 2009; *Razavi et al.*, 2011; *Cady-Pereira et al.*, 2012; *Wells et al.*, 2012], reflecting the seasonality of biogenic sources.

In the past decade, ground-based [*Schade and Goldstein*, 2001, 2006; *Karl et al.*, 2003; *Carpenter et al.*, 2004] and aircraft [*Fehsenfeld et al.*, 2006; *Singh et al.*, 2006] in situ measurements combined with space-based measurements, including the Infrared Atmospheric Sounding Interferometer (IASI) on board the MetOp-A satellite [*Razavi et al.*, 2011], the TES (Tropospheric Emission Spectrometer) nadir-viewing Fourier transform spectrometer (FTS), on board the Aura satellite [*Beer et al.*, 2008], and the solar occultations recorded by the Atmospheric Chemistry Experiment-FTS [ACE-FTS, *Bernath et al.*, 2005; *Dufour et al.*, 2006, 2007] have supplied numerous observations of CH_3OH, which have provided valuable insights on the distribution and budget of methanol at the global scale. In addition, previous studies have reported the measurement of methanol from ground-based infrared solar absorption observations performed at Kitt Peak [31.9°N, 111.6°W, 2090 m a.s.l.; *Rinsland et al.*, 2009] and at Saint- Denis [Reunion Island, 21°S, 55°E, 50 m a.s.l.; *Stavrakou et al.*, 2011; *Vigouroux et al.*, 2012]. However, there still remain large uncertainties in our knowledge of the methanol global sources and sinks, as indicated by the large discrepancies existing between different measurement-based estimates of the total sources [*Galbally and Kirstine*, 2002; *Tie et al.*, 2003; *von Kuhlmann*, 2003; *von Kuhlmann et al.*, 2003; *Jacob*, 2005; *Millet et al.*, 2008; *Stavrakou et al.*, 2011]

In this paper, we report the first long-term methanol time series (17 years) derived from ground-based high-resolution infrared spectra recorded with a Fourier transform infrared (FTIR) spectrometer operated under clear sky conditions at the high-altitude International Scientific Station of the Jungfraujoch [ISSJ, Swiss Alps, 46.5°N, 8.0°E, 3580 m a.s.l.; *Zander et al.*, 2008] providing a valuable tool for model and

satellite validation. Most of the available spectra have been recorded within the framework of the Network for Detection of Atmospheric Composition Change monitoring activities (NDACC; see http://www.ndacc.org) complementing the NDACC measurements at northern mid-latitudes. A detailed analysis was conducted to optimize the retrieval strategy of atmospheric methanol in order to minimize the fitting residuals while maximizing the information content. A thorough discussion of the retrieval strategy, data characterization (information content and error budget), long-term trend and seasonal cycle of total and partial columns of methanol above Jungfraujoch is presented here. This paper is organized as follows. A detailed description of the optimized retrieval strategy is given in Sect. 2. The characterization of our data by their eigenvectors and error budget is discussed in Sect. 3. Finally, in Sect. 4, we present and discuss the results, focusing on the intra-annual and intra-day variability of methanol at ISSJ along with comparisons with in situ measurements, satellite occultations and model calculations.

4.2.2. Retrieval strategy

Regular FTIR observations have been carried out at the ISSJ with a homemade spectrometer since 1984, complemented in the early 1990s and then definitely replaced by a commercial Bruker IFS-120HR instrument [*Zander et al.*, 2008]. This spectrometer is equipped with HgCdTe and InSb cooled detectors, allowing us to cover the 650 to 4500 cm^{-1} region of the electromagnetic spectrum. Since 1991, the FTIR instruments are affiliated with the NDACC network.

The Bruker observational database consists of more than 6500 spectra recorded between 1995 and 2012 with an optical filter covering the 700 to 1400 cm^{-1} domain encompassing the fundamental C-O stretching mode v8 of methanol at 1033 cm^{-1}. Spectral resolution, defined as the reciprocal of twice the maximum optical path difference, alternates between 0.004 and 0.006 cm^{-1}. Signal-to-noise (S/N) ratios vary between 250 and 1800 (average spectra resulting from several successive individual Bruker scans, when solar zenith angles vary slowly). The optimization of the retrieval strategy was based on a subset of 314 spectra covering the year 2010.

The CH_3OH column retrievals and profile inversions have been performed using the SFIT-2 v3.91 fitting algorithm. This retrieval code has been specifically developed to derive mixing ratio profiles of atmospheric species from ground based FTIR spectra [*Rinsland et al.*, 1998]. It is based on the semi-empirical implementation of the Optimal Estimation Method (OEM) developed by [*Rodgers*, 1990]. Vertical profiles are derived from simultaneous fits to one or more spectral intervals in at least one solar spectrum with a multilayer, line-by-line calculation that assumes a Voigt line shape [*Drayson*, 1976]. The model atmosphere adopted above the Jungfraujoch altitude consists of a 39 layers scheme with progressively increasing thicknesses, from 3.58 km to reach the 100 km top altitude. The pressure-temperature profiles are provided by the National Center for Environmental Prediction (NCEP, Washington DC, USA, http://www.ncep.noaa.gov/) while the solar line compilation supplied by F. Hase (KIT) [*Hase et al.*, 2006] has been assumed for the solar absorptions. Line parameters used in the spectral fitting process were taken from the HITRAN 2008 spectroscopic compilation [*Rothman et al.*, 2009]. Methanol lines were added to the HITRAN compilation for the first time in 2004 [*Rothman et al.*, 2005]. The parameters for the 10 µm region

are described in the paper by *Xu et al.* [2004] and were derived from measurements with two high-spectral resolution FTS instruments.

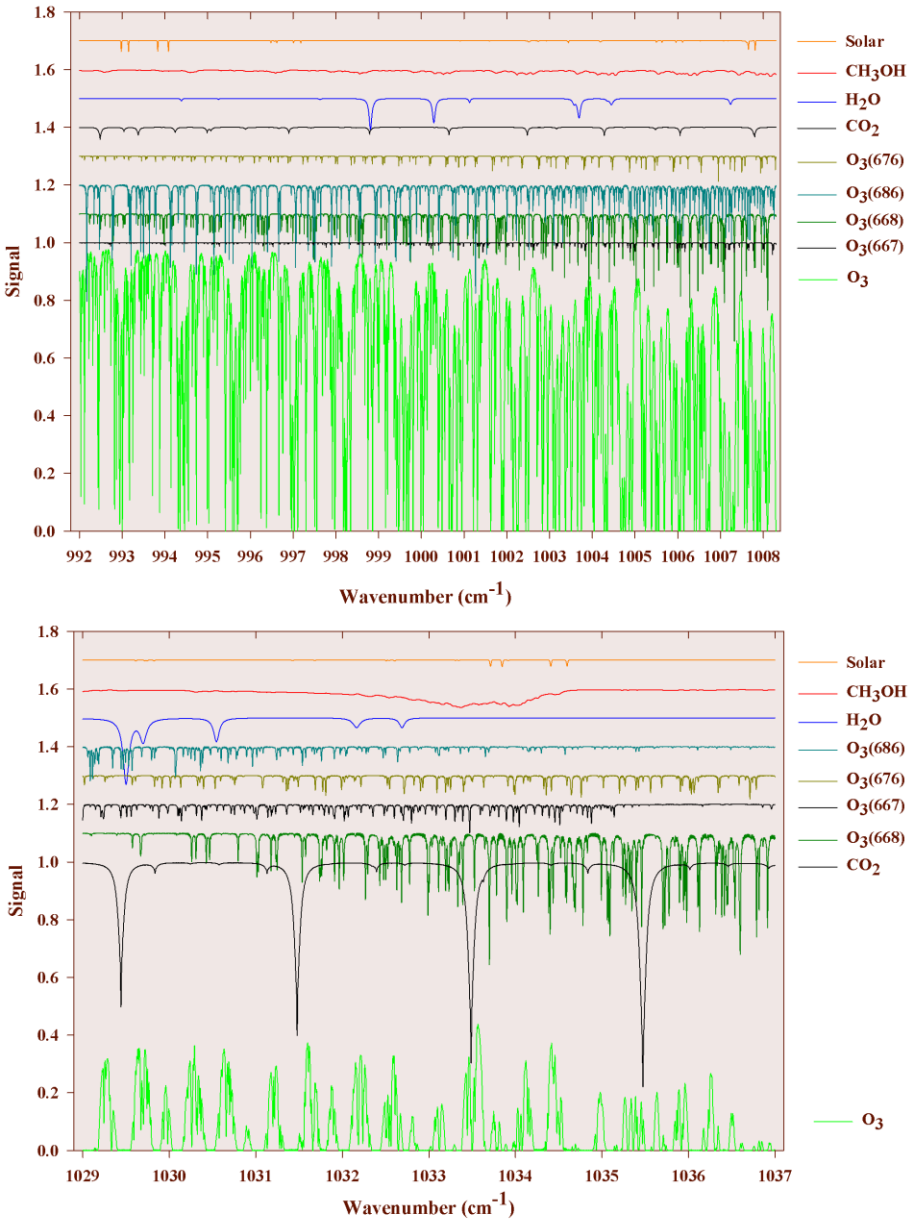

Figure 4.1. Simulation for Jungfraujoch, 80° zenith angle, 6.1 mK. For both windows, we display the synthetic spectra for individual contributors (see color codes). HITRAN 2008 and averaged mixing ratio profiles based on the WACCM model climatology have been used for the simulations, except for CH3OH for which our a priori was used (see text). For clarity, the contributions of each species have been vertically shifted.

Two spectral windows both encompassing the ν8 C–O stretch absorption band of methanol have been defined. Synthetic spectra (6.1 mK or 0.0061 cm^{-1}, zenith angle of 80°) have been computed for the first and second order absorbers in both selected windows and are illustrated in Figure 4.1. The first interval ranges from 992 to 1008.3 cm^{-1} and is based on windows used in previous investigations. A 992–998.7 cm^{-1}

window was employed for the retrieval of CH_3OH from Kitt Peak FTS spectra [*Rinsland et al.*, 2009] and a 984.9–998.7 cm^{-1} window was used for the initial retrievals of methanol from ACE-FTS occultation observations [*Dufour et al.*, 2007]. The latest ACE-FTS CH_3OH retrievals (version 3.5) use an extended window from 984.9 to 1005.1 cm^{-1}. Measuring in the limb, ACE-FTS measurements start to saturate for wavenumbers above 1005.1 cm^{-1} for occultations with higher than average O_3 levels. As ground-based observations do not have this problem, we included supplemental methanol features up to the 1008.3 cm^{-1} limit. The second interval, ranging from 1029 to 1037 cm^{-1} is used by [*Vigouroux et al.*, 2012].

Absorption by the main ozone isotopologue (^{16}O-^{16}O-^{16}O or O_3) captures nearly 93 and 98 % of the IR radiation in the "1008" and "1037" windows respectively and is close to saturation in the latter one. Methanol features are much weaker, with mean absorption of 1.7 and 1.8 % in the "1008" and "1037" windows respectively. Additional absorptions are associated with O_3 isotopologues, such as O_3(668) or (^{16}O-^{16}O-^{18}O), O_3(686) or (^{16}O-^{18}O-^{16}O), O_3(676) or (^{16}O-^{17}O-^{16}O) and O_3(667) or (^{16}O-^{16}O-^{17}O) as well as carbon dioxide (CO_2) and water vapor (H_2O). Since the CH_3OH absorption lines are quite weak, only spectra with solar zenith angles greater than 65° and up to 80° have been analyzed. During the retrievals, both windows were for the first time fitted simultaneously.

The a priori mixing ratio profile for the CH_3OH target is a zonal mean (for the 41–51°N latitude band) of 903 occultations recorded by the ACE-FTS instrument (version 3.5) between 27 March 2004 and 3 August 2012, extending from 5.5 to 30 km tangent altitudes. The profile was extrapolated to 1 ppbv to the surface [*Singh et al.*, 2001; *Heikes et al.*, 2002], and to 0.05 ppbv [*Singh et al.*, 2006; *Dufour et al.*, 2007] for upper layers. The covariance matrix is specified for each layer as a percentage of the a priori profile and an ad hoc correlation length, which is interpreted as a correlation between layers decaying along a Gaussian. For methanol, we adopted a 50 %.km^{-1} diagonal covariance and a Gaussian half width of 4 km for extra diagonal elements. A priori profiles for all interfering molecules are based on the WACCM [version 5, the Whole Atmosphere Community Climate Model, e.g. *Chang et al.*, 2008] model climatology for the 1980-2020 period and the ISSJ station. The vertical profiles of CH_3OH, O_3 and O_3(668) are fitted during the iterative process while the a priori distributions of O_3(686), O_3(676), O_3(667), H_2O and CO_2 are scaled. Since the fitting quality is significantly different in both windows, two different values for the signal-to-noise ratio for inversion have been selected, i.e. 180 and 40 for the "1008" and "1037" domains, respectively.

When fitted independently, we observe a compact correlation between the corresponding CH_3OH total columns retrieved from both windows with a small bias of 15 ± 13 % (2σ). When comparing ozone total columns respectively retrieved from the strategy described in this work and from the retrieval strategy applied within the NDACC network [window limits: 1000–1005 cm^{-1},*Vigouroux et al.*, 2012], no significant bias emerges from the comparison between the two ozone total column sets, with a mean relative difference of -0.8 ± 2.4 % (2σ), demonstrating a proper fit of the main interference involved in our methanol retrieval strategy. Additional functions are also included in the fitting process to account for deviations from a perfectly aligned FTS. As an effective apodisation function, we assumed a polynomial function of order 2 [*Barret et al.*, 2002]. The effective apodisation parameter (EAP) gives the value of the effective apodisation function at the maximum optical path difference and is synonymous of a well-aligned

instrument when it is close to 1.0. The inversion of the EAP has been included in our retrieval as well as in the NDACC's retrieval strategy of ozone. The EAP derived from both strategies proved to be consistent, with a mean relative difference of 0.7 ± 2.6 % (2σ). Those three latter points give confidence in the combination of the two selected windows and in our optimized retrieval strategy.

4.2.3. Data characterization and error budget

Information content has been carefully evaluated and typical results are displayed on Figure 4.2. The information content is significantly improved, with a typical degree of freedom for signal (DOFS) of 1.82, in comparison with DOFS of about 1 in previous studies [e.g. *Rinsland et al.*, 2009; *Vigouroux et al.*, 2012]. In Figure 4.2, the first eigenvector and eigenvalue (see left panel, in orange) show that the corresponding information is mainly coming from the retrieval (99 %). The increase of information content allows us to retrieve a tropospheric column (Tropo, from 3.58 to 10.72 km) with only 1 % of a priori dependence as well as two partial columns with less than 30 % of a priori dependence (second eigenvector), i.e. a low-tropospheric (LT, from 3.58 to 7.18 km) and an upper troposphere–lower stratosphere (UTLS, from 7.18 to 14.84 km).

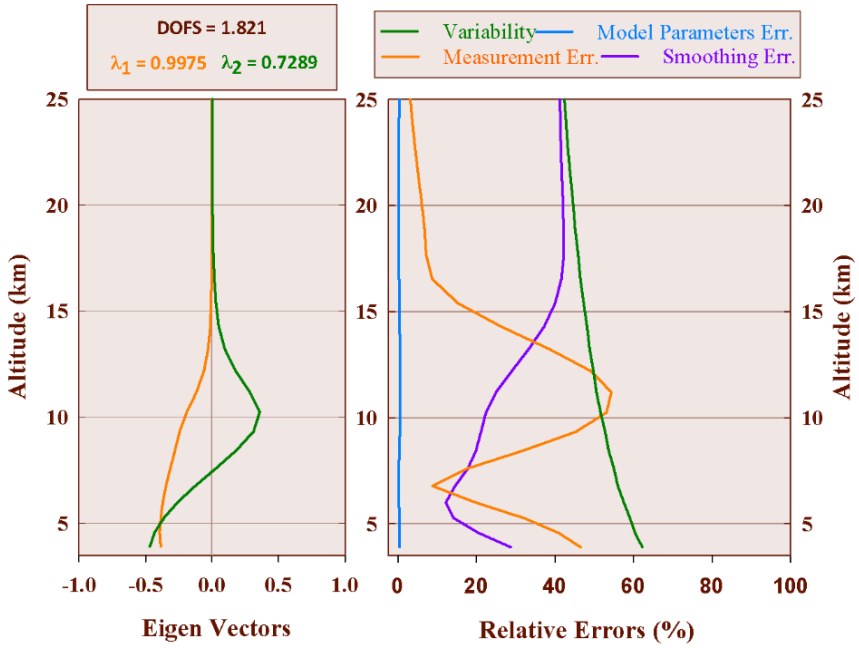

Figure 4.2. Typical results for information content and error budget. Left frame: first eigenvectors and corresponding eigenvalues. Right frame: error budget, with identification of the main error components, together with the assumed variability (see color codes and Table 4.1 for additional information).

The error budget is calculated following the formalism of *Rodgers* [2000], and can be divided into three different error sources: the smoothing error expressing the uncertainty due to finite vertical resolution of the remote sounding system, the forward model parameters error, and the measurement noise error. The right panel of Figure 4.2 gives the corresponding error budget, with identification of the main error components, together with the assumed variability. Error contributions for total and all three partial columns are reported in Table 4.1.

Through a perturbation method, we also accounted for other error sources: systematic errors, such as the spectroscopic line parameters and the misalignment of the instrument, while uncertainty on the temperature and on the solar tracking is considered to be source of random error. Table 4.1 provides an error budget resulting from major instrumental and analytical uncertainties. For the spectroscopic line parameters, we included in our error budget the uncertainty on line intensities provided by the HITRAN database. As methanol line intensities matter, a rough idea of the accuracy of the intensities can be obtained from Table 8 of the *Xu et al.* [2004] study, as it reports an RMS deviation of 7 %. It should be noted that the uncertainty on ozone and its isotopologues lines, according to HITRAN-08 parameters, amounts to between 5 and 10 % [*Rothman et al.*, 2009]. However, an extremely high accuracy of ozone spectroscopic parameters is required in order to retrieve methanol columns properly.

We noted that the SFIT-2 algorithm fails to perform a satisfying retrieval when using spectroscopic parameters with ozone lines intensity incremented by 10 %, suggesting that the error on the concerned lines intensity is more likely to be closer to 5 (or even lower) than to 10 %. Therefore, we accounted for an error on ozone and its isotopologues line intensities of 5 % in our error budget.

Error Sources	Max. Error (%)				
	TC	Tropo	LT	UTLS	
Variability	46	50	57	48	
	Systematic Errors (%)				Comments
	TC	Tropo	LT	UTLS	
Line intensity CH_3OH	7.02	7.11	6.39	9.22	Xu et al., 2004
Line intensity interfering gases	1.00	1.73	3.96	0.91	Rothman et al., 2009 and ± 5% for all O_3 isotopologues lines
ILS	0.41	0.33	1.19	2.39	± 10% misalignment
Forward model	1	< 1	< 1	< 1	Retrieval algorithm-related
Total	7.17	7.39	7.68	9.62	
	Random Errors (%)				
	TC	Tropo	LT	UTLS	
P-T profiles	1.2	2.3	11.3	8.6	From NCEP
SZA	0.2	0.4	3.1	1.4	0.2°
Smoothing	0.4	4.4	16.1	15.2	Barret et al., 2002
Measurement noise	5.2	19.4	35.9	37.5	
Model parameters	0.7	0.6	0.5	1.2	
Total	5.37	20.04	40.18	41.43	
Relative Standard Deviation	6.60	8.34	22.59	21.11	

Table 4.1. Error budget for total and all three partial columns. TC: total column, Tropo: tropospheric column, LT: lower tropospheric layer, UTLS: upper troposphere/lower stratosphere.

We accounted for an error of 10 % on the instrument alignment at the maximum path difference. By comparing the two official NDACC algorithms, *Hase et al.* [2004] and *Duchatelet et al.*, [2010] have established that the forward model may induce a maximum error of 1 % on the retrieved columns for a suite of FTIR target gases. The uncertainty on the pressure–temperature profiles is provided by NCEP with an error of 1.5 K from the ground to an altitude of about 20 km. Concerning the upper levels, the uncertainty increases with altitude, from 2 K around 25 km until 9 K at the top. The uncertainty on the solar zenith angle (SZA) is estimated at 0.2°.

We also provide in Table 4.1 the mean relative standard deviation for each daily mean for days with three or more measurements. It is found to be of the same order of magnitude as the random error. The dominant contribution to the systematic error is the error on methanol spectroscopic lines, while the measurement noise error is the main component of random error. Both systematic and random errors are given in Table 4.1, with 7 % and around 5 % respectively on the total columns.

4.2.4. Results and comparisons

Since the improvement in information content allows us to compute partial columns with only a 30 % a priori dependence and as the random error on the tropospheric column is about four times the error on total columns (see Table 4.1), we focus our trend analysis on total, LT and UTLS columns. Therefore, an analysis of the seasonal variation of methanol in the lower troposphere and the UTLS has been performed, including comparisons with in situ measurements [*Legreid et al.*, 2008] and to ACE-FTS occultation observations, respectively. Comparisons with simulations obtained from the IMAGESv2 global chemistry-transport model [*Stavrakou et al.*, 2011] have also been conducted.

4.2.4.1. Data description

In situ measurements have been performed at the ISSJ station from air samples collected on a two-stage adsorbent system connected to a gas chromatograph–mass spectrometer [GC-MS; *Legreid et al.*, 2008]. The system was in operation during four measurement campaigns in 2005, which were performed from 8 February until 8 March 2005 for the winter measurements, spring measurements followed from 22 April until 30 May, in summertime measurements start from 5 August until 19 September and autumn measurements from 14 October until 1 November, with a frequency of about one sample every 50 min. A total of 1848 measurements of methanol on 122 days have been compared with our lower-tropospheric column time series for the year 2005.

Monthly mean UTLS columns have been derived from measurements taken by the ACE-FTS instrument and compared to our UTLS product. We selected and converted into partial columns the mixing ratios measured by ACE-FTS during ~140 occultations performed in the altitude range of 7.5–14.5 km [version 3.5; *Boone et al.*, 2013] in the 41.5° to 51.5° northern latitude zone between 30 March 2004 and 20 February 2013.

Two model simulations of daily methanol mixing ratios in the 2004–2012 time period obtained from the IMAGESv2 global chemistry-transport model [fully described in *Stavrakou et al.*, 2011] are presented here. The IMAGESv2 model was run at a resolution of 2° in latitude and 2.5° in longitude and with a time step of 6h. It has 40 vertical (hybrid sigma-pressure) levels between the Earth's surface and the lower stratosphere 25 (44 hPa). Daily averaged mixing ratios calculated by the model at the model pixel comprising the ISSJ station were used to calculate the partial and total columns above the station. The first simulation "MEGAN", is performed using MEGANv2.1 bottom-up emissions, which are calculated using an emission model fitted to net ecosystem flux measurements. The second one, "IASI", uses emissions constrained by IASI vertical column data in an inverse modelling framework based on the adjoint of IMAGESv2.

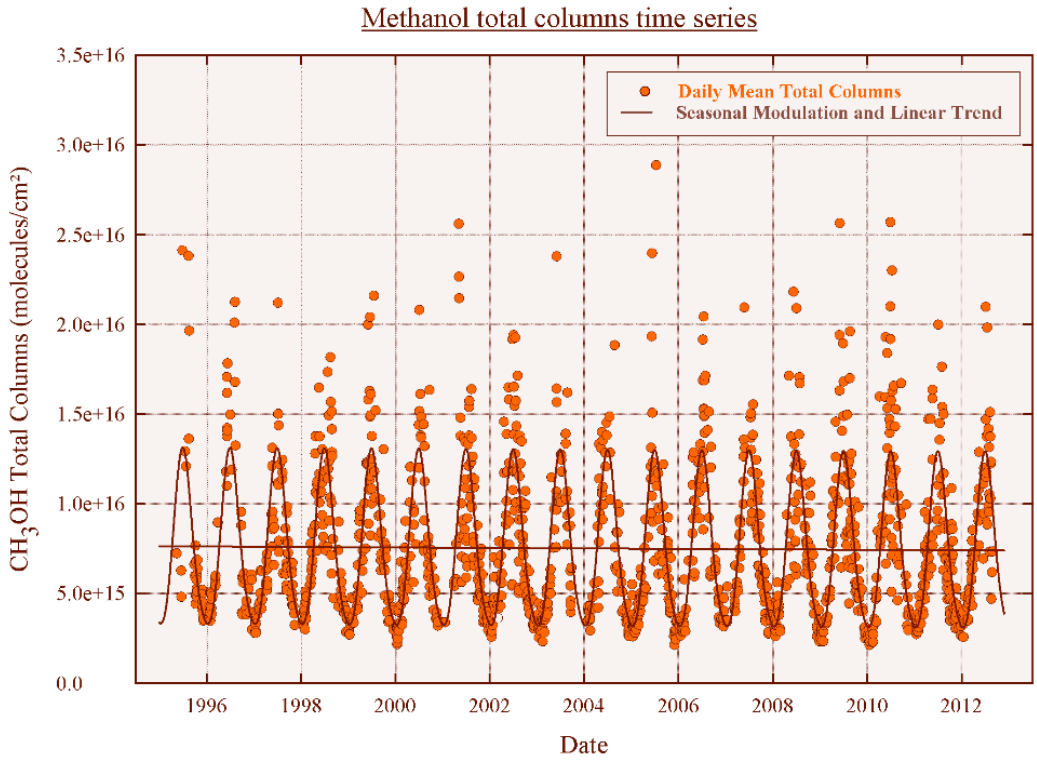

Figure 4.3. Daily mean total (orange circles) column time series of CH_3OH above Jungfraujoch. Brown curves show the linear and seasonal trend components computed with the bootstrap resampling method (Gardiner et al., 2008).

4.2.4.2. Time series and long-term trend

In order to produce the first long-term time series of atmospheric methanol above Jungfraujoch, three criteria were used to reject noisy measurements or weak absorption: (i) when negative methanol mixing ratios are retrieved; (ii) when RMS (root mean square, difference between calculated and observed absorption) was out of the interval defined by the 95 % level of confidence (2σ); (iii) when the number of iterations reached the fixed maximum. After implementation of these criteria, the total number of valid measurements is 4271 obtained on 1476 days of measurements between 1995 and 2012. For the trend calculations, we used the statistical tool developed by *Gardiner et al.* [2008] that employs a bootstrap resampling method. The function fitted to the time series is a combination of a linear component and a 3rd order Fourier series, i.e.:

$$F(t,b) = c_0 + c(t-t_0) + b_1\, cos\, 2\pi(t-t_0) + b_2\, sin\, 2\pi(t-t_0) + b_3\, cos\, 4\pi(t-t_0) + b_4\, sin\, 4\pi(t-t_0) + b_5\, cos\, 6\pi(t-t_0) + b_6\, sin\, 6\pi(t-t_0) \quad (4.1)$$

where c_0 is the abundance at the reference time t_0 for the linear component (seasonalised data), and c is the annual trend. Figure 4.3 shows the whole times series of daily mean methanol total columns above Jungfraujoch. We evaluated the trend of methanol total columns over the 1995–2012 time period and found a yearly negative trend of (-1.34 ± 2.71) x 10^{13} molecules.cm^{-2} or -0.18 ± 0.36 % (2σ), i.e. a non-significant trend at this level of confidence, which is consistent with the trend computed by *Rinsland et al.* [2009]. A non-significant trend has been computed also for both partial column subsets. Hence the results indicate a long-term trend which is not statistically significant and a strong seasonal variation.

4.2.4.3. Methanol seasonal modulation

As the results for the full time series do not indicate a statistically significant trend, we illustrate in Figure 4.4 the daily mean total columns over a 1-year time base. The strong seasonal modulation of methanol is characterized by minimum values and variability in December to February and maximum columns in June–July. The methanol maximum in summer indicated by our results is consistent with the maximum observed for free tropospheric methanol above Kitt Peak [*Rinsland et al.*, 2009] and the analysis of IASI tropospheric measurements over Europe [*Razavi et al.*, 2011]. The mean peak-to-peak amplitude of a seasonal cycle computed by Gardiner's tool and expressed as a percentage of the corresponding CH3OH yearly mean column amounts to 130.1 ± 1.6 % (1σ), while the seasonal modulation above Kitt Peak amounts to 64.6 ± 0.1 % showing a similar amplitude with the IASI measurements [*Razavi et al.*, 2011] for subtropical regions.

The IMAGESv2 model estimates a seasonal modulation of methanol in phase with the one we measured, but underestimates the peak-to-peak amplitude with 88.6 ± 1.3 % and 70.4 ± 1.2 % for "IASI" and "MEGAN" respectively. The MEGAN emission fluxes are dependent on temperature, visible ration fluxes, leaf area index and leaf age, and they show a pronounced seasonal variation at mid-latitudes, with peak values in early summer. The IASI-derived emissions peak somewhat earlier than in the MEGAN inventory, a result consistent with modelling studies using TES methanol data [*Cady-Pereira et al.*, 2012; *Wells et al.*, 2012] as well as with other studies based on in situ concentration measurements [*Jacob*, 2005] or on flux measurements [*Laffineur et al.*, 2012], which showed substantially higher methanol emission rates by young leaves compared to mature or senescent leaves.

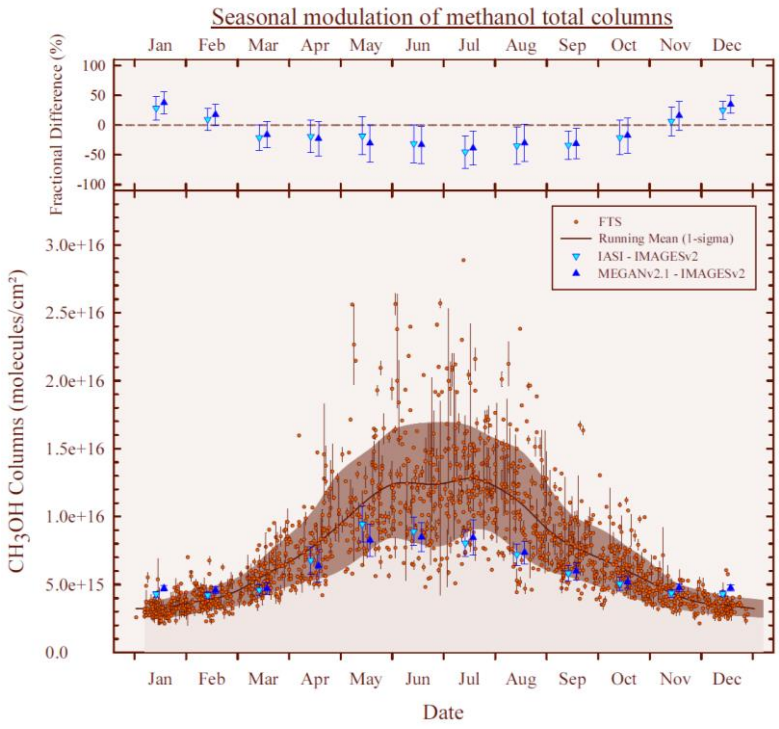

Figure 4.4. Seasonal modulation of methanol total columns. Dots with vertical lines represent the daily mean total columns over a 1-year time base and their associated standard deviation. The brown curve corresponds to a running mean fit to all data points, with a 15-day step and a 2-month wide integration time. The area corresponds to the 1_ standard deviation associated to the running mean curve. Up and down blue triangles are the monthly means of the model IMAGESv2 simulations for MEGAN and IASI respectively. Upper frame shows monthly fractional difference between FTIR results and IMAGESv2 simulations.

No systematic bias is observed on the whole time series, but a seasonal bias is characterized (see Figure 4.4): the maximum fractional difference {(IMAGES - FTIR) / [(IMAGES + FTIR) / 2]} between monthly mean results from FTIR measurements and both "IASI" and "MEGAN" simulations is found to occur in July, with -45 ± 27 % and -39 ± 28 %, respectively. The minimum fractional difference amounts to 28 ± 20 % and 38 ± 19 % respectively in January and shows an overestimation of methanol during wintertime by the IMAGESv2 model. The underestimation of methanol by the "IASI" simulation during summertime is unexpected, since this simulation reproduced very well the methanol total columns measured by IASI over Western Europe [Figure 5 in *Stavrakou et al.*, 2011]. Noting that ISSJ does not sample the lower troposphere below 3.58 km altitude, this discrepancy might reflect an overestimation of the simulated vertical gradient of methanol mixing ratios at continental mid-latitudes, which is suggested by comparisons with aircraft campaigns in spring and summer over the United States [*Stavrakou et al.*, 2011]. It is not clear, however, why this issue does not also lead to a similar model underestimation of the methanol column above ISSJ in spring. The overestimated gradient in IMAGES may be due to a well-known problem in chemical transport models, i.e. the overestimation of the hydroxyl radical concentration in the Northern Hemisphere [*Krol and Lelieveld*, 2003]. It could also be related to the large uncertainties in the ocean/atmosphere flux of methanol, given that even the sign of this flux is not well constrained [*Millet et al.*, 2008], and since IASI data were not considered sufficiently reliable over the ocean in the optimization of emissions using IMAGES by *Stavrakou et al.* [2011].

4.2.4.4. Methanol diurnal variation

The variation of the methanol abundance throughout the day has also been characterized on Figure 4.5. To this end, we extended the targeted range of solar zenith angle (SZA) going from 30° to 85° and selected only those whose retrieval provided a DOFS of at least 1. Due to the large seasonal variation, we divided our measurements into three subsets corresponding to summer (June, July, August), winter Figure 4.5. Methanol diurnal variation. Total columns versus the solar zenith angle for winter, summer and the rest of the year. Blue lines represent linear regressions and their corresponding standard deviation (1σ). (December, January, February) and the rest of the year. Even though we found no significant trend of methanol through the day in summer, a significant increase during winter and the rest of the year has been evaluated at 0.4 ± 0.3 and 1.1 ± 0.2 %.degree^{-1} in the morning. For the afternoon, the corresponding rates amount to -0.9 ± 0.2 and -0.5 ± 0.1 %.degree^{-1}, showing significant decreases. A rough approximation of those trends gives an increase of approximately 5.5 ± 10^{13} and 2.7 ± 10^{14} molecules cm^{-2}.h^{-1} in the morning and to a decrease of -1.6x10^{14} and -1.9x10^{14} molecules cm^{-2}.h^{-1} in the afternoon for winter and the rest of the year, respectively.

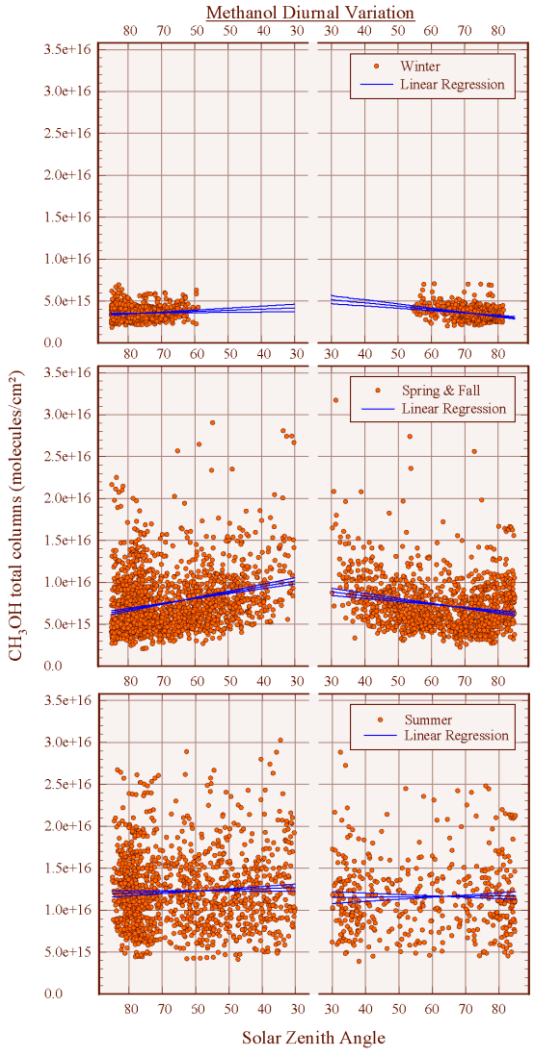

Figure 4.5. Methanol diurnal variation. Total columns versus the solar zenith angle for winter, summer and the rest of the year. Blue lines represent linear regressions and their corresponding standard deviation (1σ).

The causes for the observed diurnal variation are not clear. Major methanol sources such as biogenic production by living plants and photochemical production are stronger during daytime, due to the key role played by solar radiation in photosynthesis and other biotic processes, as well as in the generation of OH radicals through photolytic processes [*Logan et al.*, 1981]. However, these sources are expected to peak during the summer, when the diurnal variation of the column is found to be negligible. Since the photochemical sink of methanol (i.e. reaction with OH) is strongest during the day, the observed diurnal variation (and absence thereof during summer) could result from the variable balance between sources and sinks. However, OH fields, produced by the GEOS-CHEM model [*Bey et al.*, 2001] have been examined and no direct correlation with our methanol total columns has been found. Moreover, since the IMAGES model includes those processes but still fails to reproduce the observed diurnal variation, it appears likely that other factors play a significant role, e.g. orography-induced wind patterns bringing boundary layer air to the free troposphere above the station's altitude. Besides model simulations, in situ measurements have also been explored. However, the existing data sets being "campaign-type", the statistics are too weak to draw clear conclusions on this subject. More efforts should be put in further research on processes governing the methanol diurnal variation.

4.2.4.5. Methanol in the lower troposphere

In Figure 4.6, our lower tropospheric columns show a seasonal modulation with characteristics close to the seasonal variation of total columns with similar occurrence of maximum and minimum but a wider peak-to-peak amplitude of 168 ± 3 %. The upper panel of Figure 4.6 also shows monthly fractional differences between the FTIR results and both simulations from the IMAGESv2 model [*Stavrakou et al.*, 2011] as well as seasonal differences with in situ measurements performed at the Jungfraujoch [*Legreid et al.*, 2008].

Neither of the IMAGESv2 series stands out, since they both underestimate the peak-to-peak amplitude with 78 ± 2 % and 101 ± 2 % for MEGAN and IASI, respectively. For both series, methanol is overestimated in winter (DJF) and shows a good agreement in spring (MAM) as well as in October and November. During summertime, results during July are significantly underestimated but the difference for the remaining 3 months (June, August and September) is close to non-significant.

The seasonal amplitude shows a good agreement on the data dispersion (see error bars) except for the autumn season with more compact values. The high standard deviation in summer appears to be due to only a few days with high methanol mixing ratios. These days are characterized by trajectories originating from the south, where biogenic sources are more active. Indeed, it has been established by *Legreid et al.* [2008], that there is a considerable contribution of methanol from the south since methanol is emitted in large amounts from biogenic sources [*Singh et al.*, 1994; *Jacob*, 2002, 2005; *Fall*, 2003] more active in the south of the Alps than in the north. Furthermore, air masses from the south are transported over Northern Italy, which is a highly industrialized area with considerable anthropogenic emissions.

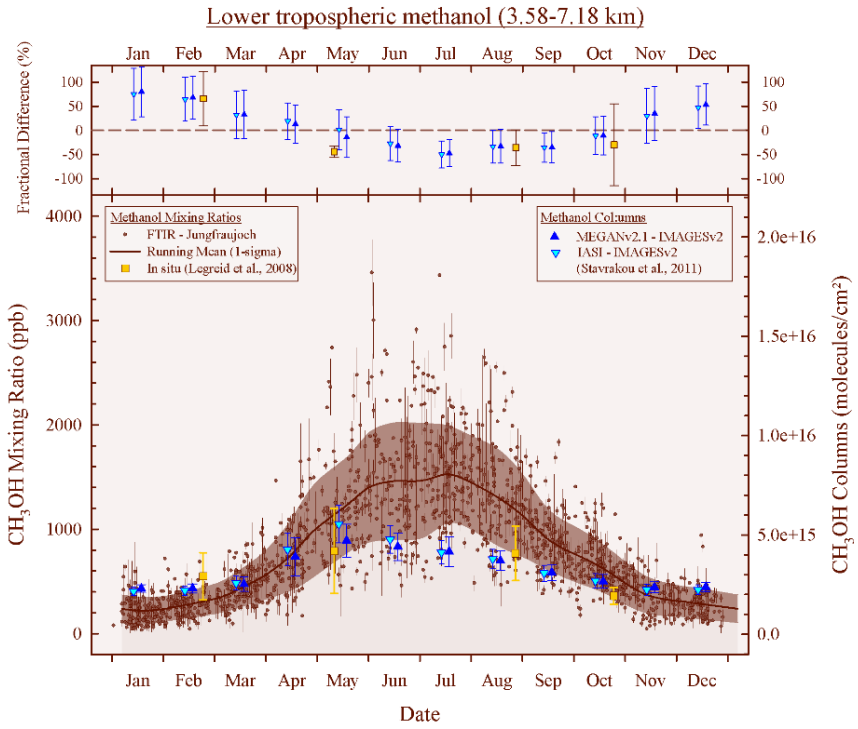

Figure 4.6. Lower-tropospheric methanol (3.58–7.18 km). Dots with vertical lines represent the daily mean lower-tropospheric columns over a 1-year time base and their associated standard deviation. The brown curve corresponds to a running mean fit to all data points, with a 15-day step and a 2-month wide integration time. The area corresponds to the 1σ standard deviation associated to the running mean curve. Up and down blue triangles are monthly means of the model IMAGESv2 simulations for MEGAN and IASI respectively [*Stavrakou et al.*, 2011]. *Yellow squares are seasonal means of methanol in situ measurements* [*Legreid et al.*, 2008]. *The upper panel shows monthly fractional difference between the FTIR results and IMAGESv2 simulations and seasonal fraction difference with in situ measurements.*

4.2.4.6. Methanol in the upper troposphere–lower stratosphere (UTLS)

The comparison between the UTLS FTIR columns, both IMAGES data sets and monthly mean results from ACE-FTS occultations illustrated in Figure 4.7 shows an overall agreement within the estimated uncertainties. As for total and lower-tropospheric columns, methanol variability is underestimated by the IMAGESv2 model. On the other hand, the seasonal cycle of methanol UTLS columns is satisfactorily characterized by FTIR results and the IMAGES simulations in terms of absolute value with a non-significant mean fractional difference with FTIR of -6 ± 49 % and 1 ± 48 %, respectively for MEGAN and IASI. The peak-to-peak amplitudes of the three series, i.e. 93 ± 2 % for FTIR, 82 ± 2 % for MEGAN and 92 ± 2 % for IASI are in very good agreement as well as the timing of the maximum (June–July).

A close to statistical agreement is observed between Jungfraujoch results and the UTLS columns derived from ACE-FTS data with a mean fractional difference of 33 ± 30 % despite substantially higher ACE methanol columns in March and May. The differences for these 2 months may be attributed to the fact that the monthly mean results from ACE-FTS encompass a 10° latitudinal band and therefore occultations may be capturing local events such as plumes from biomass burning out of range for the Jungfraujoch station.

Biases in the ACE methanol retrievals have recently been addressed by [*Harrison et al.*, 2012]. Adoption of a new set of infrared absorption cross sections for methanol led to the determination of ACE UTLS columns higher by up to 25 % [calculations based two occultations; see Figure 4.6 of Harrison et al., 2012], depending on the temperature of the measurement. Therefore, by applying those new cross sections to our Jungfraujoch retrievals, we would likely identify a bias in the same range, depending on the season and thus the vertical temperature distribution. The effect on total (and partial) columns will have to be evaluated on the basis of larger statistics for each season and using the new cross sections of *Harrison et al.* [2012].

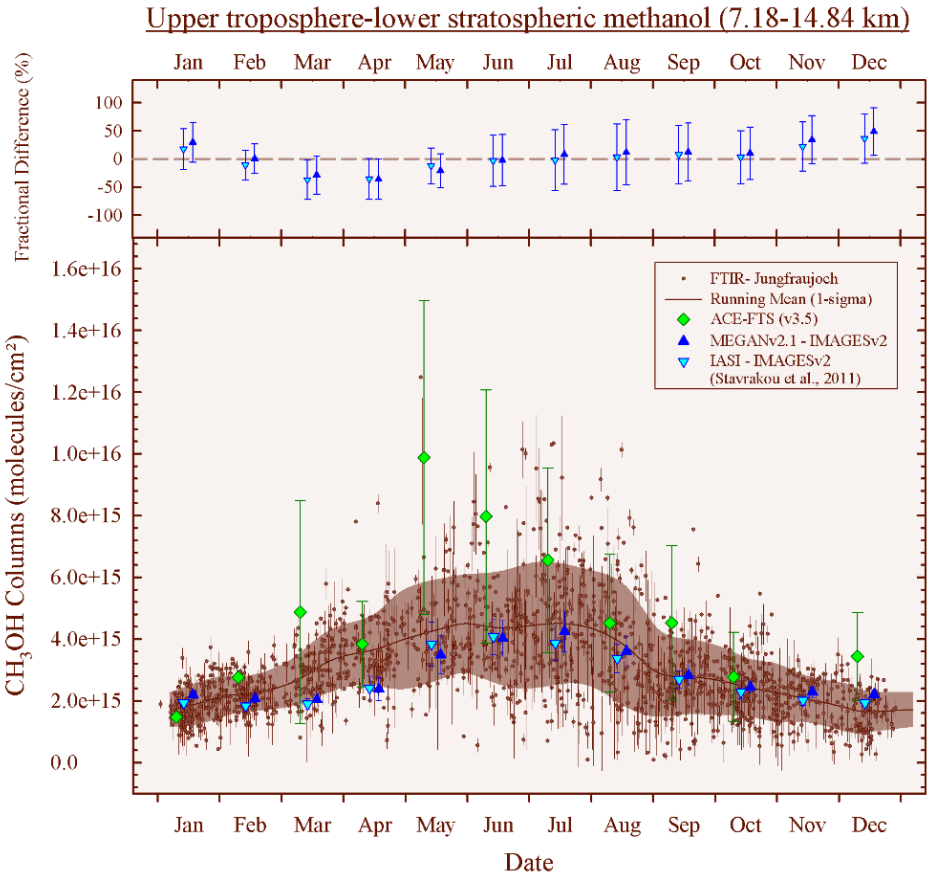

Figure 4.7. Upper troposphere–lower stratospheric methanol (7.18–14.84 km). Dots with vertical lines representing daily mean lower-tropospheric columns over a 1-year time base and their associated standard deviation. The brown curve corresponds to a running mean fit to all data points, with a 15-day step and a 2-month wide integration time. The area corresponds to the 1σ standard deviation associated to the running mean curve. Up and down blue triangles are the monthly means of the model IMAGESv2 simulations for MEGAN and IASI respectively (Stavrakou et al., 2011). Green diamonds are the monthly means of methanol retrieved from ACE-FTS occultations with the error bars representing the standard deviation (2σ). Upper frame show monthly fractional difference between FTIR results and IMAGESv2 simulations and ACE-FTS results.

4.2.5. Conclusions

A long-term time series of methanol has been determined from the analysis of a 17-year time series of infrared solar absorption spectra recorded with a commercial Fourier transform spectrometer Bruker IFS120HR, operated at the high-altitude International Scientific Station of the Jungfraujoch [ISSJ, Swiss Alps, 45° N, 8.0° E, 3580 m a.s.l.; *Zander et al.*, 2008] providing a valuable tool for model and satellite validation and complementing the NDACC measurements at northern mid-latitudes.

The results were analyzed using the SFIT-2 v3.91 fitting algorithm and thanks to the combination of spectral windows used in previous studies for the retrieval of methanol from FTS spectra [*Dufour et al.*, 2007; *Rinsland et al.*, 2009; *Vigouroux et al.*, 2012], we have significantly improved the information content. With a typical DOFS of 1.82, a total column and two partial columns time series are available, i.e. a lower-tropospheric (LT, 3.58-7.18 km) and an upper tropospheric– lower stratospheric one (UTLS, 7.18-14.84 km). Both random and systematic error sources have been identified and characterized using the spectra recorded in the year 2010, and are found to be respectively 5 and 7 % for the total column.

The analysis of the time series does not reveal a significant long-term trend but shows a high peak-to-peak amplitude of the seasonal cycle of 129.4 ± 5.5 % (1σ) for total columns. Methanol total and partial columns are characterized by a strong seasonal modulation with minimum values and variability in December to February and maximum columns in June–July. First analysis of methanol diurnal variation shows an increase of methanol in the morning and a decrease during the afternoon for all seasons but summer.

Comparisons with methanol measurements obtained with other techniques (in situ and satellite) give satisfactory results. The FTIR lower tropospheric data compared to in situ measurements generally shows a good agreement regarding the data dispersion. Concerning the UTLS partial columns, there is a close to statistical agreement with ACE-FTS occultations despite higher ACE columns of methanol in March and May.

The IMAGESv2 simulations underestimate the peak-to-peak amplitude for total and lower-tropospheric columns. Despite the absence of a systematic bias between our results and the IMAGESv2 simulations, comparisons show seasonal differences with an overestimation of winter methanol and an underestimation during summertime, which might be explained by an overestimation of the vertical gradient of methanol mixing ratios by the model. Regarding UTLS columns, the peak-to-peak amplitude and timing of the maximum (June–July) in both IMAGESv2 simulations are in very good agreement with the FTIR results.

Even though the role of plant growth in methanol budget is confirmed by its seasonality, large uncertainties remain in the methanol budget. Thanks to the improvement of the information content of our retrieval and therefore our vertical resolution, our partial column time series should contribute to better constraints for model simulations and therefore may lead to a better understanding of methanol budget.

Chapter 5 – Ethane

Chapter 5 − Ethane

5.1. Introduction

Through this work, I contributed to *Franco et al.*, [2015a] by developing and optimizing the strategy for inversion of ethane from FTIR observations recorded at the Jungfraujoch station. The development of the retrieval strategy includes the testing of 110 retrieval strategies in order to evaluate the best combination of parameters (see Table 5.0). By combining 3 micro-windows for the first time for Jungfraujoch and by including improved spectroscopic parameters such as C_2H_6 pseudo-lines [*Harrison et al.*, 2010] and updated line parameters for methyl chloride [*Bray et al.*, 2011, 2012] and ozone, we achieved a mean DOFS of 2.11 ± 0.27 which represents a significant improvement compared to previous works carried out at ISSJ, with typical DOFS of about 1.5. Selection of the best retrieval strategy has been performed on the basis of minimum residuals, maximum DOFS and realistic retrieved profiles (i.e. no ungeophysical negative mixing ratio values). Finer and careful comparisons of eigenvectors and eigenvalues have been performed when simple residuals/DOFS analysis was not sufficient to select among the tested strategies.

Parameter	Number of tests
Windows limits and combination	7
Windows, interfering species to retrieve	18
Spectroscopic linelist	25
Signal-to-noise ratio for inversion	10
C_2H_6 a priori distribution	9
Water vapor	5
Total	**74**

Table 5.0. Overview of tests performed for the optimization of the methanol retrieval strategy for Jungfraujoch.

The limits of each window have been refined based on previous work [*Mahieu et al.*, 1997; *Notholt et al.*, 1997; *Rinsland et al.*, 2000; *Zhao*, 2002; *Meier et al.*, 2004; *Gardiner et al.*, 2008; *Paton-Walsh et al.*, 2010; *Angelbratt et al.*, 2011; *Vigouroux et al.*, 2012] and the combination of those three windows has been tested for the first time for Jungfraujoch observations. Moreover, careful identification of interfering species that contribute to the absorption spectrum has been performed. We settled to five interfering species including CH_3Cl, O_3, CH_4, H_2O, and C_2H_6 as illustrated in Figure 5.0.1.

Improved spectroscopic parameters have been included in our retrieval strategy and the impact of each set of spectroscopic parameters on residuals has been quantified for each window individually and for each combination of window through this paper (see Figure 5.2).

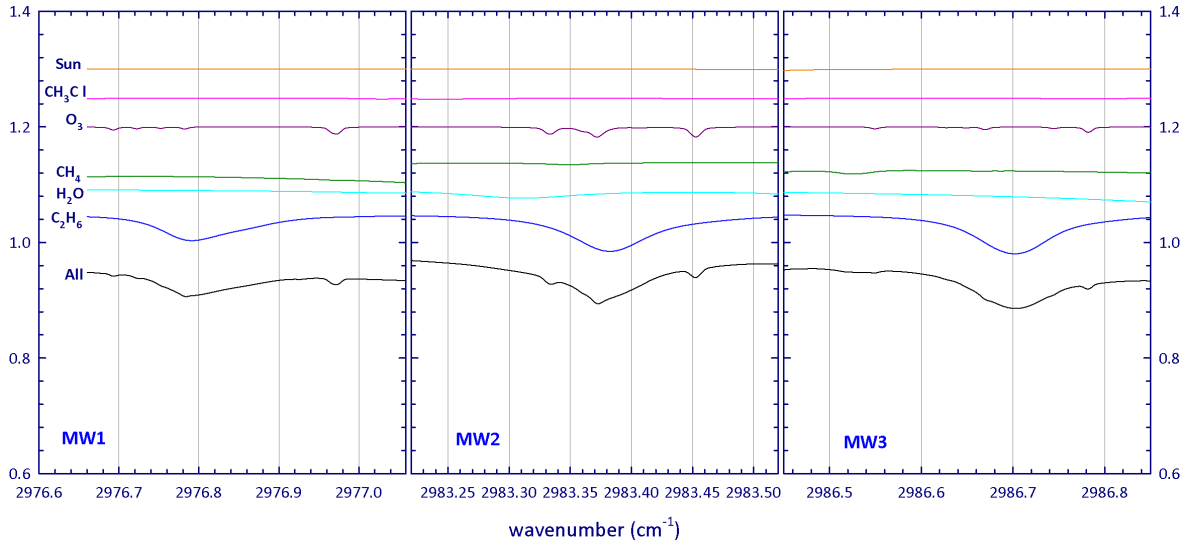

Figure 5.0.1. Simulation for Jungfraujoch, 60° zenith angle, 6.1 mK. For the three windows, we display the synthetic spectra for individual contributors (see color codes). HITRAN 2008 and averaged mixing ratio profiles based on the WACCM model climatology have been used for the simulations. For clarity, the contributions of each species have been vertically shifted.

Numerous a priori vertical distribution built from satellite observations, in situ GCMS surface measurements and CTMs and interpolated on the layering scheme adopted for Jungfraujoch retrievals were tested. They included a zonal mean (for the 41−51°N latitude band) of 771 occultations recorded by the ACE-FTS instrument [*Bernath et al.*, 2005] between the 2nd of November in 2004 and the 8th of February in 2011 extending from 8.5 to 20 km with an extension down to 3.58 km based on EMEP in situ gas chromatography surface measurements at the Rigi station (47.07 °N, 8.45 °E, 1031 m a.s.l., at a distance of 68 km from the Jungfraujoch station) and an upper extension up to 100 km from the WACCM model climatology [*Chang et al.*, 2008]. Simulations from CTMs to build a priori ethane vertical distribution included:

− simulations over the 1980–2020 time period from WACCMv5 and WACCMv6 climatology,
− daily mean C_2H_6 profiles over the 2007−2009 time period from the CHASER model [*Sudo*, 2002],
− hourly C_2H_6 profiles over the year 2005 from a Norwegian CTM developed at the university of Oslo [version 2 and version 3; *Berntsen and Isaksen*, 1997],
− daily mean C_2H_6 profiles over the 2007-2009 time period from the GEOS-Chem model [*Bey et al.*, 2001].

From careful analysis of retrieved profiles in addition to analysis of residuals, information content, and vertical sensitivity, we selected the use of a priori issued from the model CHASER in the framework of an optimized retrieval strategy of ethane for Jungfraujoch as presented in the next section. However, it has been determined that to ensure consistency between FTIR NDACC measurement stations, we will opt for a scaled version of the latest WACCM simulation (i.e. version 6) for a priori distribution of ethane for each site. The scaling factor applied to the WACCM profile will be determined from the CHASER simulation depending on the considered station.

Other parameters have been examined and included in the retrieval strategy such as the signal-to-noise ratio for inversion. Moreover, the pre-fitting of water vapor profiles has been considered in order to provide pre-adjusted water vapor profiles to the actual retrieval strategy. Indeed, water vapor captures 78.9, 78.3 and 78.03 % of the IR radiation in the MW1, MW2 and MW3 windows respectively and need to be carefully considered. However, the pre-adjustment of water vapor profiles has been discarded since it did not provide satisfactory improvement of residuals and information content while it considerably increased computing time. The situation is however not as favorable for low-altitude and/or humid NDACC sites which will likely have to include this pre-fit.

5.2. Retrieval of ethane from ground-based FTIR solar spectra using improved spectroscopy: recent burden increase above Jungfraujoch

B. Franco[1], F., W. Bader[1], G. C. Toon[2], C. Bray[3], A. Perrin[4], E. V. Fischer[5], K. Sudo[6,7], C. D. Boone[8], B. Bovy[1], B. Lejeune[1], C. Servais[1], E. Mahieu[1]

[1] Institute of Astrophysics and Geophysics, University of Liège, B -4000 Liège (Sart-Tilman), Belgium
[2] Jet Propulsion Laboratory, California Institute of Technology, Pasadena California, 91109, USA
[3] CEA, DEN, DPC, F-91191 Gif-sur-Yvette, France
[4] Laboratoire Interuniversitaire des Systèmes Atmosphériques (LISA-UMR7583) CNRS, Universités Paris Est Créteil and Paris Diderot (IPSL), F-94010 Créteil cedex, France
[5] Department of Atmospheric Science, Colorado State University, Fort Collins, CO USA
[6] Graduate School of Environmental Studies, Nagoya University, Nagoya, Japan
[7] Department of Environmental Geochemical Cycle Research, Japan Agency for Marine-Earth Science and Technology, Yokohama, Japan
[8] Department of Chemistry, University of Waterloo, Ontario, Canada

Received: 11 December 2014 − Received in revised form: 12 March 2015 − Accepted: 13 March 2015
Published in Journal of Quantitative Spectroscopy & Radiative Transfer: 20 March 2015

Edited by: L. Rothman

Abstract

An improved spectroscopy is used to implement and optimize the retrieval strategy of ethane (C_2H_6) from ground-based Fourier Transform Infrared (FTIR) solar spectra recorded at the high-altitude station of Jungfraujoch (Swiss Alps, 46.5°N, 8.0°E, 3580 m a.s.l.). The improved spectroscopic parameters include C_2H_6 pseudo-lines in the 2720−3100 cm^{-1} range and updated line parameters for methyl chloride and ozone. These improved spectroscopic parameters allow for substantial reduction of the fitting residuals as well as enhanced information content. They also contribute to limiting oscillations responsible for ungeophysical negative mixing ratio profiles. This strategy has been successfully applied to the Jungfraujoch solar spectra available from 1994 onwards. The resulting time series is compared with C_2H_6 total columns simulated by the state-of-the-art chemical transport model GEOS-Chem. Despite very

consistent seasonal cycles between both data sets, a negative systematic bias relative to the FTIR observations suggests that C_2H_6 emissions are underestimated in the current inventories implemented in GEOS-Chem. Finally, C_2H_6 trends are derived from the FTIR time series, revealing a statistically significant sharp increase of the C_2H_6 burden in the remote atmosphere above Jungfraujoch since 2009. Evaluating cause of this change in the C_2H_6 burden, which may be related to the recent massive growth of shale gas exploitation in North America, is of primary importance for atmospheric composition and air quality in the Northern Hemisphere.

5.2.1. Introduction

Ethane (C_2H_6) is the most abundant non-methane hydrocarbon in the Earth's atmosphere with a lifetime of approximately months [*Rudolph*, 1995]. On a global scale, the main sources of C_2H_6 are leakage from the production, transport of natural gas loss (62 %), biofuel consumption (20 %) and biomass burning (18 %), mainly located in the Northern Hemisphere [*Logan et al.*, 1981; *Rudolph*, 1995; *Xiao et al.*, 2008]. Biogenic and oceanic sources are generally very small [*Rudolph*, 1995]. The main sink of C_2H_6 in the troposphere is oxidation via reaction with hydroxyl radicals (OH), while in the stratosphere reaction with chlorine atoms dominates [*Aikin et al.*, 1982].

Ethane has a large impact on tropospheric composition and impacts the distribution of ozone (O_3) through several pathways, making it a compound of great interest as a sensitive indicator of tropospheric pollution and transport [*Rinsland et al.*, 2002]. By acting as a major sink for tropospheric OH, the abundance of C_2H_6 impacts the lifetime of methane (CH_4). Thus C_2H_6 is an indirect greenhouse gas with a net global warming potential of 5.5 [100 year horizon; *Collins et al.*, 2002]. Similarly, C_2H_6 influences the atmospheric content of carbon monoxide [CO; *Aikin et al.*, 1982]. Ethane also has a significant impact on air quality as it is an important source of peroxyacetyl nitrate (PAN), a thermally unstable reservoir for nitrogen oxide radicals [NO_x; *Rudolph*, 1995; *Fischer et al.*, 2014]. By providing the main NO_x source in many regions of the atmosphere, PAN has a major effect on the production and loss of O_3.

Atmospheric C_2H_6 abundances can be measured using various techniques. Previous measurements of C_2H_6 include Fourier Transform InfraRed (FTIR) spectrometer observations by the balloon-borne Jet Propulsion Laboratory MkIV Interferometer [*Toon*, 1991], aircraft air samples collected during the NASA's Global Tropospheric Experiment Field Missions Pacific Exploratory Mission [e.g., PEM-West A; *Blake et al.*, 1996 and TRACE-A; *Fishman et al.*, 1996; *Chatfield et al.*, 1998], solar occultations recorded by the Atmospheric Chemistry Experiment-Fourier Transform Spectrometer [ACE-FTS; *Rinsland*, 2005], ground-based measurements by gas chromatograph [e.g.: *Browell*, 2003; *Swanson*, 2003; *Wingenter et al.*, 2005] and finally limb-scans performed by the Michelson Interferometer for Passive Atmospheric Sounding (MIPAS) onboard the European ENVIronmental SATellite [ENVISAT; *Glatthor, N. et al.*, 2009]. Analysis of these data records has significantly increased our understanding of the long range transport of C_2H_6.

Ethane has also been measured by ground-based FTIR technique at several latitudes in both hemispheres, covering different time periods [e.g.: *Rinsland, C. P. et al.*, 1998; *Rinsland et al.*, 1999, 2000, 2002; *Zhao*, 2002; *Gardiner et al.*, 2008; *Angelbratt et al.*, 2011; *Vigouroux et al.*, 2012; *Viatte et al.*, 2014].

Nevertheless, strong latitudinal, seasonal and local fluctuations on small spatial and temporal scales make C_2H_6 secular trend determination difficult from the existing observations. Indeed, its concentration in the atmosphere is largely influenced by strong vertical mixing and dilution with background air during transport from emission sources.

In this paper, we present a 20-year long-term time series of C_2H_6 derived from ground based high-resolution infrared solar spectra recorded with a Bruker 120HR FTIR spectrometer operated under clear sky conditions at the high-altitude International Scientific Station of the Jungfraujoch [referred to below as ISSJ; Swiss Alps, 46.5°N, 8.0°E, 3580m a.s.l.; *Zander et al.*, 2008]. Such a long-term time series in the remote atmosphere allows for air quality monitoring and provides a valuable tool for model and satellite validation. The solar spectra used here have been recorded within the framework of the Network for Detection of Atmospheric Composition Change monitoring activities (NDACC; see http://www.ndacc.org).

This work furthers the C_2H_6 dataset previously published in *Rinsland et al.*, [2000] and *Mahieu et al.*, [1997] for the ISSJ station and it presents an improved retrieval strategy in terms of reduced residuals and enhanced information content, combining three spectral domains for the first time at ISSJ. A careful selection of the available spectroscopic datasets is performed in order to minimize the fitting residuals. A thorough discussion of the retrieval strategy and data characterization (information content and error budget) is presented here along with trend analysis and preliminary comparison with the three-dimensional state-of-the-art global chemical transport model (CTM) GEOS-Chem.

This paper is organized as follows. A detailed description of the optimized retrieval strategy is given in Section 5.2.2. Section 5.2.3 reports the characterization of the FTIR geophysical products and provides a detailed error budget. Supporting model simulations are described in Section 5.2.4. Section 5.2.5 presents a preliminary comparison between FTIR and GEOS-Chem seasonal cycles of the C_2H_6 burden above Jungfraujoch as well as the entire 1994−2014 time series of daily-mean total columns and corresponding trends. Section 5.2.6 concludes this study with a short summary and discussions of the results, identifying avenues for future work.

5.2.2. FTIR data set

5.2.2.1. Instrumental setup

All the spectra analyzed here have been recorded at ISSJ, located in the Swiss Alps at 3580m altitude on the saddle between the Jungfrau (4158m a.s.l.) and the Mönch (4107m a.s.l.) summits. This station offers excellent conditions to perform solar observations, particularly in the infrared, because of weak local pollution (no major industries within 20 km) and very high dryness thanks to the high-altitude and the presence of the Aletsch Glacier. Indeed, the amount of water vapor (H_2O), a strong interference in the infrared, is at least twenty times lower than at sea level. Due to these factors, the ISSJ station allows for investigating the atmospheric background conditions over central Europe and the mixing of air masses from planetary boundary layer and free troposphere [e.g.: *Zellweger et al.*, 2003; *Reimann*, 2004].

Here we use observations performed with a commercial Bruker IFS-120HR instrument [*Zander et al.*, 2008]. This spectrometer, affiliated to the NDACC network since 1991, is equipped with HgCdTe and InSb cooled detectors covering the 650-4500 cm^{-1} region of the electromagnetic spectrum.

The Bruker observational database investigated in the present study consists of more than 11 500 spectra recorded between September 1994 and August 2014 with an optical filter covering the 2400 to 3100 cm^{-1} range encompassing the perpendicular v7 fundamental stretching band of C_2H_6. Spectral resolutions, defined as the reciprocal of twice the maximum optical path difference, alternate between 0.004 and 0.006 cm^{-1}. The signal-to-noise (S/N) ratio varies between 300 and 4500 (average spectra resulting from several successive individual Bruker scans, when solar zenith angles vary slowly). The optimization of the retrieval strategy has been based on a subset of about 600 spectra during 2003.

5.2.2.2. Retrieval strategy

The C_2H_6 column retrievals and profile inversions have been performed using the SFIT-2 v3.91 fitting algorithm. This retrieval code has been specifically developed to derive mixing ratio profiles of atmospheric species from ground-based FTIR spectra [*Rinsland, C. P. et al.*, 1998]. It is based on the semi-empirical implementation of the Optimal Estimation Method (OEM) developed as in [*Rodgers*, 1990]. Vertical profiles are derived from simultaneous fits to one or more spectral intervals of at least one solar spectrum with a multilayer, line-by-line calculation that assumes a Voigt line shape [*Drayson*, 1976].

For the first time at ISSJ, C_2H_6 retrievals have been carried out using three micro windows simultaneously (see Table 5.1). The first micro-window (MW1) is centered on the well-known strong and sharp $^PQ_3$ sub-branch of the perpendicular v7 fundamental stretching band [*Pine and Rinsland*, 1999] and extends from 2976.660 to 2977.059 cm^{-1}. This $^PQ_3$-MW1 is the only one taken into account previously for the Jungfraujoch station [*Mahieu et al.*, 1997; *Rinsland et al.*, 2000] and at many other FTIR sites [e.g.: *Zhao*, 2002; *Gardiner et al.*, 2008; *Paton-Walsh et al.*, 2010; *Angelbratt et al.*, 2011]. The second micro-window (MW2) includes the $^PQ_1$ sub-branch around 2983.3 cm^{-1}, as suggested in [*Meier et al.*, 2004] and used in [*Vigouroux et al.*, 2012] in combination with MW1, and extends from 2983.200 to 2983.500 cm^{-1}. Finally, a third micro-window (MW3) encompasses the $^RQ_0$ C_2H_6 sub-branch around 2986.7 cm^{-1}, extending from 2986.450 to 2986.850 cm^{-1}. The MW3 has only been fitted at dry high-latitude sites [*Notholt et al.*, 1997; *Viatte et al.*, 2014] because of strong H_2O interferences. Within these micro-windows, the major interfering species whose vertical profiles are scaled during the retrieval process are CH_4, H_2O, O_3 and methyl chloride (CH_3Cl).

Micro-windows (cm^{-1})	Interfering species
2976.660–2977.059	H_2O, O_3, CH_3Cl, CH_4
2983.200–2983.500	H_2O, O_3, CH_3Cl, CH_4
2986.450–2986.850	H_2O, O_3, CH_3Cl, CH_4

Table 5.1. List of the micro-windows used for the FTIR retrieval of C_2H_6 at Jungfraujoch and the interfering species taken into account. Simple scaling of the corresponding vertical profiles of the interfering species is allowed throughout the iterative retrieval process.

The model atmosphere adopted above the altitude of the ISSJ station consists of a 39-layer scheme extending from 3.58 km up to 100 km with progressively increasing thicknesses. The pressure-temperature profiles are provided by the National Centers for Environmental Prediction (NCEP, Washington DC, USA, http://www.ncep.noaa.gov/) while the solar line compilation supplied by [*Hase et al.*, 2006] has been assumed for the non-telluric absorptions.

The C_2H_6 a priori mixing ratio profile corresponds to a mean of a 2007−2009 CHASER [Chemical AGCM for Study of atmospheric Environment and Radiative forcing; *Sudo*, 2002] simulation (Figure 5.1.a; see Sect. 5.2.4.1). A priori profiles for all interfering molecules are based on the 1980−2020 simulation of the WACCM model [version of WACCM profiles; the Whole Atmosphere Community Climate Model; e.g., *Chang et al.*, 2008] for the ISSJ station.

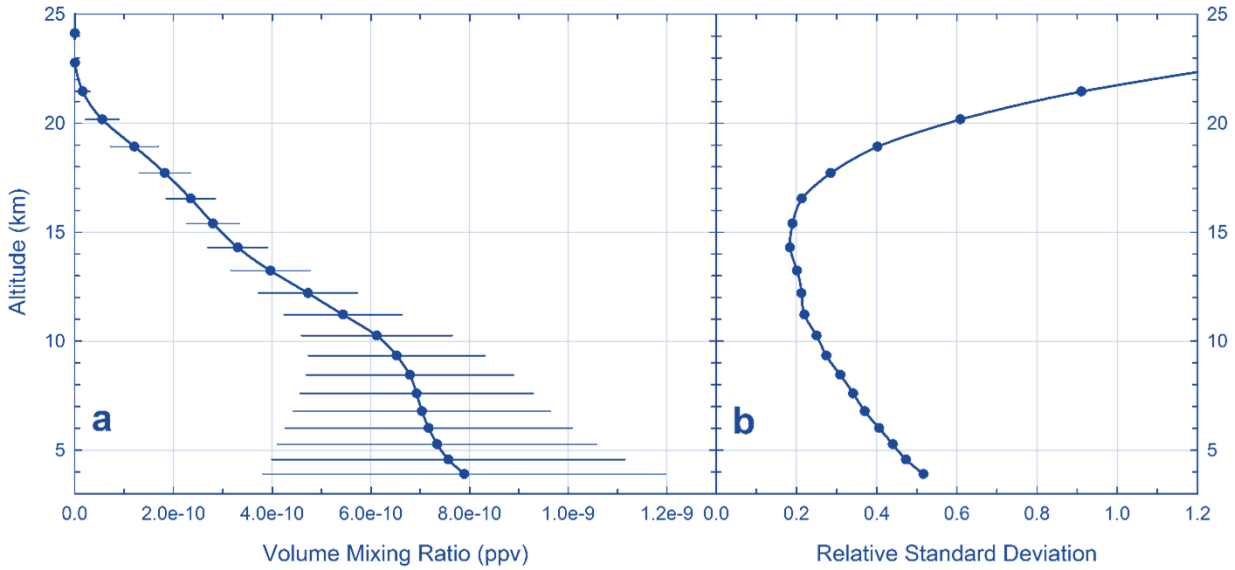

Figure 5.1. (a) C_2H_6 a prioriprofilewith1-σ standard deviation derived from a 2007–2009 CHASER simulation used for the FTIR retrievals at Jungfraujoch. (b) Averaged relative standard deviation of C_2H_6 VMR derived from the same CHASER simulation and used as diagonal elements of the covariance matrix for the FTIR retrievals.

In a usual OEM, the covariance matrix should reject the natural variability of the target gas profile [*Rodgers*, 2003]. It is specified for each layer as a percentage of the a priori profile and an ad hoc correlation length, which is interpreted as a correlation between layers decaying along a Gaussian. For C_2H_6, we have adopted the relative standard deviation profile derived from the CHASER results (Figure 5.1b) as the diagonal values of the covariance matrix and a Gaussian inter-layer correlation with a half-width length of km for extra diagonal elements of the covariance matrix.

It is worth noting that this C_2H_6 retrieval strategy has been optimized in such a way to limit the fraction of retrieved profiles presenting negative mixing ratios. By setting up an inter-layer correlation of 4 km and the S/N ratio for inversion at 300, the retrieved information content at Jungfraujoch is slightly constrained deliberately but the retrieval process is stabilized and strong oscillations in the lower levels of the retrieved

profiles are avoided. This way, less than 9 % of solar spectra have been rejected because of ungeophysical retrieved mixing ratio values. Moreover, statistics have shown that there is no correlation between the seasonality and the fraction of rejected solar spectra. Hence we ensure here homogeneous data coverage and sampling throughout the entire time series (see Section 5.2.5.2).

5.2.2.3. Spectroscopy

Ethane has a complicated spectrum with 12 interacting normal vibration modes, which makes it difficult to accurately predict the spectrum. Therefore, it is essential to take a closer look at the spectroscopic parameters. First C_2H_6 line parameters go back to the work of *Pine and Lafferty*, [1981] with the assignment of C_2H_6 transitions but no ^PQ-branches were included. In 1987, to support the Atmospheric Trace Molecule Spectroscopy Experiment (ATMOS), an empirical linelist for the strongest ^PQ-branches of C_2H_6 covering the 2973−3001 cm^{-1} region was developed [*Brown et al.*, 1987]. Pacific North West National Laboratory (PNNL, Washington, USA, http://nwir.pnl.gov) measured C_2H_6 cross-sections from 700 to 6500 cm^{-1} at a 0.1 cm^{-1} resolution while a quantum mechanically based linelist for the $^PQ_3$ branch at 2976 cm^{-1} was developed [*Pine and Rinsland*, 1999] and included in the HITRAN 2004 database [*Rothman et al.*, 2005]. The latest HITRAN C_2H_6 update (July 2007) contains Pine and Rinsland $^PQ_3$ branch as well as Brown's empirical linelist for the other ^PQ-branches but still lacks information for weaker absorptions features.

Quantum-mechanical analysis of the C_2H_6 spectrum remains very difficult and is still lacking, except for the $^PQ_3$ branch. The current state of C_2H_6 parameters in HITRAN 2004 and HITRAN 2008 [*Rothman et al.*, 2009] is rather unsatisfactory in the 3 µm region for all spectral features other than the $^PQ_3$ branch. A new set of C_2H_6 cross-sections was therefore developed [*Harrison et al.*, 2010], based on new high resolution IR spectra recorded with and without additional synthetic air at the Rutherford Appleton Laboratory Molecular Spectroscopy Facility (RAL, UK, http://www.stfc.ac.uk/ralspace/) using a high resolution FTIR spectrometer. These cross sections for C_2H_6 have been measured in the 3 µm spectral region and calibrated in intensity by using low resolution spectra from the PNNL IR database as a reference. Finally, [*Lattanzi et al.*, 2011] published a linelist including an improved representation of P- and R-branch lines of C_2H_6. However, based on the quality of fits to Harrison's lab spectra, it has been evaluated that the Q-branch features which we use for our retrieval strategy are poorly represented compared to HITRAN 2008, (evaluation of this linelist can be found at http://mark4sun.jpl.nasa.gov/report/Evaluation of Lattanzi C_2H_6 linelist.pdf).

In 2011, an empirical pseudo-line-list (PLL) was fitted to Harrison's C_2H_6 lab spectra (the PLL and description can be found at http://mark4sun.jpl.nasa.gov/pseudo.html). The PLL generally provides a convenient and accurate way of interpolating/extrapolating in temperature and pressure to conditions not covered by lab measurements (Harrison's measurements in the case of this study for C_2H_6). In the present work, these pseudo-lines have been combined and tested with three versions of HITRAN (i.e. 2004, 2008 and 2012; [*Rothman et al.*, 2005, 2009, 2013]).

As the 2950–3020 cm^{-1} region encompasses absorption features from many atmospheric gases, the related spectroscopic parameters need to be as complete and accurate as possible in order to best simulate the atmospheric spectra. To this end, in addition to the C_2H_6 PLL, two updates have been included in our linelist. The first one consists of an update for three O_3 lines (encompassed in MW1) provided by P. Chelin (Laboratoire de Physique Moléculaire pour l'Atmosphère et l'Astrophysique, Paris, France, Personal Communication, 2004) in the framework of the UFTIR (Time series of Upper Free Troposphere observations from a European ground-based FTIR network) project. The second update concerns the CH_3Cl line positions and line intensities for the ν_1, ν_4 and $3\nu_6$ CH_3Cl bands in the 3.4 µm region [*Bray et al.*, 2011, 2012]. Fourier transform spectra have been recorded at high resolution at the Laboratoire de Dynamique, Interactions et Réactivité in France. Measurements of line positions and line intensities have been performed for both isotopologues $^{12}CH_3{}^{35}Cl$ and $^{12}CH_3{}^{37}Cl$ in the ν_1, ν_4, $3\nu_6$ bands and line intensities have been compared to the recent 174 integrated intensities from PNNL.

Spectroscopic parameters	RMS (%)			Mean column
	MW1	MW2	MW3	(x 10^{16} molec.cm^{-2})
HITRAN 2004	0.2118	0.2974	0.5213	1.08
HITRAN 2004 + C_2H_6 PLL	0.1905	0.2283	0.1626	1.00
HITRAN 2004 + C_2H_6 PLL + O_3	0.1406	0.2283	0.1648	0.99
HITRAN 2004 + C_2H_6 PLL + O_3 + CH_3Cl	0.1158	0.2357	0.1410	1.01
HITRAN 2008	0.4705	0.1772	0.5200	1.03
HITRAN 2008 + C_2H_6 PLL	0.1329	0.1332	0.1627	0.97
HITRAN 2008 + C_2H_6 PLL + O_3	0.1316	0.1331	0.1623	0.98
HITRAN 2008 + C_2H_6 PLL + O_3 + CH_3Cl	0.1067	0.1179	0.1379	0.99
HITRAN 2012 + C_2H_6 PLL + O_3	0.1230	0.2151	0.1657	0.96

Table 5.2. Root mean square (RMS) residuals of the calculated spectra relative to observations (in %) for each micro-window when fitting are presentative subset of 229 solar spectra from the year 2003 and using different combinations of spectroscopic parameters (see first column). These residuals are displayed in Figure 5.2 for the HITRAN 2008 compilation and updates. Note that HITRAN 2004 includes the August 2006 updates and that the CH_3Cl update tested here is already part of the original HITRAN 2012 release. The averages of the resulting column values (x 10^{16} molec.cm^{-2}) are listed in the last column. A typical and representative standard deviation of 25 % is associated with these mean columns.

Table 5.2 summarizes the residuals (relative to observations) and mean retrieved columns associated with the use of the HITRAN 2004 [including the August 2006 updates; e.g., *Esposito et al.*, 2007], 2008 and 2012 compilations with the different spectroscopic improvements mentioned above. Note that the CH_3Cl update tested here is already part of the original HITRAN 2012 release. These tests have been performed on a subset of 229 representative solar spectra from the year 2003. Figure 5.2 displays mean observed and calculated spectra as well as residuals, and illustrates the improvement of residuals brought by each update compared to the initial HITRAN 2008 database. By comparing residuals for each micro-window, we can evaluate the major contributions brought by the C_2H_6 PLL and O_3 updates (Figure 5.2.b) compared to

the original HITRAN 2008 parameters (Figure 5.2.a). Finally, Figure 5.2.c shows a refinement of residuals on the edges of MW1 and MW3 due to the use of the CH_3Cl update. From Table 5.2 it appears that HITRAN 2008 along with the three updates minimizes the residuals in all micro-windows and hence is currently the best spectroscopic database to employ for ISSJ solar spectra. It is worth noting that the increased residuals observed with the HITRAN 2012 compilation compared to the set up using HITRAN 2008, especially in MW2 (see Table 5.2), are due to changes in H_2O parameters, more particularly in temperature and pressure-dependency parameters of the H_2O feature at 2983.316 cm^{-1}.

5.2.3. Data characterization and error budget

5.2.3.1. Characterization of the FTIR retrievals

The averaging kernel matrix (**A**) is resulted by the inversion process of FTIR solar spectra and characterizes the information content of the retrievals. It describes how the retrieved concentration and vertical distribution of an absorber in the atmosphere are related to the true profile (x_t) and also provides the contribution of the a priori (x_a) to the retrieved profile (x_r) according to Equation 5.1.

$$x_r = x_a + \boldsymbol{A}(x_t - x_a) \tag{5.1}$$

Figure 5.3 displays the mean averaging kernels for each vertical layer (Figure 5.3.b; expressed in molec.cm^{-2}/molec.cm^{-2}) and calculated on the basis of the 2008−2010 individual retrieved profiles, as well as the leading eigenvalues and eigenvectors (Figure 5.3.a). The vertical sensitivity of our retrieval strategy is illustrated by the total column averaging kernel drawn in black dashed line in Figure 5.3.b (here with values divided by 10 for visibility purpose). It indicates very good sensitivity to the true state of the atmosphere below ~13 km altitude, with 99 % of the information content independent from the a priori profile (x_a) and mainly provided by the first eigenvector. The second and third eigenvectors and their associated eigenvalues indicate that the sensitivity of the retrievals extends in the lower stratosphere up to ~20 km, with some additional vertical resolution.

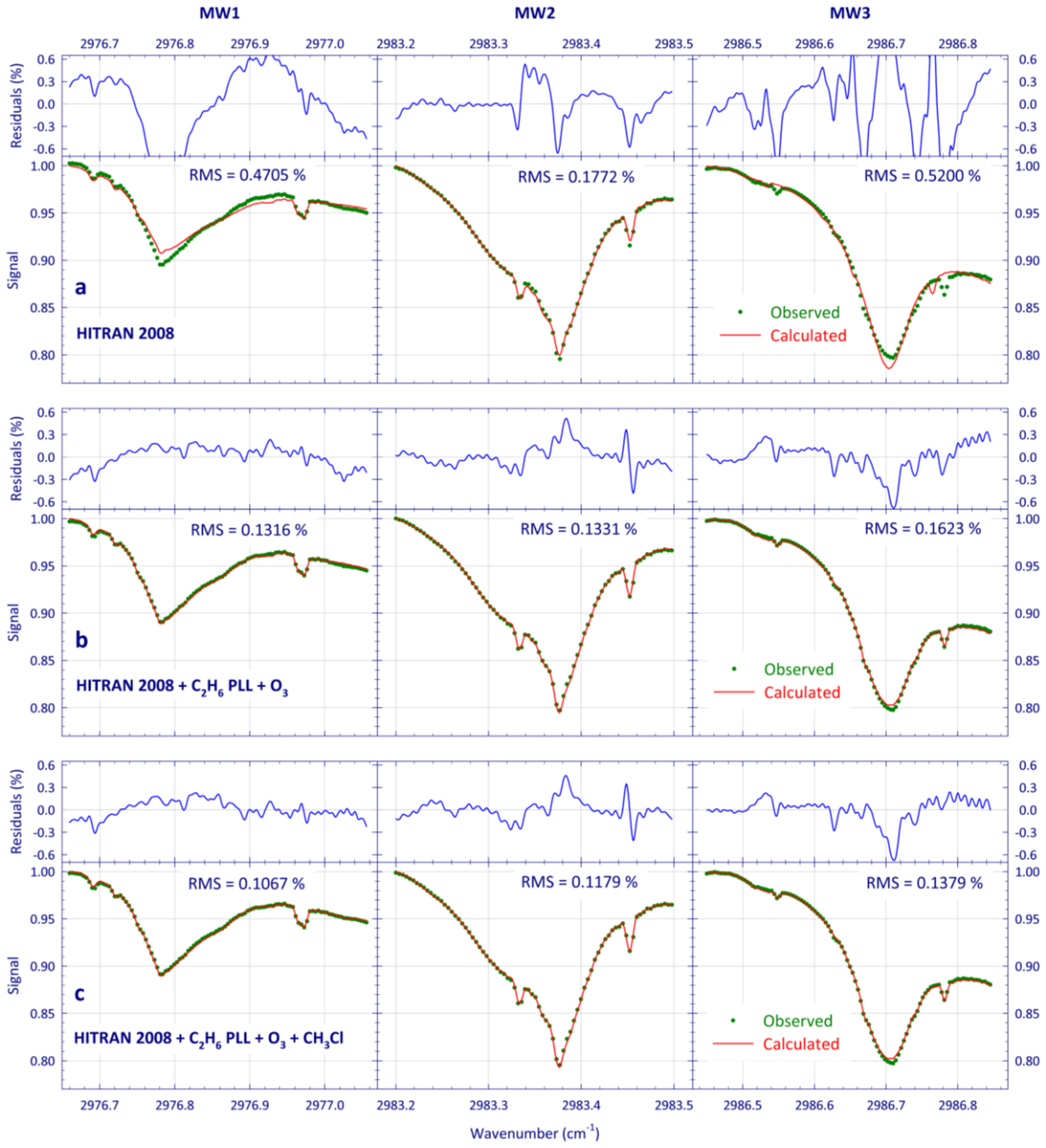

Figure 5.2 Mean observed (green dots) and calculated (red lines) spectra and associated residuals (obs. – calc.; blue lines) for a representative subset of 229 spectral fits with in the three micro-windows used for the C_2H_6 retrieval at ISSJ. Spectroscopic compilations used here are (a) the original HITRAN 2008 database, (b) HITRAN 2008 combined with the C_2H_6 PLL as well as O_3 update and (c) HITRAN 2008 combined with C_2H_6, O_3 and updated CH_3Cl lines. Note the improvements brought by the different updates on the residuals, whose mean values are provided in Table 5.2.

With a mean degree of freedom for signal (DOFS) of 2.11 ± 0.27 (1-σ confidence interval calculated over all 2008–2010 fitted spectra) and the two leading eigenvalues equal to 0.99 and 0.86, two independent pieces of information may be deduced from the averaging kernels. A first partial column is derived in the lower troposphere (from the ISSJ elevation up to ~8.5 km altitude) and a second one spanning the 8.5–22 km altitude range is identified in the upper troposphere lower stratosphere. The sensitivity of our

retrieval strategy is slightly diminishing for altitudes above ~13 km, but a large part of the information content (at least 60 %) is still provided by the measurements at the 22 km level. Although independent partial columns are available from the retrieval process at ISSJ, we will only consider total columns of C_2H_6 in this study.

When compared with other recent works using pseudo-lines to retrieve C_2H_6 amounts, the content of information obtained from our retrievals is consistent with results from e.g., [*Viatte et al.*, 2014] at Eureka, Canada (80.0°N, 86.4°W, 610 m a.s.l.; DOFS = 2.00 ± 0.20) who also employed the three micro-windows, and represents a significant improvement compared to previous works carried out at ISSJ, with typical DOFS of about 1.5 when using the $^PQ_3$ feature alone. The simultaneous use of the three non-contiguous micro-windows allows for a significant gain in retrieved information content compared to three non-simultaneous retrievals which would be subsequently averaged. The DOFS obtained from the individual use of each micro-window are 1.51 ± 0.24, 1.86 ± 0.25 and 1.70 ± 0.23 for MW1, MW2 and MW3, respectively.

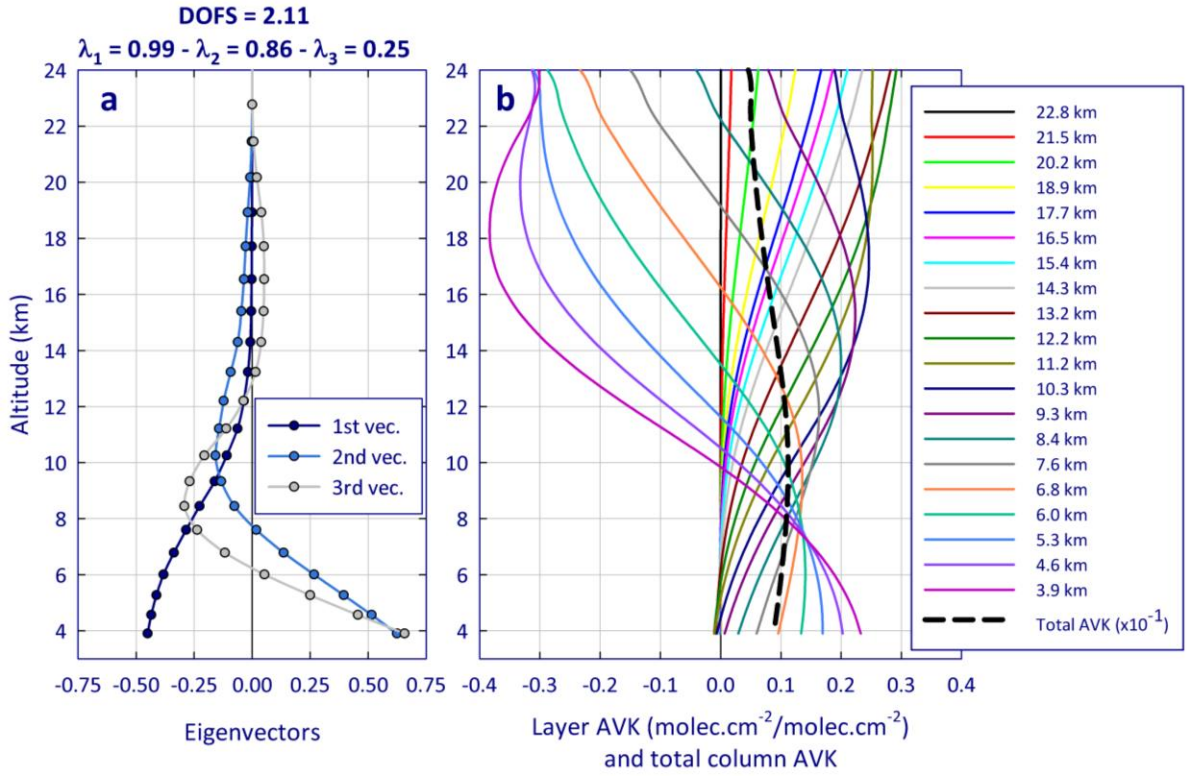

Figure 5.3. (a) First eigenvectors and associated eigenvalues, and (b) individual averaging kernels for each layer between the 3.6 and 24.0 km altitude range and total column averaging kernel (thick dashed line; divided here by 10 for visibility purpose) characterizing the FTIR retrievals of C_2H_6 at ISSJ. The information content has been established on the basis of all the individual retrieved profiles throughout the 2008–2010 timespan. The averaging kernels from 2008–2010 are used in Section 5.2.5.1 to smooth GEOS-Chem profiles in comparison with the FTIR products. Moreover, tests have shown that the DOFS, eigenvectors and averaging kernels calculated on the basis of other years provide consistent results in terms of information content.

5.2.3.2. Error budget

Table 5.3 summarizes the major sources of uncertainty that may affect the C_2H_6 columns retrieved from the ISSJ solar spectra, as well as estimates of their respective contribution to either systematic or random component of the error budget. The total errors are the square root of the sum of the squares of each of the contributing uncertainty sources. Most of the error contributions (excepting when specified below) have been calculated on the basis of all solar spectra from year 2003 according to the sensitivity tests listed in the last column of Table 5.3. The C_2H_6 retrieval is also characterized at ISSJ by an assumed variability of 29.2 % and a daily relative standard deviation (calculated here for the days with at least three observations) equal to 4.0 %.

The major contribution to the systematic component of the error budget comes from uncertainties on the C_2H_6 spectroscopy. An error of 4 % on the line intensity from the original spectra measurements has been reported in *Harrison et al.*, [2010]. In addition, the uncertainty induced by the conversion of C_2H_6 cross-sections into pseudo-lines is estimated at 4 % [*Rinsland et al.*, 2012], including the random error in the pseudo-line spectroscopic parameters and the systematic error due to an imperfect representation of the physics by the pseudo-lines. We have combined the 4 % from *Harrison et al.*, [2010] in quadrature with the 4 % from the conversion into pseudo-lines, giving a conservative 246 uncertainty of 5.6 % on the C_2H_6 absorption. When assuming this uncertainty during the inversion process, the retrieved C_2H_6 columns are affected by systematic anomalies of 5.6 %.

Retrieved column biases due to line intensity uncertainties related to the interfering species have been gauged independently by assuming the maximum errors quoted in the HITRAN 2008 (for H_2O, CH_4 and O3) and HITRAN 2012 (for the CH_3Cl updated line parameters, included in this official release) databases during the fitting process. The column anomalies corresponding to each interfering gases have been combined in quadrature and contribute for 0.9 % to the systematic component of the error budget.

Other contributions to the total systematic error are minor. The total columns are retrieved from high quality solar spectra using the SFIT algorithm within uncertainties estimated at ±1 % [*Hase et al.*, 2004]. The impact of an assumed instrumental misalignment of ±10 % at the maximum path difference on the retrieved columns is almost negligible (0.1 %). Finally, the impact of the selection of the a priori C_2H_6 state on the retrieved columns is estimated by adopting other realistic C_2H_6 mixing ratio profiles simulated by the GEOS-Chem and WACCM models as a priori, which leads to small divergences by up to 1.2 %.

As random errors, we have assumed a 0.2°error in the solar pointing and have adopted the temperature-profile uncertainties quoted by NCEP (±1.5 °C between the ground and 20 km altitude, ±2.0 °C for the 20-30 km altitude range, and from ±5 °C at 35 km up to ±9 °C at the stratopause). The corresponding biases on the retrieved C_2H_6 columns amount to 0.8 and 1.3 %, respectively. As in *Franco et al.*, [2015], we have also made the tropospheric slope of the H2O a priori profile vary by a factor 2; such perturbations only induce 0.1 % bias in the C_2H_6 columns, highlighting the independence of the C_2H_6 retrieval to the tropospheric water vapor content for a dry high-altitude site.

Error source	Error (%)	Comments
Assumed variability	29.2	
Relative standard deviation	4.0	For the days with at least 3 observations
Systematic errors		
C_2H_6 spectroscopy and conversion into pseudo-lines	5.6	± 5.6% uncertainty on line intensity
Line intensity of interfering gases	0.9	HITRAN 2008 uncertainties (up to 10% for H_2O, 20 % for O_3, 30 % for CH_4 and 20 % for CH_3Cl)
ILS	0.1	± 10% misalignment and instrument bias
Forward model	1.0	Retrieval algorithm-related
C_2H_6 a priori profile	1.2	C_2H_6 a priori profiles derived from GEOS-Chem and WACCM
Total Systematic Error	5.9	
Random errors		
Temperature profiles	1.3	NCEP profile uncertainty (see text)
H2O a priori profile	0.1	Changes by a factor of 2 in H2O a priori slope
Solar Zenith Angle(SZA)	0.8	± 0.2° bias
Measurement noise	1.6	
Smoothing	1.1	
Model parameters	0.2	
Total Random Error	2.4	

Table 5.3. Error budget of the C_2H_6 retrievals at ISSJ, including the impact of systematic and random uncertainties on total columns retrieved from all individual solar spectra recorded during the year 2003, according to specifics given in the last column. The contributions of measurement noise, smoothing and model parameters have been estimated on the basis of a representative subset of solar spectra following the formalism of Rodgers, [2000].

According to the formalism of *Rodgers* [2000] and such as detailed in Section 2.2.2 in *Vigouroux et al.*, [2009], we have computed the gain and sensitivity matrices of a subset of solar spectra representative of the ISSJ dataset in terms of S/N ratio, DOFS, solar zenith angle, residuals, etc., eventually providing the respective contributions of measurement noise (1.6 %), smoothing (1.1 %) and forward model parameters (0.2 %) to the total random error.

The estimated total systematic and random errors affecting our retrieved C_2H_6 columns amount to 5.9 and 2.4 %, respectively. The latter represents a significant improvement compared to *Rinsland et al.*, [2000], where only the 2976–2977 cm^{-1} micro-window with the $^PQ_3$ branch for inversion of the ISSJ solar spectra is used and where the random component of the error budget is estimated in a similar way at 6.6 % (and also found 5.9 % of total bias for the systematic component).

5.2.4. Supporting model simulations

5.2.4.1. CHASER

The CHASER model [*Sudo*, 2002; *Sudo and Akimoto*, 2007], developed mainly in the Nagoya University and the Japan Agency for Marine-Earth Science and Technology (JAMSTEC), is a chemistry coupled climate model, simulating atmospheric chemistry and aerosols in cooperation with the aerosol component model SPRINTARS [Spectral Radiation-Transport Model for Aerosol Species; *Takemura*, 2005]. It has also been developed in the framework of the Model for Interdisciplinary Research on Climate-Earth System Model, MIROC-ESM-CHEM [*Watanabe et al.*, 2011]. CHASER simulates detailed chemistry in the troposphere and stratosphere with an on-line aerosol simulation including production of particulate nitrate and secondary organic aerosols.

For this study, the model's horizontal resolution is selected to be 2.8°x 2.8°with 36 vertical layers extending from the surface up to about 50 km altitude. As the overall model structure, CHASER is fully coupled with the climate model core MIROC, permitting atmospheric constituents (both gases and aerosols) to interact radioactively and hydrologically with meteorological fields in the model. For replicating the past meteorological conditions in the model, this study employs a nudged chemical transport model version of CHASER in which wind fields and temperatures calculated by the MIROC's AGCM are relaxed to meteorological reanalysis data. In this study, the NCEP final reanalysis data set is used as a nudging constraint with the HadISST data set (Hadley Centre Sea Ice and Sea Surface Temperature) for distributions of sea surface temperatures and sea ice. Chemistry component of CHASER considers the chemical cycle of O_x-NO_x-HO_x-CH_4-CO with oxidation of Non-Methane Volatile Organic Compounds (NMVOCs), halogen chemistry and NH_x-SO_x-NO_3 system simulating 96 chemical species with 287 chemical reactions. In the model, NMVOCs include C_2H_6, C_2H_4, propane (C_3H_8), C_3H_6, C_4H_{10}, acetone, methanol and biogenic NMVOCs (isoprene, terpenes).

Anthropogenic emissions (for NO_x, CO, CH_4, NMVOCs, NH_3, SO_2, black carbon and organic carbon) are specified using the EDGAR-HTAP2 (Emission Database for Global Atmospheric Research, targeted for 2008: http://edgar.jrc.ec.europa.eu/) and fire emissions are based on the MACC's reanalysis data (Monitoring Atmospheric Composition & Change; https://gmes-atmosphere.eu/about/project structure/input_data/d_re/) for individual years/months. For biogenic NMVOC emissions, we employ calculation by the land ecosystem/trace gas emission model VISIT [Vegetation Integrative SImulator for Trace gases; *Ito*, 2010].

5.2.4.2. GEOS-Chem

GEOS-Chem (version 9-01-03: http://acmg.seas.harvard.edu/geos/doc/archive/man.v9-01-03/index.html) is a global 3-D CTM capable of simulating global trace gas and aerosol distributions. GEOS-Chem is driven by assimilated meteorological fields from the Goddard Earth Observing System version (GEOS-5) of the NASA Global Modeling Assimilation Office (GMAO). The GEOS-5 meteorology data have a temporal frequency of 6 h (3 h for mixing depths and surface properties) and are at a native horizontal resolution of 0.5°x 0.667°with 72 hybrid pressure-σ levels describing the atmosphere from the surface up to 0.01 hPa. In the framework of this study, the GEOS-5 fields are degraded for model input to

a 2°x 2.5°horizontal resolution and 47 vertical levels by collapsing levels above ~80 hPa. The chemical mechanism applied here is the standard full chemistry GEOS-Chem simulation, including detailed O_3-NO_x-Volatile Organic Compound (VOC)-aerosol coupled chemistry [see *Bey et al.*, 2001 and *Park et al.*, 2004 for full description] with updates by *Mao et al.*, [2010].

Ethane is emitted from anthropogenic and pyrogenic sources in GEOS-Chem. The RETRO (REanalysis of the TROpospheric chemical composition) emission inventory [*van het Bolscher et al.*, 2008] is the global default for anthropogenic NMVOC emissions aside from C_2H_6 and C_3H_8. Ethane and C_3H_8 emissions in RETRO are low compared to the GEOS-Chem inventories from *Xiao et al.*, [2008], which are unbiased relative to the pre-2004 observations presented as in *Xiao et al.*, [2008]. Thus we used the C_2H_6 and C_3H_8 emission inventories from *Xiao et al.*, [2008]. Ethane emissions from biomass burning are from the Global Fire Emissions Database (GFED3) monthly biomass burning emissions [*van der Werf et al.*, 2010].

The GEOS-Chem model output presented here covers the period July 2005 May 2013, for which the GEOS-5 meteorological fields are available. We have used a one-year run for spin-up from July 2004 to June 2005, restarted several times for chemical initialization. The model outputs consist of C_2H_6 mixing ratio profiles at a three-hour time frequency, saved at the closest 2°± 2.5°pixel of the ISSJ station. To account for the vertical resolution and sensitivity of the FTIR retrievals, the individual concentration profiles simulated by GEOS-Chem are interpolated onto the vertical grid of FTIR. They are then averaged into daily profiles and eventually smoothed by applying the FTIR averaging kernels A (see Equation 5.1) according to the formalism of *Rodgers*, [2003]. The averaging kernels used to convolve the model outputs are seasonal averages over March-May, June-August, September-November and December-February obtained from the 2008−2010 individual FTIR retrievals. The following comparison between FTIR and smoothed GEOS-Chem data involves the days with observations available within the July 2005−May 2013 time period only (i.e. 915 days of observations).

5.2.5. Ethane time series

In this section, we first present a preliminary comparison between C_2H_6 FTIR total columns and simulations by the GEOS-Chem model by illustrating the seasonal cycle of C_2H_6 at ISSJ. We have taken into account the vertical resolution and specific sensitivity of the FTIR retrievals before comparison with the model data. We then report the entire 1994−2014 time series of daily-mean total columns and corresponding trends.

5.2.5.1. Seasonal cycle

The seasonal cycle of C_2H_6 abundances above ISSJ is illustrated in Figure 5.4, which displays on a one-year time base the monthly means of FTIR total columns and associated 1-σ standard deviation as error bars. The running mean of the FTIR daily average data (not shown here), computed using a two-month integration length and a 15-day time step, is drawn in solid blue line. The shaded area corresponds to the 1-σ standard deviation around the running mean. The FTIR data subset used in Figure 5.4 spans the July 2005−May 2013 time period in order to coincide with the GEOS-Chem simulation. A similar running mean and standard deviation have also been calculated on the basis of the daily-averaged total columns

simulated by GEOS-Chem (after smoothing by the FTIR averaging kernels). These are represented by the red curve and by the shaded area in Figure 5.4, respectively.

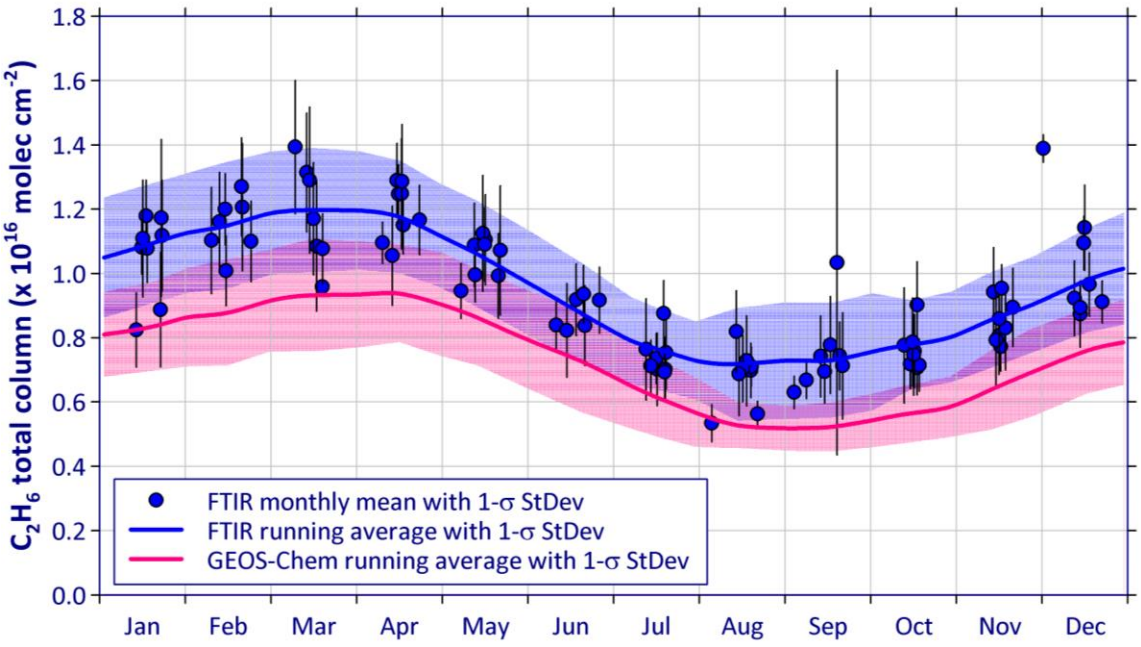

Figure 5.4. Monthly-averaged total columns of C_2H_6 and associated 1-σ standard deviation bars displayed on a 1-year time base, from the FTIR retrievals performed above ISSJ between July 2005 and May 2013. The blue curve and shaded area show on a 1-year time base the running mean fit to the daily-averaged columns (with a 2-month wide integration time and a 15-day time step) and the associated 1-σ standard deviation, respectively. The red line and shaded area represent corresponding information, but deduced from the smoothed GEOS-Chem output. Note that the 1-σ standard deviations around the running mean are calculated on the basis of the daily-averaged columns and hence include interannual fluctuations as well as variability of the monthly mean.

The seasonal cycle of C_2H_6 apparent in the FTIR total column data and model output are in good agreement, characterized by a maximum in March−April and a minimum in August−September. Since fossil fuel production is the main source of C_2H_6 emissions [*Xiao et al.*, 2008] and does not present a particular seasonal cycle during the year [*Pozzer et al.*, 2010], the strong seasonal cycle of C_2H_6 burden is primarily driven by the photochemical oxidation rate by OH radicals, which is enhanced during summer [*Schmidt et al.*, 1991; *Simpson et al.*, 2012]. At mid and high latitudes, C_2H_6 accumulates during wintertime and peaks in late winter due to its relatively long lifetime and slow exchange with lower latitudes [*Rinsland et al.*, 2000]. Consistent values of seasonal amplitude, i.e. the difference between the maximum and minimum running means divided by the annual average over the whole time period, are associated with these seasonal modulations: 50.4 % and 57.3 % for FTIR and GEOS-Chem, respectively. A direct comparison between the daily-mean C_2H_6 total columns derived from the CTM and ground-based observations is presented in Figure 5.5 and shows a correlation R of 0.77.

However, it appears clearly on Figures 5.4 and 5.5 that the C_2H_6 burden simulated by GEOS-Chem is systematically lower than the FTIR measurements. Over the mid-2005–mid-2013 time period, the daily-averaged modeled C_2H_6 columns present a systematic bias of -26.7 ± 16.5 % relative to the FTIR daily means, and the two data sets cannot be reconciled by accounting for the systematic errors affecting the observations (see Table 5.3). The systematic bias is hypothesized to be driven by an underestimation of the C_2H_6 emissions used by the model that were developed only considering data collected prior to 2004. Incorporating updated and more accurate emission inventories into GEOS-Chem is the focus of ongoing work and is beyond the scope of this paper.

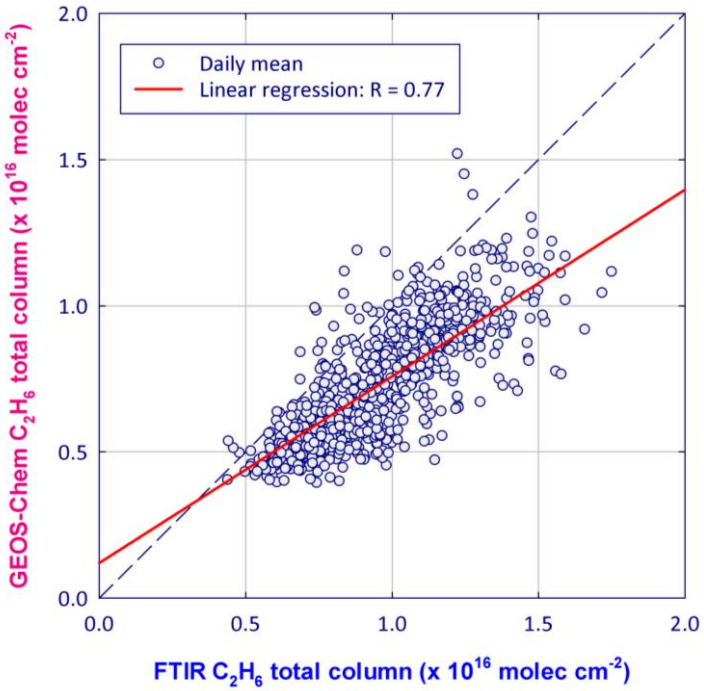

Figure 5.5. FTIR daily-averaged total columns of C_2H_6 versus daily-averaged C_2H_6 abundances derived from smoothed GEOS-Chem profiles over the July 2005–May 2013 time span. The straight red line corresponds to the linear regression (with R as the correlation coefficient) between both data sets.

The retrieved columns of C_2H_6 at ISSJ are consistent with ground-based FTIR measurements from other stations in terms of amounts and seasonal cycle, taking into account the latitude and elevation of the ISSJ station [*Rinsland et al.*, 2001, 2002; *Zhao*, 2002; *Gardiner et al.*, 2008; *Angelbratt et al.*, 2011; *Vigouroux et al.*, 2012; *Zeng et al.*, 2012; *Viatte et al.*, 2014]. At high altitude stations such as ISSJ, lower burden and seasonal amplitude are generally observed due to high concentrations of C_2H_6 in the lowest tropospheric layers [*Angelbratt et al.*, 2011]. For instance, monthly-mean columns ranging between 1.76 ± 0.40 and 3.36 ± 0.30 x 10^{16} molec.cm^{-2} and a corresponding seasonal amplitude of 63 % were obtained from ground-based FTIR solar spectra recorded over 1995-2000 at two Northern Hemisphere mid-latitude (44°N) stations located almost at sea level in Japan [*Zhao*, 2002]. The amplitude of the seasonal cycle is generally larger at high-latitude sites because of the enhanced fossil fuel emissions [*Zeng et al.*, 2012] and very weak oxidation rate by OH radicals in winter, allowing C_2H_6 to accumulate substantially during this season. At

Eureka, *Viatte et al.*, [2014] retrieved monthly-mean C_2H_6 columns between 1.2 and 2.85 x 10^{16} molec.cm^{-2} from FTIR observations for 2007−2011, and the amplitude of the seasonal cycle was 93 %.

5.2.5.2. Long-term trend

Figure 5.6 presents the long-term time series of daily-averaged C_2H_6 total columns (in molec.cm^{-2}) retrieved from the ISSJ solar spectra for the September 1994−August 2014 time period, which consists of 11 859 measurements spread over 2 224 days of observation. The error bars associated with these daily means correspond to the 1-σ standard deviation of the measurements within each day. This FTIR database homogeneously covers the investigated time span. We have used the statistical bootstrap resampling tool developed as in *Gardiner et al.*, [2008] to fit the whole daily time series in order to determine the C_2H_6 long-term linear trend (as well as the associated uncertainty) and the seasonal modulation. This bootstrap method combines a linear function and a 3rd order Fourier series taking into account the intra-annual variability of the data set.

Moreover, a running mean of the daily average data with a three-year wide integration time and a six-month step has revealed a minimum in the time series between the end of 2008 and the beginning of 2009. Therefore we have fitted both 1994−2008 and 2009−2014 time periods separately with the bootstrap tool that has returned two statistically-significant trends of C_2H_6 total columns at the 2-σ confidence level: - 9.56 ± 1.91 x 10^{13} molec.cm^{-2}.yr^{-1} and 4.35 ± 0.81 x 10^{14} molec.cm^{-2}.yr^{-1}, respectively. Then we have used both 1995.0 and 2009.0 columns modeled by the bootstrap tool as references in order to calculate the relative annual trends.

Analysis of the 1994−2008 time span reveals a regular decrease of the C_2H_6 amounts above ISSJ by -0.92 ± 0.18 %.yr^{-1} relative to 1995.0. This negative trend is consistent with measurements and corresponding trends of atmospheric C_2H_6 burden presented in *Simpson et al.*, [2012] and *Aydin et al.*, [2011], both studies attributed the decline of global C_2H_6 emissions from the mid-1980s to reduced fugitive emissions from fossil fuel sources in Northern Hemisphere rather than a decrease in biomass burning and biofuel use (the other major sources of C_2H_6). These fugitive emissions mainly include natural gas loss due to evaporation, venting and flaring as well as equipment leaks during the production and processing of natural gas and oil. Consistent trends derived from FTIR solar spectra have already been reported at ISSJ by previous studies, but over shorter time periods: - 2.70 ± 0.30 %.yr^{-1} over 1985−1995 [*Mahieu et al.*, 1997], - 1.20 ± 0.65 %.yr^{-1} over 1995−1999 [*Rinsland et al.*, 2000], -1.05 ± 0.35 %.yr^{-1} over 1995−2004 [*Gardiner et al.*, 2008] and - 1.51 ± 0.23 %.yr^{-1} over 1996−2006 [*Angelbratt et al.*, 2011]. Global C_2H_6 emissions did not decline as rapidly between 2000 and 2010 period compared to the 1980s and 1990s [*Aydin et al.*, 2011; *Simpson et al.*, 2012], and this is consistent with our reported negative trend, which is smaller than reported in previous ISSJ studies.

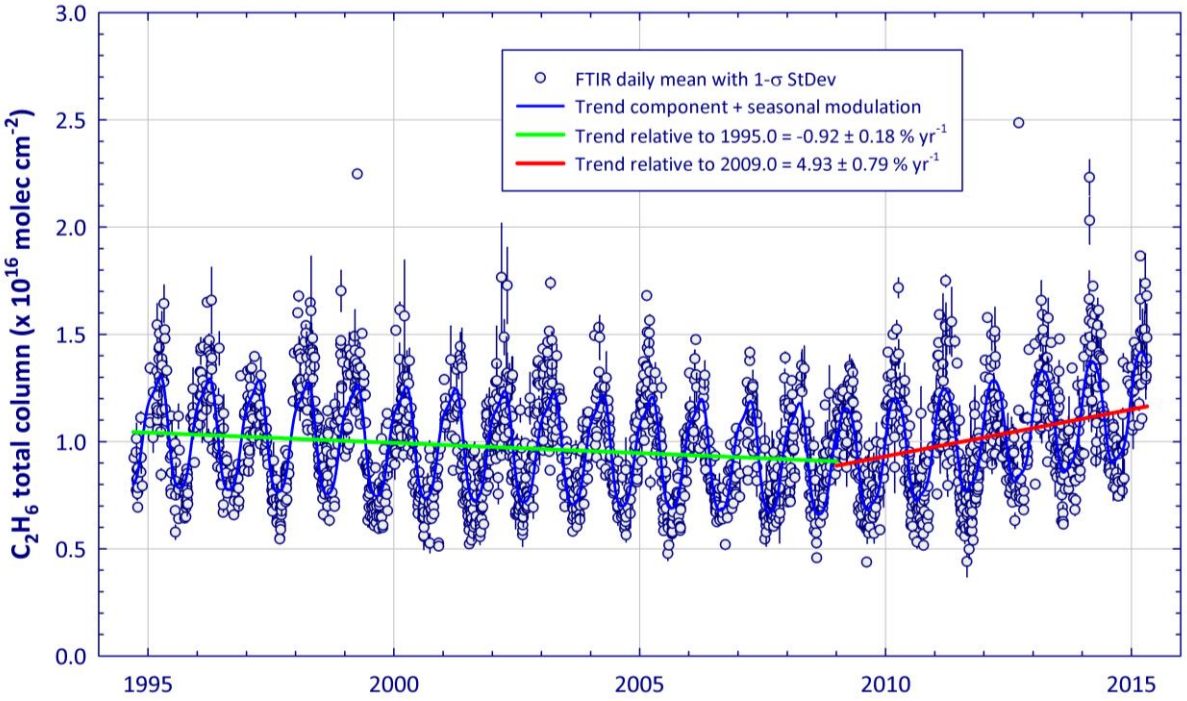

Figure 5.6. FTIR time series of daily-averaged C_2H_6 total columns and associated 1-σ standard deviation bars above ISSJ from September 1994 to August 2014. The functions fitted to all available daily means (including seasonal modulation and trend component) and calculated by the bootstrap resampling tool of [Gardiner et al., [2008] over the 1994–2008 and 2009–2014 time periods are drawn in blue curve. The green and red solid lines correspond to the trend components of these fitting functions.

Conversely, for the 2009−2014 time period, the bootstrap tool reveals a strong positive trend of C_2H_6 total columns of 4.90 ± 0.91 %.yr^{-1} relative to 2009.0 above ISSJ. We have also applied the bootstrap tool to the 3.58−8.88 and 8.88−22.10 km partial columns of C_2H_6 above ISSJ (see Section 5.2.3.1) and have found very similar positive trends relative to 2009.0, suggesting a vertically-homogeneous increase of C_2H_6 throughout the troposphere (and lower stratosphere). To our knowledge, this recent increase of the C_2H_6 burden in the background atmosphere has not been reported and its origin is still unidentified.

A hypothetical source may be enhanced fugitive emissions of C_2H_6 linked to the recent growth in the exploitation of shale gas and tight oil reservoirs. The growth has been especially massive in North America. Indeed, positive anomalies of CH_4 related to the oil and gas industries have been recently detected from space over regions of North America where the drilling productivity began to grow rapidly after 2009 (see [69]). This hypothesis is supported by measurements derived from 1 986 solar occultation observations performed over North America (16°−88°N and 173°−50°W) between 2004 and the middle of 2013 by the ACE-FTS instrument [*Bernath et al.*, 2005]. We employed the version 3.5 ACE-FTS data [*Boone et al.*, 2013], which includes an improved retrieval strategy for C_2H_6, within the 8−16 km altitude range. Applying the bootstrap tool to the ACE-FTS partial columns over the 2004-2008 and 2009-2013 time periods, we have calculated statistically-significant trends (at the 2-σ level) of - 1.75 ± 1.30 and 9.4 ± 3.2 %.yr^{-1} relative to 2005.0 and 2009.0, respectively, which are consistent with the FTIR trends when accounting for the associated uncertainty ranges. Trends derived from 906 ACE-FTS measurements between 10°−40°S do not

reveal any recent increase of the C_2H_6 burden. Instead these data show a statistically significant decrease (- 1.62 ± 1.08 %.yr^{-1}) over the 2004 to mid-2013 time period. This suggests that the observed increase of C_2H_6 is limited to the Northern Hemisphere.

It is worth noting that the GEOS-Chem CTM does not reproduce this recent increase in the abundance of C_2H_6 above ISSJ, suggesting emission inventories for C_2H_6 and other light alkanes may not be properly accounting for the enhanced fugitive emissions from recent natural gas and oil production.

5.2.6. Discussions and conclusions

In this study, we have developed and optimized a new strategy based on an improved spectroscopy to retrieve C_2H_6 total and partial columns from ground-based FTIR solar spectra recorded at the dry and high-altitude ISSJ. The selected spectroscopic parameters accounted for in the three micro-windows include C_2H_6 pseudo-lines based on cross-section laboratory spectra as well as updated line features for O_3 and CH_3Cl. Such an improved spectroscopy has yielded substantially reduced fitting residuals, enhanced information content (with a mean DOFS of 2.11 ± 0.27 for the whole data set) and less solar spectra discarded because of ungeophysical mixing ratio profiles.

We have applied this strategy to the long-term FTIR time series available at ISSJ (spanning 1994−2014) and compared the retrieved total columns to C_2H_6 columns simulated by the GEOS-Chem CTM, taking into account the vertical sensitivity of the retrievals by convolving the modeled profiles with the FTIR averaging kernels. The observations and the model present consistent seasonal cycles, but GEOS-Chem under-predicts the observed C_2H_6 burden throughout the seasonal cycle. This suggests an underestimation of C_2H_6 emissions in the model and points to the need for improved inventories for further GEOS-Chem simulations and sensitivity tests.

Finally, we have presented the 20-year ISSJ time series of C_2H_6 column abundance. Using a bootstrap resampling tool, we have calculated a statistically-significant negative trend in C_2H_6 total columns until 2009, consistent with prior studies and with our understanding of global C_2H_6 emissions. However, the ISSJ time series has also revealed a strong positive trend in C_2H_6 over the last years of the record, from 2009 onwards. Such a recent increase in the remote atmosphere is still unreported and, because of the involvement of C_2H_6 in the global VOC-HOx-NOx chemistry responsible for generating or destroying tropospheric O_3, investigating both its cause and its impact on air quality should be a high priority for the atmospheric chemistry community.

This C_2H_6 increase extends beyond previous positive short-term anomalies already observed in the Northern Hemisphere, which occur every 3−5 years and are generally associated with variability in biomass burning emissions [*Simpson et al.*, 2006, 2012]. The seasonal cycle of C_2H_6 above ISSJ is primarily driven by the photochemical cycle of its main sink (OH radicals). We argue that it is unlikely that the recent increase can be attributed to sharp fluctuations of OH concentration in the atmosphere because the global OH levels have not exhibited large interannual variability since the end of the 20th century [*Montzka et al.*, 2011]. Indeed, neither CO nor other species that have oxidation by OH as their major removal pathway

such as hydrogen cyanide (HCN) and acetylene (C_2H_2), do not present an upturn in their retrieved columns above ISSJ over the last years. However, CH_4, which is closely linked to C_2H_6 [*Simpson et al.*, 2006, 2012], has also presented globally a renewed rise after 2006 [*Kirschke et al.*, 2013]. We hypothesize that the observed recent increase in C_2H_6 above ISSJ could represent a change in C_2H_6 throughout the Northern Hemisphere and may be the product of a large increase in fugitive emissions related to the recent upturn in the development of North American shale gas and tight oil reservoirs.

The lifetime of C_2H_6 is approximately months, and this makes C_2H_6 influenced by vertical mixing and long-range transport. Ethane is therefore a convenient tracer of anthropogenic activity for remote sensing [*Schmidt et al.*, 1991]. Measurements of C_2H_6 in the remote troposphere can also be used to identify air masses that have originated in regions with significant oil and gas production [*Simpson et al.*, 2012]. Air masses impacted by intense episodes of biomass burning have already been detected in the retrieved C_2H_6 columns at ISSJ, associated with severe tropical emissions from Asia during the strong El Niño event of 1997−1998 [*Rinsland et al.*, 2000]. Our future work will focus on combining an analysis of C_2H_6 measurements from ground-based FTIR solar spectra and observations from ACE-FTS with dedicated GEOS-Chem simulations with updated inventories. The goal will be to identify the cause of the recent increase in C_2H_6 and evaluate the magnitude of emissions required to produce the observed changes.

5.3. Follow-up and ongoing work

Ongoing work carried out at GIRPAS is planned in two steps, first focused on North America and then on the global scale. The recent increase of C_2H_6 will be confirmed and quantified through the analysis of time series derived from FTIR observations at Northern American sites (e.g. Toronto, Boulder,…). This will allow verifying the hypothesis that massive shale gas exploitation in the US is responsible for the observed re-increase. Since best emission inventories currently available significantly underestimate the observed C_2H_6 burden, we need to investigate on better C_2H_6 emissions. The bottom-up approach will consist in evaluating the amount of C_2H_6 emitted to match the C_2H_6 upturn as observed by FTIR measurements while the top-down approach will assess a new emission inventory of C_2H_6 in North America, based on observations of methane from the Greenhouse Gases Observing Satellite [GOSAT, developed by the Japan Aerospace Exploration Agency, JAXA, *Kuze et al.*, 2009] and inferred using C_2H_6/CH_4 emission ratios.

The C_2H_6 re-increase will be characterized at a global level by achieving a multi-site study regrouping most ground-based FTIR observation sites (NDACC or non-affiliated that perform measurements since at least 2009). In an effort of producing harmonized C_2H_6 time series, the C_2H_6 retrieval strategy as developed and described in [*Franco et al.*, 2015a] with comments provided above will be applied to all participating stations. This global FTIR study will provide additional information for us to infer adjusted C_2H_6 emission inventories and therefore enabling us to assess the impact of the C_2H_6 re-increase on the "air quality". Indeed, thanks to the improved information content associated to this newly optimized retrieval strategy we are able to derive tropospheric C_2H_6 partial columns from FTIR observations. From tropospheric C_2H_6 partial columns, the impact on levels of tropospheric O_3 will be quantified thanks to dedicated simulations.

Chapter 6 – Methane

Chapter 6 – Methane

6.1. Introduction

The harmonization of a retrieval strategy for methane for the whole infrared working group of NDACC to which I contributed is still ongoing. The major remaining issues are the availability of highly accurate and consistent spectroscopic parameters for CH_4 and the inversion of water vapor alongside. Indeed, as mentioned by *Sussmann et al.* [2011] and *Frankenberg et al.* [2008], erroneous spectroscopic parameters can lead to airmass-dependent artifacts impacting methane seasonality. Regarding water vapor, it presents strong absorption lines close to CH_4 lines and therefore heavily impacts the interference errors associated to the retrieval of CH_4 even leading to the determination of wrong CH_4 seasonality for low altitude humid sites. Most retrieval strategies applied at ground-based FTIR stations are either based on the work of *Sepúlveda et al.*, [2012] or *Sussmann et al.*, [2011].

The manuscript presented in the following sections is in preparation for submission in Atmospheric Chemistry and Physics in the framework of the special issue "Twenty-five years of operations of the Network for the Detection of Atmospheric Composition Change (NDACC) (AMT/ACP/ESSD Inter-Journal SI)". My contributions to this multi-site study include (in chronological order):

- optimization of the retrieval strategy of CH_4 for Jungfraujoch,
- retrieval of the whole FTIR observations from the Bruker operated at the Jungfraujoch,
- analysis of total, tropospheric and stratospheric CH_4 time series as observed by the ten FTIR sites,
- determination of the trend affecting those time series over the 2005-2012 time period,
- regridding of the GEOS-Chem tagged simulations to the ten stations,
- smoothing of the GEOS-Chem simulations for each station by their respective averaging kernels,
- analysis of tropospheric, stratospheric and total columns of CH_4 since 2005 as simulated by GEOS-Chem,
- analysis of the 11 tracers and their changes since 2005 as simulated by GEOS-Chem for each FTIR stations.

The methods employed for the above mentioned tasks are fully detailed in the following sections.

6.2. Changes of atmospheric methane (CH_4) since 2005 from NDACC FTIR measurements and GEOS-Chem tagged simulation

Whitney Bader[1], B. Bovy[1], S. Conway[2], K. Strong[2], D. Smale[3], A. J. Turner[4], P. F. Bernath[5,6], T. Blumenstock[7], A. Coulon[8], B. Franco[1], O. Garcia[9], D. Griffith[10], F. Hase[7], P. Hausmann[11], N. Jones[10], B. Lejeune[1], I. Murata[12], I. Morino[13], H. Nakajima[13], C. Paton-Walsh[10], J. Robinson[3], M. Schneider[7], C. Servais[1], R. Sussmann[11] and E. Mahieu[1].

[1] Institute of Astrophysics and Geophysics, University of Liège, Liège, Belgium
[2] Department of Physics, University of Toronto, Toronto, ON, M5S 1A7, Canada
[3] National Institute of Water and Atmospheric Research, NIWA, Lauder, New Zealand
[4] School of Engineering and Applied Sciences, Harvard University, Cambridge, MA, USA.
[5] Department of Chemistry and Biochemistry, Old Dominion University, Norfolk, VA 23529, Canada
[6] Department of Chemistry, University of Waterloo, Waterloo, ON N2L 3G1, Canada
[7] Karlsruhe Institute of Technology (KIT), Institute of Meteorology and Climate Research (IMK-ASF), Karlsruhe, Germany
[8] Institute for Atmospheric and Climate Science, ETH Zurich, Zurich, Switzerland
[9] Izaña Atmospheric Research Centre (IARC), Agencia Estatal de Meteorologia (AEMET), Spain
[10] School of Chemistry, University of Wollongong, Australia
[11] Karlsruhe Institute of Technology, IMK-IFU, Garmisch-Partenkirchen, Germany
[12] Graduate School of Environment Studies, Tohoku University, Sendai 980-8578, Japan
[13] National Institute for Environment Studies (NIES), Tsukuba, Ibaraki 305-8506, Japan

Manuscript in preparation for submission in Atmospheric Chemistry and Physics.

Abstract

Changes of atmospheric methane (CH_4) since 2005 have been evaluated using Fourier Transform Infrared (FTIR) solar observations performed at 10 ground-based sites, all members of the Network for Detection of Atmospheric Composition Change (NDACC). From this, we find an increase of atmospheric methane total columns that amounts to 0.30 ± 0.04 %/year for the 2005−2012 period. We used the GEOS-Chem Chemical Transport Model tagged simulation that accounts for the contribution of each emission source and one sink in the total CH_4 simulated based on emissions inventories and transport. After regridding according to NDACC vertical layering using a conservative regridding scheme and smoothing by convolving with respective FTIR seasonal averaging kernels, GEOS-Chem simulation shows an increase of atmospheric methane of 0.35 ± 0.03 %/year which is in agreement with NDACC measurements. Analysis of the GEOS-Chem tagged simulation allows us to quantify the contribution of each tracer to the global methane change since 2005. We find that natural sources such as wetlands and biomass burning contribute to the inter-annual variability of methane. However, anthropogenic emissions such as coal mining, gas and oil transport and exploration which are mainly emitted in the Northern Hemisphere and act as secondary contributors to the global budget of methane, have played a major role in the increase of atmospheric methane observed since 2005.

Conclusions

This work has reported the study of atmospheric methane and two of its derivatives, i.e. ethane and methanol. Those three gases have an impact on air quality through their removal pathway. Indeed, in the troposphere their oxidation impacts the contents of ozone making them act as ozone precursors. In addition, in the stratosphere methane influences the content of ozone and the production of water vapor. Moreover, both methane and ethane contribute to the greenhouse radiative forcing. While the latter is an indirect greenhouse gas because of its sinks, the former is the second most important anthropogenic greenhouse gas after CO_2. Their concentrations have been primarily assessed from ground-based FTIR solar observations recorded at the high alpine International Scientific Station of the Jungfraujoch (3580 m a.s.l.), member of the Network for Detection of Atmospheric Composition Change, in the prospect of studying their long-term trend and recent changes as well as their seasonal and/or diurnal variations.

The primary challenge of this work was the development and optimization of retrieval strategies for the three studied gases from FTIR observations recorded at the Jungfraujoch. The development and optimization of a retrieval strategy is based on the selection of the best combination of parameters in order to limit interferences, minimize residuals, maximize the information content and thus maximize the altitude sensitivity range. To this end, we have performed systematic search for and evaluation of absorption lines of the target species and have determined the best combination of spectral windows. When required, several spectroscopic linelist for the target and interfering species have been tested as well as their impact on residuals and information content. We performed thorough comparisons of a priori mixing ratio profiles for target species produced from satellite observations or model simulations with support from in situ GC-MS surface measurements. Other parameters such as the signal-to-noise ratio for inversion, the solar zenith angle range, the slope and background curvature of the spectra and the effective apodisation parameter have been adjusted. Through this work a method for error analysis associated to the line parameter uncertainty has been developed and is currently of use in the GIRPAS group. It has been employed for each available combination of parameters and has served as an indicator for the selection of the best retrieval strategy to be employed.

A 17-year time series of methanol has been presented from the analysis of FTIR observations recorded at the Jungfraujoch [*Bader et al.*, 2014]. The optimized retrieval strategy consists in the combination, for the first time, of spectral windows that have been used in previous work [*Dufour et al.*, 2006; *Rinsland et al.*, 2009; *Vigouroux et al.*, 2009] resulting in the improvement of the information content. Indeed, with a typical DOFS of 1.82, a total, a lower tropospheric (3.58-7.18 km) and an upper tropospheric-lower stratospheric (UTLS, 7.18-14.84 km) columns are available. Both random and systematic error sources have been identified and characterized using the method developed through this work on spectra recorded in the year 2010, and are found to be respectively 5 and 7 % for the total column. Since the long-term trend analysis of methanol total columns shows no significant trend in the last 17 years, we analyzed the methanol seasonal cycle that exhibits a high peak-to-peak amplitude of 129.4 ± 5.5 % (1σ) for total columns. Methanol total and partial columns are characterized by a strong seasonal modulation with minimum values and variability in December to February and maximum columns in June–July. Regarding methanol diurnal variations, they are characterized by an increase of methanol in the morning and a decrease during the afternoon for all seasons but summer.

The lower tropospheric and upper tropospheric-lower stratospheric columns of methanol retrieved from Jungfraujoch FTIR spectra have been confronted with measurements respectively obtained with surface in situ GC-MS and ACE-FTS satellite measurements, giving satisfactory comparison results. The FTIR lower-tropospheric data shows good agreement with in situ measurements regarding the data dispersion while the retrieved UTLS columns have a close to statistical agreement with ACE-FTS occultations. Comparisons with simulations from the IMAGESv2 model have also been performed. They demonstrated an underestimation by IMAGES v2 of the peak-to-peak amplitude for total and lower-tropospheric columns therefore leading to seasonal differences with an overestimation of winter methanol and an underestimation in summertime by the model whereas we observed no systematic bias between FTIR results and the model IMAGESv2. Regarding UTLS columns, both IMAGESv2 and our FTIR methanol have seasonal cycles in phase and similar peak-to-peak amplitudes.

Even though the role of plant growth in methanol budget is confirmed by its seasonality, large uncertainties remain in the methanol budget. Thanks to the improvement of the information content of our retrieval and therefore our altitude sensitivity range, our total and partial columns time series provide a valuable tool for model and satellite validation and complement the NDACC measurements at northern mid-latitudes.

Regarding ethane, we have developed a new strategy that includes the use of improved spectroscopic parameters that include ethane pseudo-lines based on cross-section laboratory spectra as well as updated line features for ozone and methyl chloride. Such optimized retrieval strategy has substantially reduced fitting residuals and enhanced information content, with a mean DOFS of 2.11 (while previous work using only the branch near 2976 cm^{-1} showed a typical DOFS of 1.5). We have presented here a time series of ethane spanning 20 years of observations made at the Jungfraujoch [between 1994 and 2014; *Franco et al.*, 2015]. Total columns of ethane have been compared with columns simulated by the GEOS-Chem model. Comparisons show a good agreement regarding the seasonal cycle amplitude and phase of ethane but a systematic and significant underestimation of the ethane burden by GEOS-Chem, suggesting an underestimation of emissions of ethane by the emission inventories.

Analysis of long-term trend of ethane showed a negative trend from 1994 until 2009 and revealed a strong positive trend of ethane from 2009 onwards of 4.90 ± 0.91 $\%.year^{-1}$ (wrt 2009.0), reported for the first time [*Franco et al.*, 2015]. Since the main sink of ethane, i.e. the hydroxyl radical has not exhibited large interannual variability since the end of the 20th century [*Montzka et al.*, 2011], since no other species that are primarily removed from the atmosphere by oxidation by the hydroxyl radical present an upturn in their retrieved columns over the last years, and since methane, which shares emission sources with ethane, presents a global renewed rise after 2006 [*Kirschke et al.*, 2013]; we hypothesize that the observed recent increase in ethane above the Jungfraujoch could represent a change in ethane throughout the Northern Hemisphere and may be the product of a large increase in fugitive emissions related to the recent upturn in the development of North American shale gas and tight oil reservoirs.

This hypothesis will be further examined on the northern America continent and then on a global scale. The objective will be to confirm and quantify the recent increase over North America to reinforce the hypothesis that massive US shale gas exploitation US is responsible for the observed increase. To this end, our aim will be to evaluate more representative emission inventories, using top-down and bottom-up approaches in dedicated mode simulations. We will then characterize the ethane increase at a global level that will provide additional information to infer adjusted ethane emission inventories in order to assess the impact of the ethane increase on the air quality.

Finally, we quantified the changes of methane since 2005 from 10 ground-based NDACC sites, with a mean global increase of 0.30 ± 0.04 %.year^{-1} for the 2005-2012 period (wrt 2005.0). A GEOS-Chem tagged simulation that provides the contribution of each emission source and one sink to the total methane simulation, has been used in order to provide hypotheses for the source(s) responsible for the recent methane upturn. After regridding and smoothing of GEOS-Chem simulation results to match the spatial and vertical resolution of the ground-based observations as well as the vertical sensitivity range, comparisons between FTIR observations and a GEOS-Chem tagged simulation covering the 2005-2012 period have been presented. The global mean increase of methane as simulated by GEOS-Chem amounts to 0.35 ± 0.03 %.year^{-1} which is in good agreement with the observed mean annual changes as observed by the ground-based stations.

A detailed analysis of the GEOS-Chem tracer on both the local and global scales was performed in order to quantify the contribution of each tracer to the global methane change since 2005. From this, we determined that natural sources such as wetlands and biomass burning contribute to the inter-annual variability of methane, while the increasing anthropogenic emissions such as coal mining, gas and oil transport and exploration, mainly emitted in the Northern Hemisphere that are secondary contributors to the global budget of methane, have played a major role in the increase of atmospheric methane observed since 2005. Those conclusions are consistent with the hypothesis mentioned above of increasing exploitation of shale gas and oil leading to the increase of atmospheric ethane.

References

- Aikin, A. C., J. R. Herman, E. J. Maier, C. J. McQuillan (1982), Atmospheric chemistry of ethane and ethylene, J. Geophys. Res., 87(C4), 3105, doi:10.1029/JC087iC04p03105.
- Angelbratt, J., J. Mellqvist, D. Simpson, J. E. Jonson, T. Blumenstock, T. Borsdorff P. Duchatelet, F. Forster, F. Hase, E. Mahieu, M. De Mazière, J. Notholt, A. K. Petersen, U. Raffalski, C. Servais, R. Sussmann, T. Warneke, C. Vigouroux (2011), Carbon monoxide (CO) and ethane (C2H6) trends from ground-based solar FTIR measurements at six European stations, comparison and sensitivity analysis with the EMEP model, Atmos. Chem. Phys., 11(17), 9253–9269, doi:10.5194/acp-11-9253-2011.
- Atkinson, R., D. L. Baulch, R. A. Cox, J. N. Crowley, R. F. Hampson, R. G. Hynes, M. E. Jenkin, M. J. Rossi, J. Troe, and IUPAC Subcommittee (2006), Evaluated kinetic and photochemical data for atmospheric chemistry: Volume II: gas phase reactions of organic species, Atmos. Chem. Phys., 6(11), 3625–4055, doi:10.5194/acp-6-3625-2006.
- Aydin, M., K. R. Verhulst, E. S. Saltzman, M. O. Battle, S. a Montzka, D. R. Blake, Q. Tang, and M. J. Prather (2011), Recent decreases in fossil-fuel emissions of ethane and methane derived from firn air., Nature, 476(7359), 198–201, doi:10.1038/nature10352.
- Bader, W. (2011), Extension of the long--term total column time series of atmospheric methane above the Jungfraujoch station: analysis of grating infrared spectra between 1977 and 1989., Master's thesis, Department of Geography, University of Liège.
- Bader, W., T. Stavrakou, J.-F. Muller, S. Reimann, C. D. Boone, J. J. Harrison, O. Flock, B. Bovy, B. Franco, B. Lejeune, C. Servais, E. Mahieu (2014), Long-term evolution and seasonal modulation of methanol above Jungfraujoch (46.5° N, 8.0° E): optimization of the retrieval strategy, comparison with model simulations and independent observations, Atmos. Meas. Tech., 7(11), 3861–3872, doi:10.5194/amt-7-3861-2014.
- Baker, V. R., J. R., Everett, M. Morisawa, N. M. Short, J. M. Coleman, H. H. Roberts, O. K. Huh, A. L. Bloom, R. W. Jr. Blair, A. S. Walker, R. S. Jr. Williams, P. D. Jr. Lowman, J. B. Garvin, R. S. Hayden (1986), Geomorphology from space, edited by N. M. S. Short and R. W. J. Blair, United States Government Printing.
- Barret, B., M. De Mazière, P. Demoulin (2002), Retrieval and characterization of ozone profiles from solar infrared spectra at the Jungfraujoch, J. Geophys. Res. Atmos., 107(D24), 4788, doi:10.1029/2001JD001298.
- Bates, D. R., and M. Nicolet (1950), Atmospheric Hydrogen, Publ. Astron. Soc. Pacific, 62, 106, doi:10.1086/126244.
- Bates, N., Y. Astor, M. Church, K. Currie, J. Dore, M. Gonaález-Dávila, L. Lorenzoni, F. Muller-Karger, J. Olafsson, M. Santa-Casiano (2014), A Time-Series View of Changing Ocean Chemistry Due to Ocean Uptake of Anthropogenic CO2 and Ocean Acidification, Oceanography, 27(1), 126–141, doi:10.5670/oceanog.2014.16.
- Beer, R., M. W. Shephard, S. S. Kulawik, S. A. Clough, A. Eldering, K. W. Bowman, S. P. Sander, B. M. Fisher, V. H. Payne, M. Luo, G. B. Osterman, J. R. Worden (2008), First satellite observations of lower tropospheric ammonia and methanol, Geophys. Res. Lett., 35(9), L09801, doi:10.1029/2008GL033642.

- Bergamaschi, P., S. Houweling, A. Segers, M. Krol, C. Frankenberg, R. A. Scheepmaker, E. Dlugokencky, S. C. Wofsy, E. A. Kort, C. Sweeney, T. Schuck, C. Brenninkmeijer, H. Chen, V. Beck, C. Gerbig (2013), Atmospheric CH_4 in the first decade of the 21st century: Inverse modeling analysis using SCIAMACHY satellite retrievals and NOAA surface measurements, J. Geophys. Res. Atmos., 118(13), 7350–7369, doi:10.1002/jgrd.50480.
- Bernath, P. F., C. T. McElroy, M. C. Abrams, C. D. Boone, M. Butler, C. Camy-Peyret, M. Carleer, C. Clerbaux, P-F. Coheur, R. Colin, P. DeCola, M. DeMazière, J. R. Drummond, D. Dufour, W. F. J. Evans, H. Fast, D. Fussen, K. Gilbert, D. E. Jennings, E. J. Llewellyn, R. P. Lowe, E. Mahieu, J. C. McConnell, M. McHugh, S. D. McLeod, R. Michaud, C. Midwinter, R. Nassar, F. Nichitiu, C. Nowlan, C. P. Rinsland, Y. J. Rochon, N. Rowlands, K. Semeniuk, P. Simon, R. Skelton, J. J. Sloan, M.-A. Soucy, K. Strong, P. Tremblay, D. Turnbull, K. A. Walker, I. Walkty, D. A. Wardle, V. Wehrle, R. Zander, J. Zou (2005), Atmospheric Chemistry Experiment (ACE): Mission overview, Geophys. Res. Lett., 32(15), L15S01, doi:10.1029/2005GL022386.
- Berntsen, T. K., and I. S. A. Isaksen (1997), A global three-dimensional chemical transport model for the troposphere 1 . Model description and CO and ozone results, J. of Geophys. Res., 102, D17, 21 239-21 280, doi: 10.1029/97JD01140.
- Bertram, T. H., A. E. Perring, P. J. Wooldridge, J. Dibb, M. A. Avery, R. C. Cohen (2013), On the export of reactive nitrogen from Asia: NOx partitioning and effects on ozone, Atmos. Chem. Phys., 13(9), 4617–4630, doi:10.5194/acp-13-4617-2013.
- Bey, I., D. J. Jacob, J. A. Logan, R. M. Yantosca (2001b), Asian chemical outflow to the Pacific in spring: Origins, pathways, and budgets, J. Geophys. Res., 106(D19), 23097, doi:10.1029/2001JD000806.
- Bey, I., D. J. Jacob, R. M. Yantosca, J. a. Logan, B. D. Field, A. M. Fiore, Q. Li, H. Y. Liu, L. J. Mickley, M. G. Schultz (2001a), Global modeling of tropospheric chemistry with assimilated meteorology: Model description and evaluation, J. Geophys. Res., 106(D19), 23073, doi:10.1029/2001JD000807.
- Blake, D. R., T.-Y. Chen, T. W. Smith, C. J.-L. Wang, O. W. Wingenter, N. J. Blake, F. S. Rowland, E. W. Mayer (1996), Three-dimensional distribution of non-methane hydrocarbons and halocarbons over the northwestern Pacific during the 1991 Pacific Exploratory Mission (PEM-West A), J. Geophys. Res., 101(D1), 1763, doi:10.1029/95JD02707.
- Bloom, A. A., J. Worden, Z. Jiang, H. Worden, T. Kurosu, C. Frankenberg, D. Schimel (2015), Remote-sensing constraints on South America fire traits by Bayesian fusion of atmospheric and surface data, Geophys. Res. Lett., 42(4), 1268–1274, doi:10.1002/2014GL062584.
- Bloom, A. A., P. I. Palmer, A. Fraser, D. S. Reay, C. Frankenberg (2010), Large-Scale Controls of Methanogenesis Inferred from Methane and Gravity Spaceborne Data, Science, 327(5963), 322–325, doi:10.1126/science.1175176.
- Boone, C. D., K. A. Walker, and P. F. Bernath (2013), Version 3 Retrievals for the Atmospheric Chemistry Experiment Fourier Transform Spectrometer (ACE-FTS), in The Atmospheric Chemistry Experiment ACE at 10: A Solar Occultation Anthology, edited by P. F. Bernath, pp. 103–127, A. Deepak Publishing, Hampton, Virignia, USA.
- Bousquet, P. et al. (2006), Contribution of anthropogenic and natural sources to atmospheric methane variability, Nature, 443(7110), 439–443, doi: 10.1038/nature05132.

- Bousquet, P. et al. (2011), Source attribution of the changes in atmospheric methane for 2006–2008, Atmos. Chem. Phys., 11(8), 3689–3700, doi:10.5194/acp-11-3689-2011.
- Bray, C., A. Perrin, D. Jacquemart, N. Lacome (2011), The v1, v4 and 3v6 bands of methyl chloride in the 3.4-µm region: Line positions and intensities, J. Quant. Spectrosc. Radiat. Transf., 112(15), 2446–2462, doi:10.1016/j.jqsrt.2011.06.018.
- Bray, C., D. Jacquemart, J. Buldyreva, N. Lacome, and a. Perrin (2012), N2-broadening coefficients of methyl chloride at room temperature, J. Quant. Spectrosc. Radiat. Transf., 113(11), 1102–1112, doi:10.1016/j.jqsrt.2012.01.028.
- Brewer, A. W. (1949), Evidence for a world circulation provided by the measurements of helium and water vapour distribution in the stratosphere, Q. J. R. Meteorol. Soc., 75(326), 351–363, doi:10.1002/qj.49707532603.
- Browell, E. V. (2003), Ozone, aerosol, potential vorticity, and trace gas trends observed at high-latitudes over North America from February to May 2000, J. Geophys. Res., 108(D4), doi:10.1029/2001JD001390.
- Brown, L. R., C. B. Farmer, C. P. Rinsland, and R. A. Toth (1987), Molecular line parameters for the atmospheric trace molecule spectroscopy experiment, Appl. Opt., 36(23), 5154–5182.
- Butchart, N. (2014), The Brewer-Dobson circulation, Rev. Geophys., 52(2), 157–184, doi:10.1002/2013RG000448.
- Cady-Pereira, K. E., M. W. Shephard, D. B. Millet, M. Luo, K. C. Wells, Y. Xiao, V. H. Payne, and J. Worden (2012), Methanol from TES global observations: retrieval algorithm and seasonal and spatial variability, Atmos. Chem. Phys., 12(17), 8189–8203, doi:10.5194/acp-12-8189-2012.
- Carpenter L. J. and S. Reimann (Lead Authors), J.B. Burkholder, C. Clerbaux, B.D. Hall, R. Hossaini, J.C. Laube, and S.A. Yvon-Lewis (2014), Ozone-Depleting Substances (ODSs) and Other Gases of Interest to the Montreal Protocol, Chapter 1 in Scientific Assessment of Ozone Depletion: 2014, Global Ozone Research and Monitoring Project –Report No. 55, World Meteorological Organization, Geneva, Switzerland.
- Carpenter, L. J., A. C. Lewis, J. R. Hopkins, K. A. Read, I. D. Longley, and M. W. Gallagher (2004), Uptake of methanol to the North Atlantic Ocean surface, Global Biogeochem. Cycles, 18(4), GB4027, doi:10.1029/2004GB002294.
- Chameides, W., and J. C. G. Walker (1973), A photochemical theory of tropospheric ozone, J. Geophys. Res., 78(36), 8751–8760, doi:10.1029/JC078i036p08751.
- Chang, L., S. Palo, M. Hagan, J. Richter, R. Garcia, D. Riggin, and D. Fritts (2008), Structure of the migrating diurnal tide in the Whole Atmosphere Community Climate Model (WACCM), Adv. Sp. Res., 41(9), 1398–1407, doi:10.1016/j.asr.2007.03.035.
- Chapman, S. (1930), A theory of upper-atmospheric ozone, Mem. R. Meteorol. Soc., 3(26), 103—125.
- Chatfield, R. B., J. A. Vastano, L. Li, G. W. Sachse, and V. S. Connors (1998), The Great African Plume from biomass burning: Generalizations from a three-dimensional study of TRACE A carbon monoxide, J. Geophys. Res., 103(D21), 28059, doi:10.1029/97JD03363.
- Chen, D., Y. Wang, M. B. McElroy, K. He, R. M. Yantosca, and P. Le Sager (2009), Regional CO pollution and export in China simulated by the high-resolution nested-grid GEOS-Chem model, Atmos. Chem. Phys., 9(11), 3825–3839, doi:10.5194/acp-9-3825-2009.

- Chen, Y.-H. (2005), Atmospheric modeling of high- and low-frequency methane observations: Importance of interannually varying transport, J. Geophys. Res., 110(D10), D10303, doi:10.1029/2004JD005542.
- Chen, Y.-H., and R. G. Prinn (2006), Estimation of atmospheric methane emissions between 1996 and 2001 using a three-dimensional global chemical transport model, J. Geophys. Res. Atmos., 111(D10), D10307, doi:10.1029/2005JD006058.
- Collaud Coen, M., E. Weingartner, M. Furger, S. Nyeki, A. S. H. Prévôt, M. Steinbacher, and U. Baltensperger (2011), Aerosol climatology and planetary boundary influence at the Jungfraujoch analyzed by synoptic weather types, Atmos. Chem. Phys., 11(12), 5931–5944, doi:10.5194/acp-11-5931-2011.
- Collins, W. J., R. G. Derwent, C. E. Johnson, and D. S. Stevenson (2002), The Oxidation of Organic Compounds in the Troposphere and their Global Warming Potentials, Clim. Change, 52(4), 453–479, doi:10.1023/A:1014221225434.
- Connes, P. (1971), High resolution and high information Fourier spectroscopy, in 1970-Aspen International Conference Fourier Spectroscopy, edited by G. A. Vanasse, A. T. J. Stair, and D. J. Backer, p. 121, United States Air Force, Air Force Systems Command, Air Force Cambridge Research Laboratories.
- Connor, B. J., D. E. Siskind, J. J. Tsou, A. Parrish, and E. E. Remsberg (1994), Ground-based microwave observations of ozone in the upper stratosphere and mesosphere, J. Geophys. Res., 99(D8), 16757, doi:10.1029/94JD01153.
- Cox, C. J., V. P. Walden, and P. M. Rowe (2012), A comparison of the atmospheric conditions at Eureka, Canada, and Barrow, Alaska (2006-2008), J. Geophys. Res. Atmos., 117(D12), n/a–n/a, doi:10.1029/2011JD017164.
- Crutzen, P. J. (1970), The influence of nitrogen oxide on the atmospheric ozone content, Q. J. R. Meteorol. Soc., 96, 320.
- Crutzen, P. J. (1973), A discussion of the chemistry of some minor constituents in the stratosphere and troposphere, Pure Appl. Geophys., 106, 1385.
- Delbouille, L., and G. Roland (1963), Photometric atlas of the solar spectrum from λ 7498 to λ 12016.
- Delbouille, L., and G. Roland (1995), High-resolution solar and atmospheric spectroscopy from the Jungfraujoch high-altitude station, Opt. Eng., 34(9), 2736, doi:10.1117/12.205676.
- Delbouille, L., L. Neven, and G. Roland (1973), Photometric atlas of the solar spectrum from λ 3000 to λ 10000.
- Delmas, R., G. Mégie, and V.-H. Peuch (2005), Physique et chimie de l'atmosphère, Bélin., Echelles, Paris.
- Dlugokencky, E. J. (2003), Atmospheric methane levels off: Temporary pause or a new steady-state?, Geophys. Res. Lett., 30(19), 1992, doi:10.1029/2003GL018126.
- Dlugokencky, E. J. et al. (2009), Observational constraints on recent increases in the atmospheric CH 4 burden, Geophys. Res. Lett., 36(18), L18803, doi:10.1029/2009GL039780.
- Dlugokencky, E. J., L. P. Steele, P. M. Lang, and K. A. Masarie (1994), The growth rate and distribution of atmospheric methane, J. Geophys. Res., 99(D8), 17021, doi:10.1029/94JD01245.

- Dobson, G. M. B. (1956), Origin and Distribution of the Polyatomic Molecules in the Atmosphere, Proc. R. Soc. A Math. Phys. Eng. Sci., 236(1205), 187–193, doi:10.1098/rspa.1956.0127.
- Dobson, G. M. B., D. N. Harrison, and J. Lawrence (1929), Measurements of the Amount of Ozone in the Earth's Atmosphere and Its Relation to Other Geophysical Conditions. Part III, Proc. R. Soc. A Math. Phys. Eng. Sci., 122(790), 456–486, doi:10.1098/rspa.1929.0034.
- doi:10.1016/j.scitotenv.2007.10.018.
- Drayson, S. R. (1976), Rapid computation of the Voigt profile, J. Quant. Spectrosc. Radiat. Transf., 16(7), 611–614, doi:10.1016/0022-4073(76)90029-7.
- Duchatelet, P. (2011), Fluorine in the atmosphere: Inorganic fluorine budget and long--term trends based on FTIR measurements at Jungfraujoch., Institute of Astrophysics and Geophysics, University of Liège.
- Duchatelet, P., P. Demoulin, F. Hase, R. Ruhnke, W. Feng, M. P. Chipperfield, P. F. Bernath, C. D. Boone, K. A. Walker, and E. Mahieu (2010), Hydrogen fluoride total and partial column time series above the Jungfraujoch from long-term FTIR measurements: Impact of the line-shape model, characterization of the error budget and seasonal cycle, and comparison with satellite and model data, J. Geophys. Res., 115(D22), doi:10.1029/2010JD014677.
- Dufour, G., C. D. Boone, C. P. Rinsland, and P. F. Bernath (2006), First space-borne measurements of methanol inside aged southern tropical to mid-latitude biomass burning plumes using the ACE-FTS instrument, Atmos. Chem. Phys., 6(11), 3463–3470, doi:10.5194/acp-6-3463-2006.
- Dufour, G., S. Szopa, D. a. Hauglustaine, C. D. Boone, C. P. Rinsland, and P. F. Bernath (2007), The influence of biogenic emissions on upper-tropospheric methanol as revealed from space, Atmos. Chem. Phys. Discuss., 7(3), 9183–9202, doi:10.5194/acpd-7-9183-2007.
- Duncan, B. N. (2003), Interannual and seasonal variability of biomass burning emissions constrained by satellite observations, J. Geophys. Res., 108(D2), 4100, doi:10.1029/2002JD002378.
- Duncan, B. N., J. A. Logan, I. Bey, I. A. Megretskaia, R. M. Yantosca, P. C. Novelli, N. B. Jones, and C. P. Rinsland (2007), Global budget of CO, 1988–1997: Source estimates and validation with a global model, J. Geophys. Res. Atmos., 112(D22), D22301, doi:10.1029/2007JD008459.
- Dunkerton, T. (1978), On the Mean Meridional Mass Motions of the Stratosphere and Mesosphere, J. Atmos. Sci., 35(12), 2325–2333, doi:10.1175/1520-0469(1978)035<2325:OTMMMM>2.0.CO;2.
- Esposito, F., G. Grieco, G. Masiello, G. Pavese, R. Restieri, C. Serio, and V. Cuomo (2007), Intercomparison of line-parameter spectroscopic databases using downwelling spectral radiance, Q. J. R. Meteorol. Soc., 133(S3), 191–202, doi:10.1002/qj.131.
- Fall, R. (2003), Abundant Oxygenates in the Atmosphere: A Biochemical Perspective, Chem. Rev., 103(12), 4941–4952, doi:10.1021/cr0206521.
- Farman, J. C., B. G. Gardiner, and J. D. Shanklin (1985), Large losses of total ozone in Antarctica reveal seasonal ClO_x/NO_x interaction, Nature, 315(6016), 207–210, doi:10.1038/315207a0.
- Fehsenfeld, F. C., G. Ancellet, T. S. Bates, A. H. Goldstein, R. M. Hardesty, R. Honrath, K. S. Law, A. C. Lewis, R. Leaitch, S. McKeen, J. Meagher, D. D. Parrish, A. A. P. Pszenny, P. B. Russell, H. Schlager, J. Seinfeld, R. Talbot, R. Zbinden, (2006), International Consortium for Atmospheric Research on Transport and Transformation (ICARTT): North America to Europe—Overview of the 2004 summer field study, J. Geophys. Res. Atmos., 111(D23), D23S01, doi:10.1029/2006JD007829.

- Fischer, E. V., D. J. Jacob, R. M. Yantosca, M. P. Sulprizio, D. B. Millet, J. Mao, F. Paulot, H. B. Singh, A. Roiger, L. Ries, R. W. Talbot, K. Dzepina, S. Pandey Deolal (2014), Atmospheric peroxyacetyl nitrate (PAN): a global budget and source attribution, Atmos. Chem. Phys., 14(5), 2679–2698, doi:10.5194/acp-14-2679-2014.
- Fishman, J., J. M. Hoell, R. D. Bendura, R. J. McNeal, and V. W. J. H. Kirchhoff (1996), NASA GTE TRACE A experiment (September–October 1992): Overview, J. Geophys. Res., 101(D19), 23865, doi:10.1029/96JD00123.
- Fogal, P. F., L. M. LeBlanc, and J. R. Drummond (2013), The Polar Environment Atmospheric Research Laboratory (PEARL): Sounding the Atmosphere at 80° North., Arctic, 66(3), 377–386.
- Forster, P. et al. (2007), Changes in Atmospheric Constituents and in Radiative Forcing. In: Climate Change 2007: The Physical Science Basis. Contribution of Working Group I to the Fourth Assessment Report of the Intergovernmental Panel on Climate Change, in IPCC, edited by S. Solomon, D. Qin, M. Manning, Z. Chen, M. Marquis, K. B. Averyt, M. Tignor, and H. L. Miller, Cambridge, United Kingdom and New York, NY, USA.
- Franco, B. et al. (2015a), Retrieval of ethane from ground-based FTIR solar spectra using improved spectroscopy: Recent burden increase above Jungfraujoch, J. Quant. Spectrosc. Radiat. Transf., 160, 36–49, doi:10.1016/j.jqsrt.2015.03.017.
- Franco, B. et al. (2015b), Retrievals of formaldehyde from ground-based FTIR and MAX-DOAS observations at the Jungfraujoch station and comparisons with GEOS-Chem and IMAGES model simulations, Atmos. Meas. Tech., 8(4), 1733–1756, doi:10.5194/amt-8-1733-2015.
- Frankenberg, C., I. Aben, P. Bergamaschi, E. J. Dlugokencky, R. van Hees, S. Houweling, P. van der Meer, R. Snel, and P. Tol (2011), Global column-averaged methane mixing ratios from 2003 to 2009 as derived from SCIAMACHY: Trends and variability, J. Geophys. Res., 116(D4), D04302, doi:10.1029/2010JD014849.
- Frankenberg, C., P. Bergamaschi, A. Butz, S. Houweling, J. F. Meirink, J. Notholt, A. K. Petersen, H. Schrijver, T. Warneke, and I. Aben (2008), Tropical methane emissions: A revised view from SCIAMACHY onboard ENVISAT, Geophys. Res. Lett., 35(15), L15811, doi:10.1029/2008GL034300.
- Fraser, A., C. C. Miller, P. I. Palmer, N. M. Deutscher, N. B. Jones, and D. W. T. Griffith (2011), The Australian methane budget: Interpreting surface and train-borne measurements using a chemistry transport model, J. Geophys. Res., 116(D20), D20306, doi:10.1029/2011JD015964.
- Fung, I., J. John, J. Lerner, E. Matthews, M. Prather, L. P. Steele, and P. J. Fraser (1991), Three-dimensional model synthesis of the global methane cycle, J. Geophys. Res., 96(D7), 13033, doi:10.1029/91JD01247.
- Galbally, I. E., and W. Kirstine (2002), The Production of Methanol by Flowering Plants and the Global Cycle of Methanol, J. Atmos. Chem., 43(3), 195–229, doi:10.1023/A:1020684815474.
- Gardiner, T. et al. (2008), Trend analysis of greenhouse gases over Europe measured by a network of ground-based remote FTIR instruments, Atmos. Chem. Phys., 8(22), 6719–6727, doi:10.5194/acp-8-6719-2008.

- Glatthor, N., T. von Clarmann, G. P. Stiller, B. Funke, M. E. Koukouli, H. Fischer, U. Grabowski, M. Hoepfner, S. Kellmann, and A. Linden (2009), Large-scale upper tropospheric pollution observed by MIPAS HCN and C_2H_6 global distributions, Atmos. Chem. Phys., 9(24), 9619–9634, doi:10.5194/acp-9-9619-2009.
- Griffith, D. W. T., N. B. Jones, and W. A. Matthews (1998), Interhemispheric ratio and annual cycle of carbonyl sulfide (OCS) total column from ground-based solar FTIR spectra, J. Geophys. Res., 103(D7), 8447, doi:10.1029/97JD03462.
- Grooß, J.-U., and J. M. Russell (2005), Technical note: A stratospheric climatology for O_3, H_2O, CH_4, NO_x, HCl and HF derived from HALOE measurements, Atmos. Chem. Phys., 5(10), 2797–2807, doi:10.5194/acp-5-2797-2005.
- Gunson, M. R. et al. (1996), The Atmospheric Trace Molecule Spectroscopy (ATMOS) Experiment: Deployment on the ATLAS space shuttle missions, Geophys. Res. Lett., 23(17), 2333–2336, doi:10.1029/96GL01569.
- Gunson, M. R., C. B. Farmer, R. H. Norton, R. Zander, C. P. Rinsland, J. H. Shaw, and B.-C. Gao (1990), Measurements of CH4, N2O, CO, H2O, and O3 in the middle atmosphere by the Atmospheric Trace Molecule Spectroscopy experiment on Spacelab 3, J. Geophys. Res., 95(D9), 13867, doi:10.1029/JD095iD09p13867.
- Hao, W. M., and D. E. Ward (1993), Methane production from global biomass burning, J. Geophys. Res., 98(D11), 20657, doi:10.1029/93JD01908.
- Harrison, J. J., N. D. C. Allen, and P. F. Bernath (2010), Infrared absorption cross sections for ethane (C_2H_6) in the 3 μm region, J. Quant. Spectrosc. Radiat. Transf., 111(3), 357–363, doi:10.1016/j.jqsrt.2009.09.010.
- Harrison, J. J., N. D. C. Allen, and P. F. Bernath (2012), Infrared absorption cross sections for methanol, J. Quant. Spectrosc. Radiat. Transf., 113(17), 2189–2196, doi:10.1016/j.jqsrt.2012.07.021.
- Hase, F., J. W. Hannigan, M. T. Coffey, A. Goldman, M. Höpfner, N. B. Jones, C. P. Rinsland, and S. W. Wood (2004), Intercomparison of retrieval codes used for the analysis of high-resolution, ground-based FTIR measurements, J. Quant. Spectrosc. Radiat. Transf., 87(1), 25–52, doi:10.1016/j.jqsrt.2003.12.008.
- Hase, F., P. Demoulin, A. J. Sauval, G. C. Toon, P. F. Bernath, A. Goldman, J. W. Hannigan, and C. P. Rinsland (2006), An empirical line-by-line model for the infrared solar transmittance spectrum from 700 to 5000 cm^{-1}, J. Quant. Spectrosc. Radiat. Transf., 102(Article), 450–463, doi:10.1016/j.jqsrt.2006.02.026.
- Heikes, B. G. et al. (2002), Atmospheric methanol budget and ocean implication, Global Biogeochem. Cycles, 16(4), 1133, doi:10.1029/2002GB001895.
- Henne, S., M. Furger, and A. H. Prévôt (2005), Climatology of Mountain Venting–Induced Elevated Moisture Layers in the Lee of the Alps, J. Appl. Meteorol., 44(5), 620–633, doi:10.1175/JAM2217.1.
- Henne, S., M. Furger, S. Nyeki, M. Steinbacher, B. Neininger, S. F. J. de Wekker, J. Dommen, N. Spichtinger, A. Stohl, and A. S. H. Prévôt (2004), Quantification of topographic venting of boundary layer air to the free troposphere, Atmos. Chem. Phys., 4(2), 497–509, doi:10.5194/acp-4-497-2004.
- Holton, J. R., P. H. Haynes, M. E. McIntyre, A. R. Douglass, R. B. Rood, and L. Pfister (1995), Stratosphere-troposphere exchange, Rev. Geophys., 33(4), 403, doi:10.1029/95RG02097.

- Hough, A. M. (1991), Development of a two-dimensional global tropospheric model: Model chemistry, J. Geophys. Res., 96(D4), 7325, doi:10.1029/90JD01327.
- Huang, X., and Y. L. Yung (2004), A Common Misunderstanding about the Voigt Line Profile, J. Atmos. Sci., 61(13), 1630–1632, doi:10.1175/1520-0469(2004)061<1630:ACMATV>2.0.CO;2.
- Intergovernmental Panel on Climate Change, IPCC (2013) Climate Change 2013: The Physical Science Basis. Contribution of Working Group I to the Fifth Assessment Report of the Intergovernmental Panel on Climate Change [Stocker, T.F., D. Qin, G.-K. Plattner, M. Tignor, S.K. Allen, J. Boschung, A. Nauels, Y. Xia, V. Bex and P.M. Midgley (eds.)]. Cambridge University Press, Cambridge, United Kingdom and New York, NY, USA, 1535 pp, doi:10.1017/CBO9781107415324.
- Ito, A. (2010), Evaluation of the impacts of defoliation by tropical cyclones on a Japanese forest's carbon budget using flux data and a process-based model, J. Geophys. Res., 115(G4), doi:10.1029/2010JG001314.
- Jacob, D. J. (1999), Introduction to atmospheric chemistry, Princeton University Press, Princeton.
- Jacob, D. J. (2002), Atmospheric budget of acetone, J. Geophys. Res., 107(D10), doi:10.1029/2001JD000694.
- Jacob, D. J. (2005), Global budget of methanol: Constraints from atmospheric observations, J. Geophys. Res., 110(D8), D08303, doi:10.1029/2004JD005172.
- Jacob, D. J. (2007), Lectures on inverse modelling, p. 25, University of Harvard, Harvard.
- Jiménez, E., M. Gilles, and A. Ravishankara (2003), Kinetics of the reactions of the hydroxyl radical with CH_3OH and C_2H_5OH between 235 and 360 K, J. Photochem. Photobiol. A Chem., 157(2-3), 237–245, doi:10.1016/S1010-6030(03)00073-X.
- Johnston, H. (1971), Reduction of Stratospheric Ozone by Nitrogen Oxide Catalysts from Supersonic Transport Exhaust, Science, 173(3996), 517–522, doi:10.1126/science.173.3996.517.
- Kaiser, E. W., I. M. Lorkovic, and T. J. Wallington (1990), Pressure dependence of the ethene yield from the reaction ethyl radical + oxygen, J. Phys. Chem., 94(8), 3352–3354, doi:10.1021/j100371a030.
- Kaplan, J. O. (2002), Wetlands at the Last Glacial Maximum: Distribution and methane emissions, Geophys. Res. Lett., 29(6), 1079, doi:10.1029/2001GL013366.
- Karl, T., A. Guenther, C. Spirig, A. Hansel, and R. Fall (2003), Seasonal variation of biogenic VOC emissions above a mixed hardwood forest in northern Michigan, Geophys. Res. Lett., 30(23), 2186, doi:10.1029/2003GL018432.
- Khalil, M. a. K., and R. a. Rasmussen (1983), Sources, sinks, and seasonal cycles of atmospheric methane, J. Geophys. Res., 88(C9), 5131, doi:10.1029/JC088iC09p05131.
- Kirschke, S. et al. (2013), Three decades of global methane sources and sinks, Nat. Geosci., 6(10), 813–823, doi:10.1038/ngeo1955.
- Krol, M., and J. Lelieveld (2003), Can the variability in tropospheric OH be deduced from measurements of 1,1,1-trichloroethane (methyl chloroform)?, J. Geophys. Res., 108(D3), doi:10.1029/2002JD002423.
- Kulawik, S. S. et al. (2015), Consistent evaluation of GOSAT, SCIAMACHY, CarbonTracker, and MACC through comparisons to TCCON, Atmos. Meas. Tech. Discuss., 8(6), 6217–6277, doi:10.5194/amtd-8-6217-2015.

- Kurylo, M. J. (1991), Network for the detection of stratospheric change, in Remote sensing of atmospheric chemistry, edited by J. L. McElroy and R. J. McNeal, pp. 168–174, Society of Photo-Optical Instrumentation Engineers, Bellingham, WA, United States, Orlando, FL.
- Kuze, A., H. Suto, M. Nakajima, and T. Hamazaki (2009), Thermal and near infrared sensor for carbon observation Fourier-transform spectrometer on the Greenhouse Gases Observing Satellite for greenhouse gases monitoring, Appl. Opt., 48(35), 6716, doi:10.1364/AO.48.006716.
- Laffineur, Q., M. Aubinet, N. Schoon, C. Amelynck, J.-F. Müller, J. Dewulf, H. Van Langenhove, K. Steppe, and B. Heinesch (2012), Abiotic and biotic control of methanol exchanges in a temperate mixed forest, Atmos. Chem. Phys., 12(1), 577–590, doi:10.5194/acp-12-577-2012.
- Langerock, B., M. De Mazière, F. Hendrick, C. Vigouroux, F. Desmet, B. Dils, and S. Niemeijer (2015), Description of algorithms for co-locating and comparing gridded model data with remote-sensing observations, Geosci. Model Dev., 8(3), 911–921, doi:10.5194/gmd-8-911-2015.
- Lattanzi, F., C. di Lauro, and J. Vander Auwera (2011), Toward the understanding of the high resolution infrared spectrum of C_2H_6 near 3.3µm, J. Mol. Spectrosc., 267(1-2), 71–79, doi:10.1016/j.jms.2011.02.003.
- Legreid, G., D. Folini, J. Staehelin, J. Balzani Lööv, M. Steinbacher, and S. Reimann (2008), Measurements of organic trace gases including oxygenated volatile organic compounds at the high alpine site Jungfraujoch (Switzerland): Seasonal variation and source allocations, J. Geophys. Res. Atmos., 113(D5), doi:10.1029/2007JD008653.
- Lelieveld, J. (2002), Stability of tropospheric hydroxyl chemistry, J. Geophys. Res., 107(D23), 4715, doi:10.1029/2002JD002272.
- Liu, H., D. J. Jacob, I. Bey, and R. M. Yantosca (2001), Constraints from 210 Pb and 7 Be on wet deposition and transport in a global three-dimensional chemical tracer model driven by assimilated meteorological fields, J. Geophys. Res. Atmos., 106(D11), 12109–12128, doi:10.1029/2000JD900839.
- Logan, J. A., M. J. Prather, S. C. Wofsy, and M. B. McElroy (1981), Tropospheric chemistry: A global perspective, J. Geophys. Res., 86(C8), 7210, doi:10.1029/JC086iC08p07210.
- Madronich, S., and J. G. Calvert (1990), Permutation reactions of organic peroxy radicals in the troposphere, J. Geophys. Res. Atmos., 95(D5), 5697–5715, doi:10.1029/JD095iD05p05697.
- Mahieu, E. et al. (2014), Spectrometric monitoring of atmospheric carbon tetrafluoride (CF_4) above the Jungfraujoch station since 1989: evidence of continued increase but at a slowing rate, Atmos. Meas. Tech., 7(1), 333–344, doi:10.5194/amt-7-333-2014.
- Mahieu, E., R. Zander, L. Delbouille, P. Demoulin, G. Roland, and C. Servais (1997), Observed trends in total vertical column abundances of atmospheric gases from IR solar spectra recorded at the Jungfraujoch, J. Atmos. Chem., 28(1-3), 227–243.
- Mahieu, E., W. Bader, and B. Franco (2015), Recent results derived from regular ground-based FTIR at the Jungfraujoch and other NDACC stations, in ACE Science Team Meeting, p. 24, Waterloo, ON, Canada.
- Malbrouck, R. (1977), Spectroscopie à très haute résolution par transformée de Fourier: Application à l'étude du spectre solaire., University of Liège.
- Mao, J. et al. (2010), Chemistry of hydrogen oxide radicals (HOx) in the Arctic troposphere in spring, Atmos. Chem. Phys., 10(13), 5823–5838, doi:10.5194/acp-10-5823-2010.

- McClatchey, R. A., W. S. Benedict, S. A. Clough, D. E. Burch, R. F. Calfee, K. Fox, L. S. Rothman, and J. S. Garing (1973), AFCRL atmospheric absorption line parameters compilation., AFCRL-TR-73-0096, 434, 78 pp.
- Mégie, G. (1989), Ozone. L'équilibre rompu, Presses du CNRS.
- Meier, A., G. C. Toon, C. P. Rinsland, A. Goldman, and F. Hase (2004), Spectroscopic Atlas of Atmospheric Microwindows in the Middle Infra-Red, Kiruna, Sweden.
- Migeotte, M., and L. Neven (1950), Détection du monoxide de carbone dans l'atmosphère terrestre à 3580 mètres d'altitude, Physica, 16, 423.
- Miller, J. A., S. J. Klippenstein, and S. H. Robertson (2000), A theoretical analysis of the reaction between ethyl and molecular oxygen, Proc. Combust. Inst., 28(2), 1479–1486, doi:10.1016/S0082-0784(00)80544-5.
- Millet, D. B. et al. (2006), Formaldehyde distribution over North America: Implications for satellite retrievals of formaldehyde columns and isoprene emission, J. Geophys. Res. Atmos., 111(D24), D24S02, doi:10.1029/2005JD006853.
- Millet, D. B. et al. (2008), New constraints on terrestrial and oceanic sources of atmospheric methanol, Atmos. Chem. Phys., 8(23), 6887–6905, doi:10.5194/acp-8-6887-2008.
- Molina, M. J., and F. S. Rowland (1974), Stratospheric sink for chlorofluoromethanes: chlorine atom catalyzed destruction of ozone, Nature, 249(5460), 810–812, doi:10.1038/249810a0.
- Montzka, S. A., M. Krol, E. Dlugokencky, B. Hall, P. Jockel, and J. Lelieveld (2011), Small Interannual Variability of Global Atmospheric Hydroxyl, Science, 331(6013), 67–69, doi:10.1126/science.1197640.
- Müller, J.-F., and G. Brasseur (1995), IMAGES: A three-dimensional chemical transport model of the global troposphere, J. Geophys. Res., 100(D8), 16445, doi:10.1029/94JD03254.
- Müller, J.-F., and G. Brasseur (1999), Sources of upper tropospheric HO X : A three-dimensional study, J. Geophys. Res., 104(D1), 1705, doi:10.1029/1998JD100005.
- Murgatroyd, R. J., and F. Singleton (1961), Possible meridional circulations in the stratosphere and mesosphere, Q. J. R. Meteorol. Soc., 87(372), 125–135, doi:10.1002/qj.49708737202.
- Nielsen, A. H., and M. Migeotte (1952), Abundance and vertical distribution of telluric methane from measurements at 3580 meters elevation, Annu. Rev. Astron. Phys., 15, 134.
- Nisbet, E. G., E. J. Dlugokencky, and P. Bousquet (2014), Methane on the rise-again., Science, 343(6170), 493–5, doi:10.1126/science.1247828.
- Notholt, J., G. C. Toon, R. Lehmann, B. Sen, and J.-F. Blavier (1997), Comparison of Arctic and Antarctic trace gas column abundances from ground-based Fourier transform infrared spectrometry, J. Geophys. Res., 102(D11), 12863, doi:10.1029/97JD00358.
- Nyeki, S. et al. (2000), Convective boundary layer evolution to 4 km a.s.l over High-Alpine terrain: airborne Lidar observations in the Alps, Geophys. Res. Lett., 27(5), 689–692.
- Park, R. J., D. J. Jacob, B. D. Field, R. M. Yantosca, and M. Chin (2004), Natural and transboundary pollution influences on sulfate-nitrate-ammonium aerosols in the United States: Implications for policy, J. Geophys. Res., 109(D15), doi:10.1029/2003JD004473.
- Park, R., D. Jacob, N. Kumar, and R. Yantosca (2006), Regional visibility statistics in the United States: Natural and transboundary pollution influences, and implications for the Regional Haze Rule, Atmos. Environ., 40(28), 5405–5423, doi:10.1016/j.atmosenv.2006.04.059.

- Parrella, J. P., D. J. Jacob, Q. Liang, Y. Zhang, L. J. Mickley, B. Miller, M. J. Evans, X. Yang, J. A. Pyle, N. Theys, M. Van Roozendael. (2012), Tropospheric bromine chemistry: implications for present and pre-industrial ozone and mercury, Atmos. Chem. Phys., 12(15), 6723–6740, doi:10.5194/acp-12-6723-2012.
- Paton-Walsh, C., N. M. Deutscher, D. W. T. Griffith, B. W. Forgan, S. R. Wilson, N. B. Jones, and D. P. Edwards (2010), Trace gas emissions from savanna fires in northern Australia, J. Geophys. Res., 115(D16), doi:10.1029/2009JD013309.
- Paton-Walsh, C., S. R. Wilson, N. B. Jones, and D. W. T. Griffith (2008), Measurement of methanol emissions from Australian wildfires by ground-based solar Fourier transform spectroscopy, Geophys. Res. Lett., 35(8), L08810, doi:10.1029/2007GL032951.
- Pickett-Heaps, C. A., D. J. Jacob, K. J. Wecht, E. A. Kort, S. C. Wofsy, G. S. Diskin, D. E. J. Worthy, J. O. Kaplan, I. Bey, and J. Drevet (2011), Magnitude and seasonality of wetland methane emissions from the Hudson Bay Lowlands (Canada), Atmos. Chem. Phys., 11(8), 3773–3779, doi:10.5194/acp-11-3773-2011.
- Pine, A. S., and C. P. Rinsland (1999), The role of torsional hot bands in modeling atmospheric ethane, J. Quant. Spectrosc. Radiat. Transf., 62(4), 445–458.
- Pine, A. S., and W. J. Lafferty (1981), Torsional splittings and assignments of the Doppler-limited spectrum of ethane in the CH stretching region., J. Res. Natl. Bur. Stand. (1934)., 87(3), 237–256.
- Pison, I., B. Ringeval, P. Bousquet, C. Prigent, and F. Papa (2013), Stable atmospheric methane in the 2000s: key-role of emissions from natural wetlands, Atmos. Chem. Phys., 13(23), 11609–11623, doi:10.5194/acp-13-11609-2013.
- Plumb, R. A. (2002), Stratospheric Transport., J. Meteorol. Soc. Japan, 80(4B), 793–809, doi:10.2151/jmsj.80.793.
- Pougatchev, N. S., B. J. Connor, and C. P. Rinsland (1995), Infrared measurements of the ozone vertical distribution above Kitt Peak, J. Geophys. Res., 100(D8), 16689, doi:10.1029/95JD01296.
- Pozzer, a., J. Pollmann, D. Taraborrelli, P. Jöckel, D. Helmig, P. Tans, J. Hueber, and J. Lelieveld (2010), Observed and simulated global distribution and budget of atmospheric C2-C5 alkanes, Atmos. Chem. Phys., 10(9), 4403–4422, doi:10.5194/acp-10-4403-2010.
- Prather, M. J., and J. Hsu (2010), Coupling of Nitrous Oxide and Methane by Global Atmospheric Chemistry, Science, 330(6006), 952–954, doi:10.1126/science.1196285.
- Prather, M. J., C. D. Holmes, and J. Hsu (2012), Reactive greenhouse gas scenarios: Systematic exploration of uncertainties and the role of atmospheric chemistry, Geophys. Res. Lett., 39(9), n/a–n/a, doi:10.1029/2012GL051440.
- Razavi, a., F. Karagulian, L. Clarisse, D. Hurtmans, P. F. Coheur, C. Clerbaux, J. F. Müller, and T. Stavrakou (2011), Global distributions of methanol and formic acid retrieved for the first time from the IASI/MetOp thermal infrared sounder, Atmos. Chem. Phys., 11(2), 857–872, doi:10.5194/acp-11-857-2011.
- Reimann, S. (2004), Halogenated greenhouse gases at the Swiss High Alpine Site of Jungfraujoch (3580 m a.s.l): Continuous measurements and their use for regional European source allocation, J. Geophys. Res., 109(D5), doi:10.1029/2003JD003923.
- Rigby, M. et al. (2008), Renewed growth of atmospheric methane, Geophys. Res. Lett., 35(22), L22805, doi:10.1029/2008GL036037.

- Ringeval, B., N. de Noblet-Ducoudré, P. Ciais, P. Bousquet, C. Prigent, F. Papa, and W. B. Rossow (2010), An attempt to quantify the impact of changes in wetland extent on methane emissions on the seasonal and interannual time scales, Global Biogeochem. Cycles, 24(2), doi:10.1029/2008GB003354.
- Rinsland, C. P. (2005), Atmospheric Chemistry Experiment (ACE) measurements of elevated Southern Hemisphere upper tropospheric CO, C2H6, HCN, and C2H2 mixing ratios from biomass burning emissions and long-range transport, Geophys. Res. Lett., 32(20), doi:10.1029/2005GL024214.
- Rinsland, C. P., A. Goldman, F. J. Murcray, T. M. Stephen, N. S Pougatchev, J. Fishman, S. J. David, R. D. Blatherwick, P. C. Novelli, N. B. Jones, B. J. Connor (1999), Infrared solar spectroscopic measurements of free tropospheric CO, C2H6, and HCN above Mauna Loa, Hawaii: Seasonal variations and evidence for enhanced emissions from the Southeast Asian tropical fires of 1997–1998, J. Geophys. Res., 104(D15), 18667, doi:10.1029/1999JD900366.
- Rinsland, C. P., A. Goldman, J. W. Elkins, L. S. Chiou, J. W. Hannigan, S. W. Wood, E. Mahieu, and R. Zander (2006), Long-term trend of at northern mid-latitudes: Comparison between ground-based infrared solar and surface sampling measurements, J. Quant. Spectrosc. Radiat. Transf., 97(3), 457–466, doi:10.1016/j.jqsrt.2005.07.002.
- Rinsland, C. P., A. Meier, D. W. T. Griffith, and L. S. Chiou (2001), Ground-based measurements of tropospheric CO, C2H6, and HCN from Australia at 34 degrees S latitude during 1997-1998, J. Geophys. Res., 106(D18), 20913–20924.
- Rinsland, C. P., E. Mahieu, L. Chiou, and H. Herbin (2009), First ground-based infrared solar absorption measurements of free tropospheric methanol (CH3OH): Multidecade infrared time series from Kitt Peak (31.9°N 111.6°W): Trend, seasonal cycle, and comparison with previous measurements, J. Geophys. Res., 114(D4), D04309, doi:10.1029/2008JD011003.
- Rinsland, C. P., E. Mahieu, P. Demoulin, R. Zander, C. Servais, and J.-M. Hartmann (2012), Decrease of the carbon tetrachloride (CCl_4) loading above Jungfraujoch, based on high resolution infrared solar spectra recorded between 1999 and 2011, J. Quant. Spectrosc. Radiat. Transf., 113(11), 1322–1329, doi:10.1016/j.jqsrt.2012.02.016.
- Rinsland, C. P., E. Mahieu, R. Zander, P. Demoulin, J. Forrer, and B. Buchmann (2000), Free tropospheric CO, C_2H_6, and HCN above central Europe: Recent measurements from the Jungfraujoch station including the detection of elevated columns during 1998, J. Geophys. Res., 105(D19), 24235, doi:10.1029/2000JD900371.
- Rinsland, C. P., N. B. Jones, B. J. Connor, J. A. Logan, N. S. Pougatchev, A. Goldman, F. J. Murcray, T. M. Stephen, A. S. Pine, R. Zander, E., Mahieu, P. Demoulin (1998), Northern and southern hemisphere ground-based infrared spectroscopic measurements of tropospheric carbon monoxide and ethane, J. Geophys. Res., 103(D21), 28197–28217, doi:10.1029/98JD02515.
- Rinsland, C. P., N. B. Jones, B. J. Connor, S. W. Wood, A. Goldman, T. M. Stephen, F. J. Murcray, L. S. Chiou, R. Zander, and E. Mahieu (2002), Multiyear infrared solar spectroscopic measurements of HCN, CO , C_2H_6, and C_2H_2 tropospheric columns above Lauder , New Zealand (45 °S latitude), 107, 1–12.
- Roberts, J. M., R. L. Tanner, L. Newman, V. C. Bowersox, J. W. Bottenheim, K. G. Anlauf, K. A. Brice, D. D. Parrish, F. C. Fehsenfeld, M. P. Buhr, J. F. Meagher, E. M. Bailey (1995), Relationships between PAN and ozone at sites in eastern North America, J. Geophys. Res., 100(D11), 22821, doi:10.1029/95JD01221.

- Rodgers, C. (2000), Inverse methods for atmospheric sounding, vol. 2 of Series on Atmospheric, Oceanic and Planetary Physics.
- Rodgers, C. D. (1976), Retrieval of atmospheric temperature and composition from remote measurements of thermal radiation, Rev. Geophys., 14(4), 609, doi:10.1029/RG014i004p00609.
- Rodgers, C. D. (1990), Characterization and error analysis of profiles retrieved from remote sounding measurements, J. Geophys. Res., 95(D5), 5587.
- Rodgers, C. D. (2003), Intercomparison of remote sounding instruments, J. Geophys. Res., 108(D3), doi:10.1029/2002JD002299.
- Roland, G. (1965), Spectroscopie par transformée de Fourier, University of Liège.
- Rothman, L. S. et al. (1987), The HITRAN database: 1986 edition, Appl. Opt., 26(19), 4058–4097, doi:10.1364/AO.26.004058.
- Rothman, L. S. et al. (2003), The HITRAN molecular spectroscopic database: edition of 2000 including updates through 2001, J. Quant. Spectrosc. Radiat. Transf., 82(1-4), 5–44, doi:10.1016/S0022-4073(03)00146-8.
- Rothman, L. S. et al. (2005), The HITRAN 2004 molecular spectroscopic database, J. Quant. Spectrosc. Radiat. Transf., 96(2), 139–204, doi:10.1016/j.jqsrt.2004.10.008.
- Rothman, L. S. et al. (2009), The HITRAN 2008 molecular spectroscopic database, J. Quant. Spectrosc. Radiat. Transf., 110(9-10), 533–572, doi:10.1016/j.jqsrt.2009.02.013.
- Rothman, L. S. et al. (2013), The HITRAN2012 molecular spectroscopic database, J. Quant. Spectrosc. Radiat. Transf., 130, 4–50, doi:10.1016/j.jqsrt.2013.07.002.
- Rudolph, J. (1995), The tropospheric distribution and budget of ethane, J. Geophys. Res., 100(D6), 11369, doi:10.1029/95JD00693.
- Sanderson, M. G. (1996), Biomass of termites and their emissions of methane and carbon dioxide: A global database, Global Biogeochem. Cycles, 10(4), 543–557, doi:10.1029/96GB01893.
- Schade, G. W., and A. H. Goldstein (2001), Fluxes of oxygenated volatile organic compounds from a ponderosa pine plantation, J. Geophys. Res. Atmos., 106(D3), 3111–3123, doi:10.1029/2000JD900592.
- Schade, G. W., and A. H. Goldstein (2006), Seasonal measurements of acetone and methanol: Abundances and implications for atmospheric budgets, Global Biogeochem. Cycles, 20(1), GB1011, doi:10.1029/2005GB002566.
- Schmidt, U., D. H. Ehhalt, U. Schmidt, R. Zander, P. Demoulin, and C. P. Rinsland (1991), Seasonal cycle and secular trend of the total and tropospheric column abundance of ethane above the Jungfraujoch, J. Geophys. Res., 96(D3), 4985, doi:10.1029/90JD02229.
- Schneider, U., T. Fuchs, A. Meyer-Christoffer, and B. Rudolf (2008), Global precipitation analysis products of the GPCC, Offenbach am Main, Germany.
- Schneising, O., J. P. Burrows, R. R. Dickerson, M. Buchwitz, M. Reuter, and H. Bovensmann (2014), Remote sensing of fugitive methane emissions from oil and gas production in North American tight geologic formations: Remote sensing of fugitive methane emissions from oil and gas production, Earth's Futur., doi:10.1002/2014EF000265.

- Sepúlveda, E., M. Schneider, F. Hase, O. E. García, a. Gomez-Pelaez, S. Dohe, T. Blumenstock, and J. C. Guerra (2012), Long-term validation of tropospheric column-averaged CH4 mole fractions obtained by mid-infrared ground-based FTIR spectrometry, Atmos. Meas. Tech., 5(6), 1425–1441, doi:10.5194/amt-5-1425-2012.
- Shine, K. P., R. G. Derwent, D. J. Wuebbles, and J.-J. Morcrette (1990), Chapter 2. Radiative forcing of climate. Contribution of Working Group I to the First Assessment Report of the Intergovernmental Panel on Climate Change, IPCC, 28.
- Simpson, I. J., F. S. Rowland, S. Meinardi, and D. R. Blake (2006), Influence of biomass burning during recent fluctuations in the slow growth of global tropospheric methane, Geophys. Res. Lett., 33(22), doi:10.1029/2006GL027330.
- Simpson, I. J., M. P. Sulbaek Andersen, S. Meinardi, L. Bruhwiler, N. J. Blake, D. Helmig, F. S. Rowland, and D. R. Blake (2012), Long-term decline of global atmospheric ethane concentrations and implications for methane., Nature, 488(7412), 490–4, doi:10.1038/nature11342.
- Singh, H. B., and P. L. Hanst (1981), Peroxyacetyl nitrate (PAN) in the unpolluted atmosphere: An important reservoir for nitrogen oxides, Geophys. Res. Lett., 8(8), 941–944, doi:10.1029/GL008i008p00941.
- Singh, H. B., D. O'Hara, D. Herlth, W. Sachse, D. R. Blake, J. D. Bradshaw, M. Kanakidou, and P. J. Crutzen (1994), Acetone in the atmosphere: Distribution, sources, and sinks, J. Geophys. Res. Atmos., 99(D1), 1805–1819, doi:10.1029/93JD00764.
- Singh, H. B., W. H. Brune, J. H. Crawford, D. J. Jacob, and P. B. Russell (2006), Overview of the summer 2004 Intercontinental Chemical Transport Experiment–North America (INTEX-A), J. Geophys. Res. Atmos., 111(D24), D24S01, doi:10.1029/2006JD007905.
- Singh, H., Y. Chen, A. Staudt, D. Jacob, D. Blake, B. Heikes, and J. Snow (2001), Evidence from the Pacific troposphere for large global sources of oxygenated organic compounds, Nature, 410(6832), 1078–1081, doi:10.1038/35074067.
- Solomon, S., K. H. Rosenlof, R. W. Portmann, J. S. Daniel, S. M. Davis, T. J. Sanford, and G.-K. Plattner (2010), Contributions of Stratospheric Water Vapor to Decadal Changes in the Rate of Global Warming, Science, 327(5970), 1219–1223, doi:10.1126/science.1182488.
- Spahni, R. et al. (2011), Constraining global methane emissions and uptake by ecosystems, Biogeosciences, 8(6), 1643–1665, doi:10.5194/bg-8-1643-2011.
- Stavrakou, T. et al. (2011), First space-based derivation of the global atmospheric methanol emission fluxes, Atmos. Chem. Phys., 11(10), 4873–4898, doi:10.5194/acp-11-4873-2011.
- Stocker, T. F., D. Qin, G.-K. Plattner, M. Tignor, S. K. Allen, J. Boschung, A. Nauels, Y. Xia, V. Bex, and P. M. Midgley (2013), The Physical Science Basis. Contribution of Working Group I to the Fifth Assessment Report of the Intergovernmental Panel on Climate Change, Cambridge, United Kingdom and New York, NY, USA.
- Stolarski, R. S., and R. J. Cicerone (1974), Stratospheric chlorine: a possible sink for ozone, Can. J. Chem., 52(8), 1610–1615, doi:10.1139/v74-233.
- Strahan, S. E., L. D. Oman, A. R. Douglass, and L. Coy (2015), Modulation of Antarctic vortex composition by the quasi-biennial oscillation, Geophys. Res. Lett., 42(10), 4216–4223, doi:10.1002/2015GL063759.

- Sudo, K. (2002), CHASER: A global chemical model of the troposphere 1. Model description, J. Geophys. Res., 107(D17), doi:10.1029/2001JD001113.
- Sudo, K., and H. Akimoto (2007), Global source attribution of tropospheric ozone: Long-range transport from various source regions, J. Geophys. Res., 112(D12), doi:10.1029/2006JD007992.
- Suntharalingam, P. (2004), Improved quantification of Chinese carbon fluxes using CO 2 /CO correlations in Asian outflow, J. Geophys. Res., 109(D18), D18S18, doi:10.1029/2003JD004362.
- Sussmann, R., and K. Schäfer (1997), Infrared spectroscopy of tropospheric trace gases: combined analysis of horizontal and vertical column abundances, Appl. Opt., 36(3), 735, doi:10.1364/AO.36.000735.
- Sussmann, R., F. Forster, M. Rettinger, and N. Jones (2011), Strategy for high-accuracy-and-precision retrieval of atmospheric methane from the mid-infrared FTIR network, Atmos. Meas. Tech., 4(9), 1943–1964, doi:10.5194/amt-4-1943-2011.
- Sussmann, R., F. Forster, M. Rettinger, and P. Bousquet (2012), Renewed methane increase for five years (2007–2011) observed by solar FTIR spectrometry, Atmos. Chem. Phys., 12(11), 4885–4891, doi:10.5194/acp-12-4885-2012.
- Sussmann, R., T. Borsdorff, and F. Karlsruhe (2007), Technical Note: Interference errors in infrared remote sounding of the atmosphere, 3537–3557.
- Sussmann, R., T. Borsdorff, M. Rettinger, C. Camy-Peyret, P. Demoulin, P. Duchatelet, E. Mahieu, and C. Servais (2009), Technical Note: Harmonized retrieval of column-integrated atmospheric water vapor from the FTIR network first examples for long-term records and station trends, Atmos. Chem. Phys., 9(22), 8987–8999, doi:10.5194/acp-9-8987-2009.
- Swanson, A. L. (2003), Seasonal variations of C_2–C_4 non-methane hydrocarbons and C_1–C_4 alkyl nitrates at the Summit research station in Greenland, J. Geophys. Res., 108(D2), doi:10.1029/2001JD001445.
- Takemura, T. (2005), Simulation of climate response to aerosol direct and indirect effects with aerosol transport-radiation model, J. Geophys. Res., 110(D2), doi:10.1029/2004JD005029.
- Tie, X., A. Guenther, and E. Holland (2003), Biogenic methanol and its impacts on tropospheric oxidants, Geophys. Res. Lett., 30(17), 1881, doi:10.1029/2003GL017167.
- Tikhonov, A. (1963), On the solution of incorrectly stated problems and a method of regularization, Dokl. Acad. Nauk SSSR, 151, 501–504.
- Toon, G. C. (1991), The JPL MkIV interferometer, Opt. Photonics News, 2(10), 19, doi:10.1364/OPN.2.10.000019.
- Turner, A. J., D. J. Jacob, K. J. Wecht, J. D. Maasakkers, E. Lundgren, A. E. Andrews, S. C. Biraud, H. Boesch, K. W. Bowman, N. M. Deutscher, M. K. Dubey, D. W. T. Griffith, F. Hase, A. Kuze, J. Notholt, H. Ohyama, R. Parker, V. H. Payne, R. Sussmann, C. Sweeney, V. A. Velazco, T. Warneke, P. O. Wennberg, D. Wunch (2015), Estimating global and North American methane emissions with high spatial resolution using GOSAT satellite data, Atmos. Chem. Phys., 15(12), 7049–7069, doi:10.5194/acp-15-7049-2015.
- Turner, J., S. R. Colwell, G. J. Marshall, T. A. Lachlan-Cope, A. M. Carleton, P. D. Jones, V. Lagun, P. A. Reid, and S. Iagovkina (2004), The SCAR READER Project: Toward a High-Quality Database of Mean Antarctic Meteorological Observations, J. Clim., 17(14), 2890–2898, doi:10.1175/1520-0442(2004)017<2890:TSRPTA>2.0.CO;2.

- Tyndall, G. S., R. A. Cox, C. Granier, R. Lesclaux, G. K. Moortgat, M. J. Pilling, A. R. Ravishankara, and T. J. Wallington (2001), Atmospheric chemistry of small organic peroxy radicals, J. Geophys. Res. Atmos., 106(D11), 12157–12182, doi:10.1029/2000JD900746.
- United Nations (2011), The Cancun Agreements: Outcome of the work of the Ad Hoc Working Group on Long-term Cooperative Action under the Convention, in Conference of the Parties on its sixteenth session (COP 16), edited by Framework Convention on Climate Change, p. 31, United Nations, Cancun, Mexico.
- van der Werf, G. R., J. T. Randerson, L. Giglio, G. J. Collatz, M. Mu, P. S. Kasibhatla, D. C. Morton, R. S. DeFries, Y. Jin, and T. T. van Leeuwen (2010), Global fire emissions and the contribution of deforestation, savanna, forest, agricultural, and peat fires (1997–2009), Atmos. Chem. Phys., 10(23), 11707–11735, doi:10.5194/acp-10-11707-2010.
- van Donkelaar, A., R. V. Martin, A. N. Pasch, J. J. Szykman, L. Zhang, Y. X. Wang, and D. Chen (2012), Improving the Accuracy of Daily Satellite-Derived Ground-Level Fine Aerosol Concentration Estimates for North America, Environ. Sci. Technol., 46(21), 11971–11978, doi:10.1021/es3025319.
- van Donkelaar, A., R. V. Martin, R. J. D. Spurr, E. Drury, L. A. Remer, R. C. Levy, and J. Wang (2013), Optimal estimation for global ground-level fine particulate matter concentrations, J. Geophys. Res. Atmos., 118(11), 5621–5636, doi:10.1002/jgrd.50479.
- van het Bolscher, M., J. Pereira, A. Spessa, S. Dalsoren, T. van Nojie, and S. Szopa (2008), REanalysis of the TROpospheric chemical composition over the past 40 years, A long-term global modeling study of tropospheric chemistry funded under the 5th EU framework programme, Hamburg, Germany.
- Viatte, C., K. Strong, K. A. Walker, and J. R. Drummond (2014), Five years of CO, HCN, C_2H_6, C_2H_2, CH_3OH, HCOOH and H_2CO total columns measured in the Canadian high Arctic, Atmos. Meas. Tech., 7(6), 1547–1570, doi:10.5194/amt-7-1547-2014.
- Vigouroux, C. et al. (2009), Ground-based FTIR and MAX-DOAS observations of formaldehyde at Réunion Island and comparisons with satellite and model data, Atmos. Chem. Phys., 9(24), 9523–9544, doi:10.5194/acp-9-9523-2009.
- Vigouroux, C. et al. (2012), FTIR time-series of biomass burning products (HCN, C_2H_6, C_2H_2, CH_3OH, and HCOOH) at Reunion Island (21 °S, 55 °E) and comparisons with model data, Atmos. Chem. Phys., 12(21), 10367–10385, doi:10.5194/acp-12-10367-2012.
- Vinciguerra, T., S. Yao, J. Dadzie, A. Chittams, T. Deskins, S. Ehrman, and R. R. Dickerson (2015), Regional air quality impacts of hydraulic fracturing and shale natural gas activity: Evidence from ambient VOC observations, Atmos. Environ., 110, 144–150, doi:10.1016/j.atmosenv.2015.03.056.
- von Kuhlmann, R., M. G. Lawrence, P. J. Crutzen, and P. J. Rasch (2003), A model for studies of tropospheric ozone and nonmethane hydrocarbons: Model evaluation of ozone-related species, J. Geophys. Res. Atmos., 108(D23), 4729, doi:10.1029/2002JD003348.
- Wallace, J. M., and P. V. Hobbs (2006), Atmospheric Science: An introductory survey, Elsevier -., edited by R. Dmowska, D. Hartmann, and Rossby T., Amsterdam Boston : Elsevier Academic Press, Amsterdam Boston.
- Walter, B. P., M. Heimann, and E. Matthews (2001), Modeling modern methane emissions from natural wetlands: 1. Model description and results, J. Geophys. Res., 106(D24), 34189, doi:10.1029/2001JD900165.

- Wang, J. S., J. a. Logan, M. B. McElroy, B. N. Duncan, I. a. Megretskaia, and R. M. Yantosca (2004), A 3-D model analysis of the slowdown and interannual variability in the methane growth rate from 1988 to 1997, Global Biogeochem. Cycles, 18(3), doi:10.1029/2003GB002180.
- Wang, Y. X. (2004), A nested grid formulation for chemical transport over Asia: Applications to CO, J. Geophys. Res., 109(D22), D22307, doi:10.1029/2004JD005237.
- Warneke, C., T. Karl, H. Judmaier, A. Hansel, A. Jordan, W. Lindinger, and P. J. Crutzen (1999), Acetone, methanol, and other partially oxidized volatile organic emissions from dead plant matter by abiological processes: Significance for atmospheric HO x chemistry, Global Biogeochem. Cycles, 13(1), 9–17, doi:10.1029/98GB02428.
- Watanabe, S. et al. (2011), MIROC-ESM 2010: model description and basic results of CMIP5-20c3m experiments, Geosci. Model Dev., 4(4), 845–872, doi:10.5194/gmd-4-845-2011.
- Wecht, K. J., D. J. Jacob, M. P. Sulprizio, G. W. Santoni, S. C. Wofsy, R. Parker, H. Bösch, and J. Worden (2014), Spatially resolving methane emissions in California: constraints from the CalNex aircraft campaign and from present (GOSAT, TES) and future (TROPOMI, geostationary) satellite observations, Atmos. Chem. Phys. Discuss., 14(3), 4119–4148, doi:10.5194/acpd-14-4119-2014.
- Wells, K. C. et al. (2012), Tropospheric methanol observations from space: retrieval evaluation and constraints on the seasonality of biogenic emissions, Atmos. Chem. Phys., 12(13), 5897–5912, doi:10.5194/acp-12-5897-2012.
- Whaley, C. (2014), Improvements to our Understanding of Toronto-Area Atmospheric Composition, University of Toronto.
- Wiacek, A., J. R. Taylor, K. Strong, R. Saari, T. E. Kerzenmacher, N. B. Jones, and D. W. T. Griffith (2007), Ground-Based Solar Absorption FTIR Spectroscopy: Characterization of Retrievals and First Results from a Novel Optical Design Instrument at a New NDACC Complementary Station, J. Atmos. Ocean. Technol., 24(3), 432–448, doi:10.1175/JTECH1962.1.
- Wingenter, O. W., B. C. Sive, N. J. Blake, D. R. Blake, and F. S. Rowland (2005), Atomic chlorine concentrations derived from ethane and hydroxyl measurements over the equatorial Pacific Ocean: Implication for dimethyl sulfide and bromine monoxide, J. Geophys. Res., 110(D20), doi:10.1029/2005JD005875.
- Wofsy, S. C., M. B. McElroy, and Y. L. Yung (1975), The chemistry of atmospheric bromine, Geophys. Res. Lett., 2(6), 215–218, doi:10.1029/GL002i006p00215.
- World Meteorological Organization (1985), Atmospheric Ozone 1985: Assessment of our understanding of the processes Controlling Its Present Distribution and Change, in Global Ozone Research and Monitoring Project Report, edited by R. T. et al. Watson, Geneva, Switzerland.
- World Meteorological Organization (2014a) Scientific Assessment of Ozone Depletion: 2014, World Meteorological Organization, Global Ozone Research and Monitoring Project—Report No. 55, 416 pp., Geneva, Switzerland.
- World Meteorological Organization (2014b), Greenhouse Gas Bulletin N°10, Geneva, Switzerland.
- Xiao, Y., J. A. Logan, D. J. Jacob, R. C. Hudman, R. Yantosca, and D. R. Blake (2008), Global budget of ethane and regional constraints on U.S. sources, J. Geophys. Res., 113(D21), doi:10.1029/2007JD009415.

- Xu, L.-H., R. M. Lees, P. Wang, L. R. Brown, I. Kleiner, and J. W. C. Johns (2004), New assignments, line intensities, and HITRAN database for CH3OH at 10μm, J. Mol. Spectrosc., 228(2), 453–470, doi:10.1016/j.jms.2004.05.017.
- Yevich, R., and J. A. Logan (2003), An assessment of biofuel use and burning of agricultural waste in the developing world, Global Biogeochem. Cycles, 17(4), doi:10.1029/2002GB001952.
- Zander, R. (1975), Presence of hydrogen fluoride in the upper stratosphere, Comptes rendus des séances l'Académie des Sci. Série B Sci. Phys., 12, 213.
- Zander, R., E. Mahieu, P. Demoulin, P. Duchatelet, G. Roland, C. Servais, M. De Mazière, S. Reimann, and Zander, R., P. Demoulin, D. H. Ehhalt, and U. Schmidt (1989), Secular increase of the vertical column abundance of methane derived from IR solar spectra recorded at the Jungfraujoch station, J. Geophys. Res., 94(D8), 11029, doi:10.1029/JD094iD08p11029.
- Zellweger, C., J. Forrer, P. Hofer, S. Nyeki, B. Schwarzenbach, E. Weingartner, M. Ammann, and U. Baltensperger (2003), Partitioning of reactive nitrogen (NOy) and dependence on meteorological conditions in the lower free troposphere, Atmos. Chem. Phys., 3(3), 779–796, doi:10.5194/acp-3-779-2003.
- Zeng, G., S. W. Wood, O. Morgenstern, N. B. Jones, J. Robinson, and D. Smale (2012), Trends and variations in CO, C2H6, and HCN in the Southern Hemisphere point to the declining anthropogenic emissions of CO and C2H6, Atmos. Chem. Phys., 12(16), 7543–7555, doi:10.5194/acp-12-7543-2012.
- Zhang, L., D. J. Jacob, E. M. Knipping, N. Kumar, J. W. Munger, C. C. Carouge, A. van Donkelaar, Y. X. Wang, and D. Chen (2012), Nitrogen deposition to the United States: distribution, sources, and processes, Atmos. Chem. Phys., 12(10), 4539–4554, doi:10.5194/acp-12-4539-2012.
- Zhang, L., D. J. Jacob, N. V. Downey, D. A. Wood, D. Blewitt, C. C. Carouge, A. van Donkelaar, D. B. A. Jones, L. T. Murray, and Y. Wang (2011), Improved estimate of the policy-relevant background ozone in the United States using the GEOS-Chem global model with 1/2° × 2/3° horizontal resolution over North America, Atmos. Environ., 45(37), 6769–6776, doi:10.1016/j.atmosenv.2011.07.054.
- Zhao, Y. (2002), Spectroscopic measurements of tropospheric CO, C2H6, C2H2, and HCN in northern Japan, J. Geophys. Res., 107(D18), doi:10.1029/2001JD000748.

Internet references

- Annan, K. (2003), The Montreal Protocol, ozone hole.
  Available from: http://www.theozonehole.com/montreal.htm
  (Accessed 28 October 2015)
- United Nations Framework Convention on Climate Change, UNFCC (1997), Article 2,
  Available from:
  http://unfccc.int/essential_background/convention/status_of_ratification/items/2631.php
  (Accessed 28 October 2015)
- Grindelwald Tourismus (2015), The Jungfraujoch - "Top of Europe," Alpensicht. Available from: http://www.alpensicht.com/English/Switzerland-Hotspots/switzerland_hot_spots_jungfraujoch.htm
  (Accessed 24 October 2015)
- NOAA/ESRL (2015), NCEP reanalysis, NOAA/ESRL/PSD.
  Available from:
  http://www.esrl.noaa.gov/psd/thredds/catalog/Datasets/ncep.reanalysis.derived/tropopause/catalog.html (Accessed 13 March 2015)
- NASA Astrobiology Institute's Virtual Planetary Laboratory (2015), Carbon dioxide, Mol. database. Available from: http://vpl.astro.washington.edu/spectra/co2.htm
  (Accessed 20 October 2015)
- Toon, G. C., B. Sen, and A. Kleinboehl (2015), Derivation of pseudo-lines from laboratory cross-sections, JPL
  Available from: http://mark4sun.jpl.nasa.gov/data/spec/Pseudo/Readme
  (Accessed 14 October 2015)
- UC Davis ChemWiki (2015), Selection rules and transition moment integral,
  Available from:
  http://chemwiki.ucdavis.edu/Physical_Chemistry/Spectroscopy/Fundamentals/Selection_rules_and_transition_moment_integral
  (Accessed 26 October 2015)

Appendix A – List of molecules

Formula	Molecule name	Formula	Molecule name
Ar	Argon	C_2H_5OOH	Ethyl hydroperoxide
BrO_x	Bromine oxides	CH_3OOH	Methyl hydroperoxyde
CCl_2F_2	CFC−12	CO	Carbon monoxide
CCl_3F	CFC−11	CO_2	Carbon dioxide
C_5H_8	Isoprene	HF	Hydrochloric acid
C_4H_{10}	Butane	HCl	Hydrofluoric acid
C_3H_8	Propane	HDO	Heavy water
C_3H_6	Propene	HgCdTe	Mercury−Cadmium−Tellurium (MCT)
C_2H_6	Ethane	H_2O_2	Hydrogen peroxide
C_2H_5	Ethyl radical	H_2O	Water vapour
C_2H_4	Ethylene	HO_X	Hydrogen oxide radicals
CH_3	Methyl radical	HO_2	Hydroxyl radicals
CH_4	Methane	InSb	Indium−Antimonide
$CHClF_2$	HCFC−22	KBr	Potassium bromide
CHF_3	HFC−23	N_2	Nitrogen
CH_3Cl	Methyl chloride	N_2O	Nitrous oxide
CH_3CHO	Acetaldehyde	NO_x	Nitrogen oxides
CH_3COO_2	Peroxyacetyl radical	NO_2	Nitrogen dioxide
$CH_3C(O)O$	Acetate	NO	Nitrogen monoxide
$CHCOO_2NO_2$	PAN	O_3	Ozone
C_3H_6O	Acetone	$O_3(668)$ $O_3(686)$ $O_3(676)$ $O_3(667)$	Ozone isotopologues
$C_2H_5O_2$	Ethylperoxy radical	O_2	Oxygen
CH_3O_2	Methylperoxy radical	O_x	Oxides
CH_4O	Methanol	HO	Hydroxyl radical
CH_2O	Formaldehyde	PbS	Lead−Sulphide
CH_3OH	Methanol	PbS	Sulphur hexafluoride
CH_2OH	Hydroxymethyl radical		

Appendix B – List of acronyms

ABL – Atmospheric Boundary Layer
ACE – Atmospheric Chemistry Experiment
ACE-FTS – Atmospheric Chemistry Experiment–Fourier Transform Spectrometer
AGAGE – Advanced Global Atmospheric Gases Experiment
AGCM – Atmospheric Global Circulation Model
ATLAS – Atmospheric Laboratory for Applications and Science
ATMOS – Atmospheric Trace Molecule Spectroscopy
CFC – Chlorofluorocarbons
CHASER – Chemical AGCM for Study of atmospheric Environment and Radiative forcing
CICERO – Center for International Climate and Environmental Research Oslo
CMDL – Climate Monitoring and Diagnostics Laboratory
CTM – Chemical Transport Model
DOFS – Degree of Freedom for Signal
DPGS – Double–Pass Grating Spectrometer
EAP – Effective Apodisation Parameter
ECMWF – European Centre for Medium–Range Weather Forecasts
EDGAR – Emission Database for Global Atmospheric Research
EMEP – European Monitoring and Evaluation Programme
ENVISAT – European ENVIronmental SATellite
FTIR – Fourier Transform InfraRed spectrometer
FTS – Fourier Transform Spectrometer
GAW – Global Atmosphere Watch
GC – Gas Chromatography
GCM – Global Circulation Model
GEOS – Goddard Earth Observing System
GIRPAS – Groupe Infrarouge de l'Atmosphère Physique et Solaire
GMAO – Global Modeling Assimilation Office
GOSAT – Greenhouse Gases Observing Satellite
GWP – Global Warming Potential
HALOE – Halogen Occultation Experiment
HCFC – Hydrochlorofluorocarbon
HFC – Hydrofluorocarbons
HIRS – High-Resolution Infrared Sounder
HITRAN – HIgh-resolution TRANsmission molecular absorption database
IASI – Infrared Atmospheric Sounding Interferometer
ILC – Inter-Layer Correlation
IMAGES – Intermediate Model of the Annual and Global Evolution of Species
IPCC – International Panel for Climate Change
IR – InfraRed
IRWG – Infrared Working Group

ISSJ – International Scientific Station of the Jungfraujoch
ITCZ – InterTropical Convergence Zone
JAMSTEC – Japan Agency for Marine–Earth Science and Technology
JAXA – Japan Aerospace Exploration Agency
LT – Lower Tropospheric Layer
MACC – Monitoring Atmospheric Composition & Change
MCT – Mercury-Cadmium-Tellurium
MIPAS – Michelson Interferometer for Passive Atmospheric Sounding
MIROC-ESM – Model for Interdisciplinary Research on Climate-Earth System Model
MkIV interferometer – MkIV Fourier Transform Infrared
MLS – Microwave Limb Sounder
MOZART – Model for Ozone and Related Tracers
MS – Mass Spectrometry
MSU – Microwave Sounding Unit
MW – Micro-Window
NCAR – National Center for Atmospheric Research
NCEP – National Centers for Environmental Prediction
NDACC – Network for Detection of Atmospheric Composition Change
NDSC – Network for the Detection of Stratospheric Change
NIES – National Institute for Environmental Studies
NMV – Normal Modes of Vibration
NMVOC – Non-Methane Volatile Organic Compound
NOAA – National Oceanic and Atmospheric Administration
OEM – Optimal Estimation Method
OPD – Optical Path Difference
PAN – Peroxyacetyl Nitrate
PEM – Pacific Exploratory Mission
PNNL – Pacific North West National Laboratory
RETRO – REanalysis of the TROpospheric chemical composition
RF – Radiative Forcing
RMS – Root Mean Square
SL-3 – Spacelab 3
SNR – Signal-to-Noise Ratio
SPRINTARS – Spectral Radiation-Transport Model for Aerosol Species
SSU – Stratospheric Sounding Unit
STE – Stratospheric-Tropospheric Exchange
SZA – Solar Zenith Angle
TES – Tropospheric Emission Spectrometer
TIME – Thermosphere Ionosphere Mesosphere Electrodynamics
TIROS – Television Infrared Observation Satellite
TIVOS – Television Operational Vertical Sounder
UARS – Upper Atmosphere Research Satellite

UPAR − UARS Reference Atmosphere Project
UTLS – Upper Troposphere-Lower Stratosphere
VISIT − Vegetation Integrative SImulator for Trace
VOC − Volatile Organic Compounds
WACCM − Whole Atmosphere Community Climate Model
WMO − World Meteorological Organization
ZPD − Zero optical Path Difference

Journal of Quantitative Spectroscopy & Radiative Transfer 149 (2014) 258–274

Contents lists available at ScienceDirect

Journal of Quantitative Spectroscopy & Radiative Transfer

journal homepage: www.elsevier.com/locate/jqsrt

Infrared absorption by pure CO_2 near 3340 cm^{-1}: Measurements and analysis of collisional coefficients and line-mixing effects at subatmospheric pressures

L. Daneshvar [a], T. Földes [b], J. Buldyreva [a], J. Vander Auwera [b,*,1]

[a] Institut UTINAM UMR CNRS 6213, Université de Franche-Comté, 16 route de Gray, F-25030 Besançon, France
[b] Service de Chimie Quantique et Photophysique, C.P. 160/09, Université Libre de Bruxelles, 50 avenue F.D. Roosevelt, B-1050 Brussels, Belgium

ARTICLE INFO

Article history:
Received 27 March 2014
Received in revised form
2 August 2014
Accepted 18 August 2014
Available online 27 August 2014

Keywords:
Carbon dioxide
Pressure effects
Line mixing
Energy-Corrected Sudden model
Symmetric scalar product
Venus atmosphere

ABSTRACT

High resolution Fourier transform spectra of the 21102–00001 band of $^{12}C^{16}O_2$ near 3340 cm^{-1} have been recorded and analyzed to extract isolated-line intensities and collisional parameters, and first-order line-mixing coefficients. Voigt, hard-collision Rautian and Sobel'man, and quadratic-speed-dependent Voigt profiles have been used. The line-mixing coefficients measured for the three branches have also been evaluated using an Energy-Corrected Sudden approach employing a symmetric metric in the Liouville space. These coefficients compare very favorably with the experimental results and estimations with an algorithm available in the literature. Results of straightforward ECS-modeling of complete band shapes have been compared to the recorded spectra and future improvements of this model required at subatmospheric pressures have been outlined.

1. Introduction

The present experimental and theoretical work is focused on a rather narrow region near 3.0 μm of the spectrum of carbon dioxide. This spectral range is dominated by the weak perpendicular 21102–00001 band of $^{12}C^{16}O_2$, observed in spectra of the mesosphere of Venus recorded by the SOIR (Solar Occultation in the InfraRed) instrument onboard the ESA Venus Express spacecraft [1,2]. As the atmosphere of Venus is predominantly composed of carbon dioxide [3], reliable retrievals of concentrations of atmospheric species from SOIR spectra require an accurate knowledge of CO_2 absorption line shape parameters. The present work aimed to measure these parameters for the 21102–00001 band of $^{12}C^{16}O_2$, for the self-broadening case and accounting for pressure-induced line mixing effects. Note that, because the composition of the atmosphere of Mars is also dominated by CO_2 (yet at lower pressures), the present measurements may also prove useful for future missions to this planet [4].

Studies specifically devoted to the 21102–00001 band of $^{12}C^{16}O_2$ have already been reported. They dealt with measurements of line intensities and self-broadening coefficients [5–9]. To the best of our knowledge, first-order pressure-induced line mixing coefficients [10] were never investigated. Note that theoretical predictions employing semi-empirical parameters to get broadening, shifting and line mixing coefficients are available [11,12].

In the present contribution, intensities, and self-broadening, self-shift and first-order line mixing coefficients were measured for P-, Q- and R-branch lines of the 21102–00001 band of $^{12}C^{16}O_2$. These measurements were carried out considering line narrowing resulting from either Dicke [13] or speed dependence [14,15] effects. Self-broadening and first-order line mixing coefficients as well as transmittance for P-Q-R manifolds at various pressures were also computed

* Corresponding author. Tel.: +32 2 650 24 18; fax: +32 2 650 42 32.
E-mail address: jauwera@ulb.ac.be (J.V. Auwera).
[1] Senior research associate with the F.R.S.-FNRS (Belgium).

http://dx.doi.org/10.1016/j.jqsrt.2014.08.007
0022-4073/

using a theoretical approach of Energy-Corrected Sudden (ECS) type for the relaxation matrix. This approach, non-Markovian in its general formulation, is characterized by the use of a non-conventional symmetric metric in the Liouville space and by an automatic satisfaction of the basic relations (detailed balance, sum rules) derived from first principles. Recently adapted to the case of infrared absorption of linear molecules with stretching and bending modes [16] and tested on high-density CO_2 absorption bands influenced by Coriolis interactions [17], this method is now tested, for the first time, for the case of subatmospheric pressures where the line shapes become sensitive to Doppler broadening and collisional narrowing effects. We underline that, in contrast to Ref. [11] where a large set of semi-empirical parameters was used to reproduce experimentally observed line shape parameters, besides previously adjusted parameters (for the basic transition rates and adiabaticity factor) [18] and standard database characteristics of vibration–rotation interactions (line positions, Herman–Wallis factors, etc.), the present ECS model does not contain any additional fitting parameters.

2. Experimental details

Ten unapodized room-temperature (293 ± 1 K) absorption spectra of a natural sample of carbon dioxide (Sigma Aldrich, 99.8% stated purity) were recorded using a Bruker IFS 120 to 125HR upgraded Fourier transform spectrometer. The instrument was fitted with a Tungsten source, an entrance aperture diameter of 1.30 mm, a CaF_2 beamsplitter, a low-pass filter with cut-off at about 5000 cm^{-1} and a 77 K InSb detector. The gas sample was contained in a 1.72-m Pyrex multi-pass White-type cell closed by CaF_2 windows, adjusted for 32 transits to yield an absorption path length of 55.14(17) m. The cell was evacuated using an Adixen turbomolecular pumping system. The carbon dioxide pressures, measured using absolute MKS Baratron gauges model 690A of 10 and 1000 Torr full-scale ranges, and spectral resolutions used are listed in Table 1. All the spectra result from the co-addition of 100 interferograms, except for spectra nos. 1, 2 and 3 recorded at the highest resolution, respectively, corresponding to 500, 396 and 566 interferograms. All the spectra were recorded over 4 days. Spectrum no. 1 was used to determine the calibration factor C to apply to all the spectra according to $\tilde{\nu}_{calib} = \tilde{\nu}_{obs}(1+C)$, where $\tilde{\nu}_{calib}$ and $\tilde{\nu}_{obs}$ are, respectively, the calibrated and observed wavenumbers. $C = -2.55(14) \times 10^{-7}$ [throughout the article, numbers between parentheses are the statistical uncertainties (1σ)] was obtained by matching the observed positions of 70 water vapor lines in the range 3768–3953 cm^{-1} to information available in HITRAN [19] with a RMS deviation of 5.5×10^{-5} cm^{-1} (the uncertainty on the reference H_2O line positions used is in the range 10^{-4}–10^{-5} cm^{-1}). Four of the spectra recorded are presented in the upper parts of Figs. 2 and 3.

3. Measurements

3.1. Modeling the CO_2 absorption spectra

The line parameters were measured using a multi-spectrum least squares fitting algorithm, developed in Brussels [20]. The program adjusts a synthetic spectrum to each of any number of observed Fourier transform spectra, using a Levenberg–Marquardt least-squares fitting procedure. Each synthetic spectrum, interpolated 4 or 8 times with respect to the observed spectrum, is calculated as the convolution of a monochromatic transmission spectrum with an instrument line shape (ILS) function. The latter includes the effects of the finite maximum optical path difference and of the finite size of the entrance aperture in the interferometer as fixed contributions [21], as well as possible distortions induced by phase errors and misalignment of the interferometer [22,23].

Table 1
Carbon dioxide pressure P and spectral resolution R (equal to 0.9 divided by the maximum optical path difference). The path length and temperature are, respectively, equal to 55.14(17) cm and 293(1) K for all the spectra.

#	P[a] (hPa)	R (cm^{-1})
1	2.95 (2)	0.005
2	11.18 (6)	0.005
3	30.0 (2)	0.005
4	101.0 (5)	0.01
5	202.0 (1)	0.01
6	302.0 (2)	0.02
7	450.0 (2)	0.02
8	602.0 (3)	0.03
9	752.0 (4)	0.05
10	903.0 (5)	0.05

[a] The uncertainty on P is the square root of the sum of the square of the measurement uncertainty (conservatively estimated to be 0.5% of reading) and the square of half of the variation of the pressure during the recording of the interferograms.

In the present work, the range displayed in Figs. 2 and 3 was fitted at once, thus covering the whole 21102–00001 band. To fit the observed spectra to almost the noise level required the inclusion of 9 carbon dioxide bands in the analysis. They are the 21102–00001 cold band of $^{12}C^{16}O_2$, $^{13}C^{16}O_2$ and $^{16}O^{12}C^{18}O$, and the 22202–01101, 23302–02201, 30003–01101, 30002–01101, 31103–10002 and 31102–10001 hot bands of $^{12}C^{16}O_2$. In addition, absorption lines of the main isotopologues of water vapor (apparently mostly present in the cell; relative pressure $\lesssim 8 \times 10^{-4}$) and acetylene [$\nu_3$ and $\nu_2+(\nu_4+\nu_5)^0$ bands (in the past, the cell was extensively used to record spectra of that species)] were observed. Acetylene absorption was only observable in the low CO_2 pressure spectra (nos. 1–3; relative pressure $\lesssim 2 \times 10^{-6}$).

The profile of the lines of the 21102–00001 band of $^{12}C^{16}O_2$ was modeled using either a Voigt [24], a Rautian and Sobel'man (called "Rautian" hereafter) [25] or a speed-dependent Voigt function [14], assuming a quadratic speed dependence of the relaxation rate (i.e. a quadratic-speed-dependent Voigt function, called "qsdVoigt" hereafter) [26]. A Voigt function always modeled the shape of the other CO_2 band lines, and of the acetylene and water vapor lines. The Rautian and qsdVoigt line shapes were calculated using the algorithms of Refs. [24] and [27], respectively. The Gaussian width involved in these profiles was always held fixed to the value calculated for the Doppler broadening. The pressure-induced half-width γ, shift δ,

narrowing β and the quadratic-speed-dependence of the pressure-induced half-width γ_2 of the CO_2 lines were assumed to be proportional to the CO_2 pressure P, with the proportionality factors being identified by the parameters γ^0, δ^0, β^0 and γ_2^0 in $cm^{-1}\,atm^{-1}$, respectively. The line positions, intensities, and lower-state energies (required for the temperature correction of the line intensities) were taken from HITRAN [19]. The pressure-induced self-broadening and self-shift coefficients of all the CO_2 lines, but those of the 21102–00001 band of $^{12}C^{16}O_2$, were taken from the work of Gamache and Lamouroux [12]. In view of the weakness of the water vapor and acetylene lines, their CO_2 broadening could be satisfactorily approximated using the air-broadening coefficients provided in HITRAN [19].

The measurements involved the adjustment of the positions, intensities, and self-broadening and self-shift coefficients of the lines of the 21102–00001 band of $^{12}C^{16}O_2$ having an intensity higher than 1.0×10^{-25} $cm^{-1}/(molecule\,cm^{-2})$ in HITRAN [19]. When applicable, β^0 or γ_2^0 was also fitted. To properly model that band at higher pressure, first-order line mixing [10] was included for the P-, Q- and R-branch lines, according to (see for example [28–30])

$$g_{LM} = \mathrm{Re}(g) + Y\,\mathrm{Im}(g) \tag{1}$$

where g_{LM} represents the line profile affected by line mixing, and Re(g) and Im(g) are the real and imaginary parts of the normalized line shape function, respectively. The quantity $Y = Y^0P$ is the so-called first-order line mixing coefficient [see Eq. (14) in Section 4.3], with the proportionality factor Y^0 being fitted.

In addition, the square of the vibrational transition dipole moment of the 22202–01101 hot band of the main isotopologue had to be fitted. Indeed, as some line intensities for this latter hot band in HITRAN [19] appeared to be too large compared to the corresponding absorption observed in our spectra, they needed to be adjusted. However, because many lines of this hot band are overlapped by the corresponding cold band lines, their intensities σ_{if} (corresponding to transitions between a lower level i and an upper level f) were calculated using the following expression:

$$\sigma_{if} = A\frac{\tilde{\nu}_{if}}{Z(T)}I_a\exp\{-hcE_i/k_BT\}\left[1-\exp\{-hc\tilde{\nu}_{if}/k_BT\}\right]L_{if}|R_{if}|^2 \tag{2}$$

In Eq. (2), $A\approx4.1624\times10^{-19}$ D^{-2} cm^2, k_B is the Boltzmann constant, $\tilde{\nu}_{if}$ is the line position in cm^{-1}, $Z(T)$ is the total internal partition function at temperature T (Z=283.2455 at 293 K [31]), I_a=0.9842 is the isotopic abundance of $^{12}C^{16}O_2$ [32], E_i is the energy of the lower level (in cm^{-1}) taken from [19], L_{if} is the Hönl–London factor [33] and $|R_{if}|^2$ is the square of the vibrational transition dipole moment. It was expressed using the following Herman–Wallis expression

$$|R_{if}|^2 = |R_0|^2(1+A_1^{RP}m+A_3^{RP}m^3)^2 \tag{3}$$

for P ($m=-J$) and R ($m=J+1$) branch lines (J is the quantum number associated with the total angular momentum of the molecule in the lower level), assuming no difference between e–e and f–f transitions. $|R_{if}|^2$ was constant for Q-branch lines. The initial values of the 3 parameters were determined by fitting the line intensities available in HITRAN [19].

The background in each spectrum was represented by a slanted straight line multiplied by the following sum of two cosines, to account for the channeling generated by the optical filter used and observed in all the spectra:

$$C(\tilde{\nu}) = \sum_{i=1}^{2} A_i\,\cos\left(2\pi\frac{\tilde{\nu}+\phi_i}{\lambda_i}\right) \tag{4}$$

In Eq. (4), $\tilde{\nu}$ is the wavenumber, and A_i, ϕ_i and λ_i are the fitted parameters. The modeling of the background therefore led to the addition of 8 fitted parameters per spectrum (the program does not unfortunately allow fitting the same set of channeling parameters for all the spectra).

3.2. Experimental results

We fitted all 10 spectra using either the Voigt, Rautian, or qsdVoigt line shape models to reproduce the molecular line profiles. Assuming an ideal instrumental line shape (i.e. not distorted by phase errors or a misalignment of the interferometer, referred to as “ideal ILS” below), the spectra at pressures of 101.0 hPa and higher could be modeled close to the noise level, while asymmetrical signatures remained in the residuals obtained for spectra corresponding to the 3 lowest pressures (these signatures were independent of the line shape model for spectra nos. 1 and 2 in Table 1). The most prominent of such signatures, obtained for the spectrum recorded at 11.18 hPa, are presented in the middle panel of Fig. 1. These asymmetrical signatures do not seem to result from limited accuracy of the gas pressure measurement as observed by Cich et al. [34], because they are still present, although reduced, when single spectrum fitting is applied to these low pressure spectra. We believe that they are associated with an asymmetry of the observed line shapes, originating from some phase error or a misalignment of the interferometer at the time of recording. Therefore, we fitted all the spectra, also varying either a constant phase error φ [22] or a constant angle β between the effective optical axis of the interferometer and its true optical axis [23] for the spectra recorded at the highest resolution (nos. 1–3 in Table 1); these parameters were left to zero for spectra nos. 4–10. Adjusting a constant phase error barely improved the residuals, while a significant improvement was obtained with the second model, leading to an average angle $\beta=0.26(6)$ mrad. The corresponding residuals obtained for the spectrum recorded at 11.18 hPa are presented in the lower panel of Fig. 1.

All the results reported here were obtained with the angle β fixed to 0.26 mrad for all 10 spectra. This modeling of the instrumental line shape of the Fourier transform spectrometer is referred to as “true ILS” below. Some results obtained with the “ideal” ILS will also be presented. Note that the asymmetry of the observed line shapes had negligible effects on the measured line intensities and self-broadening coefficients. Fitting all 10 spectra using the Voigt, Rautian, and qsdVoigt line shape models to reproduce the molecular line profiles involved a total of 457, 528 and 527 adjusted parameters, respectively, leading to almost identical overall standard deviations (5.8×10^{-4},

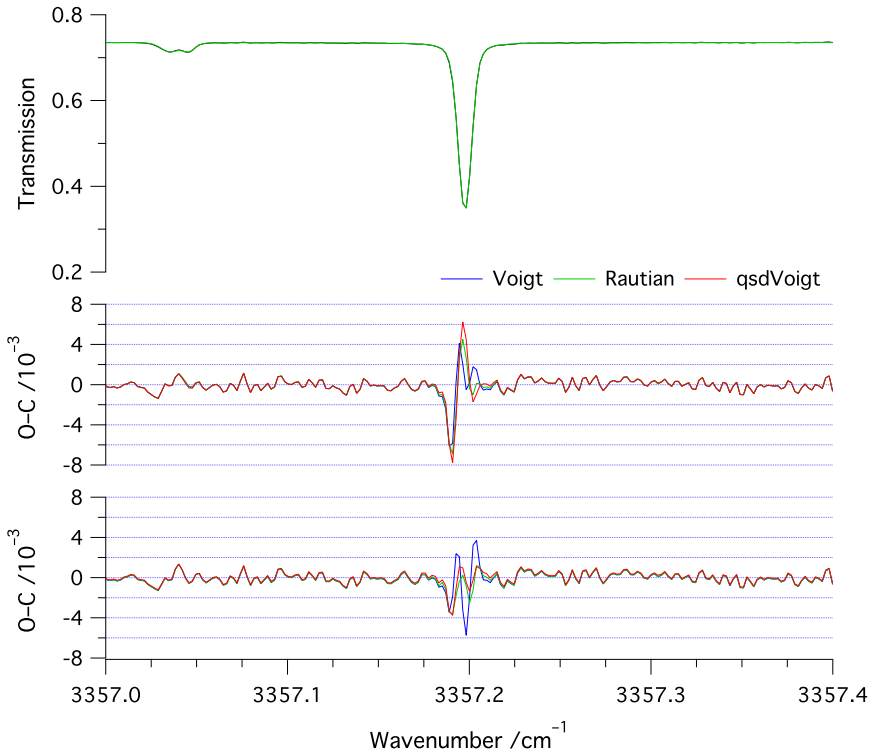

Fig. 1. Comparison of the residuals of fits using 3 line shape models of the R(22) profile observed at 11.18 hPa (spectrum no. 2 in Table 1) obtained not assuming (middle panel) and assuming (lower panel) that the effective optical axis of the interferometer makes a constant angle $\beta = 0.26(6)$ mrad with the true optical axis. The top panel shows observed (black curve) and best-fit calculated using the quadratic-speed-dependent Voigt model (green curve) spectra overlaid. (For interpretation of the references to color in this figure caption, the reader is referred to the web version of this paper.)

5.5×10^{-4} and 5.3×10^{-4}, respectively). The residuals obtained with the qsdVoigt line shape model are presented in the lower parts of Figs. 2 and 3.

The signature observed near 3341 cm^{-1} (see Figs. 2 and 3) corresponds to the Q-branch of the 22202–01101 hot band for which no line mixing effects were included. In addition, the positions of a few lines of that latter band and the 30003–01101 band in HITRAN [19] were found to slightly mismatch observed ones, leading to first derivative like signatures in the residuals observed in the R branch and on the high-J side of the P branch of the 21102–00001 band. We did not attempt to correct these small errors.

As is well known ([35] and references therein) and observed in Fig. 4, the Voigt line shape model can leave characteristic W-shaped signatures in the residuals. Because the Rautian model only applies to the Doppler component of the line profile, the signature observed in the residuals at high pressure is significantly reduced only when using the qsdVoigt model. At the lower pressure, both the Rautian and qsdVoigt models reproduce the observed line profile better than the Voigt line shape.

The squares of the vibrational transition dipole moments derived using Eq. (2) from the individual line intensities measured in this work for the 21102–00001 band of $^{12}C^{16}O_2$ with the qsdVoigt model are compared in Fig. 5 with HITRAN [19,36] and the measurements reported by Toth [7] and Devi et al. [9]. The present measurements agree within about 5% with previous data, except for those of Ref. [7]. The square of the vibrational transition dipole moment $|R_0|^2$ and Herman Wallis coefficients [Eq. (3)] determined for the 22202–01101 band of $^{12}C^{16}O_2$ with the 3 line shape models are listed in Table 2, together with the values reported by Devi et al. [9]. All the reported values of A_1^{RP} agree within 3 times the statistical uncertainties, while the presently determined A_3^{RP} coefficients and $|R_0|^2$ are significantly lower and from 2.9 to 4.1% higher than in Ref. [9], respectively. In spite of this, Fig. 6 shows that the rotational dependence of the intensities in the P and R branches calculated with the parameters obtained in this work agrees well with the measurements of Ref. [9], the present line intensities being roughly 3% lower. Fig. 6 also shows that the line intensities available for the R branch in HITRAN [19] are about 4% higher than Devi et al [9].

Self-broadening coefficients for carbon dioxide vibration–rotation lines have been quite extensively measured (see for example the review by Gamache et al. [37]). The self-broadening coefficients measured in this work for the 21102–00001 band of $^{12}C^{16}O_2$ with the 3 line shape models are presented in Fig. 7. Our results are compared with the only measurements reported for that band (using the Voigt profile) [7], with measurements published by Predoi-Cross et al. [38] for the 30013–00001 band of the same isotopologue using the qsdVoigt line shape model, with the predictions of Gamache and Lamouroux [12] and with data available in GEISA [39]. For the P and R branches, the self-broadening coefficients measured with the Voigt and Rautian models are essentially the same, and about 2.5% lower than the parameters measured for the 30013–00001 band [38] and predicted for the 21102–00001 band [12]. Note that the latter are characterized by an

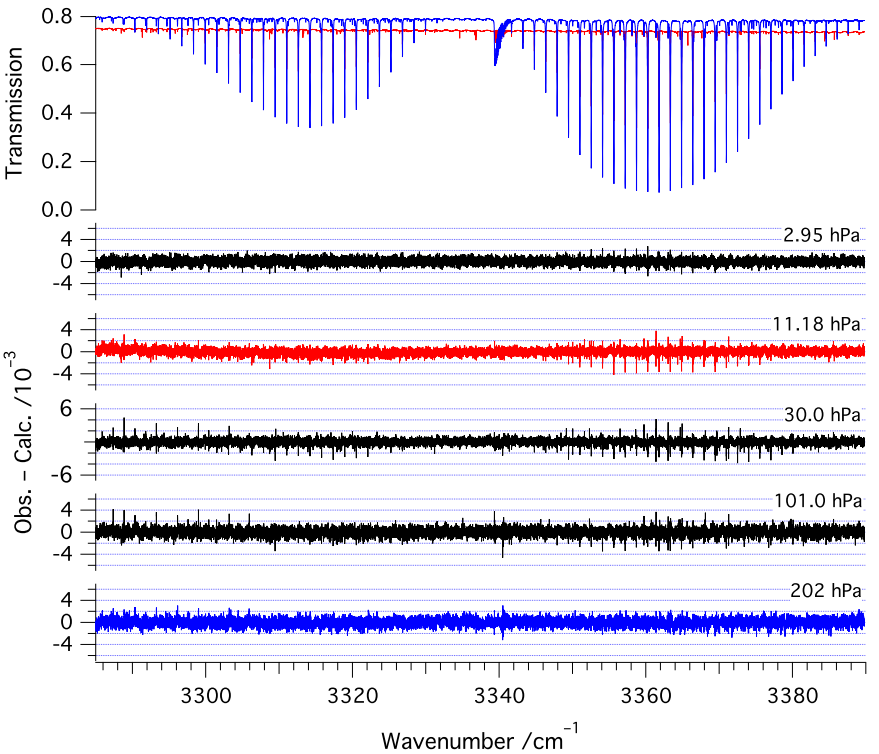

Fig. 2. Observed single beam spectra of the 21102–00001 band of $^{12}C^{16}O_2$ (nos. 2 and 5 in Table 1, upper panel) and residuals obtained for spectra nos. 1–5 by fitting the molecular line shape to a quadratic-speed-dependent Voigt line shape model.

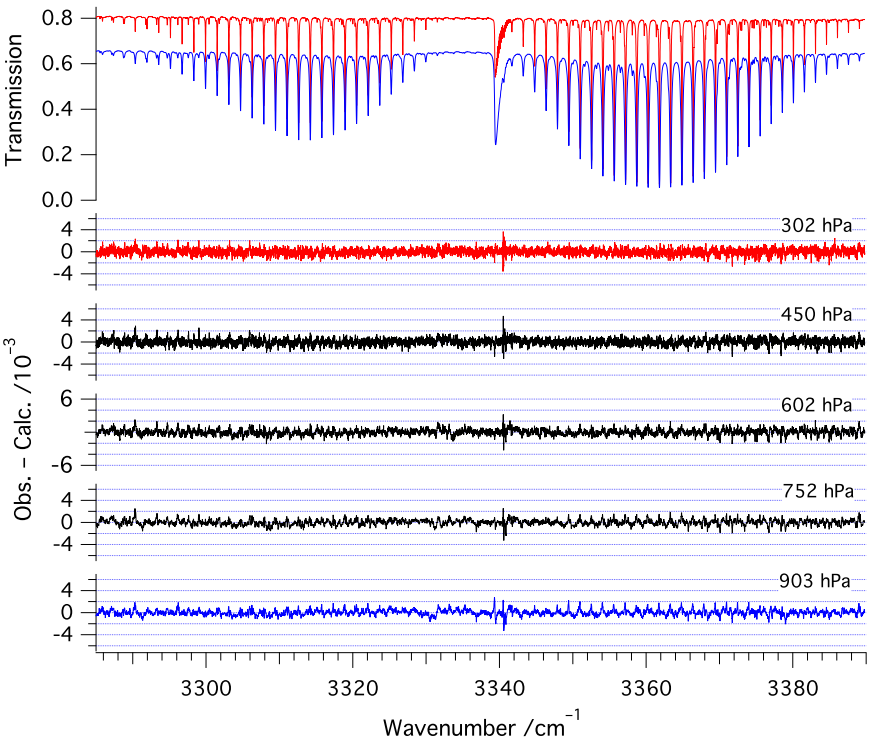

Fig. 3. Same as Fig. 2 for spectra nos. 6 and 10 (upper panel) and nos. 6–10 (lower panels) in Table 1.

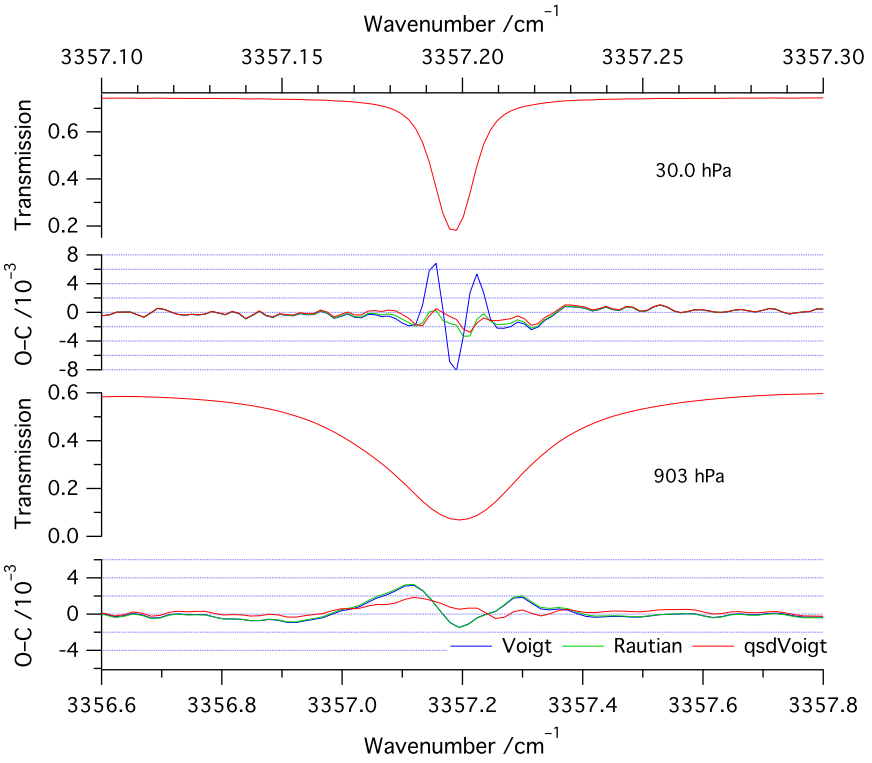

Fig. 4. Comparison of the residuals of fits obtained using 3 line shape models of the R(22) profile observed at low and the highest pressures achieved in the present work (spectra nos. 3 and 10 in Table 1).

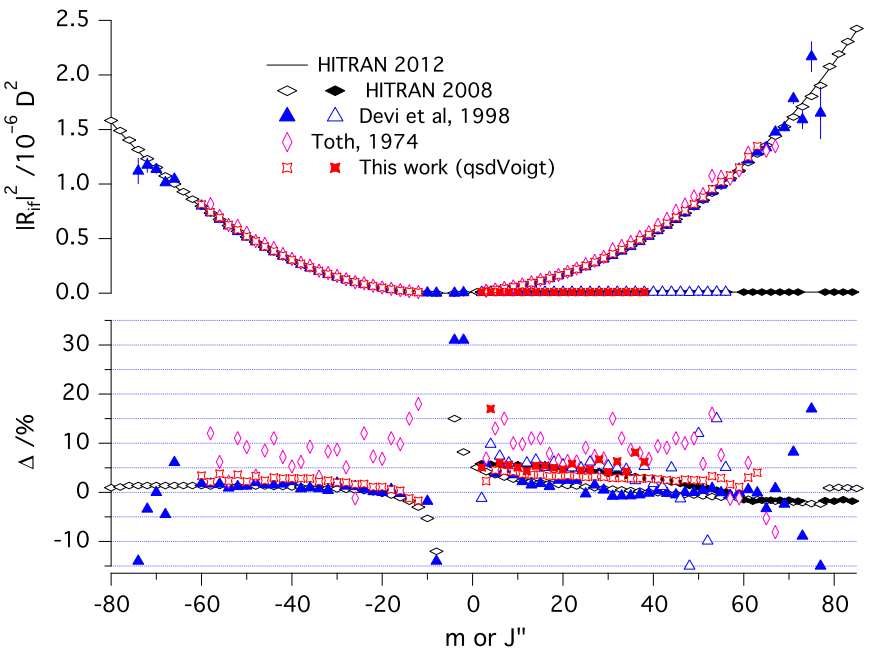

Fig. 5. Rotational dependence of the square of the vibrational transition dipole moment of the 21102–00001 band of $^{12}C^{16}O_2$, measured in this work with the quadratic-speed-dependent Voigt (qsdVoigt) model, available in HITRAN 2012 [19] and 2008 [36], and reported by Toth [7] and Devi et al. [9] (upper panel). When two symbols are provided for a data set, the first one applies to R- and P-branch lines and the second to Q-branch lines. Differences with HITRAN 2012 are presented in the lower panel. J'' applies to Q-branch lines, while $m=-J$ and $J+1$ for P- and R-branch lines, respectively. The error bars represent the uncertainty of measurement (1σ). The uncertainties reported in HITRAN 2012 and 2008 for the data presented here are $\geq 20\%$ and 2–6% [10–20% for $|m|>76$ (P- and R-branches) or $J''>58$ (Q-branch)], respectively.

uncertainty of 1–2% in HITRAN 2012 [19]. The use of the qsdVoigt model leads to a better agreement with previous work, which is excellent for the P branch. The self-broadening parameters measured for P(58) and P(60) as well as for R(56) and R(58) are slightly smaller than for neighboring lines. As the corresponding transitions involve the same $J=57$ and 59 upper levels, these smaller γ^0 coefficients may correspond to some physical phenomenon affecting these levels.

The parameters characterizing the speed dependence of the self-broadening coefficients measured using the qsdVoigt line shape model are presented in Fig. 8. They are divided by the corresponding self-broadening coefficients to allow comparison with measurements reported for the 30012–00001 [40] and 30013–00001 [41] bands. Such a comparison seems to be appropriate as the vibrational dependence of the γ_2^0 coefficients can be expected to be as small as that of the corresponding broadening parameters. Although the present measurements for the P and R branches (using the "true" ILS) are close to previous work, the rotational dependence of γ_2^0/γ^0 is somewhat smaller (in fact, almost non-existent for the P branch) indicating that the presently measured γ_2^0 have a rotational dependence similar to the self-broadening coefficients. Interestingly, the present measurements for Q-branch lines agree very well with previous work, except at low J most probably because the weak line mixing approximation does not apply in that range. As shown by the results obtained with the "ideal" ILS, neglecting the asymmetry of the line shapes systematically reduces the values of γ_2^0/γ^0 by about 10–15%.

The self-shift coefficients measured in this work for P- and R-branch lines of the 21102–00001 band of $^{12}C^{16}O_2$ are presented in Fig. 9, together with the predictions of Gamache and Lamouroux [12]. Contrary to the self-broadening, the self-shift coefficients measured with the 3 line shape models agree, except for a few low J lines. Their absolute values determined using the "true" ILS are almost systematically smaller than the predictions [12], exhibiting discrepancies of about 5–20% in the R branch and 20–30% for P-branch lines. The discrepancies observed for the R-branch lines are in line with the uncertainties stated for the air shift coefficients in HITRAN 2012 (10–20% [19]), predicted similarly [12]. The self-shift coefficients measured for R(52) to R(58) are significantly lower than for neighboring lines. It is unfortunately difficult to state that similarly reduced δ^0 coefficients are observed for P(54)–P(60). As these reduced self-shift coefficients are observed for roughly the same lines as for the self-broadening coefficients (see above), these variations in the self-shift coefficients could be associated with some perturbations affecting the upper levels, as was the case for the $\nu_1+3\nu_3$ band of acetylene [42]. Similar to what observed for the speed dependence of the self-broadening coefficients, neglecting the asymmetry of the observed line shapes almost systematically reduces the absolute values of the self-shift coefficients by about 5–10%.

The narrowing coefficients measured in the P and R branches with the Rautian line profile function using the "ideal" and "true" ILS are presented in Fig. 10. Also displayed in this figure is the frequency of velocity-changing collisions

Table 2
Square of the vibrational transition dipole moment and Herman Wallis coefficients (Eq. (3)) for the 22202–00001 band of $^{12}C^{16}O_2$. The numbers between parentheses are the statistical uncertainties (1σ).

	This work			Devi et al. [9]
Parameter	Voigt	Rautian	qsdVoigt	Voigt
$\lvert R_0\rvert^2$ (10^{-9} D^2)	5.685(12)	5.670(12)	5.617(11)	5.46(8)
A_1^{RP}	0.2184(3)	0.2185(3)	0.2189(3)	0.2223(18)
A_3^{RP} (10^{-6})	0.93(7)	0.97(7)	1.13(7)	2.5(4)

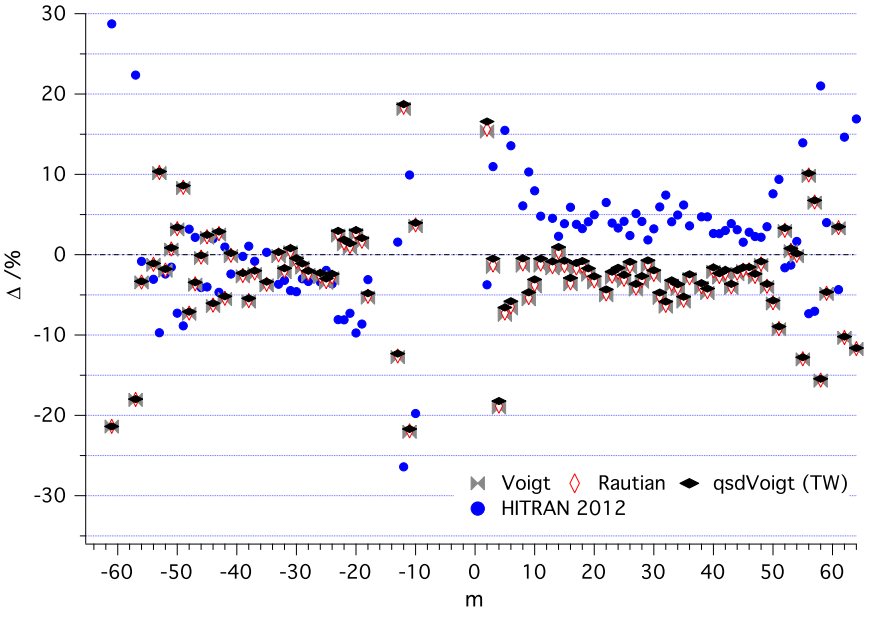

Fig. 6. Differences Δ with the measurements reported by Devi et al. [9] of the intensities of P- and R-branch lines of the 22202–01101 band of $^{12}C^{16}O_2$ calculated at 296 K with the parameters obtained in this work using the 3 line shape models (TW, listed in Table 2) and available in HITRAN [19].

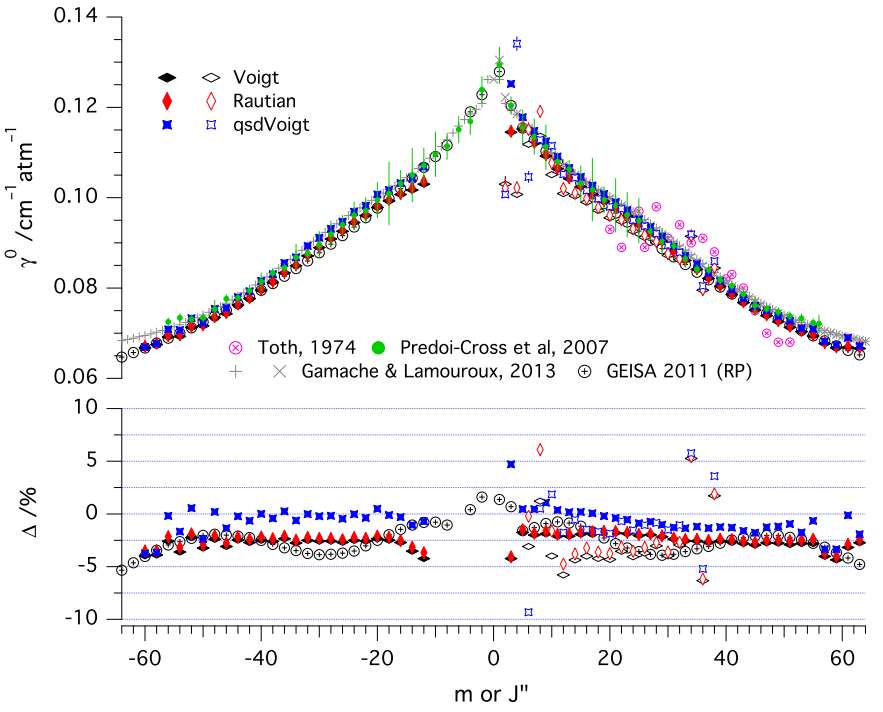

Fig. 7. Self-broadening coefficients for the 21102–00001 band of $^{12}C^{16}O_2$ measured in this work using 3 line shape models (upper panel: Rautian = hard-collision Rautian and Sobel'man; qsdVoigt = quadratic-speed-dependent Voigt). The filled and open black, red and blue symbols correspond to P-/R- and Q-branch lines, respectively. Measurements reported for the same band by Toth [7] using the Voigt line shape and for the 30013–00001 band by Predoi-Cross et al. [38] using the quadratic-speed-dependent Voigt model are also presented, together with data in GEISA [39] and the predictions of Gamache and Lamouroux [12]. The lower panel presents differences Δ of the present measurements and GEISA with the predictions of Ref. [12] (the differences for this work for $J''=2$ and 4 in the Q branch are off-scale). (For interpretation of the references to color in this figure caption, the reader is referred to the web version of this paper.)

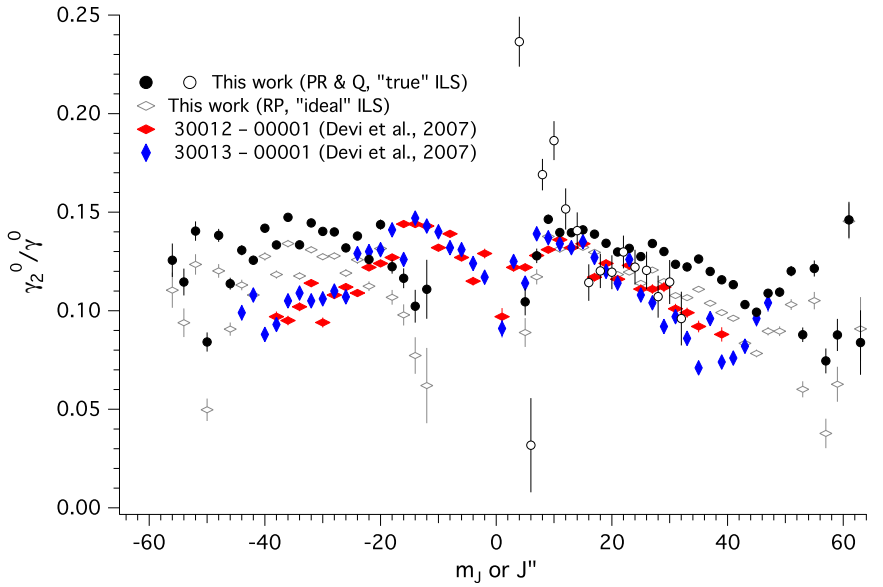

Fig. 8. Relative quadratic-speed-dependence of self-broadening coefficients measured in this work for the 21102–00001 band of $^{12}C^{16}O_2$ using a "true" or "ideal" ILS (see text for details), and measurements reported for the 30012–00001 [40] and 30013–00001 [41] bands. The error bars provided for the present measurements are the uncertainty of measurement (1σ), estimated by the least squares fitting algorithm.

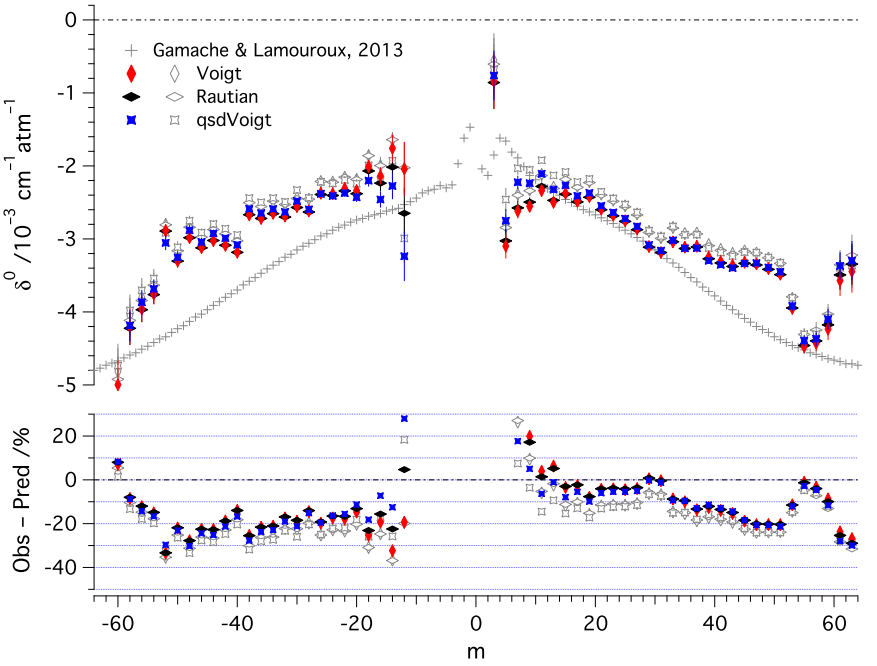

Fig. 9. Self-shift coefficients for P- and R-branch lines of the 21102–00001 band of $^{12}C^{16}O_2$ measured in this work using 3 molecular line shape models (Rautian = hard-collision Rautian and Sobel'man; qsdVoigt = quadratic-speed-dependent Voigt) and a "true" (colored symbols) or "ideal" (gray open symbols) ILS (see text for details), and predicted by Gamache and Lamouroux [12] (upper panel). The error bars are the uncertainty of measurement (1σ), estimated by the least squares fitting algorithm. The lower panel presents differences between the present measurements and the predictions of Ref. [12] (the differences for R(2) and R(4) are off-scale). (For interpretation of the references to color in this figure caption, the reader is referred to the web version of this paper.)

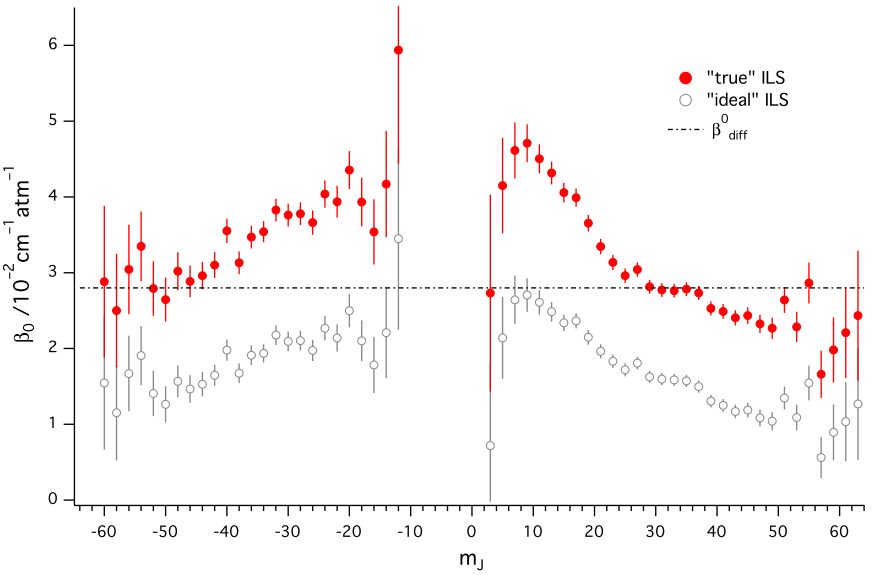

Fig. 10. Narrowing coefficients measured for P- and R-branch lines of the 21102–00001 band of $^{12}C^{16}O_2$ using a hard-collision Rautian and Sobel'man molecular line shape model and a "true" or "ideal" ILS (see text for details). The error bars are the uncertainty of measurement (1σ), estimated by the least squares fitting algorithm. The estimated frequency of velocity-changing collisions β^0_{diff} [35] is also shown.

β^0_{diff}, deduced from the relation [35]:

$$\beta^0_{\text{diff}} = \frac{k_B T}{2\pi c m_a D} \tag{5}$$

where c is the velocity of light, m_a is the mass of the active molecule and $D = 0.105\ \text{cm}^2\ \text{s}^{-1}$ is the mass self-diffusion constant of CO_2. The latter was estimated at 293 K and 1 atm assuming a Lennard–Jones CO_2–CO_2 interaction potential, with parameters $\sigma = 3.996 \times 10^{-8}$ cm and $\epsilon/k_B = 190$ K [43], leading to $\beta^0_{\text{diff}} = 0.0280\ \text{cm}^{-1}\ \text{atm}^{-1}$. As also observed

for example for self-broadened O_2 [44], the narrowing coefficients presented in Fig. 10 seem to indicate that the narrowing effect induced by velocity changing collisions decreases as the molecule rotates faster. However, this conclusion should probably be tempered as the Rautian model does not seem to be the most appropriate to reproduce the observed shape of the CO_2 lines (see Fig. 4). Additionally, most of the narrowing coefficients measured for the P- and R-branch lines with the "true" ILS are larger than β^0_{diff}, which can be interpreted as an indication that the broadening coefficients are affected by speed dependence [44]. Caution should be exercised here as the asymmetry of the observed line shapes appears to have a very strong impact on the measured narrowing coefficients. Indeed, neglecting it reduces β_0 by as much as a factor of about 2, as shown in Fig. 10. Such a strong effect is most probably related to the fact that the narrowing coefficients are determined from the spectra recorded at the higher resolutions, affected the most by distortions of the ILS. Note that, even if the absolute values of the narrowing coefficients are somewhat uncertain, their rotational dependence is almost unaffected by the ILS used.

The error bars provided in Figs. 5, 7–10 and 12–13 only reflect the statistical uncertainties (1σ) on the measured parameters, which are almost always smaller than the size of the symbols. Taking into account the accuracy of measurement of the temperature, pressure and path length provided in Table 1, we estimated that the resulting combined uncertainties are in the range 2–4% for the line intensities (from low to high J), better than 2% for the self-broadening coefficients, and better than 4% for the self-shift parameters of intermediate J lines. Note that the latter was estimated assuming that self-shift coefficients are inversely proportional to the temperature. The same assumption was used to estimate the combined uncertainties on the first-order line mixing coefficients to be better than about 10% for intermediate J lines (the uncertainties are smaller for R-branch lines). Assuming that the combined uncertainties on the quadratic-speed-dependence and narrowing coefficients scale as the ratio of these parameters to the self-broadening coefficients, we estimated that they are better than 10% for intermediate J lines. Inaccuracies in the modeling of the asymmetry of the observed line shapes provided by the "true" ILS certainly impact these estimates, however with a magnitude a priori smaller than the changes observed when comparing the use of the "true" and "ideal" ILS. The weak lines underneath the band of interest, the line shape of which being not necessarily accurately modeled, should also impact the combined uncertainties stated above.

4. Theoretical approach

4.1. Basic relations for relaxation matrix modeling and spectra calculation

The Energy-Corrected Sudden approach based on a symmetric definition of the scalar product in the Liouville space yields the symmetric spectral density $S^{(r)}(\nu)$ as a function of the rotational wavenumber ν [45–47]:

$$S^{(r)}(\nu)=\pi^{-1}\sum_{kk'}A_k^{(r)*}[i(\nu-\nu_k)\delta_{kk'}+n_b\Gamma^{(r)}(\nu)]^{-1}_{kk'}A_{k'}^{(r)}. \tag{6}$$

In this equation, the summation runs over the pairs of rotational transitions $k=\{i,f\}$ and $k'=\{i',f'\}$, the weights $A_k^{(r)}$ (the asterisk denotes the complex conjugation) are related to the intensities of isolated rotational lines ($=A_k^{(r)2}$), ν_k are the proper frequencies of the free active molecule, n_b is the bath-gas density (in amagat), and $\Gamma^{(r)}(\nu)$ is the rotational relaxation matrix describing the interactions of the active molecule with the bath, i.e. relaxation of the rth-rank molecular tensor induced by collisions with surrounding molecules. Hereafter, for brevity, the rank superscript on the quantities entering Eq. (6) will be occasionally omitted. In general, for arbitrary large wavenumber detunings, $\Gamma^{(r)}$ depends on the wavenumber of the incident radiation ν (the so-called "non-Markovian" relaxation matrix). However, in the spectral region near molecular resonances ν_k, the difference between the photon wavenumber and the rotational transition wavenumber can be neglected, and the relaxation matrix can be considered as frequency-independent (Markovian) matrix $\Gamma^{(r)}(0)\equiv\Gamma^{(r)}$. Owing to the chosen symmetric metric of the Liouville space, the relaxation matrix satisfies all fundamental relations obtained from first principles (see [45–47] for more details), including the symmetry relation and the double-sided sum rules:

$$\Gamma^{(r)}_{kk'}(\nu)=\Gamma^{(r)}_{k'k}(\nu), \tag{7}$$

$$\sum_{k'\neq k}\Gamma^{(r)}_{kk'}(\nu)A^{(r)}_{k'}=\sum_{k'\neq k}A^{(r)}_{k'}\Gamma^{(r)}_{k'k}(\nu)=-\Gamma^{(r)}_{kk}(\nu)A^{(r)}_{k}. \tag{8}$$

The first relation means that it is sufficient to model just one-half of the non-diagonal part of $\Gamma^{(r)}$. The second one enables computing the diagonal elements from the off-diagonal ones (the double-side character of the sum rules insures correct asymptotics and positive values for the intensities in the far wings). We underline that the imaginary part of the rotational relaxation matrix is completely neglected in the present model.

A non-Markovian expression for the off-diagonal elements $\Gamma^{(r)}_{kk'}(\nu)$ coupling two rotational transitions was proposed in [46] and cast into an ECS-type form in [47]. It can be written as

$$\begin{aligned}\Gamma^{(r)}_{if,i'f'}(\nu)=&-\frac{1+\exp(-hc\nu/kT)}{4n_{if}n_{i'f'}}\sum_L[L]F^{Lr}_{if,i'f'}Q'_L\\&\times\left[\frac{\rho_i\Omega(\nu-\nu_{f'i})}{1+\exp[-hc(\nu-\nu_{f'i})/kT]}\right.\\&\left.+\frac{\rho_{i'}\Omega(\nu-\nu_{fi'})}{1+\exp[-hc(\nu-\nu_{fi'})/kT]}\right]\end{aligned} \tag{9}$$

where $n_{if}=[(\rho_i+\rho_f)/2]^{1/2}$ (the norm of the line-space vector $|f\rangle\langle i|$) is determined by the rotational populations $\rho_i=Z_{rot}^{-1}\exp[-BJ_i(J_i+1)/kT]$ (B is the rotational constant), $[abc\cdots]\equiv(2a+1)(2b+1)(2c+1)\cdots$, Q'_L are the basic transition rates (related to the traditional basic rates of the ECS model $Q_L=A[L(L+1)]^{-\alpha}\exp[-\xi BL(L+1)/kT]$ [48]), $F^{Lr}_{if,i'f'}$ are the symmetrized Percival–Seaton coefficients, and $\Omega(\nu)=[1+h^2c^2b_c^2\nu^2/(12n\overline{v}^2)]^{-n}$ ($\overline{v}$ stands for the mean thermal velocity and $n=1$ or 2) is the adiabaticity factor. For a chosen n, the set of ECS parameters A, α, ξ and b_c completely determines the relaxation matrix for a given temperature.

For the infrared absorption ($r=1$) bands characterized by non-zero values of vibrational angular momenta in the initial and final states (l_i and l_f), the generalized expressions for $A_{if}^{(r)}$ and $F_{if,i'f'}^{Lr}$ were obtained in [16]

$$A_{if}^{(r)} = (-1)^{J_i+l_f}[J_iJ_f]^{1/2}\begin{pmatrix} J_i & r & J_f \\ l_i & l_f-l_i & -l_f \end{pmatrix} n_{if}, \tag{10}$$

$$F_{if,i'f'}^{Lr} = (-1)^{r+l_i+l_f}[J_iJ_fJ_i'J_f']^{1/2} \times \begin{pmatrix} J_i' & L & J_i \\ -l_i & 0 & l_i \end{pmatrix}\begin{pmatrix} J_f & L & J_f' \\ l_f & 0 & -l_f \end{pmatrix}\begin{Bmatrix} J_i & J_f & r \\ J_f' & J_i' & L \end{Bmatrix}. \tag{11}$$

Eq. (11) inserted in Eq. (9) and the ECS-parameters determined previously [18] for CO_2 Raman spectra modeling ($A=28.50\times10^{-3}\,cm^{-1}\,atm^{-1}$, $\alpha=0.8292$, $\xi=0.0194$, $b_c=2.2571$ Å with $n=1$) enable calculation of the off-diagonal matrix elements for $k'<k$ (see Ref. [47] for more details); the rest of the relaxation matrix is built with Eqs. (7) and (8). As soon as the full relaxation matrix is obtained, isolated-line parameters such as the widths and line-mixing coefficients can be calculated (Sections 4.2 and 4.3). Further use of Eq. (10) in Eq. (6) yields the symmetric spectral density which can be related to the experimentally observed transmittance (Section 4.4). It should be noted that, for the experimentally studied detunings from the band center (region of validity of the impact approximation), the results of calculations with the non-Markovian matrix are identical to those obtained with the Markovian one.

4.2. Test calculation of collisional line widths

This test is mandatory to ensure that the key spectral parameters such as line widths are reasonably well predicted by our ECS model. In general, the collisional width of the rotational line located at the wavenumber ν_k is strictly given by the diagonal element $\Gamma_{kk}^{(r)}(\nu_k)$. However, as already mentioned above, the impact approximation is valid in the region of molecular resonances and the required diagonal element can be simply taken from the impact-limit relaxation matrix obtained by setting $\nu=\nu_k$ or $\nu_{k'}$ in the appropriate arguments of the adiabaticity factors:

$$\Gamma_{if,i'f'}^{(r)impact} = -\frac{1}{2}\frac{(\rho_i\rho_{i'})^{1/2}}{\rho_i+\rho_{i'}}\left[\Omega\left(\overline{\nu}_{ff'}\right)+\Omega\left(\overline{\nu}_{ii'}\right)\right]\sum_L [L]F_{if,i'f'}^{Lr}Q_L' \tag{12}$$

(the expressions for $\overline{\nu}_{ii'}$ and $\overline{\nu}_{ff'}$ can be found in [47], where the angular frequencies ω are used instead of the wavenumber ν).

The line widths calculated for both the 21102←00001 and the 22202←01101 bands are shown in Fig. 11, together with HITRAN 2008 data [36]. We do not plot our ECS widths with the other data of Fig. 7 since they are obtained from a purely rotational relaxation scheme, without any renormalization procedure and without any fitting, so that their J-dependences for high values of the rotational quantum number are less realistic than the results of Ref. [11] with adjusted interaction potential parameters. As can be seen in Fig. 11, for the main band (upper panels), our ECS model provides very realistic values of the line broadening up to $J\approx40$ [except for the P(2) line]. For higher J, the maximum difference with HITRAN 2008 data (about 10%) is observed for the R branch, whereas it is about 6% for the P and Q branches. For the hot band (lower panels of Fig. 11), the agreement with HITRAN 2008 values can be considered as quite satisfactory.

4.3. Line-mixing coefficients for the Rosenkranz profile

According to the perturbation method of Rosenkranz [10], the shapes F_k of weakly overlapped lines can be viewed as Lorentzian functions corrected for the line interference:

$$F_k(\nu-\nu_k) = \pi^{-1}\frac{\gamma_k+(\nu-\nu_k-\delta_k)Y_k}{\gamma_k^2+(\nu-\nu_k-\delta_k)^2}, \tag{13}$$

where the correction factors, the so-called first-order line-mixing coefficients, read [10,28,35]

$$Y_k = 2\sum_{k'\neq k}\frac{|R_{i'f'}|}{|R_{if}|}\frac{W_{kk'}}{\nu_k-\nu_{k'}} \tag{14}$$

and are determined experimentally from fitting on the observed line shapes. The reduced dipole transition moments as well as the relaxation matrix W correspond to the traditional (i.e. non-symmetric) definition of the scalar product in the Liouville space. The non-symmetric relaxation matrix W can be easily related to the symmetric matrix $\Gamma^{(1)}$ via [47]

$$W_{kk'} = \left(\frac{[J']\rho_{J'}}{[J]\rho_J}\right)^{1/2}\Gamma_{kk'}. \tag{15}$$

Since the ratio $|R_{i'f'}|/|R_{if}|$ is equivalent to the ratio $([J]\rho_J)^{1/2}A_{k'}/\{([J']\rho_{J'})^{1/2}A_k\}$, the structure of Eq. (14) is conserved when the symmetric metric in the Liouville space applies

$$Y_k = 2\sum_{k'\neq k}\frac{A_{k'}}{A_k}\frac{\Gamma_{kk'}}{\nu_k-\nu_{k'}}. \tag{16}$$

At the experimentally studied pressures, significant line-mixing effects are observed solely for the rotational structure of the Q-branch ($k=\{J,J\}$, $k'=\{J',J'\}$). The first-order line-mixing coefficients computed using Eq. (16) are presented and compared to their experimentally deduced values in Section 5.

4.4. Band-shape calculations

The transmittance τ at the wavenumber $\tilde{\nu}$ is defined as the ratio of the transmitted $I(\tilde{\nu})$ and incident $I_0(\tilde{\nu})$ radiations and can be calculated from the absorption coefficient $\alpha(\tilde{\nu})$ and the optical pathlength L as $\tau(\tilde{\nu})=\exp[-\alpha(\tilde{\nu})L]$. The absorption coefficient, determining the shape of an infrared band centered at the vibrational wavenumber $\tilde{\nu}_0$ as a function of the detuning $\nu=\tilde{\nu}-\tilde{\nu}_0$, can be viewed as the product of the normalized to unit area spectral density $F(\nu)$ (in cm) and the integrated absorption coefficient A (in cm^{-2}). Owing to the Boltzmann relation of detailed balance, $F(\nu)$ can be connected to its symmetric form $S(\nu)$ via a quantum asymmetry factor: $F(\nu)=2[1+\exp(-hc\nu/kT)]^{-1}S(\nu)$. The integrated absorption coefficient, in turn, can be expressed as $A=A_NN$, where A_N (in cm molecule^{-1}) is the integrated band intensity per active molecule and N (in molecule cm^{-3})

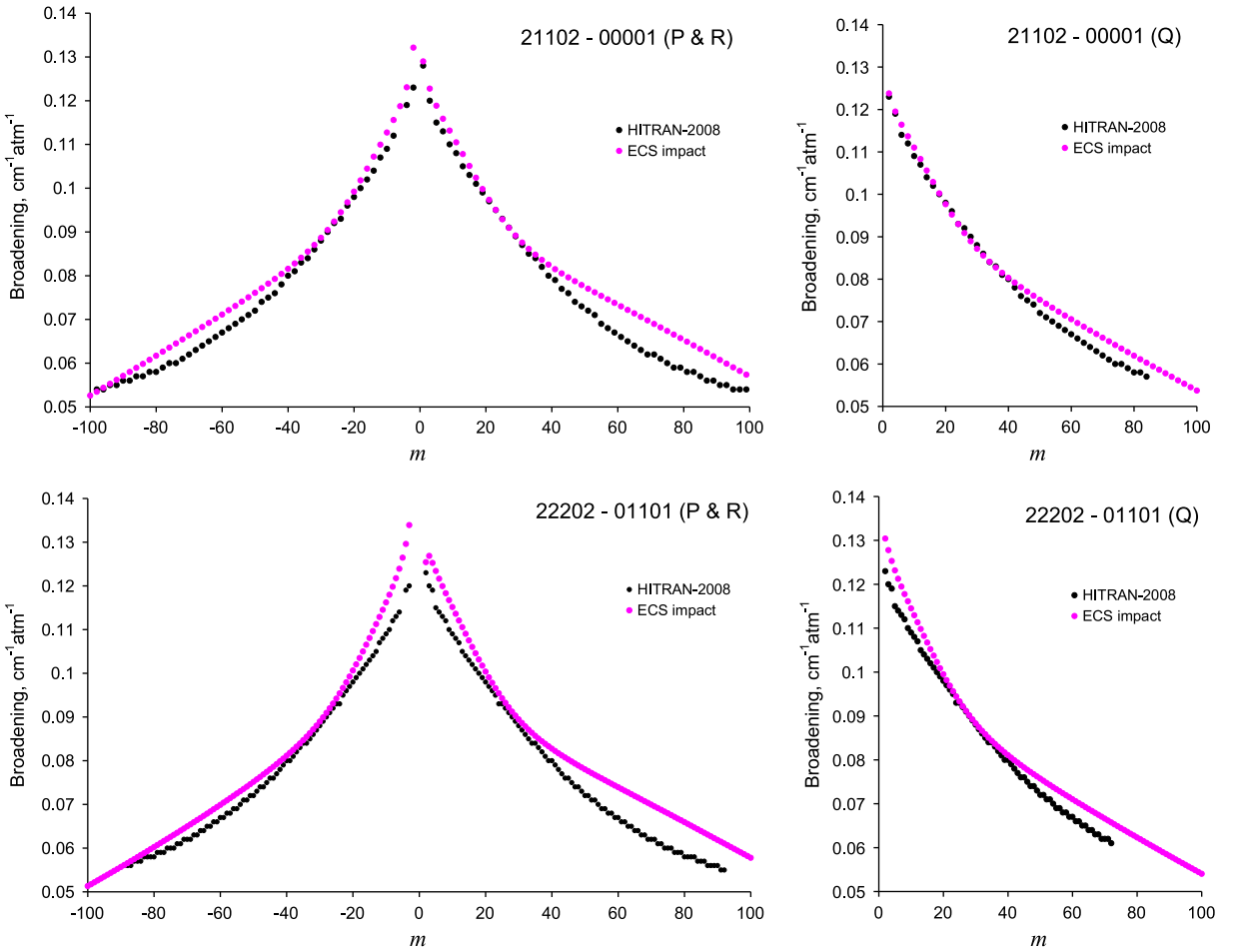

Fig. 11. Comparison of ECS-calculated self-broadening coefficients with those available in the HITRAN database [36] for the main band 21102←00001 (upper panel) and the most intense hot band 22202←01101 (lower panel). The quantum number m is determined as $m=-J$ for the P branch, as $m=J$ for the Q branch and as $m=J+1$ for the R branch.

is the number of active molecules per unit volume. The numerical value of A_N for a given band can be obtained by a simple summation of isolated-line intensities listed in spectroscopic databases, whereas N can be evaluated from the active-gas density n_a (in amagat): $N=N_L n_a$, where $N_L=2.686754\times10^{19}\ \mathrm{cm}^{-3}$ is Loschmidt's number. Therefore, the theoretical transmittance reads

$$\tau(\nu)=\exp\{-2[1+\exp(-hc\nu/kT)]^{-1}A_N N_L n_a LS(\nu)\}. \quad (17)$$

For infrared bands with Coriolis interactions, the rotational isolated-line intensities are perturbed by intensity transfer from/to the other bands involved in the same resonance interaction of vibrational states. Therefore, to calculate the spectral density $S(\nu)$ with Eq. (6), the "symmetric" intensities A_k^2 should be multiplied by the Herman–Wallis factors F_k^{HW}. As the unit-area normalization of the spectral density is no more conserved after this multiplication, only the rotationless part S_ν^0 of the integrated band intensity A_N should be used to get the absorption coefficient. [Alternatively, $S(\nu)$ calculated with A_k corrected by $(F_k^{HW})^{1/2}$ can be renormalized to unity and the absorption coefficient obtained via the usual multiplication by A_N.] In addition, the usual factor $\tilde{\nu}/\tilde{\nu}_0[1-\exp\{-hc\tilde{\nu}/kT\}]$ should be introduced. For the purposes of the present work, the proper rotational frequencies ν_k were deduced from the line positions available in HITRAN 2008 [36], whereas F_k^{HW} and S_ν^0 were taken from Ref. [49]. For convenience, the latter are reproduced in Table 3.

Table 3
Rotationless band strengths S_ν^0 (in 10^{-22} cm molec^{-1}) and parameters involved in the Herman-Wallis factor $F_k^{HW}\equiv F(m)=(1+a_1m+a_3m^3)^2$ applied to P ($m=-J$) and R ($m=J+1$) branches (adapted from Ref. [49]). $F(m)=1$ for Q-branch lines.

Band	S_ν^0	a_1	a_3
21102←00001	0.1219	0.1615	0.14
22202←01101	0.00553	0.22	0.23

It should also be noted that, for the low-pressure regime, the spectral density calculated from molecular collisions should be corrected for the Doppler broadening effects. In the present work, we assumed that collisional broadening and Doppler broadening are statistically independent (which is equivalent to the use of the Voigt profile model for isolated lines) and accounted for the latter by convoluting $S(\nu)$ with a

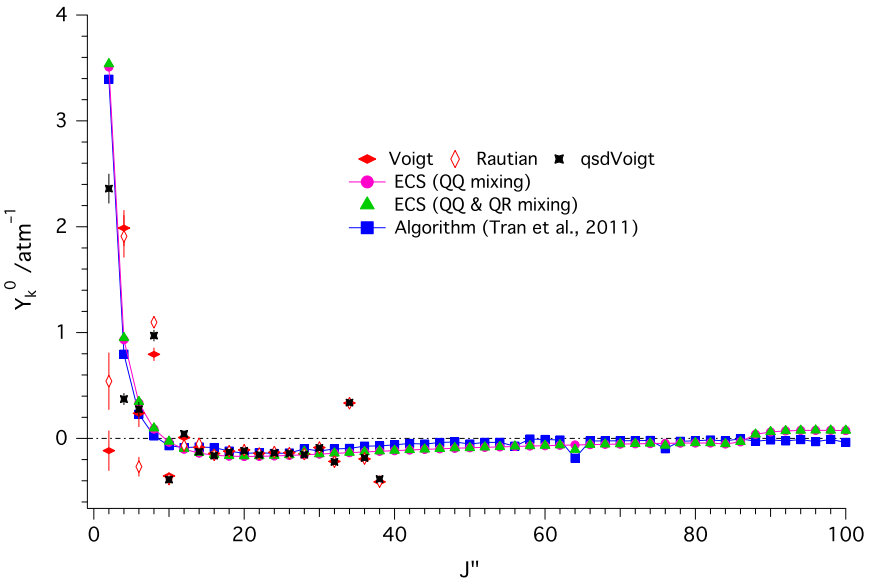

Fig. 12. Comparison of line-mixing coefficients (Rautian, hard-collision Rautian and Sobel'man; qsdVoigt, quadratic-speed-dependent Voigt) measured with the "true" ILS with values calculated from the ECS relaxation matrix and with the approach of Ref. [11] for the Q branch of the 21102–00001 band of $^{12}C^{16}O_2$. The error bars are the uncertainty of measurement (1σ) estimated by the least squares fitting algorithm. (For interpretation of the references to color in this figure caption, the reader is referred to the web version of this paper.)

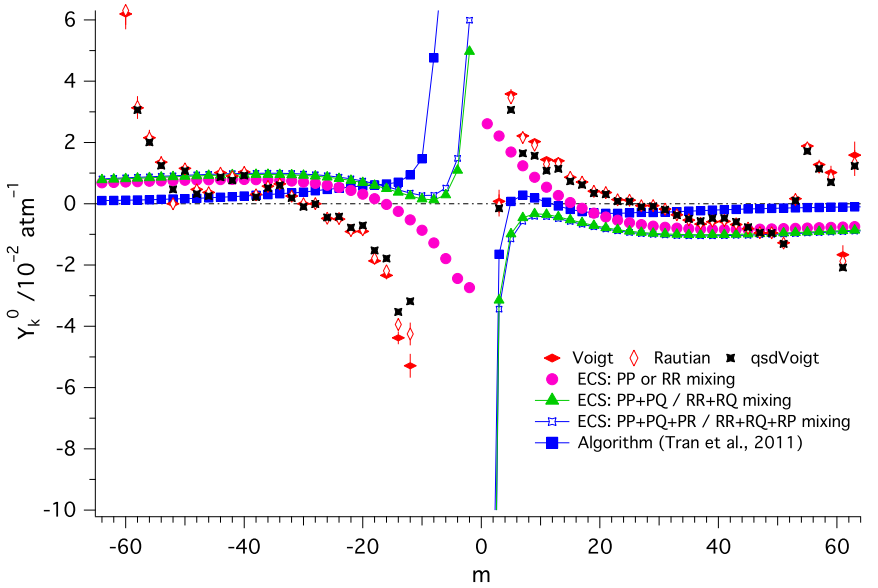

Fig. 13. Comparison of line-mixing coefficients (Rautian, hard-collision Rautian and Sobel'man; qsdVoigt, quadratic-speed-dependent Voigt) measured with the "true" ILS with values calculated from the ECS relaxation matrix and with the approach of Ref. [11] for the R and P branches of the 21102–00001 of band of $^{12}C^{16}O_2$. The error bars are the uncertainty of measurement (1σ) estimated by the least squares fitting algorithm. (For interpretation of the references to color in this figure caption, the reader is referred to the web version of this paper.)

Gaussian function of fixed half-width $\gamma_D = 3.581163139 \times 10^{-7}(T/m_a)^{1/2}\tilde{\nu}_0 = 0.0031016\ \mathrm{cm}^{-1}$ (m_a is the mass of the active molecule in a.m.u.). Moreover, for comparison with the recorded spectra, the calculated transmittance has been multiplied by the experimentally determined baseline, expressed as the product of a slanted straight line and the channeling spectrum $C(\tilde{\nu})$ given by Eq. (4). Some ECS-calculated band shapes are presented and compared to the experimental spectra in the next section.

5. Comparison of theory with the present measurements

The first-order line mixing coefficients Y_k^0 measured with the 3 line shape models are presented in Fig. 12 (Q-branch) and Fig. 13 (R and P branches). The measured values are generally independent of the line shape model, except at low J most probably as a result of the corresponding stronger line mixing. The rotational dependence observed for the P and R branches is similar to that

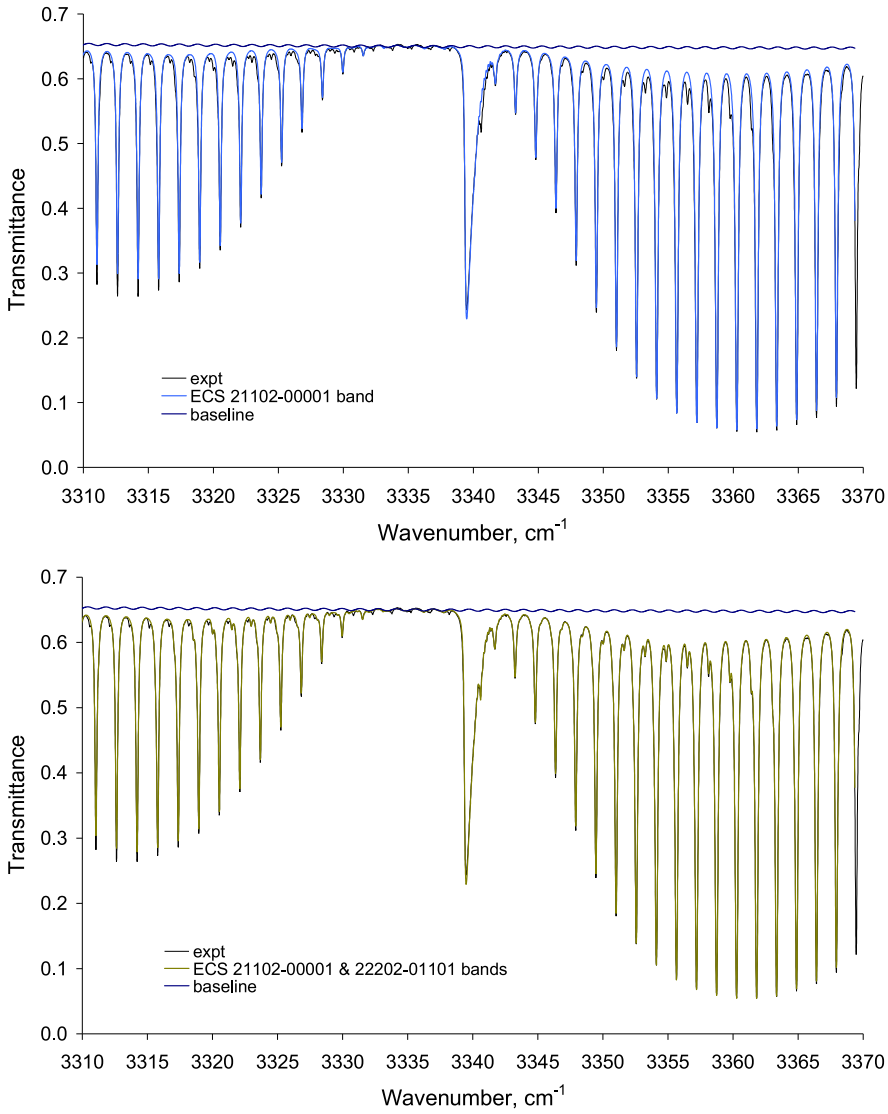

Fig. 14. Transmittance calculated by the ECS approach for the main band (upper panel) as well as for both the main and the most intense hot bands (lower panel), compared with the experimental spectrum (no. 10 in Table 1).

observed for other bands [38]. These figures also include the ECS coefficients $Y_k^0 = Y_k/P$ (P is the CO_2 pressure) calculated with Eq. (16), and those estimated with the algorithm of Tran et al. [11].

For the Q-branch case (Fig. 12), the present calculations were first performed considering only the interferences within the Q-branch itself (summation on the off-diagonal relaxation matrix elements $k' = \{J', J'\}$ coupling Q–Q transitions). Then, the interferences with the R-branch lines were added (summation on the off-diagonal elements $k' = \{J', J'\}, \{J', J'+1\}$ coupling Q–Q and Q–R transitions). The incorporation of interferences with the P-branch did not change the Y_k^0 values (since the P-lines are quite far from the Q-lines), so that only the first two theoretical series are shown. With the single intra-Q-branch coupling included, the calculated values (pink circles) agree very well with both our Voigt profile measurements and the estimations by the algorithm of Tran et al. [11] for $J=2$. For higher J-values, our approach gives generally more significant line-mixing than the predictions by the algorithm of Ref. [11], and the ECS results vary smoothly with increasing J, as expected for a well isolated Q-branch. Note that the change of sign observed for our values for $J \geq 86$ is due to the absence of line positions above $J=84$ in HITRAN 2008 [36] and errors introduced by the calculations of these positions with the rotational constants of the initial and final vibrational states. When the interference with the R-branch is added (green triangles), our calculations for $J=28$, 64 and 76 get closer to the corresponding predictions by the algorithm of Ref. [11]. Indeed, for these J-values, the Q-branch lines are perturbed by the very closely lying R(0), R(4) and R(6) lines (with separations of 0.00746, 0.003243 and 0.006653 cm^{-1}, respectively). The Q(50) and R(2) lines do not interfere as they are separated by 0.066534 cm^{-1}.

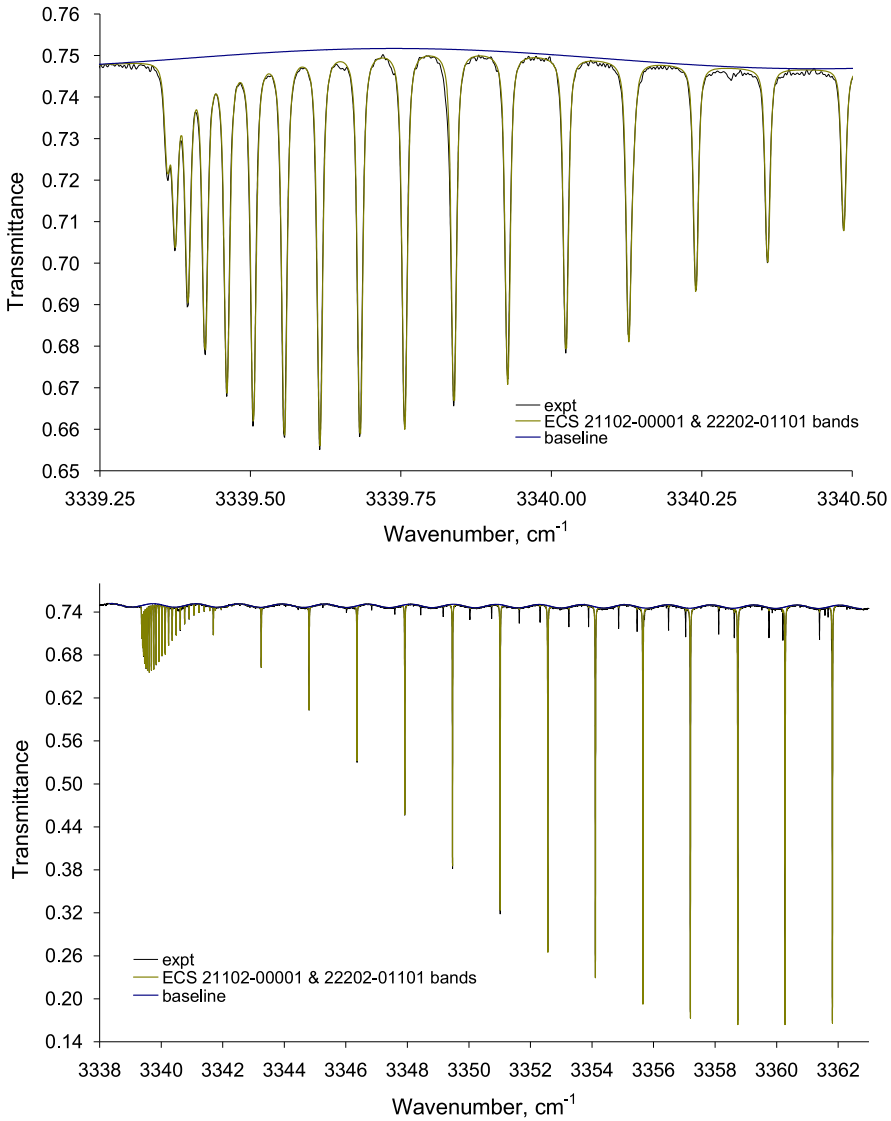

Fig. 15. Transmittance calculated by the ECS approach (the main plus the most important hot bands) in the Q branch region (upper panel) and in an enlarged region including a portion of the R branch (lower panel), compared with the experimental spectrum (no. 3 in Table 1).

For the P and R branches (Fig. 13), accounting for the line interferences in the complete P–Q–R manifolds leads to similar m-dependences for the ECS values of the present approach (blue open symbols connected by a solid blue line) and for the values obtained with the algorithm of Ref. [11] (blue squares connected by a solid blue line). However, for small $|m|$ values, both theoretical approaches provide the sign opposite to the measurements. To seek for the origins of this discrepancy, we performed additional ECS calculations considering first the P and R branches as completely isolated (interferences between P–P or R–R lines only, represented by solid magenta circles) and then adding the interferences with the Q-branch (P–P plus P–Q or R–R plus R–Q interferences, shown by solid green triangles). When the branches are treated as isolated, the sign of our ECS line-mixing coefficients becomes coherent with that of our measurements. As soon as the Q-branch is included, the sign changes and the retrieved Y_k^0 values nearly correspond to those obtained for the completely interfering P–Q–R manifolds. This means that the interferences with the (strongly mixed) Q-lines significantly perturb the theoretical Y_k^0 values, so that their asymptotic behavior for $|m|\rightarrow 0$ is reversed. (We remember that the line-mixing coefficients in the Rosenkranz model are obtained in the first order of the perturbation theory, whereas the ECS parameters are determined from Q-branch characteristics).

The full band shapes calculated with the ECS approach for the highest studied pressure of ~ 0.89 atm are compared to the recorded spectrum in Fig. 14. The upper panel of this figure shows the theoretical transmission due to the main band $21102\leftarrow 00001$ only. One can see that, for this pressure, the modelling yields a very realistic shape of the P–Q–R manifold. Adding the absorption of the hot band

22202←01101 (lower panel of Fig. 15) improves significantly the theoretical transmission in the inter-line regions and leads to an almost perfect match of experimental intensities for R-branch lines.

Similar calculations for a low pressure of ~0.03 atm (no. 3 in Table 1) are presented in Fig. 15. Looking at the main portion of the Q branch (upper panel) and at an extended region including the Q branch and a portion of the R branch (lower panel), we see that, in this low-density regime, the collisional narrowing effects become visible on first Q lines, but in general the ECS approach developed for high pressures (where the collisional broadening and the line-mixing mechanisms determine the allowed absorption) still works well. It is now well established and widely recognized [35,50] that two main sources of line narrowing are the velocity-changing collisions (reducing the Doppler component of the total line width) and the speed-dependence of the relaxation rates. For the ECS approach operating with purely collisionally broadened line shapes (homogeneous Lorentzian profiles for the limit case of isolated lines), a coherent way to include the line narrowing seems to be accounting for the former of the abovementioned mechanisms. This improvement will be the subject of a separate study.

6. Conclusion

High resolution Fourier transform spectra of the weak 21102–00001 band of $^{12}C^{16}O_2$ near 3340 cm^{-1} have been recorded at 293 K and 10 different CO_2 pressures ranging from about 3 to 900 hPa. Modeling the observed asymmetry of the lines assuming a misaligned Fourier transform spectrometer, isolated-line intensities and collisional parameters, as well as first-order line-mixing coefficients was retrieved using Voigt, hard-collision Rautian and Sobel'man, and quadratic-speed-dependent Voigt profiles. Consistent self-broadening coefficients were obtained with the first 2 line shape models, while agreement with previous work [12,38] was better with the latter (it was excellent for the P branch). All 3 line profiles led to consistent line intensities, self-shift coefficients and first-order line mixing coefficients (except for some low *J* lines, probably as a result of stronger mixing). This is the first time that self-shift and first-order line mixing coefficients are measured for this band. Comparison of the measured parameters with previous measurements and predictions puts forward the agreements and discrepancies. The measured parameters are provided as supplementary material in this paper.

The line-mixing coefficients for the Q, R and P branches have also been obtained theoretically by the use of the Energy-Corrected Sudden approach with a symmetric definition of the scalar product in the Liouville space. Without any additional adjustable parameter, with the single previously determined for the isotropic Raman scattering set of parameters, this method yielded very realistic values, comparing very favorably with both our experimental data and estimations performed with the algorithm of Ref. [11]. After having introduced some corrections for the vibration–rotation interactions (Herman–Wallis coefficients for the isolated line intensities, line positions taken from HITRAN database) and having related the spectral density to the radiation transmittance, we computed the complete band shapes for the main band of interest and the most important hot band for the highest and the lowest (computationally accessible) pressures taking account of the Doppler effect. Comparison of this "straightforward" ECS-modeling of complete band shapes with the experimentally recorded spectra has shown that for most pressures considered in the present work the collisional line narrowing effects are still negligible and should be properly incorporated in the theoretical model for very low gas densities.

Acknowledgments

The authors thank F. Thibault (Institut de Physique de Rennes) and H. Tran (LISA, Université de Paris Est Créteil) for helpful comments and suggestions. J.V.A. gratefully acknowledges financial support from the Belgian Federal Science Policy Office (contract SD/CS/07A, Advanced exploitation of Ground-based measurements for Atmospheric Chemistry and Climate-II) and the Fonds de la Recherche Scientifique (F.R.S.-FNRS, Belgium, contract FRFC no. 2.4.542.08F). He also thanks A.C. Vandaele (BISA, Belgium) for suggesting the experimental work, and M. Sanzharov and S. Léonis for their participation to the early stage of the analysis.

Appendix A. Supplementary data

Supplementary data associated with this article can be found in the online version at http://dx.doi.org/10.1016/j.jqsrt.2014.08.007.

References

[1] Vandaele AC, De Mazière M, Drummond R, Mahieux A, Neefs E, Wilquet V, et al. Composition of the Venus mesosphere measured by Solar Occultation at Infrared on board Venus Express. J Geophys Res 2008;113:E00B23.
[2] Nevejans D, Neefs E, Van Ransbeeck E, Berkenbosch S, Clairquin R, De Vos L, et al. Compact high-resolution spaceborne echelle grating spectrometer with acousto-optical tunable filter based order sorting for the infrared domain from 2.2 to 4.3 μm. Appl Opt 2006;45:5191–206.
[3] Vinogradov AP, Surkov Yu A, Andreichikov BM, Kalinkina OM, Grechishcheva IM. The chemical composition of the atmosphere of Venus. In: Sagan C, Owen T, Smith H, editors. Planetary atmospheres. Dordrecht, Holland: D. Reidel Publishing Company; 1971. p. 16–30.
[4] Zurek RW, Chicarro A, Allen MA, Bertaux JL, Clancy RT, Daerden F, et al. Assessment of a 2016 mission concept. The search for trace gases in the atmosphere of Mars. Planet Space Sci 2011;59:284–91.
[5] Plyler EK, Tidwell ED, Benedict WS. Absorption bands of carbon dioxide from 2.8–4.2 μ. J Opt Soc Am 1962;52:1017–22.
[6] Korb CL, Stafurik JW, Hunt RH, Plyler EK. Collision broadened line widths and the effects of Coriolis interaction on the line strengths of the 3339 cm^{-1} band of CO_2. Presented at the 36th International Symposium on Molecular Spectroscopy, Ohio State University, Columbus, 1971, and reported in [7] and [8].
[7] Toth RA. Wavenumbers, strengths, and self-broadened widths of CO_2 at 3 μm. J Mol Spectrosc 1974;53:1–14.
[8] Benner DC, Devi VM, Rinsland CP, Ferry-Leeper PS. Absolute intensities of CO_2 lines in the 3140–3410 cm^{-1} spectral region. Appl Opt 1988;27:1588–97.
[9] Devi VM, Benner DC, Rinsland CP, Smith MAH. Absolute rovibrational intensities of $^{12}C^{16}O_2$ absorption bands in the 3090–3850 cm^{-1} spectral region. J Quant Spectrosc Radiat Transf 1998;60:741–70.

[10] Rosenkranz PW. Shape of the 5 mm oxygen band in the atmosphere. IEEE Trans Antennas Propag 1975;23:498–506.
[11] Tran H, Boulet C, Stefani S, Snels M, Piccioni G. Measurements and modelling of high pressure pure CO_2 spectra from 750 to 8500 cm^{-1}. I—central and wing regions of the allowed vibrational bands. J Quant Spectrosc Radiat Transf 2011;112:925–36.
[12] Gamache RR, Lamouroux J. Predicting accurate line shape parameters for CO_2 transitions. J Quant Spectrosc Radiat Transf 2013;130:158–71.
[13] Dicke RH. The effect of collisions upon the Doppler width of spectral lines. Phys Rev 1953;89:472–3.
[14] Berman PR. Speed-dependent collisional width and shift parameters in spectral profiles. J Quant Spectrosc Radiat Transf 1972;12:1331–42.
[15] Luijendijk SCM. On the shape of pressure-broadened absorption lines in the microwave region. I. Deviations from the Lorentzian line shape. J Phys B 1977;10:1735–9.
[16] Buldyreva J, Daneshvar L. Extension of the non-Markovian Energy-Corrected Sudden model to the case of parallel and perpendicular infrared absorption bands. J Chem Phys 2013;139:164107.
[17] Filippov NN, Asfin RE, Sinyakova TN, Grigoriev IM, Petrova TM, Solodov AM, et al. Experimental and theoretical studies of CO_2 spectra for planetary atmosphere modelling: region 600–9650 cm^{-1} and pressures up to 60 atm. Phys Chem Chem Phys 2013;15:13826–34.
[18] Daneshvar L, Buldyreva J. Line mixing in Raman scattering spectra of CO_2 modelled by a non-Markovian Energy-Corrected Sudden approach. Mol Phys 2012;110:2077–89.
[19] Rothman LS, Gordon IE, Babikov Y, Barbe A, Benner DC, Bernath PF, et al. The HITRAN 2012 molecular spectroscopic database. J Quant Spectrosc Radiat Transf 2013;130:4–50.
[20] Tudorie M, Földes T, Vandaele AC, Vander J Auwera. CO_2 pressure broadening and shift coefficients for the 10 band of HCl and DCl. J Quant Spectrosc Radiat Transf 2012;113:1092–101.
[21] Davis SP, Abrams MC, Brault JW. Fourier transform spectrometry. San Diego, California, USA: Academic Press; 2001.
[22] Dana V, Mandin JY, Hamdouni A. Phase errors on interferograms: influence on the determination of positions, intensities, and widths of lines in the infrared. Appl Opt 1992;31:1937–41.
[23] Kauppinen J, Saarinen P. Line-shape distortions in misaligned cube corner interferometers. Appl Opt 1992;31:69–74.
[24] Wells RJ. Rapid approximation to the Voigt/Faddeeva function and its derivatives. J Quant Spectrosc Radiat Transf 1999;62:29–48.
[25] Rautian SG, Sobel'man II. The effect of collisions on the Doppler broadening of spectral lines. Sov Phys Usp 1967;9:701–16.
[26] Rohart F, Mäder H, Nicolaisen HW. Speed dependence of rotational relaxation induced by foreign gas collisions: studies on CH_3F by millimeter wave coherent transients. J Chem Phys 1994;101:6475–86.
[27] Tran H, Ngo NH, Hartmann JM. Efficient computation of some speed-dependent isolated line profiles. J Quant Spectrosc Radiat Transf 2013;129:199–203.
[28] Gentry B, Strow LL. Line mixing in a N_2-broadened CO_2 Q branch observed with a tunable diode laser. J Chem Phys 1987;86:5722–30.
[29] Brault JW, Brown LR, Chackerian C, Freedman R, Predoi-Cross A, Pine AS. Self-broadened $^{12}C^{16}O$ line shapes in the $\nu=2\leftarrow0$ band. J Mol Spectrosc 2003;222:220–39.
[30] Ngo NH, Lisak D, Tran H, Hartmann JM. An isolated line-shape model to go beyond the Voigt profile in spectroscopic databases and radiative transfer codes. J Quant Spectrosc Radiat Transf 2013;129:89–100 (Erratum. J Quant Spectrosc Radiat Transf 2014;134:105).
[31] Fischer J, Gamache RR, Goldman A, Rothman LS, Perrin A. Total internal partition sums for molecular species in the 2000 edition of the HITRAN database. J Quant Spectrosc Radiat Transf 2003;82:401–12.
[32] De Bièvre P, Gallet M, Holden NE, Barnes IL. Isotopic abundances and atomic weights of the elements. J Phys Chem Ref Data 1984;13:809–91.
[33] Johns JWC, Vander Auwera J. Absolute intensities in CO_2: the ν_2 fundamental near 15 μm. J Mol Spectrosc 1990;140:71–102.
[34] Cich MJ, Forthomme D, McRaven CP, Lopez GV, Hall GE, Sears TJ, et al. Temperature-dependent, nitrogen-perturbed line shape measurements in the $\nu_1+\nu_3$ band of acetylene using a diode laser referenced to a frequency comb. J Phys Chem A 2013;117:13908–18.
[35] Hartmann JM, Boulet C, Robert D. Collisional effects on molecular spectra. laboratory experiments and models, consequences for applications. Amsterdam: Elsevier; 2008.
[36] Rothman LS, Gordon IE, Barbe A, Benner DC, Bernath PF, Birk M, et al. The HITRAN 2008 molecular spectroscopic database. J Quant Spectrosc Radiat Transf 2009;110:533–72.
[37] Gamache RR, Lamouroux J, Blot-Lafon V, Lopes E. An intercomparison of measured pressure-broadening, pressure shifting parameters of carbon dioxide and their temperature dependence. J Quant Spectrosc Radiat Transf 2014;135:30–43.
[38] Predoi-Cross A, Unni AV, Liu W, Schofield I, Holladay C, McKellar ARW, et al. Line shape parameters measurement and computations for self-broadened carbon dioxide transitions in the 30012–00001 and 30013–00001 bands, line mixing, and speed dependence. J Mol Spectrosc 2007;245:34–51.
[39] Jacquinet-Husson N, Crepeau L, Armante R, Boutammine C, Chédin A, Scott NA, et al. The 2009 edition of the GEISA spectroscopic database. J Quant Spectrosc Radiat Transf 2011;112:2395–445.
[40] Devi VM, Benner DC, Brown LR, Miller CE, Toth RA. Line mixing and speed dependence in CO_2 at 6348 cm^{-1}: positions, intensities and air- and self-broadening derived with constrained multispectrum analysis. J Mol Spectrosc 2007;242:90–117.
[41] Devi VM, Benner DC, Brown LR, Miller CE, Toth RA. Line mixing and speed dependence in CO_2 at 6227.9 cm^{-1}: constrained multispectrum analysis of intensities and line shapes in the 30013←00001 band. J Mol Spectrosc 2007;245:52–80.
[42] Herregodts F, Hepp M, Hurtmans D, Vander Auwera J, Herman M. Laser spectroscopy of the $\nu_1+3\nu_3$ absorption band in $^{12}C_2H_2$. II. Self-collisional lineshift measurements. J Chem Phys 1999;111:7961–5.
[43] Hirschfelder JO, Curtiss CF, Bird RB. Molecular theory of gases and liquids. Corrected printing with notes added. New York, USA: John Wiley and Sons, Inc.; 1964.
[44] Lisak D, Masłowski P, Cygan A, Bielska K, Wójtewicz S, Piwiński M, et al. Line shapes and intensities of self-broadened O_2 $b^1\Sigma_g^+$ $(\nu=1)\leftarrow X^3\Sigma_g^-$ $(\nu=0)$ band transitions measured by cavity ring-down spectroscopy. Phys Rev A 2010;81:042504.
[45] Kouzov AP, Buldyreva JV. Orthogonal transformations in the line space and modelling of rotational relaxation in the Raman spectra of linear tops. Chem Phys 1997;221:103–19.
[46] Kouzov AP. Rotational relaxation matrix for fast non-Markovian collisions. Phys Rev A 1999;60:2931–9.
[47] Buldyreva JV, Bonamy L. Non-Markovian energy-corrected sudden model for the rototranslational spectrum of N_2. Phys Rev A 1999;60:370–6.
[48] Millot G. Rotationally inelestic rates over a wide temperature range based on an energy-corrected sudden-exponential-power theoretical analysis of Raman line broadening coefficients and Q-branch collapse. J Chem Phys 1990;93:8001–10.
[49] Rothman LS, Hawkins RL, Wattson RB, Gamache RR. Energy levels, intensities, and linewidths of atmospheric carbon dioxide bands. J Quant Spectrosc Radiat Transf 1992;48:537–66.
[50] Buldyreva J, Lavrentieva N, Starikov V. Collisional line broadening and shifting of atmospheric gases: a practical guide for line shape modelling by current semi-classical approaches. London: Imperial College Press; 2010.

Atmos. Chem. Phys., 14, 12251–12270, 2014
www.atmos-chem-phys.net/14/12251/2014/
doi:10.5194/acp-14-12251-2014

Atmospheric Chemistry and Physics Open Access

Relations between erythemal UV dose, global solar radiation, total ozone column and aerosol optical depth at Uccle, Belgium

V. De Bock, H. De Backer, R. Van Malderen, A. Mangold, and A. Delcloo

Royal Meteorological Institute of Belgium, Ringlaan 3, 1180 Brussels, Belgium

Correspondence to: V. De Bock (veerle.debock@meteo.be)

Received: 25 April 2014 – Published in Atmos. Chem. Phys. Discuss.: 24 June 2014
Revised: 7 October 2014 – Accepted: 7 October 2014 – Published: 20 November 2014

Abstract. At Uccle, Belgium, a long time series (1991–2013) of simultaneous measurements of erythemal ultraviolet (UV) dose (S_{ery}), global solar radiation (S_g), total ozone column (Q_{O_3}) and aerosol optical depth (τ_{aer}) (at 320.1 nm) is available, which allows for an extensive study of the changes in the variables over time. Linear trends were determined for the different monthly anomalies time series. S_{ery}, S_g and Q_{O_3} all increase by respectively 7, 4 and 3 % per decade. τ_{aer} shows an insignificant negative trend of −8 % per decade. These trends agree with results found in the literature for sites with comparable latitudes. A change-point analysis, which determines whether there is a significant change in the mean of the time series, is applied to the monthly anomalies time series of the variables. Only for S_{ery} and Q_{O_3}, was a significant change point present in the time series around February 1998 and March 1998, respectively. The change point in Q_{O_3} corresponds with results found in the literature, where the change in ozone levels around 1997 is attributed to the recovery of ozone. A multiple linear regression (MLR) analysis is applied to the data in order to study the influence of S_g, Q_{O_3} and τ_{aer} on S_{ery}. Together these parameters are able to explain 94 % of the variation in S_{ery}. Most of the variation (56 %) in S_{ery} is explained by S_g. The regression model performs well, with a slight tendency to underestimate the measured S_{ery} values and with a mean absolute bias error (MABE) of 18 %. However, in winter, negative S_{ery} are modeled. Applying the MLR to the individual seasons solves this issue. The seasonal models have an adjusted R^2 value higher than 0.8 and the correlation between modeled and measured S_{ery} values is higher than 0.9 for each season. The summer model gives the best performance, with an absolute mean error of only 6 %. However, the seasonal regression models do not always represent reality, where an increase in S_{ery} is accompanied with an increase in Q_{O_3} and a decrease in τ_{aer}. In all seasonal models, S_g is the factor that contributes the most to the variation in S_{ery}, so there is no doubt about the necessity to include this factor in the regression models. The individual contribution of τ_{aer} to S_{ery} is very low, and for this reason it seems unnecessary to include τ_{aer} in the MLR analysis. Including Q_{O_3}, however, is justified to increase the adjusted R^2 and to decrease the MABE of the model.

1 Introduction

The discovery of the Antarctic ozone hole in the mid-1980s triggered an increased scientific interest in the state of stratospheric ozone levels on a global scale (Garane et al., 2006). The ozone depletion not only occurred above the Antarctic; there is strong evidence that stratospheric ozone also diminished above midlatitudes (Bartlett and Webb, 2000; Kaurola et al., 2000; Smedley et al., 2012). While ozone depletion continued in the 2000s over the polar regions, it has leveled off at midlatitudes, although ozone amounts still remain lower compared to the amounts in the 1970s (Garane et al., 2006). Stratospheric ozone is expected to recover in response to the ban on ozone-depleting substances (ODSs) agreed upon in the Montreal Protocol in 1987 (WMO, 2006; Fitzka et al., 2012). However, it is difficult to predict future changes in ozone as the predictions suffer from uncertainties caused by the general climate change; numerical errors of simulation models; and by human behavior, which is not well controllable in several parts of the world. The decline in stratospheric ozone has shifted the focus of the scientific community and the general public towards the variability of

surface UV irradiance (Krzýscin et al., 2011). If all other factors influencing UV irradiance remain stable, reductions in stratospheric ozone would lead to an increase in UV irradiance at the ground, particularly at wavelengths below 320 nm (Garane et al., 2006). Increases of UV irradiance in response to the ozone decline have already been reported for different sites during the 1990s (Garane et al., 2006, and references therein).

The possible increase in UV irradiance raises concerns because of its adverse health and environmental effects. Overexposure can lead to the development of skin cancers, cataract, skin aging and the suppression of the immune system (Rieder et al., 2008; Cordero et al., 2009). UV irradiance also has adverse effects on terrestrial plants (Tevini and Teramura, 1989; Cordero et al., 2009) and on other elements of the biosphere (Diffey, 1991). On the other hand, UV radiation does enable the production of vitamin D in the skin, which is positively linked to health effects as it supports bone health and may decrease the risk of several internal cancers (United Nations Environment Programme, 2010). It is important to assess the changes in UV irradiance over prolonged periods of time. Not only do adverse health and environmental effects often relate to long-term exposure (from years to a lifetime); also the timescales of the atmospheric processes that are involved, such as ozone depletion and recovery, are beyond decades (Chubarova, 2008; den Outer et al., 2010).

Physically, UV trends can only be detected from direct measurements on Earth. Reconstructed data can be based on proxy data such as the abundance of ozone, solar irradiance, sunshine duration or regional reflectivity of the Earth–atmosphere system measured from space (Lindfors et al., 2003). Different sorts of reconstruction models have been used in several studies. They all use various kinds of statistical or model approaches and different meteorological or irradiance data sets (Lindfors et al., 2007; Chubarova, 2008; Rieder et al., 2010; den Outer et al., 2010; Bais et al., 2011). Techniques are either based on modeling of clear-sky UV irradiance or on empirical relationships between surface UV irradiance and the factors influencing the penetration of UV irradiance through the atmosphere (Kaurola et al., 2000; Trepte and Winkler, 2004). In addition to the reconstruction studies, changes in surface UV irradiance have also been studied using ground-based measurements at different locations (e.g., den Outer et al., 2000; Sasaki et al., 2002; Bernhard et al., 2006; Fitzka et al., 2012; Zerefos et al., 2012; Eleftheratos et al., 2014) or even in combination with satellite retrievals (Herman et al., 1996; Matthijsen et al., 2000; Kalliskota et al., 2000; Ziemke et al., 2000; Zerefos et al., 2001; Fioletov et al., 2004; Williams et al., 2004). Some studies combine both models and observations to investigate possible UV irradiance changes (e.g., Kaurola et al., 2000).

Not only stratospheric ozone influences the intensity of UV irradiance reaching the surface of the Earth. Long-term changes in solar elevation, tropospheric ozone, clouds, Rayleigh scattering on air molecules, surface albedo, aerosols, absorption by trace gases and changes in the distance between the Sun and the Earth can lead to trends in UV irradiance (WMO, 2006). Some studies show that increased amounts of aerosols and trace gases from industrial emissions, which absorb UV irradiance in the troposphere, could even compensate for the UV effects caused by the stratospheric ozone decline (Krzýscin et al., 2011; Fitzka et al., 2012). Clouds induce more variability in surface UV irradiance than any other geophysical factor, besides the solar elevation, but their effects depend very much on local conditions (Krzýscin et al., 2011). Surface albedo is determined mostly by snow amount and snow depth (Rieder et al., 2010) and plays a significant role at high-altitude and high-latitude sites, where UV irradiance can be strongly enhanced due to multiple occurrences of scattering and reflection between snow-covered ground and the atmosphere (Fitzka et al., 2012). Several studies have been conducted to quantify the effects of the abovementioned variables on the amount of UV irradiance reaching the ground, and many of them have done so by constructing empirical models with UV irradiance (or a related quantity) as a dependent variable (Díaz et al., 2000; Fioletov et al., 2001; de La Casinière et al., 2002; Foyo-Moreno et al., 2007; Antón et al., 2009; De Backer, 2009; Huang et al., 2011; Krishna Prasad et al., 2011; El Shazly et al., 2012).

At Uccle, Belgium, simultaneous measurements of erythemal UV dose, global solar radiation, total ozone column and aerosol optical depth at 320.1 nm are available for a time period of 23 years (1991–2013). The time series is long enough to allow for reliable determination of significant changes (a minimum of 15 years is required as shown in Weatherhead et al., 1998, and Glandorf et al., 2005). The availability of the simultaneous time series allows an extensive analysis in which three analysis techniques (linear trend analysis, change-point analysis and multiple linear regression analysis) will be combined in order to increase our insights on the relations between the variables. First, a linear trend analysis will be applied to the monthly anomalies of the time series (both on a daily and seasonal timescale), and the results will be compared with results found in the literature. Monthly anomalies are used here to reduce the influence of the seasonal cycle on the analysis and are calculated by subtracting the long-term monthly mean from the individual monthly means. The monthly anomalies time series will also be the subject of change-point analysis, where the homogeneity of the time series will be investigated. Finally, the multiple linear regression (MLR) technique (with daily erythemal UV doses as the dependent variable and daily values of global solar radiation, total ozone column and aerosol optical depth at 320.1 nm as explanatory variables) will allow us to study the influence of the explanatory variables on the dependent variable on a daily and seasonal basis.

2 Data

In this study, the (all-sky) erythemal UV dose, (all-sky) global solar radiation, total ozone column and (clear-sky) aerosol optical depth at 320.1 nm are investigated over a time period of 23 years (1991–2013). These measurements are performed at Uccle, Belgium (50°48′ N, 4°21′ E, 100 m a.s.l.), a residential suburb of Brussels located about 100 km from the North Sea shore.

2.1 Daily erythemal UV dose

In 1989, the Brewer spectrophotometer instrument #016, a single monochromator, was equipped with a UV-B monitor (De Backer, 2009). This is an optical assembly which enables the Brewer to measure UV-B irradiance using a thin disc of Teflon as a transmitting diffuser (SCI TEC Brewer #016 manual, 1988). The Brewer measures the horizontal spectral UV irradiance with a spectral resolution of approximately 0.55 nm, full width at half maximum. The instrument performs UV scans from 290 to 325 nm with 0.5 nm wavelength steps (Fioletov et al., 2002). The erythemal irradiances are calculated using the erythemal action spectrum as determined by the Commission Internationale de l'Eclairage and are integrated to daily erythemal doses (De Backer, 2009). For wavelengths above 325 nm, for which Brewer#016 does not provide data, the intensities are extrapolated using a theoretical spectrum weighted by the intensity at 325 nm. This is justified by the fact that, at those wavelengths, the UV intensity is no longer strongly dependent on ozone and the erythemal weighting function is low. For the calculation of the daily sum, a linear interpolation between the different measurement points is performed. When there is an interruption of 2 h or more between the measurements between sunrise and sunset, the calculated daily sum is rejected. The data (in joules per square meter, $\mathrm{J\,m^{-2}}$) are available on a regular basis from 1991. The instrument is calibrated with 50W lamps on a monthly basis and with 1000 W lamps during intercomparisons in 1994, 2003, 2006, 2008, 2010 and 2012. The instrument was also compared with the traveling QUASUME (QUality Assurance of Spectral UV Measurements in Europe) unit in 2004 (Gröbner et al., 2004).

2.2 Global solar radiation

The global solar radiation is a measure of the rate of total incoming solar energy (both direct and diffuse) on a horizontal plane at the surface of the Earth (Journée and Bertrand, 2010). The measurements at Uccle are performed by CM11 pyranometers (Kipp & Zonen; http://www.kippzonen.com). For this study, the daily values in $\mathrm{J\,m^{-2}}$, derived from 10 and 30 min data, are used. The data are quality-controlled in two steps: first a preliminary fully automatic quality control is performed prior to the systematic manual check of the data (Journée and Bertrand, 2010). In May 1996 we switched to a new system, and in 2005 half of the instruments were replaced. Corrections to the measurements were made in 2000, 2001, 2004, 2005, 2007 and 2012. For the period before 1996, no information is available concerning possible calibrations of the instrument.

2.3 Total ozone column

Total ozone column values (in Dobson Units, DU) are available from Brewer#016 direct sun (DS) measurements. The instrument records raw photon counts of the photomultiplier at five wavelengths (306.3, 310.1, 313.5, 316.8 and 320.1 nm) using a blocking slit mask, which opens successively one of the five exit slits. The five exit slits are scanned twice within 1.6 s, and this is repeated 20 times. The whole procedure is repeated five times for a total of about 3 min. The total ozone column is obtained from a combination of measurements at 310.1, 313.5, 316.8 and 320.1 nm, weighted with a predefined set of constants chosen to minimize the influence of SO_2 and linearly varying absorption features from, e.g., clouds or aerosols (Gröbner and Meleti, 2004). Brewer#016 was calibrated relative to the Dobson instrument in 1984 (De Backer and De Muer, 1991) and regularly recalibrated against the traveling standard Brewer instrument #017 in 1994, 2003, 2006, 2008, 2010 and 2012. The stability is also continuously checked against the colocated instruments Dobson#40 (from 1991 until May 2009) and Brewer#178 (since 2001). Internal lamp tests are performed on a regular basis to check whether the instrument itself is drifting. When instrumental drift is detected, it is corrected for.

2.4 Aerosol optical depth

Cheymol and De Backer (2003) developed a method that enables the retrieval of τ_{aer} values (at 306.3, 310.1, 313.5, 316.8 and 320.1 nm) using the DS measurements of the Brewer instrument. It is also possible to retrieve τ_{aer} values at 340 nm using sun scan (SS) measurements of the Brewer instrument (De Bock et al., 2010). Together with the retrieval method, De Bock et al. (2010) developed a cloud-screening procedure to select the clear-sky τ_{aer} values. However, this screening method did not perform well. Hence an improved cloud-screening method (described in Sect. 3.1) has been developed and applied to τ_{aer} values retrieved from DS and SS measurements. For this study only the cloud-screened τ_{aer} values at 320.1 nm, retrieved from the DS measurements of the single monochromator Brewer#016, will be used.

3 Method

3.1 Improved aerosol optical depth cloud-screening method

The initial cloud-screening algorithm, as described in De Bock et al. (2010), did not perform well and improvements

Table 1. Comparison of Brewer and Cimel aerosol optical depth values (2006–2013).

		Correlation	Slope	Intercept
DS 320 nm	Brewer#016	0.97	1.004 ± 0.006	-0.067 ± 0.003
DS 320 nm	Brewer#178	0.99	1.007 ± 0.005	0.017 ± 0.002
SS 340 nm	Brewer#178	0.98	0.993 ± 0.007	0.073 ± 0.002

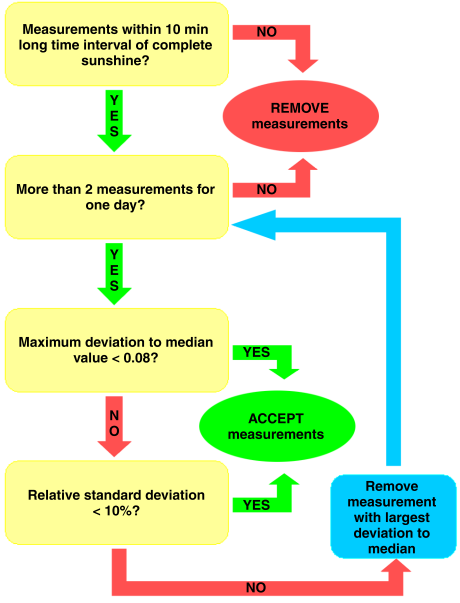

Figure 1. Improved cloud-screening procedure.

were needed. The improved cloud-screening method makes use of sunshine duration data from four pyrheliometers at Uccle and is also based on the assumption that the variability of the τ_{aer} in the course of 1 day is either lower than 10 % or lower than 0.08 τ_{aer} units, which is the maximum uncertainty of the τ_{aer} retrieval algorithm. Figure 1 gives a schematic overview of the improved cloud-screening technique. First it is determined whether the individual τ_{aer} measurements were taken within a 10 min interval of continuous sunshine. The measurements for which this is not the case are removed, after which more than two individual measurements per day must remain in order to continue. For each day, we then determine the maximum deviation to the median value. If this value is less than 0.08, we accept all measurements for that day. However, if the maximum deviation exceeds 0.08, the relative standard deviation for that day is calculated. In case this value is less than 10 %, which would guarantee a given stability within the diurnal pattern of τ_{aer}, all the τ_{aer} values for that day are accepted. In the other case, the τ_{aer} measurement with the largest contribution to the standard deviation is removed, as this measurement is most likely influenced by clouds. The median value will then be recomputed and the previous steps are repeated. Days with two or less individual τ_{aer} measurements are excluded from the results, since it does not make sense to calculate the deviation to the median and the standard deviation.

The cloud-screened τ_{aer}, both from DS and SS Brewer measurements, were compared to quasi-simultaneous and colocated Cimel level 2.0 quality-assured values (with a maximum time difference of 3 min). The Cimel sun photometer, which belongs to BISA (Belgium Institute of Space Aeronomy), is located approximately 100 m from the Brewer instrument. It is an automatic sun–sky scanning filter radiometer allowing the measurements of the direct solar irradiance at wavelengths 340, 380, 440, 500, 670, 870, 940 and 1020 nm. These solar extinction measurements are used to compute aerosol optical depth at each wavelength except for the 940 nm channel, which is used to retrieve total atmospheric column precipitable water in centimeters. The instrument is part of the AErosol RObotic NETwork (AERONET; http://aeronet.gsfc.nasa.gov/; Holben et al., 2001). The accuracy of the AERONET τ_{aer} measurements at 340 nm is 0.02 (Eck et al., 1999). For the period of comparison (2006–2013), the correlation coefficient, slope and intercept of the regression lines have been calculated, and the values are presented in Table 1. The results of the comparison show that the cloud-screened Brewer τ_{aer} values agree very well with the Cimel data.

The advantages of the improved cloud-screening method are the removal of the arbitrary maximum level of τ_{aer} values and the fact that it runs completely automatically, whereas the old one needed manual verification afterwards. This method has now been applied not only to the τ_{aer} retrieval using SS measurements at 340 nm but also to the method using DS measurements.

3.2 Data analysis methods

Since most statistical analysis tests, such as linear regression and change-point tests, rely on independent and identically distributed time series (e.g., Van Malderen and De Backer, 2010, and references therein), most data used in this study are in their anomaly form. Monthly anomalies are used to reduce the influence of the seasonal cycle on the analysis and are calculated by subtracting the long-term monthly mean from the individual monthly means. Monthly means are only calculated for months with at least 10 individual daily values. For S_{ery}, S_g and Q_{O_3}, accepting monthly means with only 10 daily individual values does not have an impact on the calculated trends, as respectively 85, 99 and 100 % of the

months consist of more than 20 individual daily values. For τ_{aer}, however, the number of available monthly mean values is dramatically reduced (from 92 to only 5 remaining values) when only accepting monthly means based on 20 individual values. There is a risk in accepting months with only 10 daily values, as those days could be concentrated at the beginning or end of a month, which could bias the calculated trend. However, the benefit of using 92 instead of 5 monthly mean values for τ_{aer} trend calculations outweighs this potential bias. For the multiple linear regression analysis, daily values will be used instead of anomaly values.

3.2.1 Linear trend analysis

Linear trends are calculated for the monthly anomalies of S_{ery}, S_g, Q_{O_3} and τ_{aer} at 320.1 nm. To determine the significance of the linear trends, the method described in Santer et al. (2000) is used. The least-squares linear regression estimate of the trend in $x(t)$, b, minimizes the squared differences between $x(t)$ and the regression line $\hat{x}(t)$:

$$\hat{x}(t) = a + b(t); t = 1, \ldots, n_t. \quad (1)$$

Whether a trend in $x(t)$ is significantly different from 0 is tested by computing the ratio between the estimated trend (b) and its standard error (s_b):

$$t_b = \frac{b}{s_b}. \quad (2)$$

Under the assumption that t_b is distributed as Student's t, the calculated t ratio is then compared with a critical t value, t_{crit}, for a stipulated significance level α and $n_t - 2$ degrees of freedom (Santer et al., 2000).

However, if the regression residuals are autocorrelated, the results of the regression analysis will be too liberal and the original approach must be modified. The method proposed in Santer et al. (2000) involves the use of an effective sample size n_e in the computation of the adjusted standard error and calculated t value, but also in the indexing of the critical t value. To test for autocorrelation in the residuals of a time series, the Durbin–Watson test is used (Durbin and Watson, 1971).

The above-described linear trend analysis is also applied to the monthly anomalies of the extreme values (minima and maxima) of the variables. The extreme values are calculated by determining the lowest and highest measured value for each month. These trends will be studied together with the relative frequency distribution of the daily mean values. This distribution is determined by using the minimum and maximum values of the entire study period as boundaries and by dividing the range between the boundaries into a certain amount of bins of equal size. The daily values are distributed over the different bins, and the relative frequency in percent is calculated. This will be done for two different time periods: 1991–2002 and 2003–2013. Additionally, the medians for these periods are calculated. In this way, it is possible to investigate whether there is a shift in the frequency distribution of the variables from the first period to the second one. The results of the analysis of the frequency distribution will only be presented in case they show a significant shift in the data.

3.2.2 Change-point analysis

Change points are times of discontinuity in a time series (Reeves et al., 2007) and can either arise naturally or as a result of errors or changes in instrumentation, recording practices, data transmission, processing, etc. (Lanzante, 1996). A change point is said to occur at some point in the sequence if all the values up to and including it share a common statistical distribution and all those after the point share another. The most common change-point problem involves a change in the mean of the time series (Lanzante, 1996). There are different tests that can be used to detect a change point in a time series. In this study we use the combination of three tests: the non-parametric Pettitt–Mann–Whitney (PMW) test (based on the ranks of the values in the sequence), the Mann–Whitney–Wilcoxon (MWW) test (a rank sum test) and the cumulative sum technique (CST). The details of these tests are described in Hoppy and Kiely (1999). The change points discussed further in this study are detected by all three tests (except when mentioned otherwise), and only the change points that exceeded the 90 % confidence level were retained. The change points are determined for the monthly anomalies time series of S_{ery}, S_g, Q_{O_3} and τ_{aer} at 320.1 nm. When there is a clear and large-enough, statistically significant trend present in the time series, this automatically leads to the detection of a change point in the middle of the time series as, at this point, the change in the mean is large enough to be significant. In this case, it is necessary to detrend the time series, i.e., subtract the general trend from the time series.

3.2.3 Multiple linear regression analysis

The goal of a MLR analysis is to determine the values of parameters for a linear function that cause this function to best describe a set of provided observations (Krishna Prasad et al., 2011). In this study, the MLR technique is used to explore whether there is a significant relationship between S_{ery} and three explanatory variables (S_g, Q_{O_3} and τ_{aer}) both on a daily and seasonal scale. We use a linear model where the coefficients are determined with the least-squares method:

$$S_{ery} = a \times S_g + b \times Q_{O_3} + c \times \tau_{aer} + d + \epsilon \quad (3)$$

with

- S_{ery}: erythemal UV dose (in J m^{-2})
- S_g: global solar radiation (in J m^{-2})

- Q_{O_3}: total ozone column (in DU)
- τ_{aer}: aerosol optical depth at 320.1 nm
- a, b, c: regression coefficients
- d: constant term
- ϵ: error term.

Although the attenuation of radiation by ozone is not linear (according to the Beer–Lambert law), we consider total ozone column as a linear independent variable, based on the limited variation of this variable throughout the year and throughout the different seasons.

The model will be developed based on data from 1991 to 2008. Data from 2009 to 2013 will be used for validation of the model. For the MLR analysis to produce trustworthy results, the distribution of the errors of the model should be normal. Non-normal errors may mean that the t and F statistics of the coefficients may not actually follow t and F distributions and that the model might underestimate reality (Williams et al., 2013). However, as stated in Williams et al. (2013), even if errors are not normally distributed, the sampling distribution of the coefficients will approach a normal distribution as sample size grows larger, assuming some reasonably minimal preconditions. As we have a large data set available at Uccle for the MLR analysis, we can assume that the distribution of the coefficients of the MLR model approaches normality.

The performance of the model and its parameters will be evaluated through different statistical parameters. The adjusted R^2 value is the measure for the fraction of variation in UV explained by the regression, accounting for both the sample size and the number of explanatory variables. Compared to the R^2 value, the adjusted R^2 value will only increase if a new variable has additional explanatory power. It is possible to test the null hypothesis that a regression coefficient is equal to 0, which would mean that the variable associated with this regression coefficient does not contribute to explaining the variation in UV. This is done by looking at the p value. If we want to test whether a regression coefficient differs significantly from 0 at the 5 % level, the p value should be less than or equal to 0.05. The influence of the variation in the three parameters on the variation of S_{ery} is determined by multiplying the standard deviation of each parameter with its corresponding regression coefficient and dividing this by the average S_{ery} value.

The mean bias error (MBE) and the mean absolute bias error (MABE) are also calculated in order to evaluate the performance of the regression model. The MBE (given in %) provides the mean relative difference between modeled and measured values (Antón et al., 2009):

$$\mathrm{MBE} = 100 \times \frac{1}{N} \sum_{i=1}^{N} \frac{S_{ery_i}^{\mathrm{modeled}} - S_{ery_i}^{\mathrm{measured}}}{S_{ery_i}^{\mathrm{measured}}}. \quad (4)$$

The MABE (given in %) reports on the absolute value of the individual differences between modeled and measured data (Antón et al., 2009):

$$\mathrm{MABE} = 100 \times \frac{1}{N} \sum_{i=1}^{N} \frac{|S_{ery_i}^{\mathrm{modeled}} - S_{ery_i}^{\mathrm{measured}}|}{S_{ery_i}^{\mathrm{measured}}}. \quad (5)$$

Table 2. Seasonal trends of erythemal UV doses (1991–2013).

Season	Trend per decade	Significance level
Spring	+9 % (± 3 %)	99 %
Summer	+6 % (± 2 %)	99 %
Autumn	+7 % (± 3 %)	95 %
Winter	−12 % (± 4 %)	99 %

4 Results and discussion

4.1 Linear trend analysis

4.1.1 Erythemal UV dose

A significant positive trend (at the 99 % significance level) can be detected in the time series of monthly anomalies of S_{ery} (Fig. 2). These values increase by 7 % (± 2 %) per decade. The seasonal trends are presented in Table 2. In spring (March, April and May), summer (June, July and August) and autumn (September, October and November), S_{ery} increases significantly, whereas in winter (December, January and February) the trend is negative. The increase in S_{ery} is the largest in spring.

A significant positive trend has been found in the monthly anomalies of both the minimum and maximum values of S_{ery}. The minimum values show an increase of 10 % (± 4 %) per decade and the maximum values increased by 7 % (±1 %) per decade (respectively at the 95 and 99 % level). The increase in the median value from 825 J m^{-2} (1991–2002) to 987 J m^{-2} (2003–2013) shows that higher S_{ery} values are more frequent in the latter period.

4.1.2 Global solar radiation

The values of S_g show an increase of 4 % (± 1 %) per decade at the 99 % significance level, which corresponds to an absolute change of +0.5 (± 0.2) W m^{-2} per year for the observed time period (Fig. 2). On a seasonal scale, spring and autumn exhibit a significant positive trend (Table 3). The seasonal trends of S_g, although not significant in summer and winter,

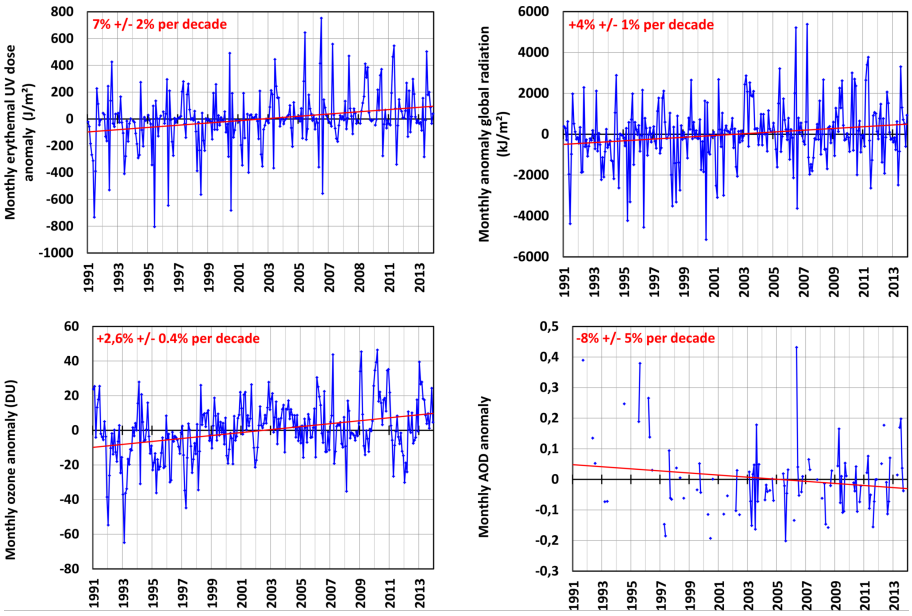

Figure 2. Trends of monthly anomalies at Uccle for erythemal UV dose (upper left panel), global solar radiation (upper right panel), total ozone column (lower left panel) and aerosol optical depth at 320.1 nm (lower right panel) for the time period 1991–2013. The blue lines represent the time series, whereas the red lines represent the trend over the time period.

Table 3. Seasonal trends of global solar radiation (1991–2013).

Season	Trend per decade	Significance level
Spring	+6 % (± 3 %)	95 %
Summer	+2 % (± 2 %)	not significant
Autumn	+6 % (± 3 %)	95 %
Winter	−4 % (± 4 %)	not significant

Table 4. Seasonal trends of total ozone column (1991–2013).

Season	Trend per decade	Significance level
Spring	+3 % (± 1 %)	95 %
Summer	+1.6 % (± 0.6 %)	95 %
Autumn	+1.8 % (± 0.9 %)	not significant
Winter	+3 % (± 2 %)	not significant

Table 5. Seasonal trends of aerosol optical depth at 320.1 nm (1991–2013).

Season	Trend per decade	Significance level
Spring	+2 % (± 7 %)	not significant
Summer	−18 % (± 8 %)	95 %
Autumn	−36 % (± 14 %)	95 %
Winter	not enough data	

have the same sign as the seasonal S_{ery} trends. The trends of S_g are smaller than the S_{ery} trends, both on an annual and seasonal scale.

There is a clear difference between the trends of the monthly anomalies of minimum and maximum values of S_g. Both trends are positive, but the increase in the minimum values (12 % (± 5 %) per decade at 99 % significance level) is much larger than the one in the maximum values (3.2 % (± 0.7 %) per decade at 99 % significance level). Study of the median values reveals the presence of an increase from 7880 kJ m^{-2} (1991–2002) to 8902 kJ m^{-2} (2003–2013). As the global radiation data are all-sky data, it is obvious that the minimum values are the ones that are influenced by clouds. If the minimum values increase in time, the cloud properties, i.e., their amount and/or water content, must have changed over the past 23 years.

4.1.3 Total ozone column

The monthly anomalies of Q_{O_3} show a positive trend of 2.6 % (± 0.4 %) per decade (significant at 99 %) (Fig. 2). Significant positive trends occur in spring and summer (Table 4), with the trend in spring being the largest one. As opposed to the seasonal trends of S_{ery} and S_g, the ones for Q_{O_3} are positive for each season. We would expect an increase in Q_{O_3} over the past 23 years to be accompanied by a decrease in S_{ery}, which is not the case for the Uccle time series. This indicates that other variables might contribute to the change in S_{ery} and that the contribution of Q_{O_3} might be washed out by the influence of these other variables.

Both the minimum and maximum Q_{O_3} values increased significantly (99 % level) at the same rate: 3.0 % (± 0.6 %)

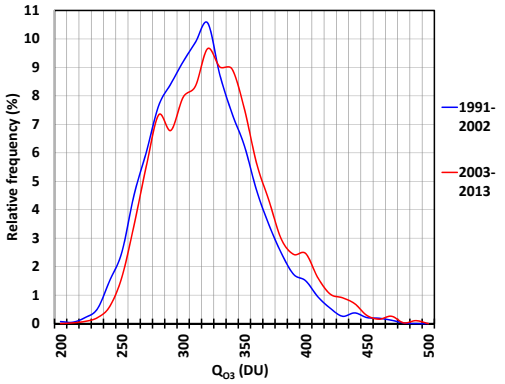

Figure 3. Relative frequency distribution of daily total ozone column values for the two time periods: 1991–2002 (in blue) and 2003–2013 (in red).

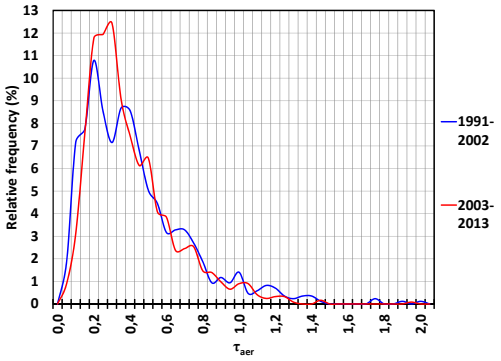

Figure 4. Relative frequency distribution of daily aerosol optical depth values for the two time periods: 1991–2002 (in blue) and 2003–2013 (in red).

per decade for the minimum values and 3.1 % (± 0.6 %) per decade for the maximum values over the past 23 years. A clear shift can be seen in the frequency distribution (Fig. 3) of the daily Q_{O_3} values. During the second period (2003–2013), higher values are more frequent than during the previous period (1991–2002), which is supported by the increase in median values from 319.3 DU (199–2002) to 327.9 DU (2003–2013). The entire curve of the frequency distribution is shifted, which means that the minimum values of the distribution have also increased between the two decades. After a period with lower Q_{O_3} values in the 1990s, it seems that ozone has been recovering over the past 10 years. Removing the Pinatubo period (1991–1993) from our analysis does not change the trend in ozone significantly, which means that the observed recovery in ozone is not very much related to the return of the stratosphere to pre-Pinatubo time but rather that it is more likely a result of the regulations of the Montreal Protocol.

4.1.4 Aerosol optical depth at 320.1 nm

While the overall trends of S_{ery}, S_g and Q_{O_3} are all positive, the τ_{aer} values at 320.1 nm show a negative trend of −8 % (± 5 %) per decade. This trend, however, is not significant (Fig. 2). The seasonal trends (Table 5) show that the summer and autumn trends are significantly negative, with the largest trend being observed during autumn. Due to a lack of sufficient clear-sky data, it was not possible to determine the winter trend for τ_{aer}.

There are no significant changes in the minimum and maximum τ_{aer} values over the 1991–2013 period. From the relative frequency distribution of the daily τ_{aer} values (Fig. 4), it can be seen that the frequency of lower τ_{aer} values ($\tau_{aer} < 0.4$) was higher during the second period (2003–2013). The frequency of high τ_{aer} values ($\tau_{aer} > 0.7$) has also decreased towards the second decade. This is in agreement with the overall decrease in τ_{aer} over the last 23 years. However, this is not obvious from the median values as they decreased only slightly from 0.38 (1991–2002) to 0.36 (2003–2013).

4.2 Comparison of Uccle trends with other stations

4.2.1 Erythemal UV dose

Long-term UV trends for different locations around the world have been the subject of many research articles (e.g., den Outer et al., 2000; Zerefos et al., 2012; Eleftheratos et al., 2014), and it is worth checking the consistency of our results with these studies even though the time periods are never exactly the same as the one studied in this paper (1991–2013). Some trends (observed or modeled/reconstructed) found in the literature are presented in Table 6. Looking at these trends, it can be seen that for the stations with comparable latitude to Uccle (45–55° N), the trends in UV range from −2.1 to +14.2 % per decade. The increase of 7 % (± 2 %) per decade observed at Uccle falls within the range of trends reported in the literature. However, for the comparison of these trends, it has to be taken into account that not all trends in Table 6 are calculated in the same say as the one at Uccle. At Uccle, trends are based on monthly anomalies which are essentially calculated from daily doses. As such, all effects such as those from clouds are included in our analysis. Some of the studies from Table 6 report trends at a certain fixed solar zenith angle, which does not cover the same range of effects as the daily sum does, and thus the trends may not be truly comparable. The possible effect of a different concept of UV could be the subject of a later study. On a more global scale, Zerefos et al. (2012) examined UV irradiance over selected sites in Canada, Europe and Japan between 1990 and 2011. The results, based on observations and modeling for all stations, showed an increase in UV irradiances of 3.7 % (± 0.5 %) and 5.5 % (± 0.3 %) per decade at respectively 305 and 325 nm. For Europe, only the trend at 325 nm (3.4 % (± 0.4 %) per decade) was significant. The COST 726 action (Litynska et al., 2009; www.cost726.org) calculated

Table 6. Trends of UV radiation at different stations from (a) Bais et al. (2007), (b) Krzyścin et al. (2011), (c) Smedley et al. (2012), (d) Fitzka et al. (2012), (e) den Outer et al. (2010) and (f) Chubarova (2008).

Station, country	Latitude/longitude	Period	Trend/decade	Reference
Measured UV trends				
Sodankylä, Finland	67.42° N/26.59° E	1990–2004	+2.1 % (60° SZA)	(a)
Jokioinen, Finland	60.80° N/23.49° E	1996–2005	−1.9 % (60° SZA)	(a)
Norrköping, Sweden	58.36° N/16.12° E	1996–2004	+12 % (60° SZA)	(a)
Bilthoven, the Netherlands	52.13° N/5.20° E	1996–2004	+8.6 % (60° SZA)	(a)
Belsk, Poland	51.83° N/20.81° E	1976–2008	+5.6 %	(b)
Reading, United Kingdom	51.45° N/0.98° W	1993–2008	+6.6 %	(c)
Hradec Kralove, Czech Rep.	50.21° N/15.82° E	1994–2005	−2.1 % (60° SZA)	(a)
Lindenberg, Germany	47.60° N/9.89° E	1996–2003	+7.7 % (60° SZA)	(a)
Hoher Sonnblick, Austria	47.05° N/12.96° E	1997–2011	+14.2 % (65° SZA)	(d)
Thessaloniki, Greece	40.63° N/22.95° E	1990–2004	+3.4 % (60° SZA)	(a)
Reconstructed or Modeled UV trends				
Sodankylä, Finland	67.42° N/26.59° E	1980–2006	+3.6 %	(e)
Jokioinen, Finland	60.80° N/23.49° E	1980–2006	+2.8 %	(e)
Norrköping, Sweden	58.36° N/16.12° E	1980–2006	+4.1 %	(e)
Moscow, Russia	55.75° N/37.62° E	1980–2006	+6 %	(f)
Bilthoven, the Netherlands	52.13° N/5.20° E	1980–2006	+2.9 %	(e)
Hradec Kralove, Czech Rep.	50.21° N/15.82° E	1980–2006	+5.2 %	(e)
Lindenberg, Germany	47.60° N/9.89° E	1980–2006	+5.8 %	(e)
Thessaloniki, Greece	40.63° N/22.95° E	1980–2006	+4.4 %	(e)

trend values for European sites and saw a mean positive trend of 4.5 % (± 0.5 %) per decade since 1980, which was derived from reconstruction models, based on Q_{O_3} and measured total solar irradiance.

4.2.2 Global solar radiation

Concerning the global solar radiation, many publications agree on the existence of a solar dimming period between 1970 and 1985 and a subsequent solar brightening period (Norris and Wild, 2007; Solomon et al., 2007; Makowski et al., 2009; Stjern et al., 2009; Wild et al., 2009; Sanchez-Lorenzo and Wild, 2012). Different studies have calculated the trend in S_g after 1985. The trend in S_g from GEBA (Global Energy Balance Archive; http://www.iac.ethz.ch/groups/schaer/research/rad_and_hydro_cycle_global/geba) between 1987 and 2002 is equal to +1.4 (± 3.4) W m^{-2} per decade according to Norris and Wild (2007). Stjern et al. (2009) found a total change in the mean surface solar radiation trend over 11 stations in northern Europe of +4.4 % between 1983 and 2003. In the Fourth Assessment Report of the IPCC (Solomon et al., 2007), 421 sites were analyzed; between 1992 and 2002, the change of all-sky surface solar radiation was equal to 0.66 W m^{-2} per year. Wild et al. (2009) investigated the global solar radiation from 133 stations from GEBA/World Radiation Data Centre belonging to different regions in Europe. All series showed an increase over the entire period, with a pronounced upward tendency since 2000. For the Benelux region, the linear change between 1985 and 2005 is equal to +0.42 W m^{-2} per year, compared to the pan-European average trend of +0.33 W m^{-2} per year (or +0.24 W m^{-2} if the anomaly of the 2003 heat wave is excluded) (Wild et al. 2009). Our trend at Uccle of +0.5 (± 0.2) W m^{-2} per year (or +4 % per decade) agrees within the error bars with the results from Wild et al. (2009), but seems to be somewhat at the high end range.

4.2.3 Total ozone column

Ozone and its trends have been the subject of scientific research since the discovery of ozone depletion. Many studies agree that ozone has decreased since 1980 to the mid-1990s as a consequence of anthropogenic emissions of ozone depleting substances. This period of decrease is followed by a period of significant increase (Steinbrecht et al., 2006; Harris et al., 2008; Vigouroux et al., 2008; Krzyścin and Borkowski, 2008; Herman, 2010; Bais et al., 2011). For the period before the mid-1990s, studies report on decreasing ozone values at Brussels (Bojkov et al., 1995 and Zerefos et al., 1997), Reading (Bartlett and Webb, 2000), Lerwick (Smedley et al., 2012), Arosa (Bojkov et al., 1995 and Staehelin et al., 1998), Hohenpeissenberg (Bojkov et al., 1995), Sodankylä (Glandorf et al., 2005) and Thessaloniki (Glandorf et al., 2005) (see Table 7). After the mid-1990s, most studies report on a plateau or a limited increase in ozone. For example, Smedley

Table 7. Trends of total ozone column at different stations from (a) Glandorf et al. (2005), (b) Smedley et al. (2012), (c) Bartlett and Webb (2000), (d) Bojkov et al. (1995), (e) Zerefos et al. (1997), (f) Fitzka et al. (2012), (g) Staehelin et al. (1998) and (h) Vigouroux et al. (2008).

Station, country	Latitude/longitude	Period	Trend/decade	Reference
Sodankylä, Finland	67.42° N/26.59° E	1979–1998	−5.7 %	(a)
Lerwick, United Kingdom	60.15° N/1.15° W	1979–1993	−5.8 %	(b)
Reading, United Kingdom	51.45° N/0.98° W	1993–1997	−5.9 %	(c)
Brussels, Belgium	50.84° N/4.36° E	1971–1994	−2.6 %	(d)
Brussels, Belgium	idem	1993–1996	−15.0 %	(e)
Hradec Kralove, Czech Rep.	50.21° N/15.82° E	1994–2005	−2.2 %	(d)
Hohenpeisenberg, Germany	47.80° N/11.00° E	1968–1994	−3.5 %	(d)
Hoher Sonnblick, Austria	47.05° N/12.96° E	1997–2011	+1.9 %	(f)
Arosa, Switzerland	46.77° N/9.67° E	1964–1994	−2.7 %	(d)
Arosa, Switzerland	idem	1970–1996	−2.3 %	(g)
Jungfraujoch, Switzerland	46.55° N/7.98° E	1995–2004	+4.1 %	(h)
Thessaloniki, Greece	40.63° N/22.95° E	1993–1996	−4.0 %	(e)
Thessaloniki, Greece	idem	1990–1998	−4.5 %	(a)

et al. (2012) found no clear ozone trend in the 1993–2008 period for Reading. Ozone observations from a Brewer instrument at Hoher Sonnblick (Fitzka et al., 2012) showed a small but significant increase between 1997 and 2011. Similar behavior was reported for Jungfraujoch in Vigouroux et al. (2008). Our result, a trend of +2.6 % per decade, compares well with the trend observed at Hoher Sonnblick, which is the only station with a time period comparable to the one at Uccle. From Figs. 2 and 6, it can be seen that a negative trend occurred in the Q_{O_3} values before 1998 and that this trend was followed by a positive one. However, neither trend is significant at Uccle. It is difficult to unambiguously attribute the ozone trends to changes in ODSs because other factors also contribute to ozone variability and trends. These factors are large volcanic eruptions, Arctic ozone depletion, long-term climate variability, changes in the stratospheric circulation and the 11-year solar cycle (Harris et al., 2008; Vigouroux et al., 2008). According to Rieder et al. (2013), the equivalent effective stratospheric chlorine and the 11-year solar cycle can be identified as major contributors, but the influence of dynamical features (such as the El Niño–Southern Oscillation, North Atlantic Oscillation and Quasi-Biennial Oscillation) on the ozone variability and trends can not be neglected at a regional level.

4.2.4 Aerosol optical depth at 320.1 nm

Trend analysis studies of long time series of aerosol optical depth are still very scarce at the moment. Some studies, however, do report on aerosol trends (Table 8). Mishchenko and Geogdzhayev (2007) observed a significant decrease in τ_{aer} from 1991 to 2005 over much of Europe within the GACP (Global Aerosol Climatology Project; http://gacp.giss.nasa.gov/) data. Alpert et al. (2012) studied τ_{aer} trends from MODIS (MODerate-resolution Imaging Spectroradiometer) and MISR (Multi-angle Imaging SpectroRadiometer) satellite measurements over the 189 largest cities in the world and saw a decrease in τ_{aer} over Europe for the 2002–2010 period. The decadal trend observed by de Meij et al. (2012) over Europe between 2000 and 2009 was negative for MODIS (−30 %), MISR (−9 %) and AERONET (−25 %). Zerefos et al. (2012) – who investigated the τ_{aer} over Europe, Japan and Canada – discovered a general decline in τ_{aer} exceeding 10 % per year. For Europe specifically, the trend of τ_{aer} varied between −16.6 % (± 6 %) per decade when using the GACP data set and −42.8 % (± 5.7 %) for the MODIS data set. The insignificant trend of −8 % ± 5 % per decade observed at Uccle lies within the range of trends observed at other European stations. The long-term τ_{aer} decrease over much of Europe is quite consistent with the supposed reversal from increasing to decreasing anthropogenic sulfur and black carbon emissions owing to the enactment of clean-air legislation in many countries (Mishchenko and Geogdzhayev, 2007; Chiaccio et al., 2011; Alpert et al., 2012; de Meij et al., 2012; Hsu et al., 2012; Nabat et al., 2013). This change occurred after 1988–1989, the time period when a maximum was reached in the emissions of sulfate aerosols over Europe (Chiaccio et al., 2011). Many scientists believe that the decadal changes in aerosols have influenced the amount of solar radiation reaching the surface of the Earth and that the decrease in aerosols has played a part in the switch from global dimming to global brightening, which occurred around 1980–1990 (Augustine et al., 2008; Chiaccio et al., 2011). According to Wild et al. (2009), the reduction of aerosols may have played a role during the 1990s but not after 2000. Decreases in cloudiness or cloud albedo may have enabled the continuation of the increase in surface solar radiation over Europe beyond 2000, despite the stabilization of aerosol concentrations.

Table 8. Absolute and relative trends of aerosol optical depth at different stations from (a) Alpert et al. (2012), (b) Nyeki et al. (2012), (c) Fitzka et al. (2012) and (d) Kazadzis et al. (2007). MODIS-Terra, MODIS-Aqua and MISR measurements are represented by respectively "a", "b" and "c" after the station name.

Station, country	Latitude/longitude	Period	Trend/decade	Reference
Berlin (a), Germany	52.50° N/13.40° E	2002–2010	−20.5 %	(a)
Berlin (b), Germany	idem	2002–2010	−17.9 %	(a)
Berlin (c), Germany	idem	2002–2010	−12.3 %	(a)
Warsaw (a), Poland	52.30° N/21.00° E	2002–2010	−2.4 %	(a)
Warsaw (b), Poland	idem	2002–2010	−0.4 %	(a)
Warsaw (c), Poland	idem	2002–2010	+12.9 %	(a)
Ruhr Area (a), Germany	51.50° N/7.50° E	2002–2010	−15.7 %	(a)
Ruhr Area (b), Germany	idem	2002–2010	−9.3 %	(a)
Ruhr Area (c), Germany	idem	2002–2010	−9.3 %	(a)
Paris (a), France	48.90° N/2.40° E	2002–2010	−8.1 %	(a)
Paris (b), France	idem	2002–2010	+5.0 %	(a)
Paris (c), France	idem	2002–2010	+9.8 %	(a)
Hohenpeisenberg, Germany	47.80° N/11.00° E	1995–2010	−10.6 %	(b)
Hoher Sonnblick, Austria	47.05° N/12.96° E	1997–2011	−5 to −6 %	(c)
Barcelona (a), Spain	41.40° N/2.20° E	2002–2010	−8.8 %	(a)
Barcelona (b), Spain	idem	2002–2010	+4.2 %	(a)
Barcelona (c), Spain	idem	2002–2010	−2.3 %	(a)
Thessaloniki, Greece	40.63° N/22.95° E	1997–2006	−29.0 %	(d)
Madrid (a), Spain	40.40° N/3.70° W	2002–2010	−18.3 %	(a)
Madrid (b), Spain	idem	2002–2010	−10.0 %	(a)
Madrid (c), Spain	idem	2002–2010	−7.4 %	(a)

4.3 Change-point analysis

4.3.1 Erythemal UV dose

According to the three tests (PMW, MWW and CST) of the change-point analysis, there is a significant shift in the mean of the monthly anomalies of S_{ery} around January 2003. The change point is located suspiciously close to the middle of the time series, however. To remove the influence of the presence of one general increasing trend, which would lead to the discovery of a change point in the middle of the time series, the time series was detrended. This is done by subtracting the general trend from the original time series. The change point in the detrended time series is located around February 1998 (Fig. 5). Since there was no change in the calibration constants of the Brewer instrument around that period, it seems that the change point is not caused by known instrumental changes but rather by natural/environmental changes.

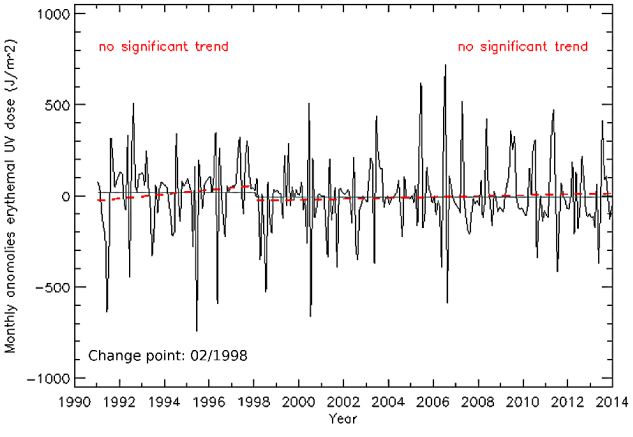

Figure 5. The black line represents the detrended time series of monthly anomalies of erythemal UV dose (1991–2013). The red (dashed) lines represent the (insignificant) positive trends before and after the detected change point. The grey lines represent the mean before and after the change point.

4.3.2 Global solar radiation

A significant change point was detected (only by the PMW test) around January 2003 in the time series of S_g. Similar to the S_{ery} time series, there is one general positive trend present, which explains the detection of a change point near the middle of the time series. Thus, it was again decided to look at the detrended time series of S_g. However, the detected change point around January 2006 (only by the PMW test) was not significant at the 90 % significance level.

4.3.3 Total ozone column

All three tests confirmed the presence of a significant change point around March 1998 in the time series of monthly anomalies of Q_{O_3}, where the mean before the change point is clearly lower than the one after the change point (Fig. 6). As there is clearly more than one general trend within the

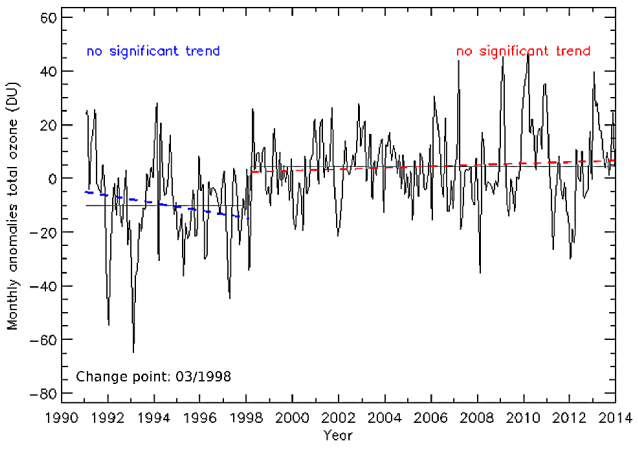

Figure 6. The black line represents the time series of monthly anomalies of total ozone column (1991–2013). The blue (dashed) line represents the (insignificant) negative trend before the detected change point, and the red (dashed) line represents the (insignificant) positive trend after the change point. The grey lines represent the mean before and after the change point.

entire time series, there is no need for detrending in this case. There was no change in the calibration constants of the Brewer instrument around 1998, so the change point has no known instrumental cause. To further exclude an instrumental cause for the step change in the mean of the Uccle ozone time series, we investigated the total ozone time series of De Bilt (the Netherlands; 52.10° N/5.18° E; data obtained from www.woudc.org). This time series is also characterized by a step change and change point in the beginning of 1998 (March 1998). At that time, there was no change in the calibration constants of the Brewer instrument at De Bilt. This confirms that the change point seen in the Uccle time series must have a natural/environmental cause.

4.3.4 Aerosol optical depth at 320.1 nm

According to the change-point analysis, no significant change was found in the mean of the monthly anomalies of τ_{aer}.

4.3.5 Overview and explanations

The change points in the time series of S_{ery} and Q_{O_3} occur around the same time period (February/March 1998). Since we were able to rule out known instrumental causes for the detected change points in both time series, we can assume that they have some natural/environmental cause and are related to each other.

The change point in the Q_{O_3} time series corresponds with results found in the literature. Recent studies have shown that, for other stations, the ozone recovery started around 1997 (Steinbrecht et al., 2006; Reinsel et al., 2005). Ozone levels seem to follow the change in chlorine concentrations resulting from the regulations of the Montreal Protocol in 1987. When ozone starts to increase, it is expected to have some implications on the UV irradiance as ozone is a strong absorber of UV irradiance in the stratosphere (Wenny et al., 2001). An increase in ozone would normally lead to a decrease in UV irradiance, which is not what was observed at Uccle, where the UV irradiance levels continue to increase after 1998. Before 1998, the (insignificant) trends in the time series of Q_{O_3} and S_{ery} are opposite, which is what would be expected. However, after 1998, both the (insignificant) Q_{O_3} and S_{ery} trend are positive. So the behavior of Q_{O_3} can only partly explain the changes observed in the UV irradiance time series, and other parameters, such as aerosols and cloudiness, might play an important role.

4.4 Multiple linear regression analysis

Before applying the MLR technique, it has to be verified that the explanatory variables (S_{g}, Q_{O_3} and τ_{aer}) are independent variables. This is done by calculating the correlation coefficients between these parameters. The correlation coefficients between the three variables are low enough (< 0.25) to allow using these variables as independent explanatory variables for the multiple regression analysis. As opposed to the previous analysis methods, the MLR is applied to daily values, instead of monthly anomaly values. For S_{ery} and S_{g}, the daily sums are used, whereas for Q_{O_3} and τ_{aer} daily mean values are used.

4.4.1 MLR analysis of daily values using total ozone column, global solar radiation and aerosol optical depth

The MLR analysis has been applied to 1246 simultaneous daily values of erythemal UV dose (S_{ery}), global solar radiation (S_{g}), total ozone (Q_{O_3}) and aerosol optical depth (τ_{aer}) between 1991 and 2008. The amount of regression days was highly limited by the available τ_{aer} measurements. The resulting regression equation is

$$S_{\text{ery}} = 690 + 0.000169 \times S_{\text{g}} - 5.01 \times Q_{\text{O}_3} + 70.0 \times \tau_{\text{aer}} + \epsilon \quad (6)$$

(with S_{ery} in J m^{-2}; S_{g} in J m^{-2}; and Q_{O_3} in DU).

The adjusted R^2 value of the multiple regression is 0.94, which means that S_{g}, Q_{O_3} and τ_{aer} together explain 94 % of the variation in daily S_{ery}. The changes in S_{ery} caused by the variation of each of the three parameters can be calculated by multiplying the standard deviation of each parameter with its corresponding regression coefficient and dividing this by the average S_{ery} value. From the results, it is clear that S_{g}, whose variation leads to a change in S_{ery} of 56 %, has the biggest influence on S_{ery}, followed by Q_{O_3} (change in S_{ery} of −9 %) and τ_{aer} (change in S_{ery} of 1 %).

The data from 2009–2013 are used to validate the model (see Fig. 7). The regression equation between the modeled and measured S_{ery} values ($f(x) = 0.93x + 113.45$ with x:

Table 9. Performance of the seasonal regression models.

	Spring	Summer	Autumn	Winter
Correlation	0.95	0.93	0.97	0.90
Regression equation	$y = 0.89x + 145.17$	$y = 0.94x + 104.36$	$y = 0.90x + 102.48$	$y = 0.91x + 8.13$
MBE	−4 %	−2 %	0.06 %	−7 %
MABE	14 %	6 %	15 %	15 %

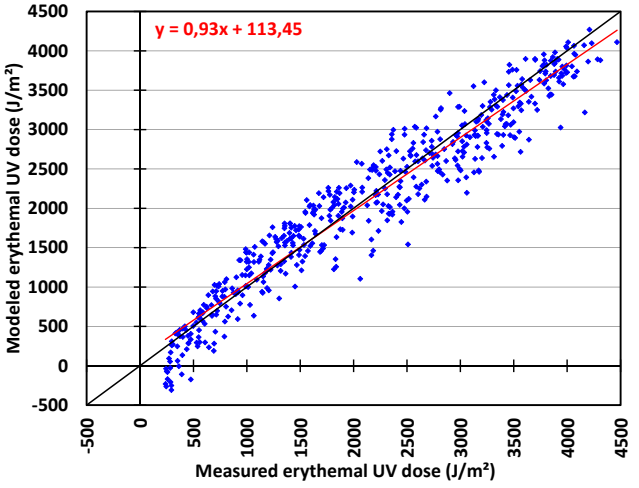

Figure 7. Scatterplot of the measured and modeled erythemal UV doses at Uccle for the 2009–2013 validation period. The red line represents the regression line of the data ($f(x) = 0.93x + 113.45$). The black line is the $f(x) = x$ line.

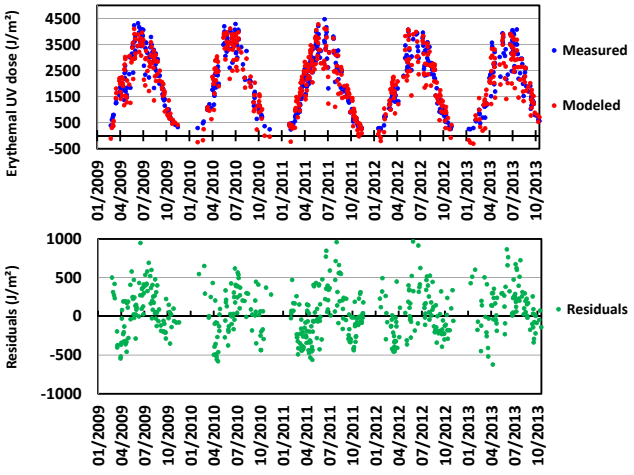

Figure 8. Validation of the multiple linear regression equation: the upper panel shows the measured (in blue) and modeled (in red) erythemal UV values; the lower panel presents the absolute residuals.

measured values) and the correlation coefficient (0.96) reveal the good agreement between model and reality. The MBE of the model is −3 %, meaning that the model has a slight tendency to underestimate the measurements, which can be seen in Figs. 7 and 8. The MABE, which is a useful measure to evaluate the overall performance of the model, equals 18 %. This means that the model proposed here estimates the S_{ery} with a mean error of 18 %. Figure 7 and the upper panel of Fig. 8 show that, in some cases, negative S_{ery} doses are modeled, which is a sign that the model does not always give realistic results. This is the case only during winter, when the S_g values are much lower than during the other seasons. When moderate to high Q_{O_3} values are combined with low S_g values, this leads to negative modeled S_{ery} values according to the regression equation. From Fig. 8 it is also clear that there is a seasonal cycle in the residual values. Therefore, it would be better to perform the multiple regression analysis on a seasonal scale.

4.4.2 Seasonal MLR analysis using total ozone column, global solar radiation and aerosol optical depth

The multiple regression equations for the different seasons are presented below.

Spring:

$$S_{ery} = 1016 + 0.0001542 \times S_g - 5.660 \times Q_{O_3} + 92.11 \times \tau_{aer} + \epsilon \quad (7)$$

Summer:

$$S_{ery} = 2010 + 0.0001481 \times S_g - 6.737 \times Q_{O_3} - 134.2 \times \tau_{aer} + \epsilon \quad (8)$$

Autumn:

$$S_{ery} = -195 + 0.000143 \times S_g - 1.22 \times Q_{O_3} + 120 \times \tau_{aer} + \epsilon \quad (9)$$

Winter:

$$S_{ery} = 325 + 0.0000750 \times S_g - 1.50 \times Q_{O_3} + 101 \times \tau_{aer} + \epsilon \quad (10)$$

For all seasons, more than 80 % of the total variation in S_{ery} is explained by the combination of S_g, Q_{O_3} and τ_{aer}. This could be concluded from the adjusted R^2 values for each season. What might seem strange is the negative value of the constant term in the regression equation for autumn. However, the p value for this term is higher than 0.05, which means that this coefficient does not significantly differ from 0 at the 95 % significance level.

From Fig. 9 and Table 9, it can be concluded that the seasonal models perform well in estimating the measured S_{ery} values. The correlation between the modeled and measured

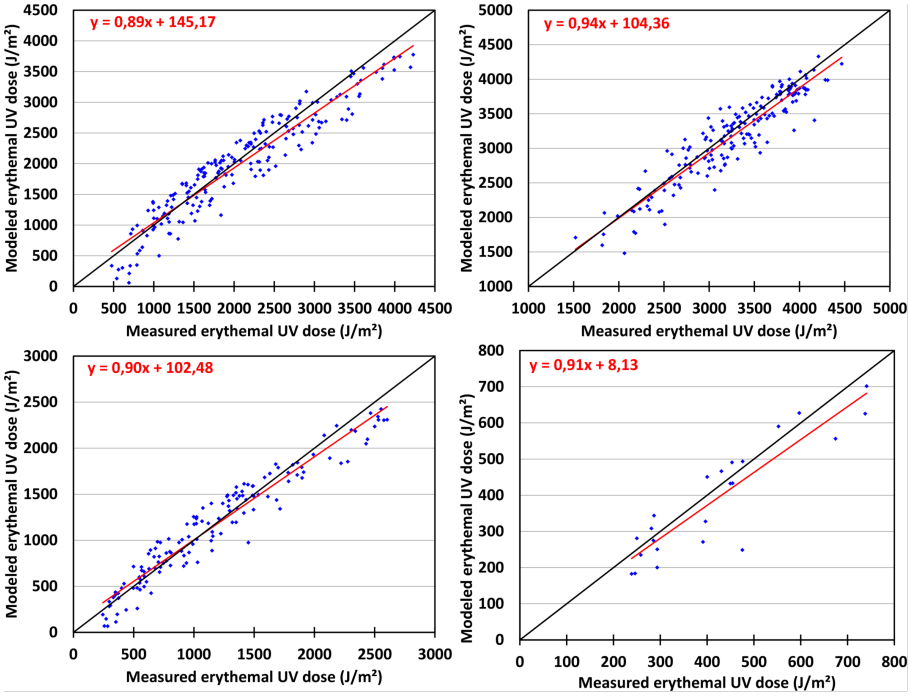

Figure 9. Scatterplots of the measured and modeled erythemal UV doses at Uccle for the 2009–2013 validation period for spring (upper left panel), summer (upper right panel), autumn (lower left panel) and winter (lower right panel). The red lines represent the regression lines of the data, and the black lines are the $f(x) = x$ lines.

Table 10. Seasonal influence of the variation of S_g, Q_{O_3} and τ_{aer} on S_{ery}.

	Spring	Summer	Autumn	Winter
τ_{aer}	1 %	−1 %	2 %	4 %
Q_{O_3}	−9 %	−4 %	−2 %	−15 %
S_g	37 %	18 %	53 %	32 %

values varies between 0.90 (in winter) and 0.97 (in autumn). The regression equations are shown in both Fig. 9 and Table 9. The negative MBE values (except for autumn, which has a value close to 0) show that each model has a tendency to underestimate the measured values. The summer model performs best, with an absolute mean model error of only 6 %. The relative residuals (shown in Fig. 10) are smallest in summer, which again points out that the performance of the summer model in estimating the measured S_{ery} is the best. The spring and autumn models have much higher relative residuals.

To determine the influence of the variation in the parameters on the variation in UV, the standard deviation of each parameter is multiplied with its corresponding regression coefficient, which is then divided by the average S_{ery} value. This will give an idea of the magnitude of the influence of each parameter on UV. The results are given in Table 10. Changes in the variation of S_g (Table 10) are the most important and

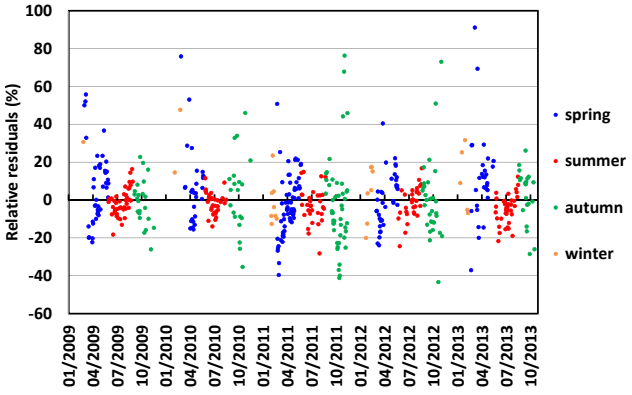

Figure 10. Relative residuals (= (measured−modeled) / measured × 100) of the seasonal multiple regression models. The colors represent the different seasons: blue – spring; red – summer; green – autumn; and orange – winter.

lead to changes in S_{ery} between 18 % (in summer) and 53 % (in autumn). The influence of the variation in Q_{O_3} and τ_{aer} is much smaller. Changes in the variation of Q_{O_3} always lead to negative changes in S_{ery} (from −2 % in summer to −15 % in winter), whereas the influence of a change in variation of τ_{aer} varies from a negative value (−1 % change in S_{ery}) in summer to positive values in the other seasons, with a maximum of 4 % in winter (Table 10). τ_{aer} and S_g have their low-

est contribution in summer. Q_{O_3} on the other hand has the lowest contribution in autumn. The influence of Q_{O_3} is highest during winter and spring, and this is in accordance with the variation in Q_{O_3} itself, which is largest during winter and early spring. For τ_{aer} also, the absolute contribution to the variation in S_{ery} is the highest in winter. As the path length of UV irradiance is higher during winter, aerosols and ozone have more opportunity to influence UV irradiance on its way to the Earth's surface.

The influence of τ_{aer} on S_{ery} in the seasonal models is positive (except in summer), which is also the case when the τ_{aer} is used as the only explanatory variable in the models. This does not agree with what was observed in the trend analysis of the monthly anomalies time series, where an increase in S_{ery} is accompanied by a decrease in τ_{aer}. It has to be taken into account, however, that the negative general τ_{aer} trend is not significant. Also, this negative trend in τ_{aer} is too much driven by the high but sparse values at the beginning of the studied time period. Depending on the circumstances and the physical and optical properties of aerosols, the influence of τ_{aer} on global and UV irradiance can be either positive or negative. An increase in τ_{aer} could lead to an increase in global and UV radiation if the increase in τ_{aer} were caused by an increase in the amount of small scattering aerosol particles. If there were predominantly particles of size much smaller than the UV wavelengths (i.e., freshly formed particles, Aitken mode particles) and of high single-scattering albedo (SSA), the UV radiation could be enhanced by the multiple scattering by these aerosols. However, if the amount of all particles exceeded a certain (albeit in this study not possible to determine) threshold value, extinction would take over, and from this point an increase in τ_{aer} would lead to a decrease in UV irradiance. The aerosol composition, which determines whether a mixture is rather scattering or absorbing, the aerosol amount and the aerosol size distribution determine whether an increase in τ_{aer} will lead to either an increase or decrease in UV irradiance. At Uccle there is no information on these parameters; hence it is difficult to unambiguously characterize the influence of τ_{aer} on UV irradiance. The aerosol effects on UV in this study are solely based on τ_{aer} and not on aerosol absorption property changes. Recently, a nephelometer and an aethalometer have been installed at our site in Uccle, so in the future their measurements can be combined to derive the SSA. This will shine a new light on the influence of the aerosols on the UV radiation at Uccle. Antón et al. (2011) already reported that it is hard to determine the effect of aerosols due to their temporal and spatial variability and the difficulties associated with their characterization.

It has already been shown that S_g has the largest influence on S_{ery}, so an important issue that needs to be addressed is whether Q_{O_3} and τ_{aer} are actually necessary to capture the variation in S_{ery}. This was investigated by performing the MLR analysis using (1) only S_g, (2) S_g combined with Q_{O_3} and (3) S_g combined with τ_{aer} as explanatory variables. The adjusted R^2 value, the MABE and the correlation between modeled and measured S_{ery} values are given in Table 11. From these values, it becomes clear that τ_{aer} only has a minor contribution to the regression model and that, to describe the changes in S_{ery}, τ_{aer} might not be needed, except perhaps for spring. For this reason it seems unnecessary to include τ_{aer} in the MLR analysis. Q_{O_3} seems to be a more important explanatory variable, as the adjusted R^2 increases for all seasons, except summer, and the MABE of the models decreases, except in summer, when combining S_g and Q_{O_3}. The correlation between modeled and measured values does not change much, except in winter (from 0.75 when using only S_g to 0.89 when combining S_g and Q_{O_3}). The developed regression models are only valid for Uccle. For other sites, it might be necessary to include all three parameters in the regression models in order to explain the observed variation in S_{ery}.

Table 11. Results of MLR analysis with only S_g, S_g combined with Q_{O_3} and S_g combined with τ_{aer} as explanatory variables.

	S_g	S_g+Q_{O_3}	S_g+τ_{aer}
Adjusted R^2			
Spring	0.85	0.90	0.85
Summer	0.81	0.85	0.81
Autumn	0.95	0.95	0.95
Winter	0.65	0.81	0.65
MABE (in %)			
Spring	14.53	14.40	14.33
Summer	6.39	6.21	6.21
Autumn	15.45	15.25	14.89
Winter	22.20	14.25	21.47
Correlation modeled and measured UV values			
Spring	0.93	0.95	0.93
Summer	0.91	0.93	0.91
Autumn	0.96	0.96	0.96
Winter	0.75	0.89	0.76

5 Conclusions

Of the variables known to influence the UV irradiance that reaches the ground, the variability of global solar radiation, total ozone column and aerosol optical depth (at 320.1 nm) are studied by performing a trend analysis, a change-point analysis and a multiple linear regression analysis. This is done in order to determine their changes over a 23 year time period (1991–2013) and their possible relation to the observed UV changes at Uccle, Belgium. S_{ery}, Q_{O_3} and τ_{aer} are measured by the Brewer spectrophotometer instruments, and S_g measurements are performed by a CM11 pyranometer.

The trend over the past 23 years was determined for each variable using their monthly anomaly values. An overall positive trend was present in the time series of S_{ery}, S_g and Q_{O_3} of respectively +7 % (± 2 %), +4 % (± 1 %) and +2.6 % (± 0.4 %) per decade. In contrast, the trend of τ_{aer}, equal to −8 % (± 5 %) per decade, is insignificantly negative over the investigated time period. The sign and magnitude of the trends observed at Uccle agree with results found in the literature for stations of comparable latitude. The increase in S_g since 1991 could be interpreted as a sign of continuing global brightening over Belgium. The decrease in sulfur and black carbon emissions after 1989, which resulted in enhanced global solar radiation at the Earth's surface, is most probably also the driving mechanism for the decrease in τ_{aer}, which in turn could have an influence by increasing the UV irradiance.

For both S_{ery} and S_g, there is an increase in the frequency of higher values towards the second part of the study period (2003–2013), without the entire frequency distribution shifting. This could be explained by a decrease in cloudiness towards 2003–2013. Several studies report on a decrease in cloud cover over the past decades and a tendency for cumuliform clouds to replace stratiform clouds (Norris and Slingo, 2009; Eastman and Warren, 2013). This would increase both S_g and S_{ery} due to enhanced scattering. However, other parameters (such as ozone and aerosols) could also influence the values of S_{ery} and S_g. As opposed to S_{ery} and S_g, a clear shift can be seen in the entire frequency distribution of daily Q_{O_3} values, with both minimum and maximum values having increased from the 1991–2002 period to the 2003–2013 period, which supports literature findings about an ozone recovery around the end of the 1990s. From the frequency distribution of daily τ_{aer} values, it can be derived that, between 1991 and 2002, higher τ_{aer} values were more frequently present than during the last period (2003–2013), which is in agreement with the overall decrease over the last 23 years.

The seasonal trends of the four variables were also studied and are similar between S_{ery} and S_g, with a positive trend for all seasons except winter. The Q_{O_3} trend is positive for spring and summer. Normally, we would expect a positive Q_{O_3} trend to be accompanied with a negative trend in S_{ery}. The fact that the observed trends have the same sign could indicate that the change in UV irradiance is not only influenced by a change in total ozone values. The τ_{aer} trend is negative during summer and autumn. The trend in spring is not significant, and not enough winter data were present to calculate a winter trend.

For Q_{O_3} and S_{ery}, a significant change point (i.e., a significant shift in the mean of the monthly anomalies) was detected around February/March 1998, which has no known instrumental cause. The timing of the change point in ozone corresponds to results found in the literature where studies define the change around this time period as the start of ozone recovery, following the regulations of the Montreal Protocol. The trend in the ozone time series at Uccle does not seem very affected by the eruption of the Pinatubo, which took place in June 1991.

To investigate the influences of S_g, Q_{O_3} and τ_{aer} on S_{ery}, a multiple linear regression was performed using daily values between 1991 and 2008. The three variables together explain 94 % of the total variation in the observed S_{ery} values. S_g has the largest influence on S_{ery}, followed by Q_{O_3} and τ_{aer}. Data of 2009–2013 were used to validate the model, and the MBA and MABE were calculated to evaluate the model performance in terms of overestimation and average error. The MBE value of the model is −3 %, which means that the model has a slight tendency to underestimate the measured UV irradiance values. The average error of the model in the estimation of the measurements is equal to 18 %. Overall, the model represents reality well; however sometimes during winter, negative S_{ery} values were modeled. For this reason, seasonal regression models have been developed.

All seasonal models perform rather well in explaining the variation in UV irradiance, with adjusted R^2 values being larger than 0.8. The negative MBE values show the models' tendencies to underestimate UV irradiance. Again, S_g has the largest influence on S_{ery}, followed by Q_{O_3} and τ_{aer}. The summer regression model performs best, based on the very low MABE values.

What is seen in reality (i.e., an increase in S_{ery} accompanied with an increase in Q_{O_3} and a decrease in τ_{aer}) is not always what is represented by the models. According to the regression models, Q_{O_3} and τ_{aer} respectively always have a negative and positive influence on S_{ery}. However, as S_g is obviously the most important factor in explaining the variation in S_{ery}, the increase in Q_{O_3} (which would be expected to lead to a decrease in S_{ery}) and the change in τ_{aer} seem to be compensated for by the increase in S_g.

The question that remains is whether Q_{O_3} and τ_{aer} are needed as explanatory variables in the multiple linear regression models. It has been shown that the contribution of τ_{aer} to explaining the variation in S_{ery} is very small, and it can be concluded that this variable is not really needed in the multiple linear regression model. Also its influence is already partly represented by S_g. Q_{O_3}, however, does seem to be a more important factor in capturing the variation in S_{ery} and cannot be discarded from the regression models. It has to be kept in mind that the regression models are only valid for Uccle, which means that for other sites it might be necessary to include all three parameters in the regression models.

Acknowledgements. This research was performed under the project AGACC-II, contract SD/CS/07A, of the Belgian Science Policy. We thank Christian Hermans (Belgian Institute for Space Aeronomy, Belgium) for establishing and maintaining the AERONET site at Uccle. We would also like to thank the anonymous reviewers and the editor (S. Kazadzis) for their useful input.

Edited by: S. Kazadzis

References

Alpert, P., Shvainshtein, O., and Kishcha, P.: AOD trends over megacities based on space monitoring using MODIS and MISR, Am. J. Clim. Change, 12, 117–131, doi:10.4236/ajcc.2012.13010, 2012.

Antón, M., Serrano, A., Cancillo, M. L., and García, J. A.: An empirical model to estimate ultraviolet erythemal transmissivity, Ann. Geophys., 27, 1387–1398, doi:10.5194/angeo-27-1387-2009, 2009.

Antón, M., Gil, J. E., Fernández-Gálvez, J., Lyamani, H., Valenzuela, A., Foyo-Moreno, I., Olmo, F. J., and Alados-Arboledas, L.: Evaluation of the aerosol forcing efficiency in the UV erythemal range at Granada, Spain, J. Geophys. Res., 116, D20214, doi:10.1029/2011JD016112, 2011.

Augustine, J. A., Hodges, G. B., Dutton, E. G., Michalsky, J. J., and Cornwall, C. R.: An aerosol optical depth climatology for NOAA's national surface radiation budget network (SURFRAD), J. Geophys. Res., 113, D11204, doi:10.1029/2007JD009504, 2008.

Bais, A. F., Kazadzis, S., Meleti, C., Kouremeti, N., Kaurola, J., Lakkala, K., Slaper, H., den Outer, P. N., Josefsson, W., Feister, U., and Janouch, M.: Variability in spectral UV irradiance at seven European stations, edited by: Gröbner J., One century of UV radiation research. Proceedings of the UV conference, Davos, Switzerland, July 2007, 1, 27–28, 2007.

Bais, A. F., Tourpali, K., Kazantzidis, A., Akiyoshi, H., Bekki, S., Braesicke, P., Chipperfield, M. P., Dameris, M., Eyring, V., Garny, H., Iachetti, D., Jöckel, P., Kubin, A., Langematz, U., Mancini, E., Michou, M., Morgenstern, O., Nakamura, T., Newman, P. A., Pitari, G., Plummer, D. A., Rozanov, E., Shepherd, T. G., Shibata, K., Tian, W., and Yamashita, Y.: Projections of UV radiation changes in the 21st century: impact of ozone recovery and cloud effects, Atmos. Chem. Phys., 11, 7533–7545, doi:10.5194/acp-11-7533-2011, 2011.

Bartlett, L. M. and Webb, A. R.: Changes in ultraviolet radiation in the 1990s: Spectral measurements from Reading, England, J. Geophys. Res., 105, 4889–4893, doi:10.1029/1999JD900493, 2000.

Bernhard, G., Booth, C. R., Ehramjian, J. C., and Nichol, S. E.: UV climatology at McMurdo Station, Antarctica, based on Version 2 data of the National Science Foundation's Ultraviolet Radiation Monitoring Network, J. Geophys. Res., 111, D11201, doi:10.1029/2005JD005857, 2006.

Bojkov, R. D., Bishop, L., and Fioletov, V. E.: Total ozone trends from quality-controlled ground-based data (1964–1994), J. Geophys. Res., 100, 25867–25876, doi:10.1029/95JD02907, 1995.

Cheymol, A. and De Backer, H.: Retrieval of the aerosol optical depth in the UV-B at Uccle from Brewer ozone measurements over a long time period 1984–2002, J. Geophys. Res., 108, 4800, doi:10.1029/2003JD003758, 2003.

Chiaccio, M., Ewen, T., Wild, M., Chin, M., and Diehl, T.: Decadal variability of aerosol optical depth in Europe and its relationship to the temporal shift of the North Atlantic Oscillation in the realm of dimming and brightening, J. Geophys. Res., 116, D02108, doi:10.1029/2010JD014471, 2011.

Chubarova, N. Y.: UV variability in Moscow according to long term UV measurements and reconstruction model, Atmos. Chem. Phys., 8, 3025–3031, doi:10.5194/acp-8-3025-2008, 2008.

Cordero, R. R., Seckmeyer, G., Pissulla, D., and Labbe, F.: Exploitation of spectral direct UV irradiance measurements, Metrologia, 46, 19–25, doi:10.1088/0026-1394/46/1/003, 2009.

De Backer, H.: Time series of daily erythemal UV doses at Uccle, Belgium, Int. J. Remote Sens., 30, 4145–4145, doi:10.1080/01431160902825032, 2009.

De Backer, H. and De Muer, D.: Intercomparison of total ozone data measured with Dobson and Brewer ozone spectrophotometers at Uccle (Belgium) from January 1984 to March 1991, including zenith sky observations, J. Geophys. Res., 96, 20711–20719, doi:10.1029/91JD02159, 1991.

De Bock, V., De Backer, H., Mangold, A., and Delcloo, A.: Aerosol optical depth measurements at 340 nm with a Brewer spectrophotometer and comparison with Cimel sunphotometer observations at Uccle, Belgium, Atmos. Meas. Tech., 3, 1577–1588, doi:10.5194/amt-3-1577-2010, 2010.

de La Casinière, A., Lamine Touré, M., Masserot, D., Cabot, T., and Pinedo Vega, J. L.: Daily doses of biologically active UV radiation retrieved from commonly available parameters, Photochem. Photobiol., 76, 171–175, doi:10.1562/0031-9655(2002)0760171DDOBAU2.0.002, 2002.

de Meij, A., Pozzer, A., and Lelieveld, J.: Trend analysis in aerosol optical depths and pollutant emission estimates between 2000 and 2009, Atmos. Environ., 51, 75–85, doi:10.1016/j.atmosenv.2012.01.059, 2012.

den Outer, P. N., Slaper, H., Matthijsen, J., Reinen, H. A. J. M., and Tax, R.: Variability of ground-level ultraviolet: Model and Measurement, Radiat. Prot. Dos., 91, 105–110, 2000.

den Outer, P. N., Slaper, H., Kaurola, J., Lindfors, A., Kazantzidis, A., Bais, A. F., Feister, U., Junk, J., Janouch, M., and Josefsson, W.: Reconstructing of erythemal ultraviolet radiation levels in Europe for the past 4 decades, J. Geophys. Res., 115, D10102, doi:10.1029/2009JD012827, 2010.

Díaz, S., Deferrari, G., Martinioni, D., and Oberto, A.: Regression analysis of biologically effective integrated irradiances versus ozone, clouds and geometric factors, J. Atmos. Sol-Terr. Phy., 62, 629–638, doi:10.1016/S1364-6826(00)00055-9, 2000.

Diffey, B. L.: Solar ultraviolet radiation effects on biological systems, Phys. Med. Biol., 36, 299–328, doi:10.1088/0031-9155/36/3/001, 1991.

Durbin, J. and Watson, G. S.: Testing for serial correlation in least squares regression III, Biometrika, 58, 1–19, 1971.

Eastman, R. and Warren, S. G.: A 39-yr survey of cloud changes from land stations worldwide 1971–2009: long-term trends, relation to aerosols and expansion of the tropical belt, J. Climate, 26, 1286-1303, doi:10.1175/JCLI-D-12-00280.1, 2013.

Eck, T. F., Holben, B. N., Reid, J. S., Dubovik, O., Smirnov, A., O'Neill, N. T., Slutsker, I., and Kinne, S.: Wavelength dependence of the optical depth of biomass burning, urban, and desert dust aerosols, J. Geophys. Res., 104, 31333–31349, doi:10.1029/1999JD900923, 1999.

Eleftheratos, K., Kazadzis, S., Zerefos, C. S., Tourpali, K., Meleti, C., Balis, D., Zyrichidou, I., Lakkala, K., Feister, U., Koskela, T., Heikkilä, A., and Karhu, J. M.: Ozone and Spectroradiometric UV Changes in the Past 20 Years over High Latitudes, Atmos.-Ocean, doi:10.1080/07055900.2014.919897, 2014.

El Shazly, S. M., Kassem, Kh. O., Hassan, A. A., and El-Nobi, E. F.: An empirical model to estimate UV index in

some upper Egypt regions, Resour. Environ., 2, 216–227, doi:10.5923/j.re.20120205.05, 2012.

Fioletov, V. E., McArthur, L. J. B., Kerr, J. B., and Wardle, D. I.: Long-term variations of UV-B irradiance over Canada estimated from Brewer observations and derived from ozone and pyranometers measurements, J. Geophys. Res., 106, 23009–23027, doi:10.1029/2001JD000367, 2001.

Fioletov, V. E., Kerr, J. B., Wardle, D. I., Krotkov, N., and Herman, J. R.: Comparison of Brewer ultraviolet irradiance measurements with total ozone mapping spectrometer satellite retrievals, Opt. Eng., 41, 3051–3061, doi:10.1117/1.1516818, 2002.

Fioletov, V. E., Kimlin, M. G., Krotkov, N., McArthur, L. J. B., Kerr, J. B., Wardle, D. I., Herman, J. R., Meltzer, R., Mathews, T. W., and Kaurola, J.: UV index climatology over the United States and Canada from ground-based and satellite estimates, J. Geophys. Res., 109, D22308, doi:10.1029/2004JD004820, 2004.

Fitzka, M., Simic, S., and Hadzimustafic, J.: Trends in spectral UV radiation from long-term measurements at Hoher Sonnblick, Austria, Theor. Appl. Climatol., 110, 585–593, doi:10.1007/s00704-012-0684-0, 2012.

Foyo-Moreno, I., Alados, I., and Alados-Arboledas, L.: Adaptation of an empirical model for erythemal ultraviolet irradiance, Ann. Geophys., 25, 1499-1508, doi:10.5194/angeo-25-1499-2007, 2007.

Garane, K., Bais, A. F., Kazadzis, S., Kazantzidis, A., and Meleti, C.: Monitoring of UV spectral irradiance at Thessaloniki (1990–2005): data re-evaluation and quality control, Ann. Geophys., 24, 3215–3228, doi:10.5194/angeo-24-3215-2006, 2006.

Glandorf, M., Arola, A., Bais, A., and Seckmeyer, G.: Possibilities to detect trends in spectral UV irradiance, Theor. Appl. Climatol., 81, 33–44, doi:10.1007/s00704-004-0109-9, 2005.

Gröbner, J. and Meleti, C.: Aerosol optical depth in the UVB and visible wavelength range from Brewer spectrophotometer direct irradiance measurements: 1991–2002, J. Geophys. Res., 109, D09202, doi:10.1029/2003JD004409, 2004.

Gröbner, J., Kazadzis, S., Schreder, J., Bolsée, D., Brogniez, C., De Backer, H., Di Sarra, A. G., Feister, U., Görts, P., Henriques, D., Jaroslawski, J., Simic, S., Stanec, M., Steinmetz, M., Tax, R., and Villaplana Guerrero, J. M.: Report of site visits round 2004, European Commission, Joint Research Centre, EUR 21398 EN, 171–182, 2004.

Harris, N. R. P., Kyrö, E., Staehelin, J., Brunner, D., Andersen, S.-B., Godin-Beekmann, S., Dhomse, S., Hadjinicolaou, P., Hansen, G., Isaksen, I., Jrrar, A., Karpetchko, A., Kivi, R., Knudsen, B., Krizan, P., Lastovicka, J., Maeder, J., Orsolini, Y., Pyle, J. A., Rex, M., Vanicek, K., Weber, M., Wohltmann, I., Zanis, P., and Zerefos, C.: Ozone trends at northern mid- and high latitudes – a European perspective, Ann. Geophys., 26, 1207–1220, doi:10.5194/angeo-26-1207-2008, 2008.

Herman, J. R.:, Global increase in UV irradiance during the past 30 years (1979–2008) estimated from satellite data, J. Geophys. Res., 115, D04203, doi:10.1029/2009JD012219, 2010.

Herman, J. R., Bhartia, P. K., Ziemke, J., Ahmad, Z., and Larko, D.: UV-B increases (1979–1992) from decreases in total ozone, Geophys. Res. Lett., 23, 2117–2120, doi:10.1029/96GL01958, 1996.

Holben, B. N., Tanré, D., Smirnov, A., Eck, T. F., Slutsker, I., Abuhassan, N., Newcomb, W. W., Schafer, J. S., Chatenet, B., Lavenu, F., Kaufman, Y. J., Vande Castle, J., Setzer, A., Markham, B., Clark, D., Frouin, R., Halthore, R., Karneli, A., O'Neill, N. T., Pietras, C., Pinker, R. T., Voss, K., and Zibordi, G.: An emerging ground-based aerosol climatology: Aerosol optical depth from AERONET, J. Geophys. Res., 106, 12067–12097, doi:10.1029/2001JD900014, 2001.

Hoppe, H. and Kiely, G.: Precipitation over Ireland: observed change since 1940, Phys. Chem. Earth B, 24, 91–96, 1999.

Hsu, N. C., Gautam, R., Sayer, A. M., Bettenhausen, C., Li, C., Jeong, M. J., Tsay, S.-C., and Holben, B. N.: Global and regional trends of aerosol optical depth over land and ocean using SeaWiFS measurements from 1997 to 2010, Atmos. Chem. Phys., 12, 8037–8053, doi:10.5194/acp-12-8037-2012, 2012.

Huang, M., Jiang, H., Ju, W., and Xiao, Z.: Ultraviolet radiation over two lakes in the middle and lower reaches of the Yangtze river, China: An innovative model for UV estimation, Terr. Atmos. Ocean. Sci., 22, 491–506, doi:10.3319/TAO.2011.05.02.01(A), 2011.

Journée, M. and Bertrand, C.: Improving the spatio-temporal distribution of surface solar radiation data by merging ground and satellite measurements, Remote Sens. Environ., 114, 2692–2704, doi:10.1016/j.rse.2010.06.010, 2010.

Kalliskota, S., Kaurola, J., Taalas, P., Herman, J., Celarier, E. A., and Krotkov, N. A.: Comparison of daily UV doses estimated from Nimbus 7/TOMS measurements and ground-based spectroradiometric data, J. Geophys. Res., 105, 5059–5067, doi:10.1029/1999JD900926, 2000.

Kaurola, J., Taalas, P., Koskela, T., Borkowski, J., and Josefsson, W.: Long-term variations of UV-B doses at three stations in northern Europe, J. Geophys. Res., 105, 20813–20820, doi:10.1029/2000JD900258, 2000.

Kazadzis, S., Bais, A., Amiridis, V., Balis, D., Meleti, C., Kouremeti, N., Zerefos, C. S., Rapsomanikis, S., Petrakakis, M., Kelesis, A., Tzoumaka, P., and Kelektsoglou, K.: Nine years of UV aerosol optical depth measurements at Thessaloniki, Greece, Atmos. Chem. Phys., 7, 2091–2101, doi:10.5194/acp-7-2091-2007, 2007.

Krishna Prasad, N. V., Niranjan, K., Sarma, M. S. S. R. K., and Madhavi, N.: Regression analysis of biologically effective UV-B irradiance versus ozone at Visakhapatnam, Int. J. Phys. Sci., 6, 7838–7843, doi:10.5897/IJPS11.581, 2011.

Krzýscin, J. W. and Borkowski, J. L.: Variability of the total ozone trend over Europe for the period 1950–2004 derived from reconstructed data, Atmos. Chem. Phys., 8, 2847–2857, doi:10.5194/acp-8-2847-2008, 2008.

Krzýscin, J. W., Sobolweski, P. S., Jaroslawski, J., Podgórski, J., and Rajewska-Wiech, B.: Erythemal UV observations at Belsk, Poland, in the period 1976–2008: data homogenization, climatology and trends, Acta Geophys., 59, 155–182, doi:10.2478/s11600-010-0036-3, 2011.

Lanzante, J. R.: Resistant, Robust and Non-parametric techniques for the analysis of climate data: theory and examples, including applications to historical radiosonde station data, Int. J. Climatol., 16, 1197–1226, doi:10.002/(SICI)1097-0088(199611)16:11<1197::AID-JOC89>3.0.CO;2-L, 1996.

Lindfors, A. V., Arola, A., Kaurola, J., Taalas, P., and Svenøe, T.: Longterm erythemal UV doses at Sodankylä estimated using total ozone, sunshine duration, and snow depth, J. Geophys. Res., 108, 4518, doi:10.1029/2002JD003325, 2003.

Lindfors, A., Kaurola, J., Arola, A., Koskela, T., Lakkala, K., Josefsson, W., Olseth, J. A., and Johnsen, B.: A method for reconstruction of past UV radiation based on radiative transfer modeling: applied to four stations in northern Europe, J. Geophys. Res., 112, D23201, doi:10.1029/2007JD008454, 2007.

Litynska, Z., Koepke, P., De Backer, H., Gröbner, J., Schmalwieser, A., and Vuilleumier, L.: COST action 726 final report: Long term changes and climatology of UV radiation over Europe, ISBN 978-92-898-0052-5, Luxembourg: Publications office of the European Union, doi:10.2831/12065, 2012.

Makowski, K., Jaeger, E. B., Chiacchio, M., Wild, M., Ewen, T., and Ohmura, A.: On the relationship between diurnal temperature range and surface solar radiation in Europe, J. Geophys. Res., 114, D00D07, doi:10.1029/2008JD011104, 2009.

Matthijsen, J., Slaper, H., Reinen, A. J. M. H., and Velders, G. J. M: Reduction of solar UV by clouds: A comparison between satellite-derived cloud effects and ground-based radiation measurements, J. Geophys. Res., 105, 5069–5080, doi:10.1029/1999JD900937, 2000.

Mishchenko, M. I. and Geogdzhayev, I. V.: Satellite remote sensing reveals regional tropospheric aerosol trends, Opt. Express, 15, 7423–7438, doi:10.364/OE.15.007423, 2007.

Nabat, P., Somot, S., Mallet, M., Chiapello, I., Morcrette, J. J., Solmon, F., Szopa, S., Dulac, F., Collins, W., Ghan, S., Horowitz, L. W., Lamarque, J. F., Lee, Y. H., Naik, V., Nagashima, T., Shindell, D., and Skeie, R.: A 4D climatology (1979–2010) of the monthly tropospheric aerosol optical depth distribution over the Mediterranean region from a comparative evaluation and blending of remote sensing and model products, Atmos. Meas. Tech., 6, 1287–1314, doi:10.5194/amt-6-1287-2013, 2013.

Norris, J. R. and Slingo, A.: Chapter 2: trends in observed cloudiness and earth's radiation budget, in: Clouds in the perturbed climate system: their relationship to energy balance, atmospheric dynamics and precipitation, edited by: Heintzenberg, J. and Charlson, R. J., 2009.

Norris, J. R. and Wild, M.: Trends in aerosol radiative effects over Europe inferred from observed cloud cover, solar "dimming", and solar "brightening", J. Geophys. Res., 112, D08214, doi:10.1029/2006JD007794, 2007.

Nyeki, S., Halios, C. H., Baum, W., Eleftheriadis, K., Flentje, H., Gröbner, J., Vuilleumier, L., and Wehrli, C.: Ground-based aerosol optical depth trends at three high-altitude sites in Switzerland and southern Germany from 1995 to 2010, J. Geophys. Res., 117, D18202, doi:10.1029/2012JD017493, 2012.

Reeves, J., Chen, J., Wang, X. L., Lund, R., and Lu, Q. Q.: A review and comparison of changepoint detection techniques for climate data, J. Appl. Meteorol. Clim., 46, 900–915, doi:10.1175/JAM2493.1, 2007.

Reinsel, G. C., Miller, A. J., Weatherhead, E. C., Flynn, L. E., Nagatani, R. M., Tiao, G. C., and Wuebbles, D. J.: Trend analysis of total ozone data for turnaround and dynamical contributions, J. Geophys. Res., 110, D16306, doi:10.1029/2004JD004662, 2005.

Rieder, H. E., Holawe, F., Simic, S., Blumthaler, M., Krzyscin, J. W., Wagner, J. E., Schmalwieser, A. W., and Weihs, P.: Reconstruction of erythemal UV-doses for two stations in Austria: a comparison between alpine and urban regions, Atmos. Chem. Phys., 8, 6309–6323, doi:10.5194/acp-8-6309-2008, 2008.

Rieder, H. E., Staehelin, J., Weihs, P., Vuilleumier, L., Maeder, J. A., Holawe, F., Blumthaler, M., Lindfors, A., Peter, T., Simic, S., Spichtinger, P., Wagner, J. E., Walker, D., and Ribatet, M.: Relationship between high daily erythemal UV doses, total ozone, surface albedo and cloudiness: An analysis of 30 years of data from Switzerland and Austria, Atmos. Res., 98, 9–20, doi:10.1016/j.atmosres.2010.03.006, 2010.

Rieder, H. E., Frossard, L., Ribatet, M., Staehelin, J., Maeder, J. A., di Rocco, S., Davison, A. C., Peter, T., Weihs, P., and Holawe, F.: On the relationship between total ozone and atmospheric dynamics and chemistry at midlatitudes – Part 2: The effects of the El Niño/Southern Oscillation, volcanic eruptions and contributions of atmospheric dynamics and chemistry to long-term total ozone changes, Atmos. Chem. Phys., 13, 165–179, doi:10.5194/acp-13-165-2013, 2013.

Sanchez-Lorenzo, A. and Wild, M.: Decadal variations in estimated surface solar radiation over Switzerland since the late 19th century, Atmos. Chem. Phys., 12, 8635–8644, doi:10.5194/acp-12-8635-2012, 2012.

Santer, B. D., Wigley, T. M. L., Boyle, J. S., Gaffen, D. J., Hnilo, J. J., Nychka, D., Parker, D. E., and Taylor, K. E.: Statistical significance of trends and trend differences in layer-average atmospheric temperature time series, J. Geophys. Res., 105, 7337–7356, doi:10.1029/1999JD901105, 2000.

Sasaki, M., Takeshita, S., Oyanagi, T., Miyake, Y., and Sakata, T.: Increasing trend of biologically active solar ultraviolet-B irradiance in mid-latitude Japan in the 1990s, Opt. Eng., 41, 3062–3069, doi:10.1117/1.1516823, 2002.

SCI TEC: Brewer ozone spectrophotometer, Acceptance manual, Document number AM-BA-CO5-Rev C, SCI TEC Instruments, 1988.

Smedley, A. R. D., Rimmer, J. S., Moore, D., Toumi, R., and Webb, A. R.: Total ozone and surface UV trends in the United Kingdom: 1979–2008, Int. J. Climatol., 32, 338–346, doi:10.1002/joc.2275, 2012.

Solomon, S., Qin, D., Manning, M., Alley, R. B., Berntsen, T., Bindoff, N. L., Chen, Z., Chidthaisong, A., Gregory, J. M., Hegerl, G. C., Heimann, M., Hewitson, B., Hoskins, B. J., Joos, F., Jouzel, J., Kattsov, V., Lohmann, U., Matsuno, T., Molina, M., Nicholls, N., Overpeck, J., Raga, G., Ramaswamy, V., Ren, J., Rusticucci, M., Somerville, R., Stocker, T. F., Whetton, P., Wood, R. A. and Wratt, D.: Technical Summary, in: Climate Change 2007: The Physical Science Basis. Contribution of Working Group I to the Fourth Assessment Report of the Intergovernmental Panel on Climate Change, edited by: Solomon, S., Qin, D., Manning, M., Chen, Z., Marquis, M., Averyt, K. B., Tignor, M., and Miller, H. L., Cambridge University Press, Cambridge, United Kingdom and New York, NY, USA, 19–91, 2007.

Staehelin, J., Kegel, R., and Harris, N. R. P.: Trend analysis of the homogenized total ozone series of Arosa (Switzerland) 1926–1996, J. Geophys. Res., 103, 8389–8399, doi:10.1029/97JD03650 , 1998.

Steinbrecht, W., Claude, H., Schönenborn, F., McDermid, I. S., Leblanc, T., Godin, S., Song, T., Swart, D. P. J., Meijer, Y. J., Bodeker, G. E., Connor, B. J., Kämpfer, N., Hocke, K., Calisesi, Y., Schneider, N., de la Noë, J., Parrish, A. D., Boyd, I. S., Brühl, C., Steil, B., Giorgetta, M. A., Manzini, E., Thomason, L. W., Zawodny, J. M., McCormick, M. P., Russell III, J. M., Bhartia, P. K., Stolarski, R. S., and Hollandsworth-Frith, S. M.: Long-term evolution of upper stratospheric ozone at selected stations of the

Network for the Detection of Stratospheric Change (NDSC), J. Geophys. Res., 111, D1027, doi:10.1029/2005JD006454, 2006.

Stjern, C. W., Egill Kristjánsson, J., and Hansen, A. W.: Global dimming and global brightening: an analysis of surface radiation and cloud cover data in northern Europe, Int. J. Climatol., 29, 643–653, doi:10.1002/joc.1735, 2009.

Tevini, M. and Teramura, A. H.: UV-B effects on terrestrial plants, Photochem. Photobiol., 50, 479–487, doi:10.1111/j.1751-1097.1989.tb05552.x, 1989.

Trepte, S. and Winkler, P.: Reconstruction of erythemal UV irradiance and dose at Hohenpeissenberg (1968–2001) considering trends of total ozone, cloudiness and turbidity, Theor. Appl. Climatol., 77, 159–171, doi:10.1007/s00704-004-0034-y, 2004.

United Nations Environment Programme (UNEP): Environmental effects of ozone depletion and its interactions with climate change: 2010 assessment, 236 pp., UNEP, Nairobi, Kenya, ISBN:ISBN 92-807-2312-X, 2010.

Van Malderen, R. and De Backer, H.: A drop in upper tropospheric humidity in autumn 2001, as derived from radiosonde measurements at Uccle, Belgium, J. Geophys. Res., 115, D20114, doi:10.1029/2009JD013587, 2010.

Vigouroux, C., De Mazière, M., Demoulin, P., Servais, C., Hase, F., Blumenstock, T., Kramer, I., Schneider, M., Mellqvist, J., Strandberg, A., Velazco, V., Notholt, J., Sussmann, R., Stremme, W., Rockmann, A., Gardiner, T., Coleman, M., and Woods, P.: Evaluation of tropospheric and stratospheric ozone trends over Western Europe from ground-based FTIR network observations, Atmos. Chem. Phys., 8, 6865–6886, doi:10.5194/acp-8-6865-2008, 2008.

Weatherhead, C. E., Reinsel., G. C., Tiao, G. C., Meng, X.-L., Choi, D., Cheang, W.-K., Keller, T., DeLuisi, J., Wuebbles, D. J., Kerr, J. B., Miller, A. J., Oltmans, S. J., and Frederick, J. E.: Factors affecting the detection of trends: Statistical considerations and applications to environmental data, J. Geophys. Res., 103, 17149–17161, doi:10.1029/98JD00995, 1998.

Wenny, B. N., Saxena, V. K., and Frederick, J. E.: Aerosol optical depth measurements and their impact on surface levels of ultraviolet-B radiation, J. Geophys. Res., 106, 17311–17319, doi:10.1029/2001JD900185, 2001.

Wild, M., Trüssel, B., Ohmura, A., Long, C. N., König-Langlo, G., Dutton, E. G., and Tsvetkov, A.: Global dimming and brightening: an update beyond 2000, J. Geophys. Res., 114, D00D13, doi:10.1029/2008JD011382, 2009.

Williams, J. E., den Outer, P. N., Slaper, H., Matthijsen, J., and Kelfkens, G.: Cloud induced reduction of solar UV-radiation: A comparison of ground-based and satellite based approaches, Geophys. Res. Lett., 31, L03104, doi:10.1029/2003GL018242, 2004.

Williams, M. N., Gómez Grajales, C. A., and Kurkiewicz, D.: Assumptions of multiple regression: correcting two misconceptions, Pract. Ass. Res. Eval., 18, ISSN 1531-7714, 2013.

WMO (World Meteorological Organization), Scientific Assessment of Ozone Depletion: 2006, Global Ozone Research and Monitoring Project-Report No. 50, 572 pp., Geneva, Switzerland, 2006

Zerefos, C. S., Balis, D. S., Bais, A. F., Gillotay, D., Simon, P. C., Mayer, B., and Seckmeyer, G.: Variability of UV-B at four stations in Europe, Geophys. Res. Lett., 24, 1363–1366, 1997.

Zerefos, C., Balis, D., Tzortziou, M., Bais, A., Tourpali, K., Meleti, C., Bernhard, G., and Herman, J.: A note on the interannual variations of UV-B erythemal doses and solar irradiance from ground-based and satellite observations, Ann. Geophys., 19, 115–120, doi:10.5194/angeo-19-115-2001, 2001.

Zerefos, C. S., Tourpali, K., Eleftheratos, K., Kazadzis, S., Meleti, C., Feister, U., Koskela, T., and Heikkilä, A.: Evidence of a possible turning point in solar UV-B over Canada, Europe and Japan, Atmos. Chem. Phys., 12, 2469–2477, doi:10.5194/acp-12-2469-2012, 2012.

Ziemke, J. R., Chandra, S., Herman, J., and Varotsos, C.: Erythemally weighted UV trends over northern latitudes derived from Nimbus 7 TOMS measurements, J. Geophys. Res., 105, 7373–7382, 2000.